AD-A136 124 THE STRENGTH AND BEHAVIOR OF STEEL FIBER-REINFORCED CONCRETE UNDER COMBIN..(U) COLORADO UNIV AT BOULDER DEPT OF CIVIL ENVIRONMENTAL AND ARCH.. 1/4

UNCLASSIFIED R W MEIER ET AL. MAY 83 AFOSR-TR-83-0974 F/G 13/3 NL

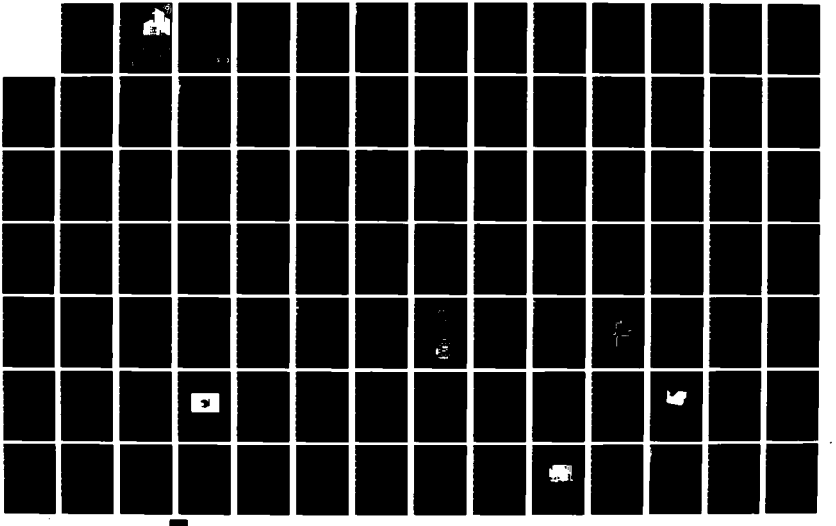

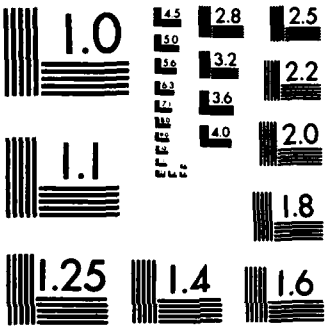

AFOSR-TR- 83-0974

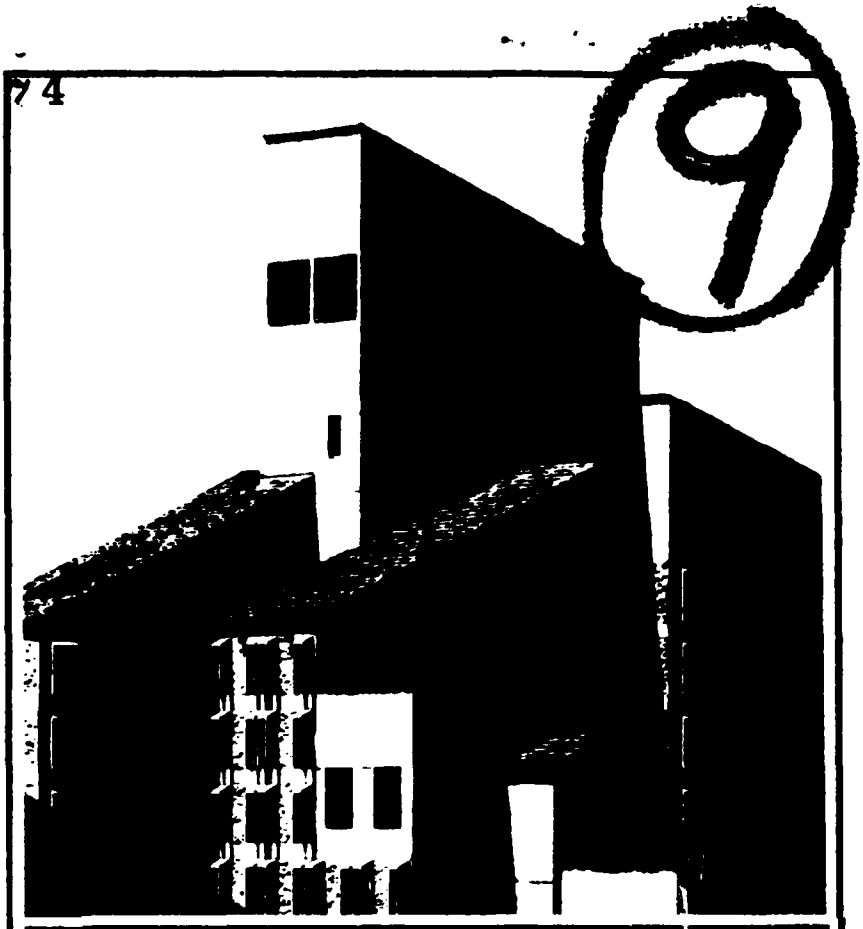

THE STRENGTH AND BEHAVIOR OF STEEL FIBER-REINFORCED CONCRETE UNDER COMBINED TENSION-COMPRESSION LOADING

by

Roger W. Meier, Hon-Yim Ko
Stein Sture and Chuan C. Feng

Department of Civil, Environmental, and Architectural Engineering

University of Colorado, Boulder
Box 428
Boulder, CO 80309

83 12 20 061

THE STRENGTH AND BEHAVIOR OF STEEL FIBER-REINFORCED CONCRETE UNDER COMBINED TENSION-COMPRESSION LOADING

by

Roger W. Meier, Hon-Yim Ko
Stein Sture and Chuan C. Feng

Submitted to Air Force Office of Scientific Research

under

Grant No. AFOSR-81-0072

Hon-Yim Ko
Project Director

May, 1983

UNCLASSIFIED

SECURITY CLASSIFICATION OF THIS PAGE (When Data Entered)

REPORT DOCUMENTATION PAGE	READ INSTRUCTIONS BEFORE COMPLETING FORM
1. REPORT NUMBER: AFOSR-TR-83-0974	2. GOVT ACCESSION NO.: AD-A136124
3. RECIPIENT'S CATALOG NUMBER	
4. TITLE (and Subtitle): THE STRENGTH AND BEHAVIOR OF STEEL FIBER-REINFORCED CONCRETE UNDER COMBINED TENSION-COMPRESSION LOADING	5. TYPE OF REPORT & PERIOD COVERED: INTERIM
	6. PERFORMING ORG. REPORT NUMBER
7. AUTHOR(s): ROGER W MEIER, CHUAN C FENG, HON-YIM KO, STEIN STURE	8. CONTRACT OR GRANT NUMBER(s): AFOSR-81-0072
9. PERFORMING ORGANIZATION NAME AND ADDRESS: UNIVERSITY OF COLORADO, BOULDER, DEPT. OF CIVIL, ENVIRONMENTAL & ARCHITECTURAL ENGR, BOULDER, CO 80309	10. PROGRAM ELEMENT, PROJECT, TASK AREA & WORK UNIT NUMBERS: 61102F, 2307/C2
11. CONTROLLING OFFICE NAME AND ADDRESS: AIR FORCE OFFICE OF SCIENTIFIC RESEARCH /NA, BOLLING AFB, DC	12. REPORT DATE: May 1983
	13. NUMBER OF PAGES: 351
14. MONITORING AGENCY NAME & ADDRESS (if different from Controlling Office)	15. SECURITY CLASS. (of this report): Unclassified
	15a. DECLASSIFICATION/DOWNGRADING SCHEDULE

16. DISTRIBUTION STATEMENT (of this Report)

Approved for Public Release; Distribution Unlimited.

17. DISTRIBUTION STATEMENT (of the abstract entered in Block 20, if different from Report)

18. SUPPLEMENTARY NOTES

19. KEY WORDS (Continue on reverse side if necessary and identify by block number)

STEEL FIBER-REINFORCED CONCRETE; DIRECT TENSION LOADING APPARATUS; BIAXIAL COMPRESSION; BIAXIAL TENSION-COMPRESSION; CONTTITUTIVE MODELING.

20. ABSTRACT (Continue on reverse side if necessary and identify by block number)

The addition of steel fibers to concrete-type materials has been shown to improve many of the engineering properties of those materials. Notable among them is an enhancement in the tensile strength of an otherwise weak and brittle material. Although much is known about the tensile strength of steel-fiber reinforced concrete (SFRC) under one-dimensional state of stress, little is known with regard to the strength behavior under multi-dimensional tension-compression loading. This is attributable to a lack (contd)

DD FORM 1 JAN 73 1473 EDITION OF 1 NOV 65 IS OBSOLETE

UNCLASSIFIED

SECURITY CLASSIFICATION OF THIS PAGE (When Data Entered)

Item 20 (cont'd)

of suitable equipment for simultaneously applying tensile and compressive stresses. The research program described herein is focused on developing such equipment to study the behavior of SFRC under combined loadings.

A review of the state-of-the-art research on the tensile strength of SFRC is given and a review of various methods of applying tensile stresses to concrete specimens is presented. The problems to be overcome in applying a pure principal tensile stress are discussed.

A tensile loading apparatus has been designed and fabricated for use with an existing fluid-cushion cubical test cell in applying simultaneously a pure principal tensile stress and transverse principal compressive stresses. This apparatus was employed in a test program to determine the strength behavior of one type of SFRC under biaxial tension-compression loading. The design of the apparatus and a description of the test program are presented.

Among the findings of this test program is that the split-cylinder and flexure tests commonly used to determine tensile strength greatly exaggerate the strength enhancement provided by the fibers when compared to the results of direct uniaxial tension tests. Notable strength enhancement was found, however, when a small transverse compressive stress was applied prior to tensile loading. As the magnitude of the compressive preload increased, the reinforcing ability of the fibers was lost due to internal microcracking.

The results of this test program were used to calibrate two mathematical constitutive models for concrete-type materials. These models were found to reflect only some of the characteristics of strength behavior exhibited by the SFRC.

ABSTRACT

The addition of steel fibers to concrete-type materials has been shown to improve many of the engineering properties of those materials. Notable among them is an enhancement in the tensile strength of an otherwise weak and brittle material. Although much is known about the tensile strength of steel-fiber reinforced concrete (SFRC) under one-dimensional states of stress, little is known with regard to the strength behavior under multidimensional tension-compression loading. This is attributable to a lack of suitable equipment for simultaneously applying tensile and compressive stresses. The research program described herein is focused on developing such equipment to study the behavior of SFRC under combined loadings.

A review of the state-of-the-art research on the tensile strength of SFRC is given and a review of various methods of applying tensile stresses to concrete specimens is presented. The problems to be overcome in applying a pure principal tensile stress are discussed.

A tensile loading apparatus has been designed and fabricated for use with an existing fluid-cushion cubical test cell in applying simultaneously a pure principal tensile stress and transverse principal compressive stresses. This apparatus was employed in a test program to determine the strength behavior of one type of SFRC under biaxial tension-compression loading. The design of the apparatus and a description of the test program are presented.

Among the findings of this test program is that the split-cylinder and flexure tests commonly used to determine tensile strength greatly exaggerate the strength enhancement provided by the fibers when comapred to the results of direct uniaxial tension tests. Notable strength enhancement was found, however, when a small transverse compressive stress was applied prior to tensile loading. As the magnitude of the compressive preload increased, the reinforcing ability of the fibers was lost due to internal microcraking.

The results of this test program were used to calibrate two mathematical constitutive models for concrete-type materials. These models were found to reflect only some of the characteristics of strength behavior exhibited by the SFRC.

CONTENTS

Contents

TABLES

FIGURES

Figure

Figure

Figure

Figure

Figure

CHAPTER 1

INTRODUCTION AND PREVIOUS WORK

1.1 Introduction

Although a significant amount of research has been done on fiber reinforced concrete (FRC) in the past two decades, there is still a considerable void in the knowledge of the strength and behavior of FRC under complex states of stress. This stems mainly from a lack of suitable equipment for applying multi-dimensional stresses and, in particular, for simultaneously applying combinations of tension and compression. The latter is of considerable importance because past investigations have shown that the addition of fibers to cementitious materials noticeably improves the tensile performance of those materials.

A review of the literature, summarized in Table 1.1, shows that an overwhelming majority of past investigations has utilized flexure testing as the basis for determining the property enhancement afforded by the addition of fiber reinforcing. In light of this, it is hardly surprising that the first uses of fiber reinforced concrete, and a majority of the applications to date, have been in flexural situations. Among the many applications in the past ten years are bridge deck overlays, highway overlays and repairs, aircraft runways, aprons, and landing mats, industrial floors, tilt-up panels and curtain walls, and utility poles.

TABLE 1.1

TEST TYPES PERFORMED BY VARIOUS RESEARCHERS

Reference	Compression	Flexure	Splitting	Direct Tension
Buckley & Everard (1974)	X	X	X	X
Chen & Carson (1971)	X		X	
Craig, et al. (1981)		X		
Craig & Radici (1981)	X	X	X	
Halvorsen & Kesler (1979)		X		
Johnston & Coleman (1974)				X
Komlos (1975)	X	X	X	X
Kormeling, et al. (1980)		X		
Krenchel (1974)		X		
Parameswaran & Rajagopalan (1975)		X		
Parimi & Rao (1974)		X		
Rajagopalan, et al. (1974)		X		
Ramakrishnan, et al. (1980)	X	X		
Ramakrishnan, et al. (1981)	X	X		
Romualdi & Mandel (1964)		X	X	
Schnutgen (1975)		X	X	
Shah & Naaman (1976)	X	X	X	X
Shah & Rangan (1971)	X	X		X
Snyder & Lankard (1972)		X		
Swamy & Al-Noori (1975)		X		
Swamy & Al-Ta'an (1981)		X		
Swamy & Staurides (1975)	X	X		
Walkus, et al. (1979)				X
Zollo (1980)		X		

All of these applications are based on the enhanced flexural performance of FRC. Although the above list is not, by any means, inclusive, it does represent some of the most frequent applications of fiber reinforcing.

There is currently some interest in using fiber reinforced concrete in more complex stress situations. One such idea is to use fiber reinforcing to eliminate some of the reinforcing bar congestion in beam-column connections, particularly in seismic applications where the enhanced ductility of FRC can be utilized. Another application is in pressure vessels where the use of fibers might cut down on the amount of hoop reinforcement needed. Yet another application is in the construction of hardened missile silos, where the superior impact resistance of FRC makes it a likely candidate.

Before designers can confidently include FRC in such structures, more information is needed regarding the performance of FRC subjected to two- and three-dimensional stress states, and as mentioned before, under combined tension-compression loading situations.

1.2 Scope of Work

A first step in this direction was taken at the University of Colorado in 1979 with a research program incorporating multiaxial compressive loading of one type of steel-fiber reinforced concrete (Egging, 1981). The research detailed herein is an extension of that test program to include tensile loading as well. This necessitated the development of an apparatus capable of applying tensile

stresses to a concrete specimen while it is simultaneously loaded in compression in other directions.

This report describes the design of this new apparatus and the results of an experimental program which utilized this apparatus to study the strength and behavior of the same fiber reinforced concrete as that used by Egging under biaxial tension-compression loading. The experimental data are analyzed exclusive of Egging's results to define the biaxial failure envelope and to determine the effectiveness of fiber reinforcing in these loading situations. Additionally, the data are examined with reference to Egging's data and the analytical models he formulated, on the basis of which the models are refined accordingly.

1.3 Previous Work

The research program presently being discussed is composed of two distinct parts. The first involves the design of a device which can apply tensile stresses to concrete and rock specimens with a minimum of boundary constraints. The second part concerns the utilization of this device in a test program to determine the effectiveness of steel-fiber reinforcing under biaxial tension-compression loading conditions. Therefore, the first two parts of this section will examine some of the methods used in the past to achieve tensile states of stress and some ways of eliminating boundary effects. The last part will review some of the properties of fiber reinforced concrete and the benefits of fiber reinforcing, and examine several theories on the mechanism of reinforcement.

1.3.1 Tensile Loading

Tensile strength is one of the most fundamental properties of concrete and yet it remains one of the least well-defined due to the lack of a test method which is both practical and reliable. Probably the most prevalent method used to determine tensile strength is the split-cylinder (Brazilian) test. The popularity of this test stems from the fact that it is not only easy to perform, but uses the same type of cylinders and testing equipment as are used to determine compressive strength. Despite its popularity, it does not accurately measure tensile strength. Past studies (Wright, 1955) have shown that the tensile strength as determined by the split-cylinder test may overestimate the true tensile strength by as much as 50 percent.

The basis of the split-cylinder test is the theoretical elastic stress distribution in a thin disk loaded along a diametral plane. By assuming plane stress conditions and analyzing the problem in two dimensions, it can be shown (Timoshenko, 1970) that a uniform tensile stress exists on the diametral plane containing the applied loads. The familiar equation

$$\sigma t = \frac{2P}{\pi dt} \tag{1.1}$$

in which σ_t is the tensile stress resulting from a load P applied to a disk of diameter d and thickness t, represents an exact solution for the idealized conditions.

The actual test as it is performed deviates from this ideal case, however, in a number of ways:

1. The test specimens are usually cylindrical and, if they are the same specimens as are used for compression testing, have a height equal to at least twice their diameter. These conditions would be better approximated as plane strain rather than plane stress. Hondros (1959) found that the stress distribution at the ends of the cylinder differs somewhat from that in the middle by virtue of having analyzed the strains in those regions. If it can be assumed that the center of the cylinder tends toward plane strain conditions while the ends tend toward a state of plane stress, the use of equations based solely on the assumption of plane stress is obviously in error.

2. The theoretical equations are based on the assumption that the applied loads are point loads. Although this could be extended to the three-dimensional case of a cylindrical specimen as line loads, the test is actually performed using packing strips between the platens of the testing machine and the specimen. These packing strips distribute the applied load over a band with some finite width which causes the stress distribution to deviate somewhat from the idealized formulation. Hondros (1959) derived an equation to describe this stress distribution by assuming the applied load to be evenly distributed over a small portion of the circumference of the disk as shown in Fig. 1.1. The general shape of the stress distribution is indicated in the upper half of Fig. 1.2 which was determined for a loaded width one-twelfth the diameter of the disk, a value chosen by Wright (1955) as being representative of the actual widths achieved with commonly used packing materials.

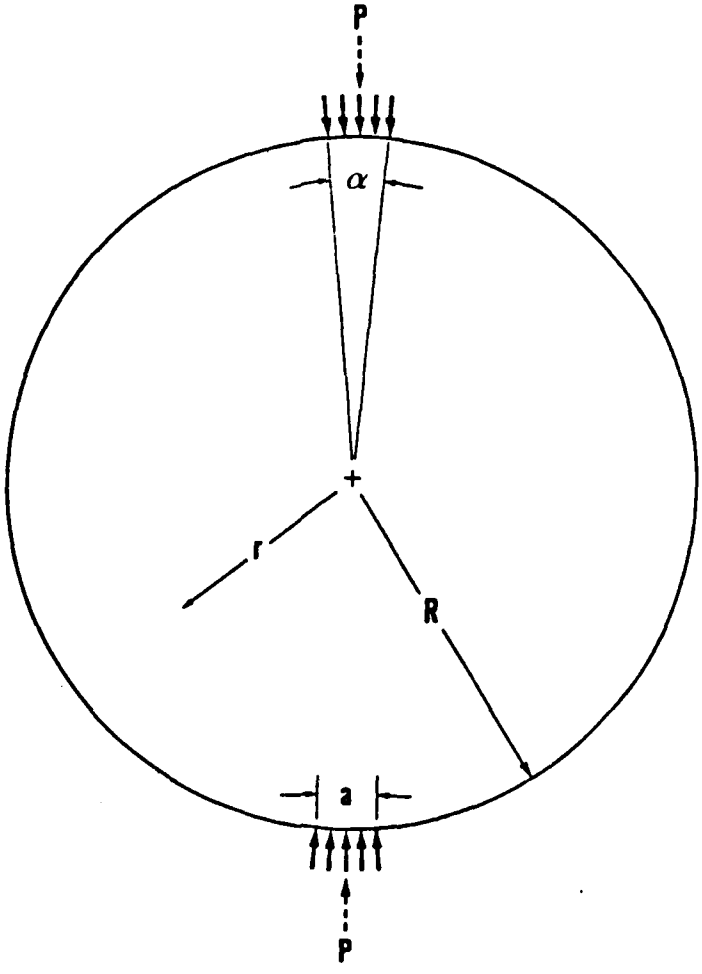

Fig. 1.1 Loading Geometry in the Split-Cylinder Test

Although the tensile stress is very closely aproximated by Equation 1.1 over the central two-thirds of the diameter, this stress quickly reverses to a very high compressive stress as the boundaries are approached.

3. It is implicitly assumed that the accompanying vertical compressive stress has no influence on the measured tensile strength. The vertical stress distribution along the splitting plane was also determined by Hondros (1959) and, as shown in the lower half of Fig. 1.2, the magnitude of these stresses is considerable in comparison to the tensile stresses. At the center of the specimen, the vertical stress is three times the horizontal splitting stress (which is, coincidently, the same ratio as predicted by Timoshenko (1934) for the ideal case of point loading) and rises to nearly twelve times the splitting stress at the point where the horizontal stress becomes zero.

4. The problem is further compounded by the existence of a longitudinal stress which results from friction between the packing strips and the specimen. The existence of this longitudinal stress can be inferred from the fact that the specimen does not fail in compression beneath the packing strips. From Fig. 1.2, it can be seen that a state of equibiaxial compression exists at the edges which is nearly twenty times the tensile splitting stress. Unless a third compressive stress perpendicular to the other two exists (i.e. a state of triaxial compression) this would be sufficient to cause compressive failure in most concretes.

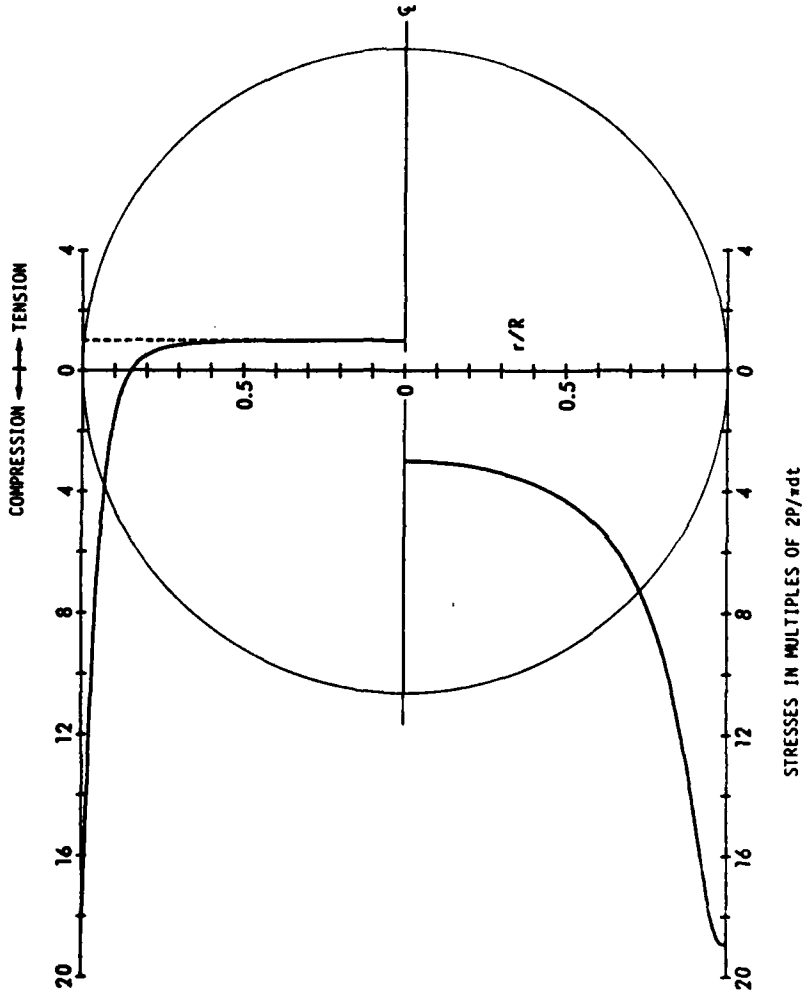

Fig. 1.2 Stress Distributions in the Split-Cylinder Test

5. Most importantly, the entire analysis is valid only if Hooke's Law is obeyed up to the point of rupture. Even brittle materials such as concrete exhibit some plastic straining prior to failure. These plastic strains tend to cause a redistribution of stress, reducing the stresses where they are highest. This would, in effect, delay failure and could be a major reason for the over-estimation of strength noted earlier.

6. Finally, the loading conditions dictate the plane on which failure will occur. This has two related effects. First, the effective sample size is quite small, being limited to the central two-thirds of the diametral plane and a band perhaps one-quarter to one-half inch wide, depending on the diameter of the specimen and the width of the packing strips. Since the measured strength of specimens tends to increase with decreasing specimen size (Pratt, et al., 1972; Heuze, 1980) the limitations on the actual amount of material being tested would promote artificially high measured strengths. The reason for this is that the range of strengths exhibited by the individual elements within any sample decreases as the number of elements decrease (i.e. the probability of an element having any one particular strength decreases as the statistical population decreases and so fewer strengths are represented). Therefore, the "weakest link" in a large specimen should exhibit a lower strength than the weakest link in a small specimen. This helps to explain why the variability of split-cylinder test results is generally less than for other types of tension tests. Similarly, since only one plane through the specimen is loaded in such a

manner as would produce failure, the probability of this being the weakest plane in the specimen is rather low, especially in comparison to a direct tension test in which, if a uniform stress distribution is achieved, every plane perpendicular to the direction of loading is a potential failure plane.

Many of these same inherent problems are shared by another commonly used "tensile" test - the loading of beams in flexure. The quotation marks are used because it is generally agreed that the flexure test does not measure tensile strength but measures a related quantity most often referred to as the Modulus of Rupture.

Extensive research has been done on the relationship between the modulus of rupture and the splitting strength. Figure 1.3 shows some of these results, all of which indicate that the flexural strength exceeds the splitting strength. Furthermore, since the slopes of the lines in Fig. 1.3 (which were determined by a least squares regression analysis of each author's data) are greater than unity, the amount by which the modulus of rupture exceeds the splitting strength increases as the splitting strength decreases. This is apparent in Fig. 1.4 which shows the ratio of the modulus of rupture to the splitting strength as a function of the splitting strength.

Probably the foremost difficulty in trying to determine tensile strength from flexure tests lies again in the fact that plastic straining occurs near failure while the formulas used to determine the tensile stress distribution in the specimen are based on elastic theory. As mentioned previously, an overestimation of

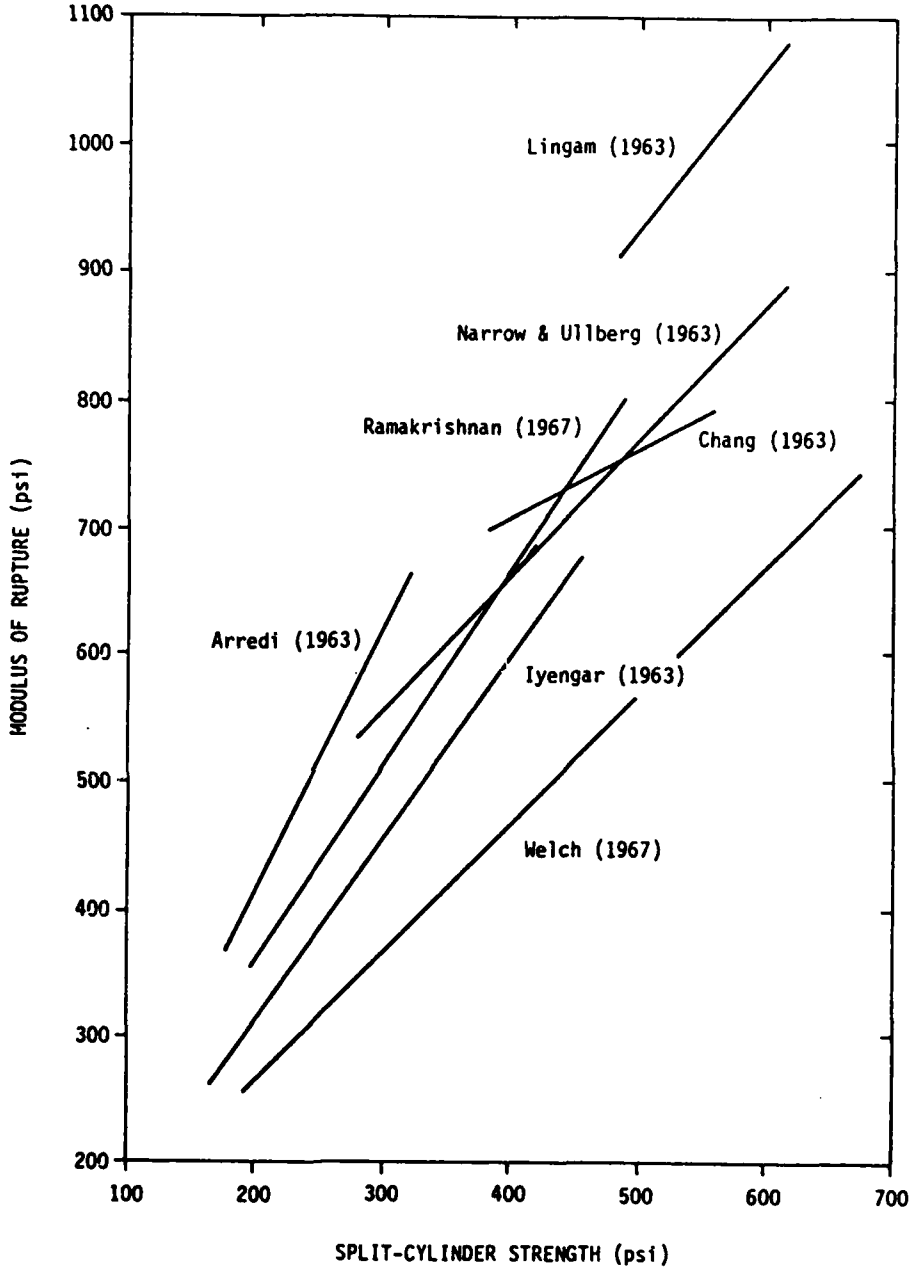

Fig. 1.3 Relationships Between Modulus of Rupture and Split-Cylinder Strength

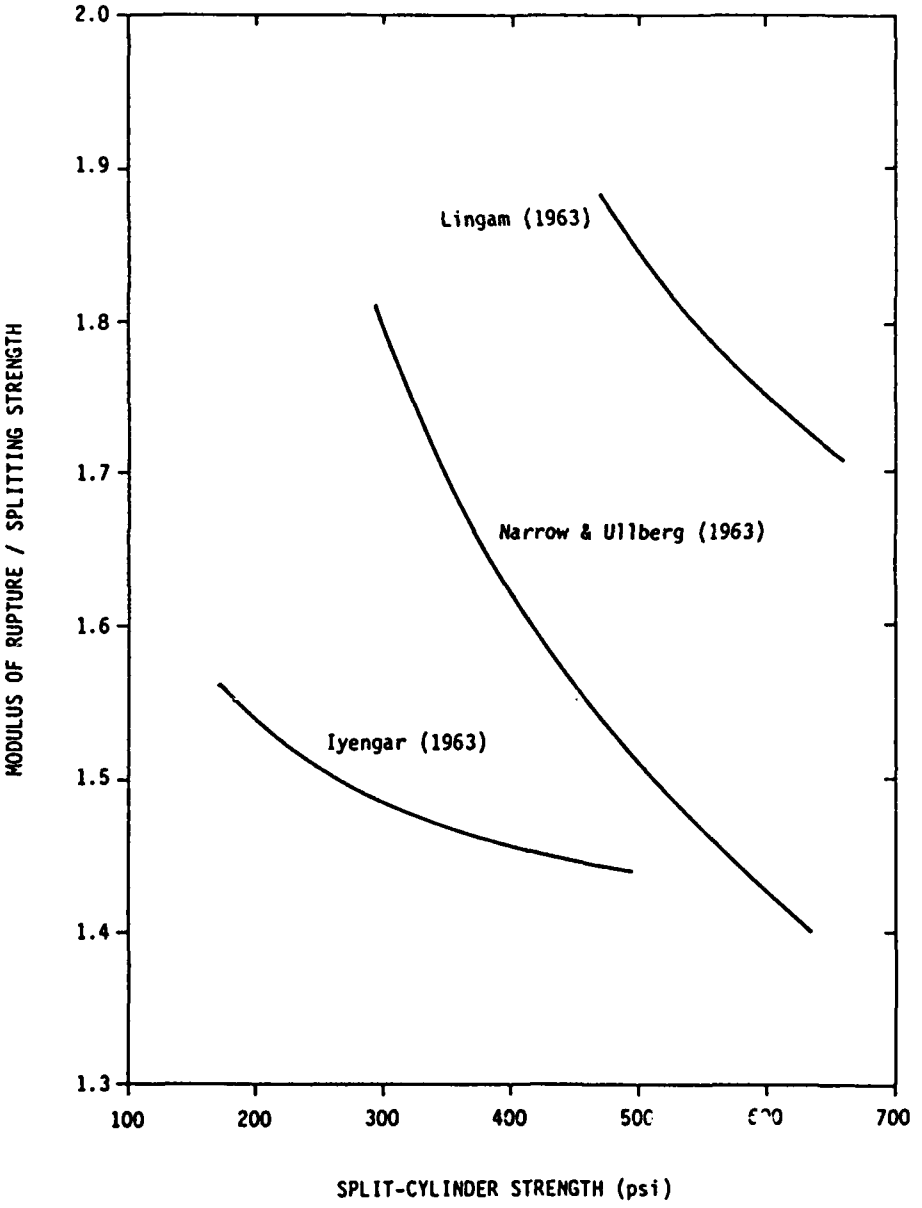

Fig. 1.4 Ratio of Modulus of Rupture to Splitting Strength as a Function of Splitting Strength

the tensile stress would result from assuming elastic behavior. Not only does plastic straining redistribute and reduce the peak tensile stress, but as plastic straining occurs, the neutral axis of the beam moves away from the tensile face, a fact not considered in the calculation of the modulus of rupture which is based on a neutral axis at midheight in the beam.

The other major limitation of the flexure test is related to the relatively small sample size. If center-point loading is used, the plane on which failure will occur is dictated by the loading conditions just as it is in split-cylinder testing. Third-point loading is used to overcome this problem as it results in a constant-moment region between the two applied loads. Even in this test, however, the concrete subjected to the maximum tensile stress is only that material near the bottom face of the specimen.

The double-punch test (Chen, 1970) is a more recent addition to methods of indirect tension testing and represents an attempt to overcome some of the problems which have been mentioned. In this test, a compressive stress is applied along the longitudinal axis of a cylindrical specimen through steel punches placed at both ends of the specimen. From classical limit plasticity analyses, a cone of material directly beneath the punch will be pushed into the specimen as a rigid body and thus split the specimen in two along a vertical diametral plane as shown in Fig. 1.5.

The advantage of this test over the split-cylinder test is that every diametral plane is a potential failure surface. Tests performed by Chen and Yuan (1980) have, in fact, shown that failure

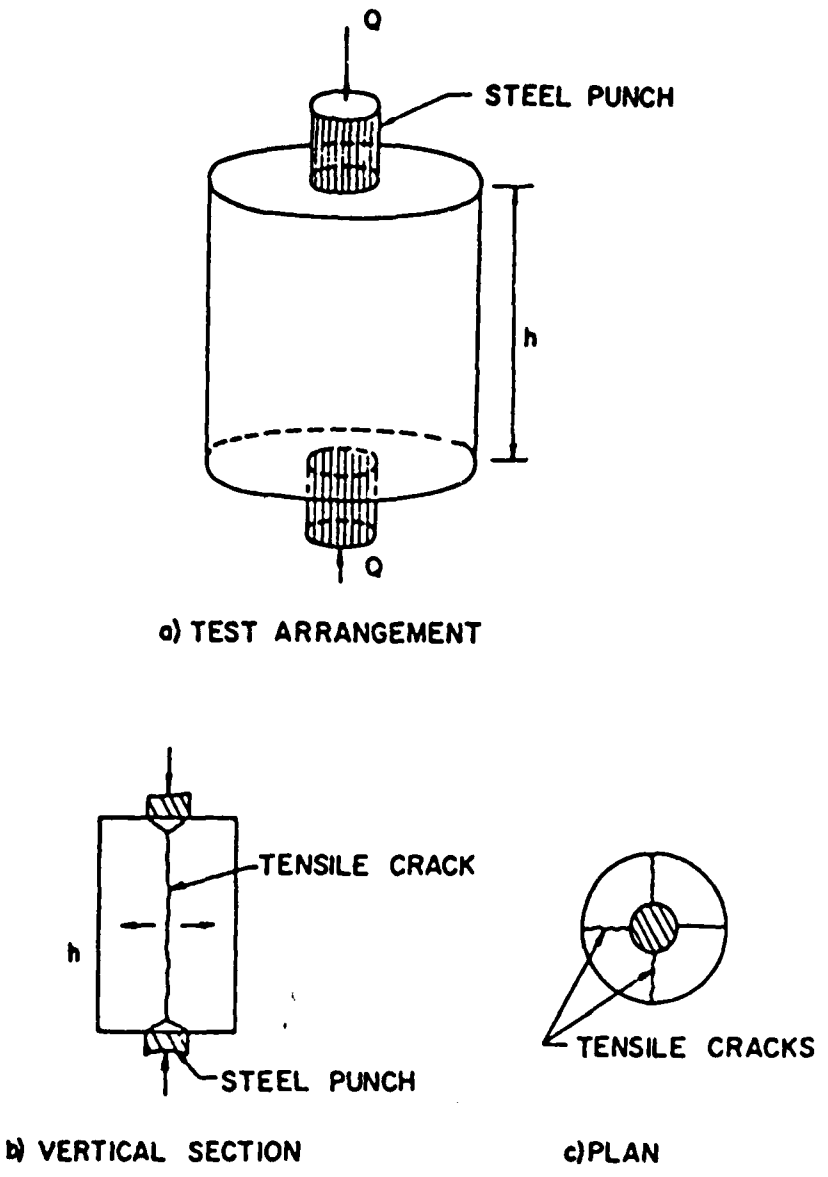

Fig. 1.5 The Double-Punch Test
(Chen [1970])

often occurs simultaneously on more than one plane. This could explain why these same investigators found that strengths measured by split-cylinder testing were generally higher than the strengths of identical concrete measured by the double-punch test. The strength difference, however, was not significant, especially in the strength range normally observed in concrete testing (Fig. 1.6). Therefore, the often large differences in measured strength between split-cylinder tests and direct tension tests have not been completely accounted for. This is probably due, in part, to the semi-empirical nature of the strength equation used with the double-punch test, and the fact that this equation was derived from a limit analysis based on the assumption of perfect plasticity at failure. This does not accurately describe the stress-strain response of concrete either.

As a rule, nearly all of the other methods of tension testing (diagonal splitting of cubes, splitting of beams, torsion of solid and hollow cylinders) suffer from the same problems already mentioned. The solution, of course, is to load the specimens in direct tension. Many different methods have been used in the past to achieve uniaxial tension[1] but most of them have the common feature that a special specimen with a reduced cross-sectional area is required. This, in addition to the often elaborate equipment necessary to grip and hold the specimen and apply the loads, has precluded their use on a widespread basis. The special shapes are required to ensure that failure will occur sufficiently far from the

---

[1] A comprehensive review of many methods proposed for direct tension testing appears in "Direct Tensile Test of Concrete: Survey Results," RILEM Bull. No. 21 (1963).

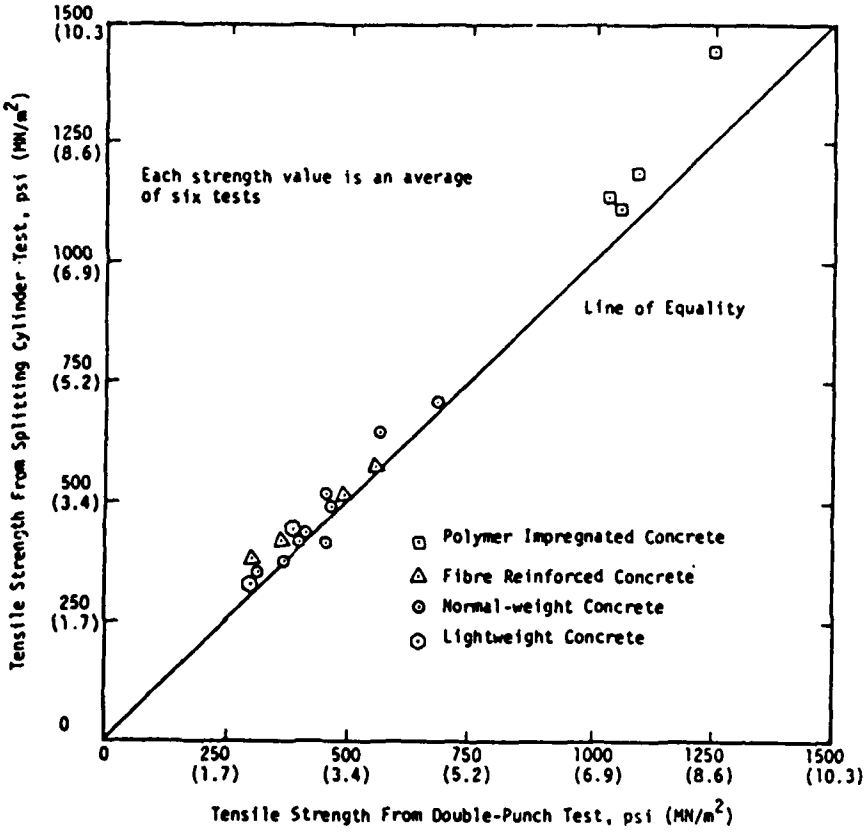

Fig. 1.6 Relationship Between Tensile Strengths as Measured in the Double-Punch and Split-Cylinder Tests (Chen and Yuan [1980])

ends of the specimen and beyond the influence of the gripping devices. In practice, this has not always been achieved. Often the specimens fail near the change in cross-section due to local stress concentrations. Another problem frequently encountered is eccentricity in the line of action of the applied force. This can be caused by imperfect alignment of the gripping devices (a problem frequently encountered with methods which incorporate studs cast into the ends of the specimens as a means of affixing the specimen to the loading platen) or the inability of the gripping devices to freely rotate during the test in order to compensate for any small eccentricities in the loads which develop.

1.3.2 Boundary Effects

The difficulties faced by researchers in designing loading systems for concrete testing go beyond the problem of applying a desired stress to a specimen. For the properties measured during a test to be an accurate indication of the true material behavior, the loads must be applied in such a manner that the physical boundaries of the specimen have no influence on the stress distribution within the specimen. This requires the elimination of the boundary effects which result from strain incompatibility between the specimen and that portion of the test apparatus through which the loads are transferred to the specimen. If boundary effects are not minimized, the actual state of stress in the specimen will be complex and non-uniform, thus invalidating any constitutive relations formulated on the basis of the applied loads.

The effects of strain incompatibility at the boundaries of a specimen are easily seen in the conventional uniaxial compression test on concrete cylinders. During the test, the specimen takes on a barrel-like shape, deforming more in the lateral direction at the center of the specimen than at the ends. Because of the difference in elastic moduli of the steel loading platens and the concrete cylinder, the concrete should strain more in the lateral direction than the steel. Friction at the interface between the platens and the specimen, however, prevents the concrete from achieving these strains and instead induces transverse shear stresses on the ends of the cylinder. These additional stresses decrease toward the center of the specimen, allowing the concrete to expand more in the middle than at the ends.

Failure in concrete and other brittle-ductile materials is associated with the formation and growth of microscopic cracks (microcracks) in planes parallel to the direction of the maximum applied load as was first theorized by Griffith (1920). As these cracks grow and coalesce, they open up and the concrete thus expands in the directions perpendicular to the maximum applied load. Failure results when these cracks grow to such an extent that physical separation of the specimen occurs.

Because boundary constraints prevent the specimen from expanding, failure is effectively delayed and the measured strength exceeds the actual strength of the material. The fact that lateral compressive stresses delay failure is evident in the results of biaxial compression and triaxial compression tests. Even in the

absence of boundary effects, the maximum principal stress at failure exceeds that which could be achieved with uniaxial loading.

Many attempts have been made to overcome the effects of boundary constraint. Some of these were aimed at minimizing the disparity in elastic moduli between the platens and the specimen by introducing various packing materials. These attempts have met with limited success, however, because the packing materials must be neither stiffer nor softer than the material being tested. The use of softer materials leads to boundary effects which are exactly the opposite of those imposed by stiff platens, namely that the softer packing materials induce tensile transverse stress transverse stresses which promote rather than delay failure.

Other researchers sought to eliminate the friction between the platens and the specimen by applying lubricants (both solid and viscous) at the interface. The degree to which boundary effects were eliminated in these attempts is, of course, a function of the resulting coefficient of friction.

Still other investigators have developed loading platens which are simply incapable of transmitting transverse (shear) stresses. One of these is fluid cushions (Ko and Sture, 1974). Here, loads are applied to the sides of the specimen by pressurizing hydraulic fluid contained within flexible membranes. Neither the low elastic modulus of the membrane nor the friction between the membrane and the specimen is a factor since only normal stresses can be applied through fluid pressure. Another method utilizes brush platens (Hilsdorf, 1965) which consist of a rectangular array of

steel bristles. Each bristle can move independently of those around it to follow the lateral deformations of the specimen rather than resisting those deformations.

A comprehensive investigation into the effects of boundary constraints and the effectiveness of the various methods used to overcome them for concrete testing was undertaken in a cooperative project coordinated from the University of Colorado (Gerstle, et al. 1978). In this research project, seven institutions used identically cast and cured specimens in a variety of biaxial and triaxial loading conditions common to all participants. By eliminating material variability, any systematic differences in the test results could be attributed to the differences in the test methods employed. The participants in this project were:

Bundesanstalt fur Materialprufung,
Berlin, Germany (BAM)

Ente Nazionale per l'Energia Elettrica,
Milano, Italy (ENEL)

Imperial College of Science and Industry,
London, England (ICL)

Institut fur Massivbau, Technical University,
Munich, Germany, (TUM)

New Mexico State University, Las Cruces,
New Mexico, U.S.A. (NMSU)

University of California at Davis,
California, U.S.A. (UCD)

University of Colorado, Boulder,

Colorado, U.S.A. (CU)

The various specimen geometries and loading conditions are tabulated in Table 1.2 and the loading systems are shown schematically in Fig. 1.7.

The different systems can be categorized both by the degree of lateral constraint present and the degree of constraint normal to the specimen boundary. At one extreme, the normal boundary conditions can be one of uniform applied stress and variable normal strains, such as that which is provided by fluid cushions, while at the other extreme the boundary condition is one of uniform applied displacements and variable normal stresses, as is produced with rigid steel platens. In the testing of nonhomogeneous materials, the type of loading condition must be considered as well as the degree of lateral restraint. Uniform boundary displacement loading offers the possibility of stress redistribution which will delay failure until the average specimen strength is achieved, whereas uniform boundary stress loading will result in failure occurring when the strength of the weakest element is reached. The relative degrees of boundary constraint for the thirteen systems incorporated into this program are depicted schematically in Fig. 1.8. Here, the parameter associated with lateral constraint is the shear stress imposed at the specimen boundary and the parameter used to describe normal constraint is the rigidity of the loading platens.

For all of the aforementioned reasons, one would expect that the strengths in uniaxial compression would increase with both

TABLE 1.2

Types of Tests Employed in Past Investigations of FRC

Laboratory	Series	Ref.	Specimen Size	Description	Loading Rate
RAW	DP	1,2	10 cm cubes	Unlubricated steel platens	Stress Rate
	FP		" " "	Cushion type system with 16 steel pistons 2.5 x 2.5 cm on elastomeric pad	Biaxial Tests: 0.03 $N/mm^2/sec$ Triaxial Tests: 0.075 $N/mm^2/sec$
ENEL	DP	3	10 cm cubes	Unlubricated steel platens	Stress Rate
	LP		" " "	Lubricated steel platens (four polyethylene sheets with molybdenum sulphide grease)	Normally: 0.5 $kg/cm^2/sec$ Series T8 and T9 10 $kg/cm^2/sec$
	CYL		16 cm x 32 cm cylinders	Axial load through steel platens, confining pressure through membrane	
ICL	LP	4,5	10 x 10 x 4" plates	Rigid steel platens with specimen surfaces treated with 'Febcure' curing membrane to minimize friction	Stress Rate 2.0 ksi/min
			4" x 10" cylinders	Axial load through steel platens, confining pressure through membrane	
TUM	BR	6,7	10 cm cubes	Brush bearing platens (bristles 4x4x35 mm)	Strain Rate Biaxial: 0.0002/min Triaxial: 0.0005-.0010/min
NMSU	DP	8	3" cubes	Unlubricated steel platens	Stress Rate
	LP			Lubricated steel platens (two 4 mil polyethylene sheets with axle grease)	3 to 5 ksi/min
UCD	DP	9	2" cubes	Unlubricated aluminum platens	Stress Rate
	LP			Lubricated aluminum platens (one layer grease)	3.0 to 4.5 ksi/min
	BR			Brush bearing platens (bristle diameter .025", length 5/16")	
CU	DP	10	4" cubes	Unlubricated steel platens	Stress Rate
	FC			Fluid cushion	0.2 ksi min

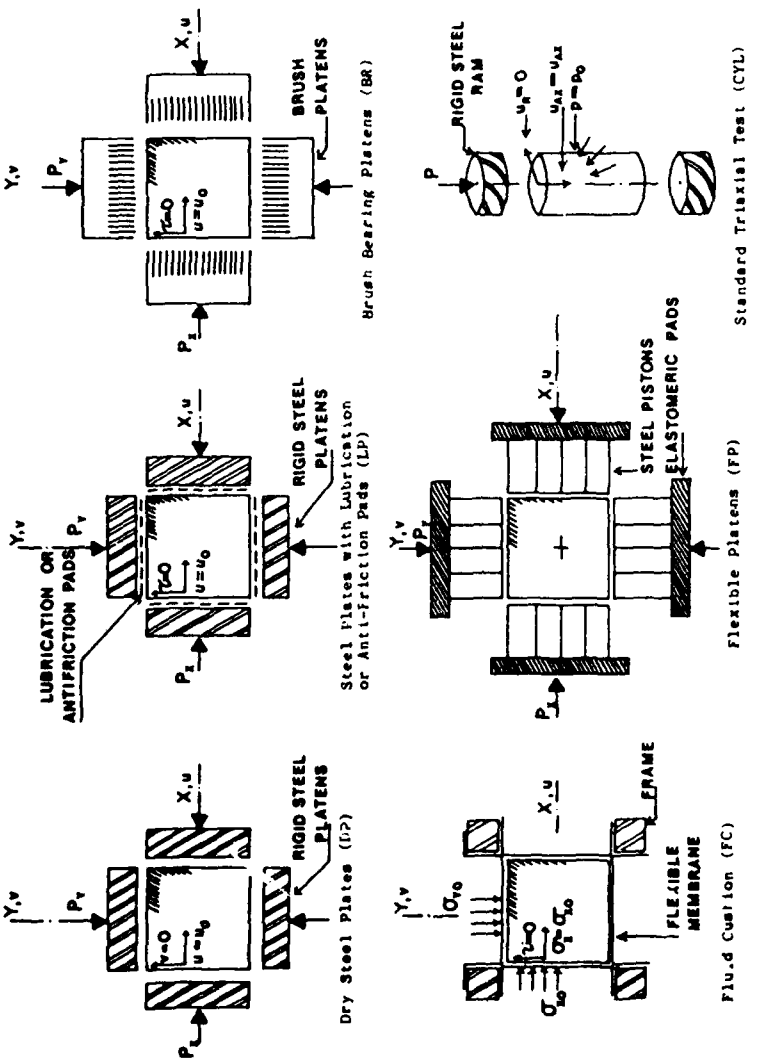

Fig. 1.7 Multiaxial Test Methods (Gerstle, et al. [1978])

increasing normal constraint and increasing lateral constraint. If such a trend did exist, it could be depicted graphically by plotting the strength results as a function of some parameter relating to the amount of constraint present in the test methods employed. For convenience, the parameter chosen was the distance of each point in Fig. 1.8. from the origin, expressed by the location of projection of those points onto the diagonal. This is equivalent to assuming that the normal and lateral constraints affect the measured strength equally, an intuitive assumption which may or may not be true.

The top half of Fig. 1.9 shows the uniaxial compression test results (normalized with respect to the strengths of conventionally-tested control cylinders) plotted against this parameter. The suspected trend is, indeed, indicated but it should be noted that, despite large differences in the degree of normal constraint, the fluid cushions, flexible platens, and the TUM brush platens all give similar results. This would suggest that the degree of normal constraint is of much less importance than the degree of lateral constraint. It also suggests that these three systems perform equally well at eliminating boundary effects.

The degree of lateral boundary constraint plays yet another role when multiaxial stress states are attempted. If laterally stiff platens are employed on adjacent faces of a specimen, a portion of the load applied in one direction will be transmitted to the loading platens in the other directions. This will result in a high measured strength since the state of stress in the specimen will be something less than stresses assumed from the applied

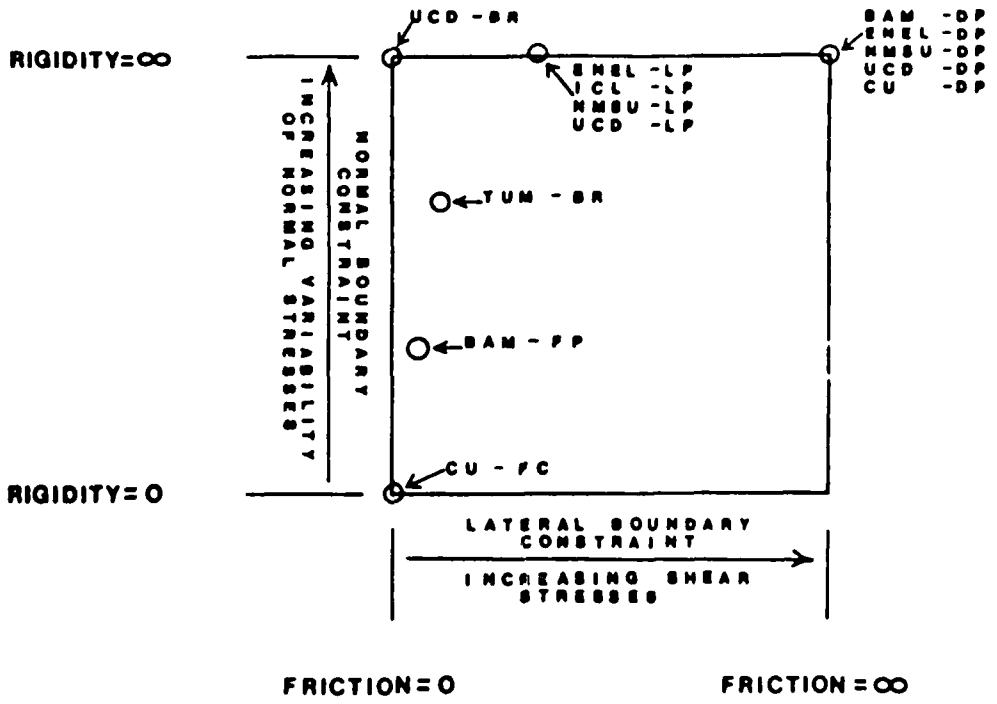

Fig. 1.8 Qualitative Representation of Degrees of Boundary Constraint (Gerstle, et al. [1978])

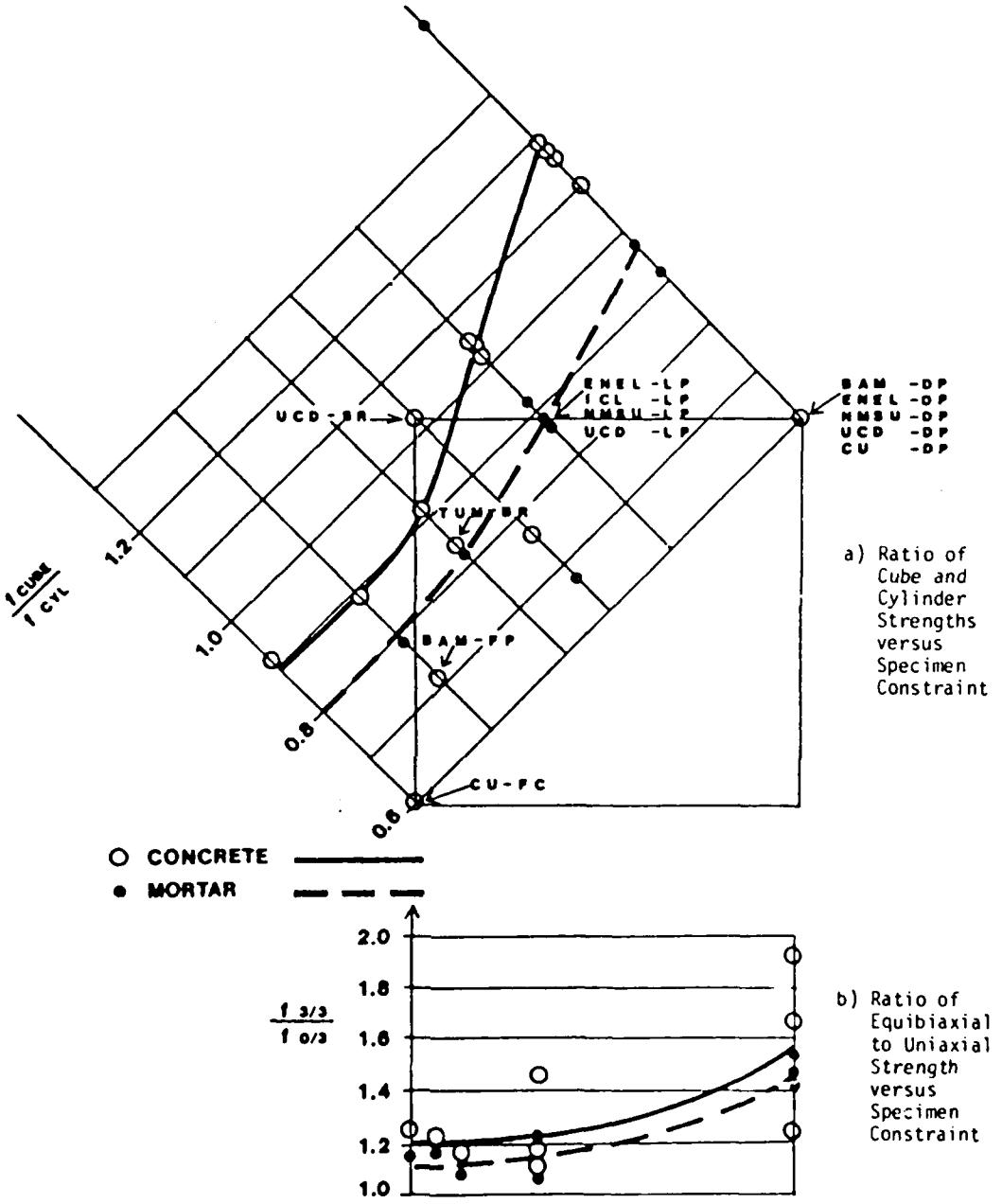

a) Ratio of Cube and Cylinder Strengths versus Specimen Constraint

b) Ratio of Equibiaxial to Uniaxial Strength versus Specimen Constraint

Fig. 1.9 Effects of Boundary Constraint on Measured Strength (Gerstle, et al. [1978])

loads. As a means of showing this, the results of equibiaxial tests were normalized with respect to the uniaxial strengths of the cubes tested in the various systems. This ratio of equibiaxial to uniaxial strength should only vary with the degree to which loads are transferred to adjacent platens if it is assumed that the other phenomena mentioned affect the two strengths involved equally.

In Fig. 1.9, this ratio is plotted against the degree of lateral boundary constraint and the expected trend is indicated to some degree. The phenomenon of load transfer to adjacent platens should be completely absent in the fluid cushion testing since stresses are applied directly in the form of fluid pressures. The effect should only become apparent with methods in which forces rather than stresses are applied to the platens. The fact that even lower ratios of biaxial to uniaxial strength were obtained with some of the other methods suggests that other phenomenon may be involved here.

1.3.3. Strength of Fiber Reinforced Concrete

Although the concept of using fibrous material to reinforce brittle materials with inherently low tensile strength is not new, research into the use of steel fibers to reinforce concrete did not begin in earnest until Romauldi and Batson (1963) proposed that, on the basis of linear-elastic fracture mechanics, inforced concrete could be made to behave as a two-phase material if the reinforcing was placed at suitably close spacings. They showed that, whereas conventional reinforcing merely compensates for the low tensile strength of concrete, the same amount of reinforcing incorporated as

closely-spaced thin wires would acutally increase the tensile strength of concrete by arresting the growth of cracks which leads to failure.

Romauldi and Batson assumed that the strength of concrete in tension is predicted by Griffith's formula:

$$\sigma^2 = \frac{G_c E}{(1 - \mu^2) \pi a} \qquad (1.2)$$

where

σ = average tensile strength

G_c = critical elastic energy release rate

a = half length of the critical flaw

E = modulus of elasticity

μ = Poisson's ratio

They argued that a crack propagatng in a plane perpendicular to the wires would be unable to extend beyond the boundaries imposed by the wires immediately surrounding it and therefore the tensile strength would be a function of the inverse square root of the wire spacing just as it is related to the inverse square root of the crack length in Equation 1.2.

The resulting theoretical relationship between wire spacing and cracking stress for one particular value of G_c is shown in Fig. 1.10. Here the four curves represent four different volume percentages of reinforcing.

To validate this theory, often referred to as the "spacing concept" (ACI Committee 544, 1982), Romauldi and Batson performed a series of flexure tests on mortar beams reinforced with rectangular

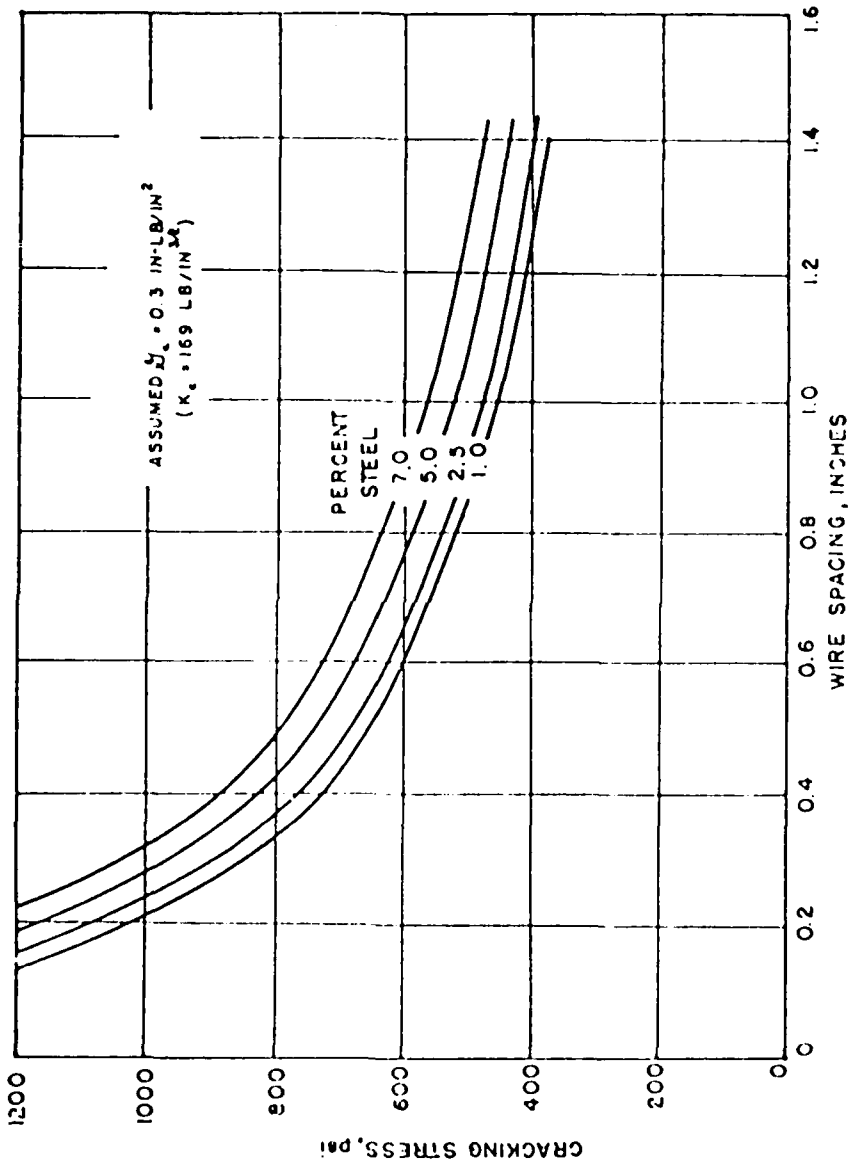

Fig. 1.10 Theoretical Relationship Between Tensile Strength and the Spacing of Wire Reinforcement (Romualdi and Batson [1963])

arrays of parallel wires set at different spacings. The results of these tests appear to confirm the theoretical relationship as shown in Fig. 1.11. Realizing that in order to keep the volume percentage of reinforcing constant, larger spacings would require the use of "wires" which approached conventional rebars in size, they plotted the results as a ratio of beam strength to the strength which would be predicted from design equations for conventionally-reinforced beams. From Fig. 1.11, it can be seen that at spacings larger than 0.6 inches, the conventional equations govern the behavior.

Romauldi and Mandel (1964) further proposed that the same results could be achieved in a much more practical manner by introducing short, discrete lengths of wire directly into the concrete mix as long as the volume percentage of reinforcing was increased to compensate for the fact that not every "fiber" would be properly oriented for crack control. To determine a suitable correction, they assumed that the fraction of fibers which would be oriented so as to arrest crack growth was equal to the ratio of the sum of the projected lengths of all the wires in any one direction to the sum of the lengths of all the wires. The resulting amount of "effective" fibers is 41 percent.

They next computed the number of "effective" fibers which could be expected to cross any one plane in a specimen to be

$$n_w = 0.41\ NL/V \qquad (1.3)$$

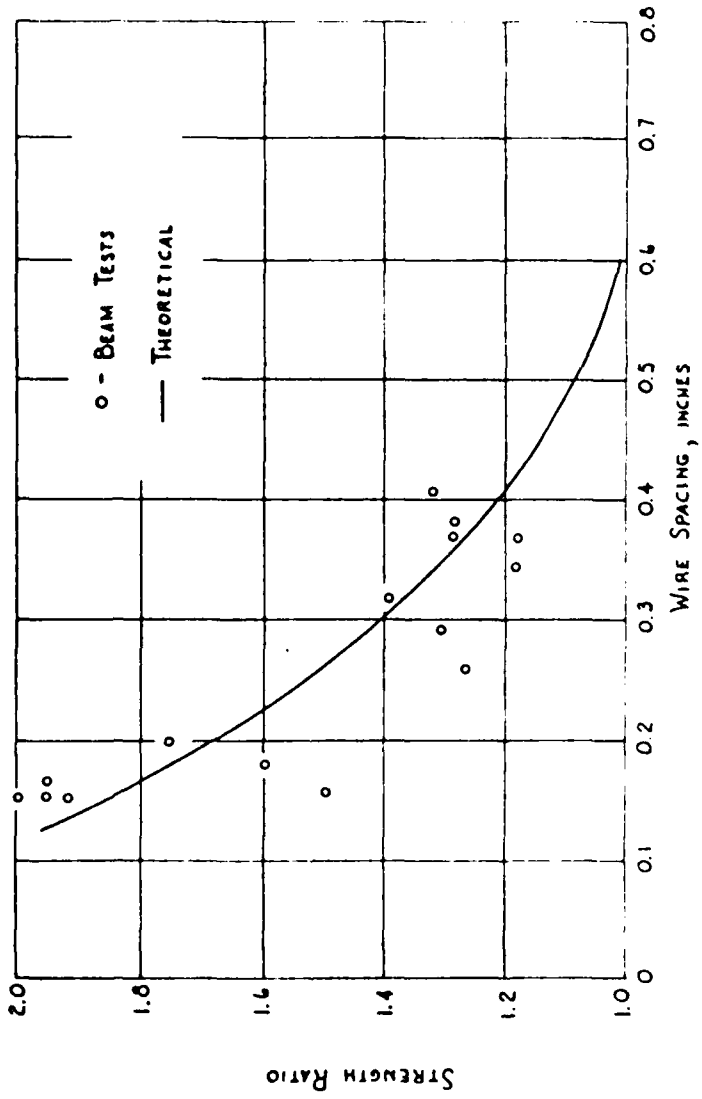

Fig. 1.11 Comparison Between Theoretical and Experimental Values of Flexural Strength for Continuous Wire Reinforcing (Romualdi and Batson [1963])

where N is the total number of fibers, L is their length, and V is the specimen volume. Taking the inverse square root of this to be the average spacing between wires and expressing the number of wires as a function of the volume percentage of reinforcing, they found the equivalent continuous wire spacing to be

$$S = 13.8\ d\ \sqrt{1/p} \qquad (1.4)$$

where d is the fiber diameter and p is the volume percentage of fibers. This permitted a comparison between the results of a series of tests on mortar beams reinforced with varying sizes and amounts of fibers and the theoretical relationship derived by Romauldi and Mandel. These results appear here as Fig. 1.12.

Critical examination of the theories and equations used plus subsequent testing by other researchers have refuted the spacing concept. Broms and Shah (1964) and Abeles (1964) pointed out that in order to achieve different wire spacings with the same volume of reinforcing, Romauldi and Mandel had used wires with different diameters. They argued that because the different sizes of wires also had different strengths and because these strengths were substantially higher than that of conventional reinforcing steel, the use of a strength ratio based on the predicted strength of conventionally reinforced beams was in error. Correcting for the different strengths of the reinforcing, they found almost no increase in strength with decreasing wire spacing. Shah and Rangan (1971) performed a series of tests on both concrete and mortar using wires with different diameters but similar strengths and, after

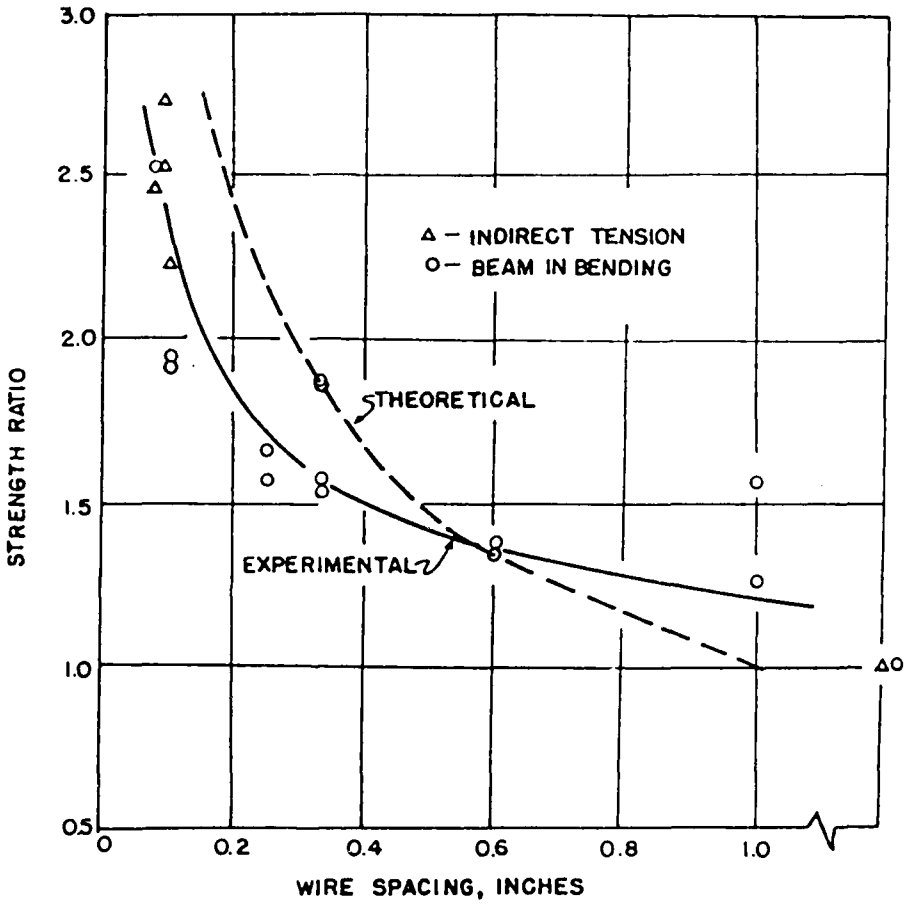

Fig. 1.12 Comparison Between Theoretical and Experimental Values of Flexural Strength for Discrete Wire Reinforcing (Romualdi and Mandel [1964])

correcting the strength ratio to reflect the higher strength of the wires, also found almost no increase in strength with decreasing wire spacing as shown in Fig. 1.13.

Similarly, a reexamination of the data from which Fig. 1.12 was generated indicates that the shape of the experimental curve can be attributed to the use of different fiber volumes to achieve different spacings. The theoretical curve in Fig. 1.12 corresponds to 1 percent reinforcing by volume, a value which was chosen because the majority of the beams were reinforced with 2.1 percent fibers and it was expected that only 41 percent of these would be effective, as mentioned previously. If only those data points corresponding to 2.1 percent reinforcement are used (Fig. 1.14) the trend is almost perfectly linear and similar to the corrected results in Fig. 1.13.

Another observation is that at a wire spacing of 0.33 inches, the two highest strength ratios (1.34 and 1.35) were obtained for beams with 1.5 inch long fibers, while the lower two (1.51 and 1.56) were for beams with 1 inch fibers. Two other results not included in the original plot, with strength ratios of 0.99 and 1.20, were obtained for beams with 0.75 inch fibers. This indicates a dependence on fiber length which is inconsistent with the spacing concept.

Snyder and Lankard (1972) noticed a similar dependence on fiber length as shown in Fig. 1.15. Here, the fiber spacing was calculated using Equation 1.4 but a unique relationship between fiber spacing and strength was not found. Instead, a family of

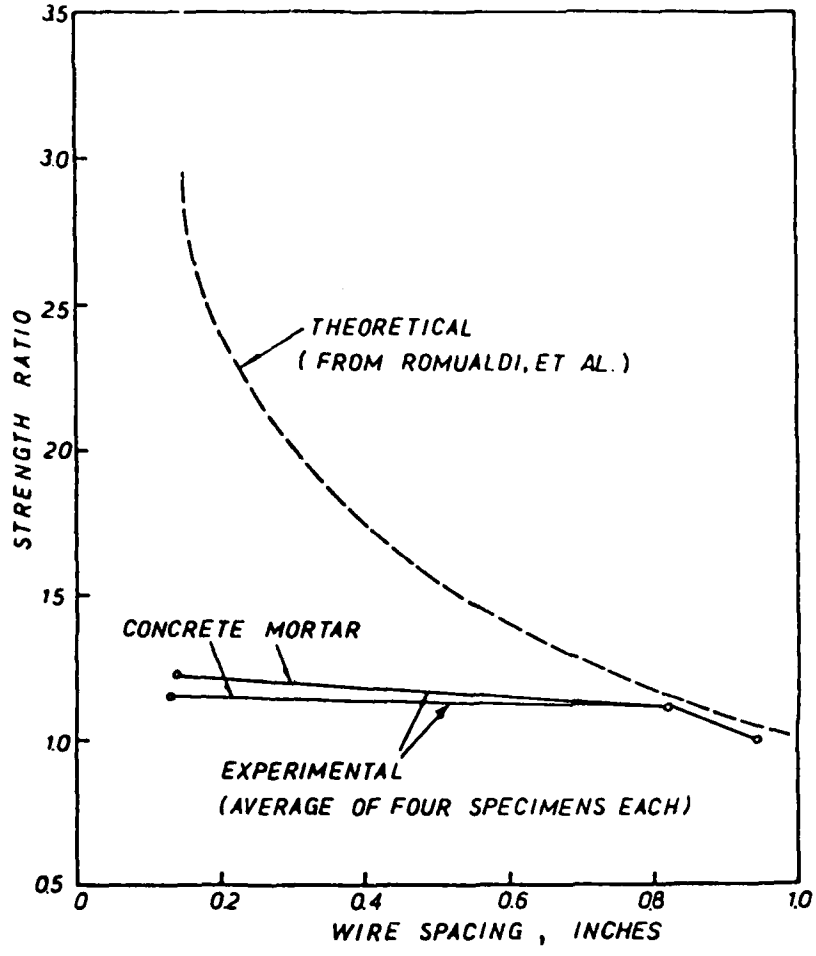

Fig. 1.13 Experimental Relationship Between Flexural Strength and Wire Spacing (Shah and Rangan [1971])

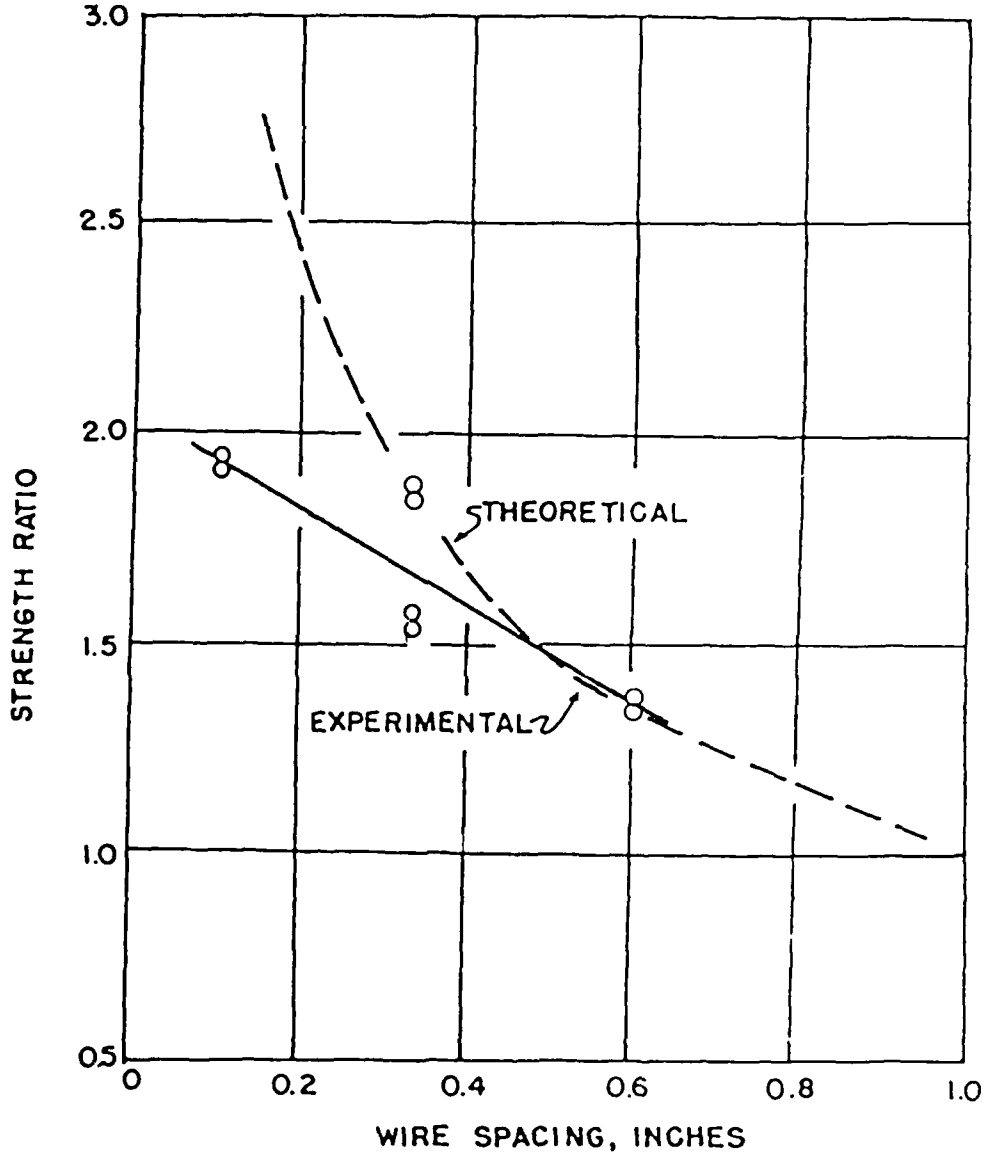

Fig. 1.14 Comparison Between Theoretical and Experimental Values of Flexural Strength for a Constant Volume Percentage of Reinforcing

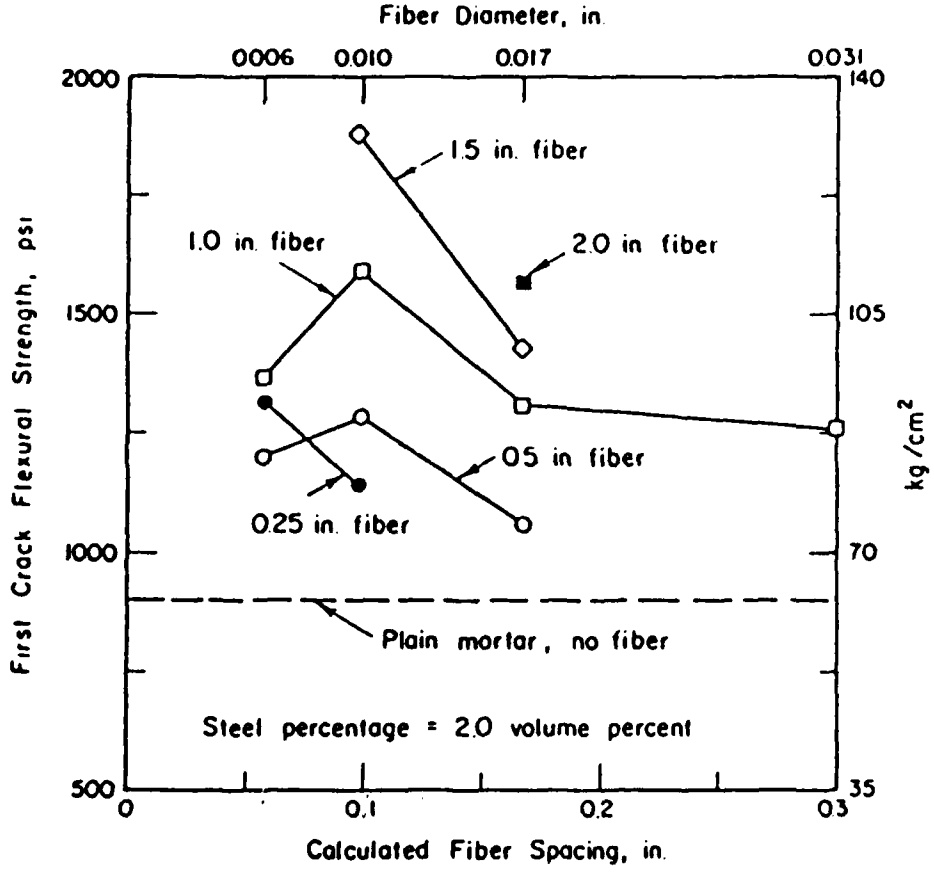

Fig. 1.15 Relationships Between Flexural Strength and Wire Spacing for Different Lengths of Fiber (Snyder and Lankard [1972])

curves is indicated with each curve representing a different fiber length.

Snyder and Lankard (1972) also found that for a given fiber size, both the stress at which the first crack appears and the ultimate strength are linear functions of the fiber volume as shown in Fig. 1.16. Similar results, shown in Fig. 1.17, led Shah and Rangan (1971) to the conclusion that fiber-reinforced concrete and mortar could be treated as a composite material similar to conventionally-reinforced concrete rather than as a two-phase material. They further pointed out that beams with continuous wire reinforcing failed when the wires failed, but beams with fiber reinforcing failed when the fibers pulled out of the matrix. This helps to explain the dependence of strength on fiber length as the longer fibers would have more surface area and thus greater resistance to pull-out. They found that fibers below a certain length could not resist loads above those at which the concrete matrix cracked. This was postulated by Romauldi and Mandel as the reason for the negligible strength increase seen for the 0.75 inch fibers and was the argument they used for not including those results in Fig. 1.12.

It is now generally agreed that the strength of fiber-reinforced concrete and mortar is dependent on not only the amount of reinforcing but also the length and diameter of the reinforcing. Specifically, most researchers relate the strength increases afforded by fiber reinforcing to the aspect ratio of the fibers (the ratio of length to diameter) for a constant volume of fibers and the

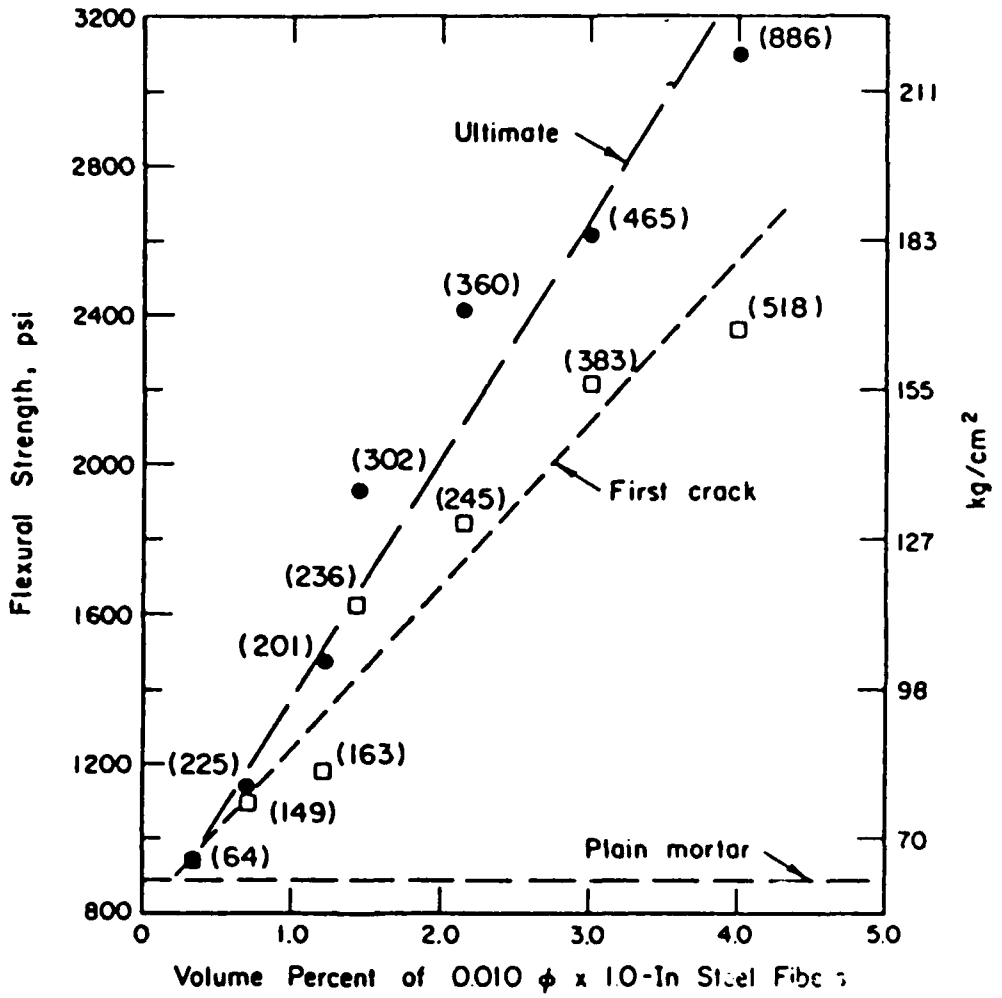

Fig. 1.16 Flexural Strength as a Function of Volume Percentage of Reinforcing (Snyder and Lankard [1972])

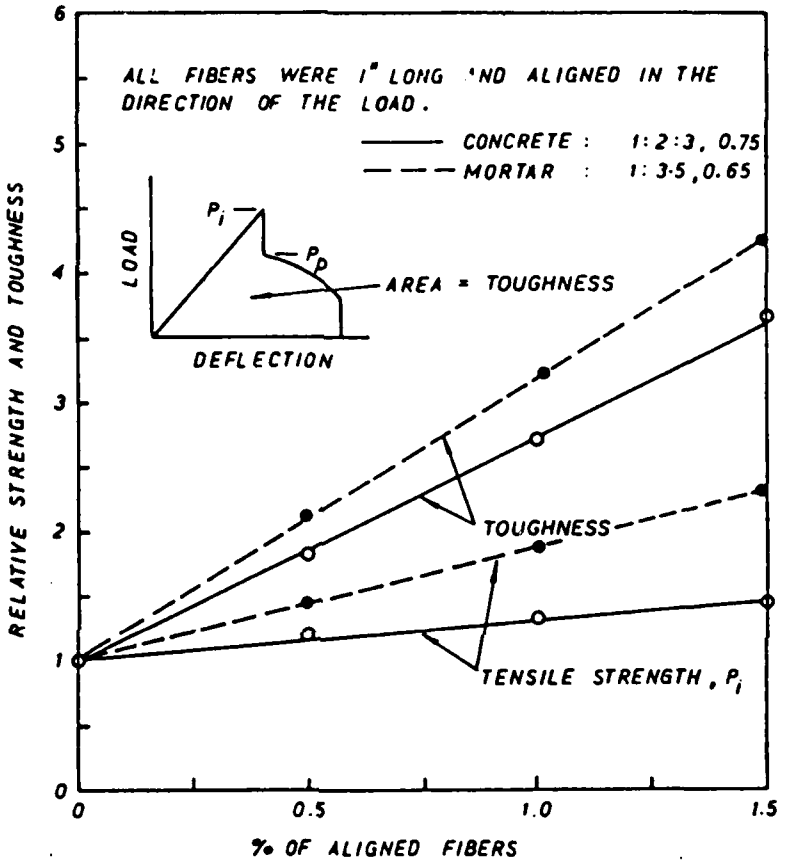

Fig. 1.17 Tensile Strength and Toughness as a Function of Volume Percentage of Reinforcing (Shah and Rangan [1971])

volume of fiber for a constant aspect ratio. This is shown in Figs. 1.18 and 1.19.

One final point, observed by both Snyder and Lankard (1972) and Shah and Rangan (1971), is that the addition of fiber reinforcing to mortar specimens has a much greater effect on strength than does the addition of fibers to concrete. In Fig. 1.17, for example, the increase in strength of the mortar specimens was three or four times the strength increase of concrete for the same amount of reinforcing. These more modest strength increases in concrete appear to be the rule. This helps to explain the large strength increases often observed in some of the earlier investigations of fiber reinforcing, all of which utilized mortar specimens. The difference appears to be attributed to the increased resistance of fibers in mortar to pullout due to a better (more complete) bond.

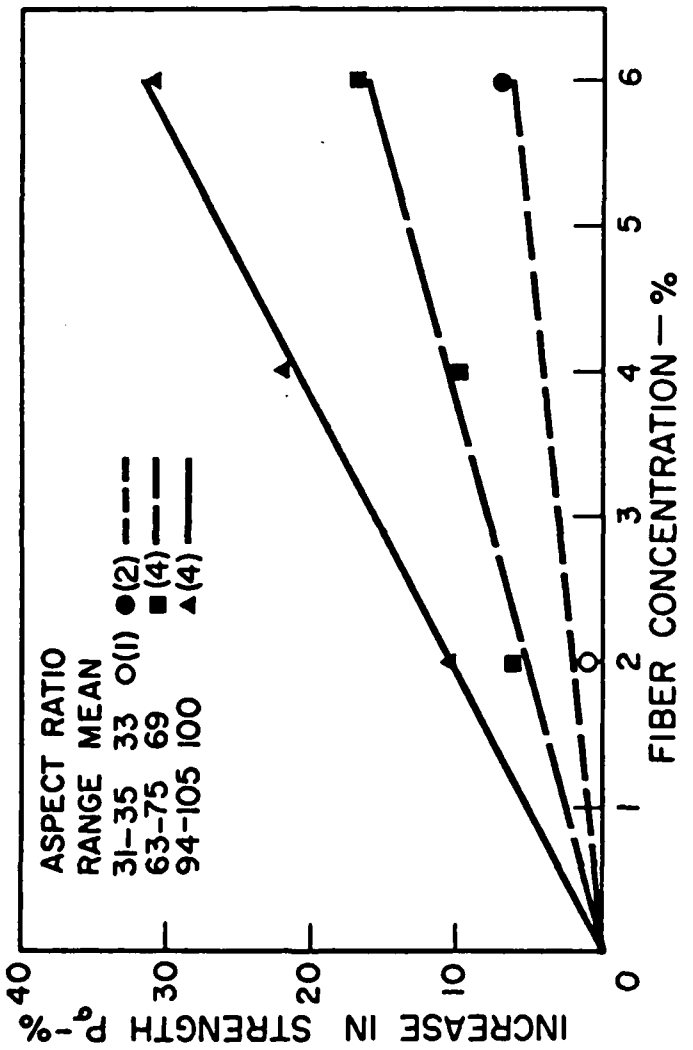

Fig. 1.18 Effect of Fiber Volume on Strength for Different Fiber Aspect Ratios (Johnston and Coleman [1974])

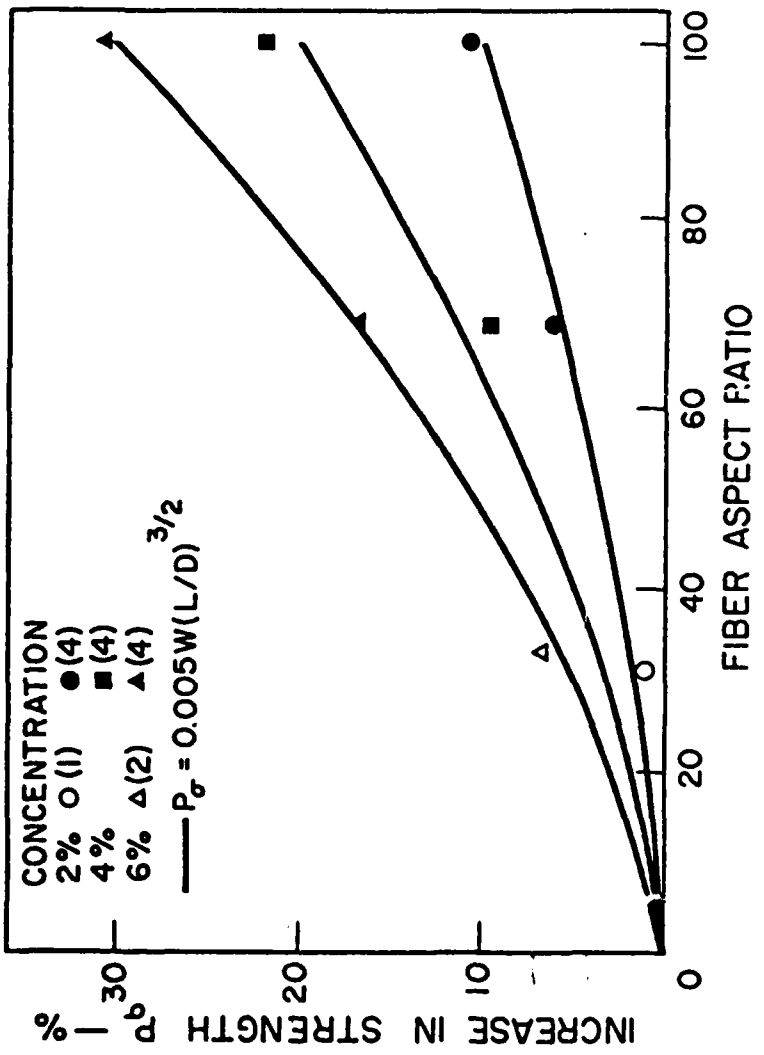

Fig. 1.19 Effect of Aspect Ratio on Strength for Different Fiber Volumes (Johnston and Coleman [1974])

CHAPTER 2

THE MULTIAXIAL TEST APPARATUS[1]

2.1 Introduction

A brief description of the multiaxial test cell used in this test program is presented here. A more detailed description is given by Egging (1981) and the original development of the apparatus is presented by Sture (1973). This chapter has been derived, in part, from these two references.

The multiaxial (cubical) test cell consists of a rigid space frame enclosed by six walls. The cubical frame has three orthogonal holes, square in cross-section, machined through it as shown in Figs. 2.1 and 2.2. The intersection of these three holes forms a cubical cavity in the center of the frame, within which the test specimen resides. The six square openings in the frame, together with the adjoining walls, act as pressure vessels. Each face of the test specimen becomes the interior wall of one of these pressure vessels. A fluid cushion loading system is established through the use of flexible polyurethane membranes attached to the inside face of each wall. These membranes, which fit into the square openings, retain the hydraulic fluid pumped into the cell. The fluid pressure generated within these membranes is resisted by the specimen and the

---

[1] The figures which appear in this chapter, unless otherwise noted, have been adapted from figures originally appearing in Reference (70).

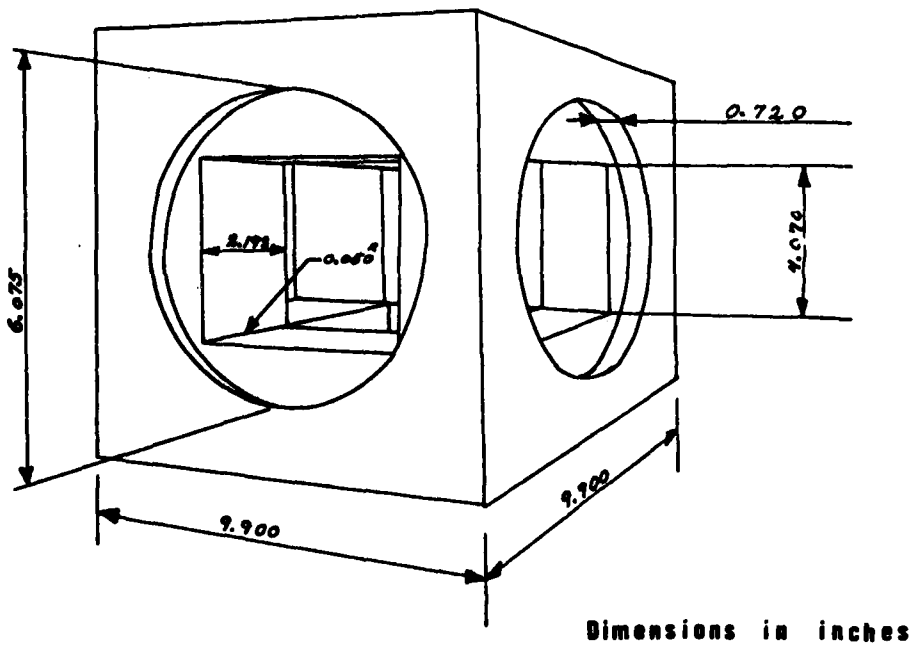

Fig. 2.1 Cubical Cell Frame

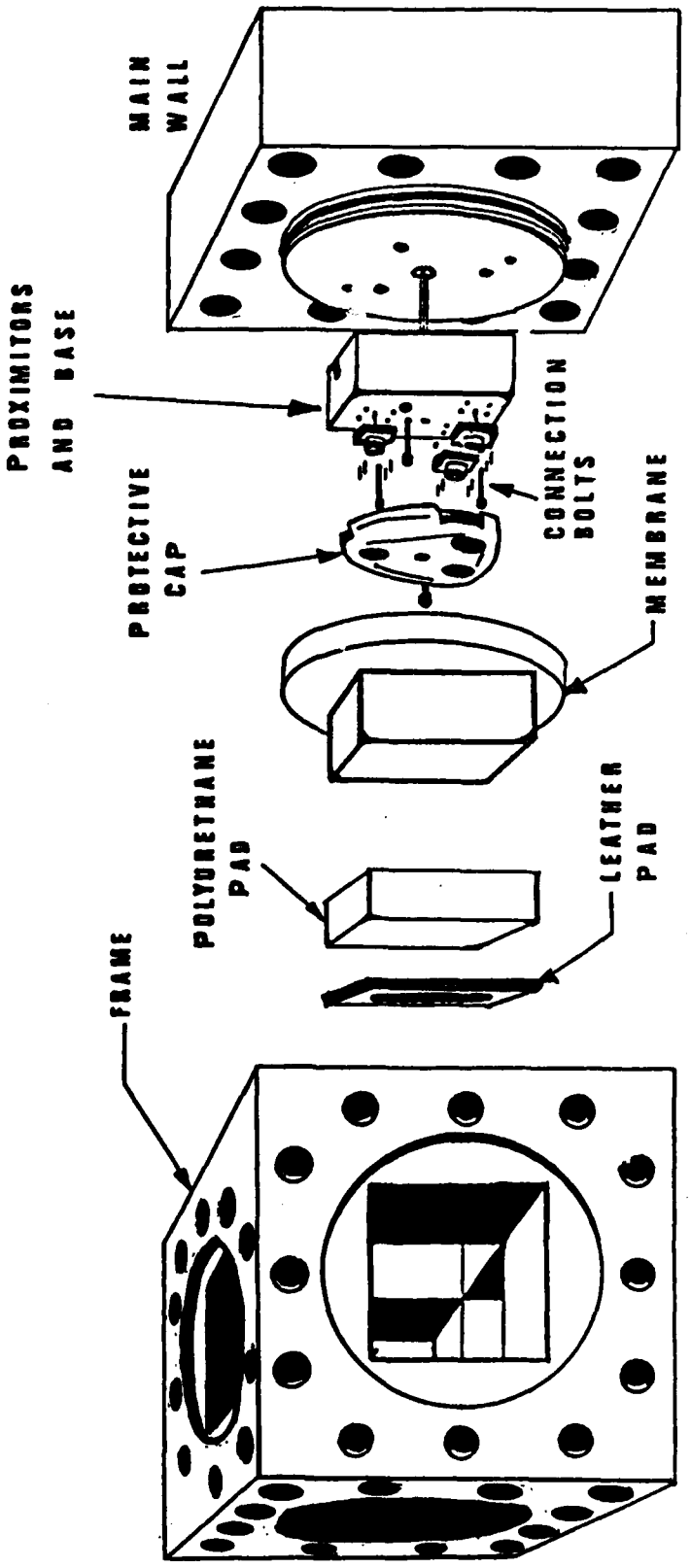

Fig. 2.2 Exploded View of Cubical Cell

exterior walls. A cross-section through the assembled apparatus is shown in Fig. 2.3.

The walls are built up from three main components as shown in Fig. 2.2. The main wall, which serves as a lid for the pressure vessel, is a thick, square plate of aluminum through which counterbored holes have been drilled to accept the Allen bolts which secure the wall to the frame. Attached onto the inside face of the main wall is an aluminum disk which has two O-ring grooves around its perimeter. This disk fits into a corresponding counterbored hole in the side of the frame. The groove furthest from the frame houses a rubber O-ring which serves to seal the pressure vessel. The groove closest to the frame clamps the sleeved flange of the membrane which acts as an O-ring to seal the hydraulic fluid within the fluid cushion. This pressure seal arrangement is shown in detail in Fig. 2.4. Attached onto this disk is the aluminum probe block which serves as the base for the transducers used to measure specimen deformations. (These transducers are described in the next section.) A protective cap over the transducers completes the wall. These components are shown in Fig. 2.2.

To prevent the membranes from extruding into adjacent cavities as the specimen deforms, a flexible polyurethane cap is placed over the end of the membrane. For testing at higher pressures, a leather pad is placed between this cap and the specimen to further ensure the competency of the membrane. A beveled hole in the center of this pad allows the fluid cushion to come into contact

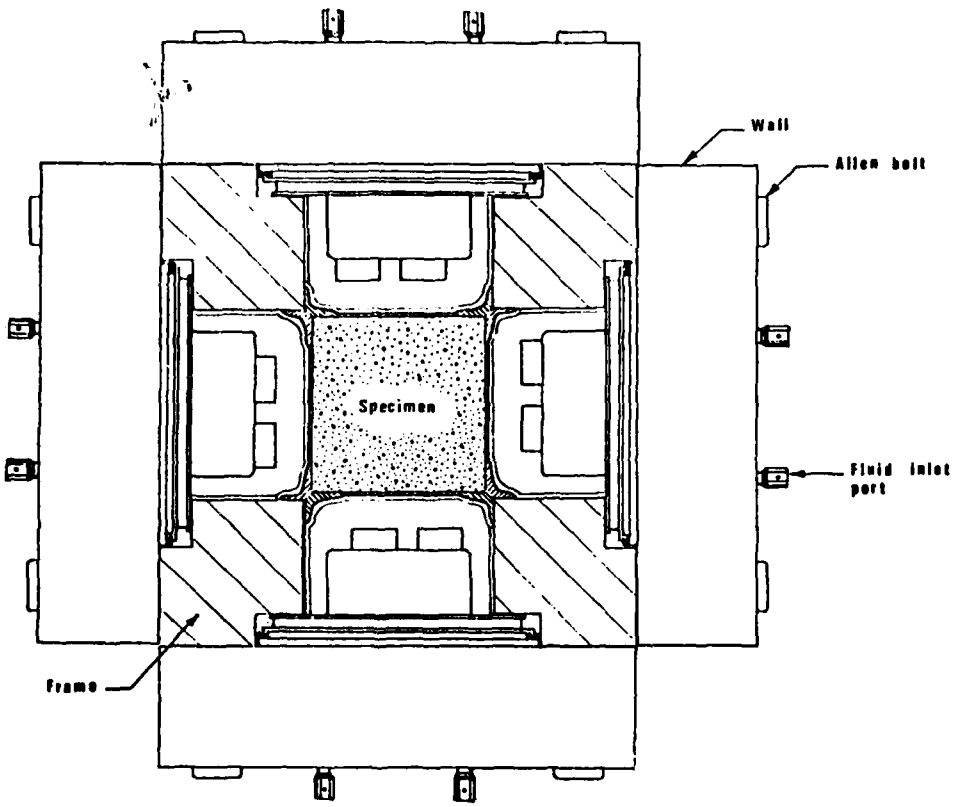

Fig. 2.3 Cross-Section Through Assembled Cubical Cell

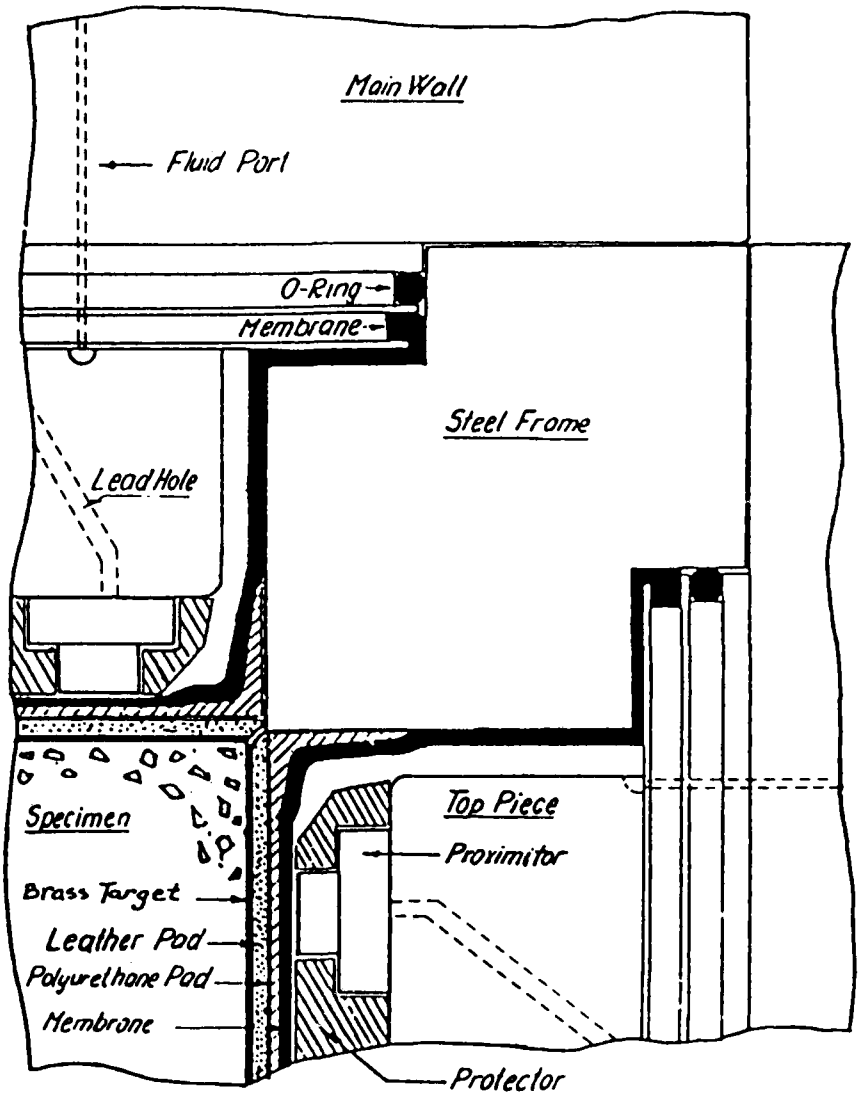

Fig. 2.4 Details of the Pressure Seal Arrangement

with the specimen, as shown in Fig. 2.5, while reinforcing the perimeter against failure.

2.2 Deformation Measurement System

The deformations of the specimen are measured with an 18-channel proximity transducer system. These transducers operate on the principle of impedance variation in a coil caused by an electric current induced in a nearby conductive target. The permeability of the magnetic field in front of the coil is directly related to the separation between the coil and the target. An electrical signal proportional to the permeability of the magnetic field is rectified into a DC voltage which can be read through a data acquisition system. The advantage of this type of deformation measurement system is that no physical contact is required between the transducer and the specimen. The voltage output can be equated to a gap width by reference to a previously established calibration curve. The only requirement is that the separating medium (in this case, the hydraulic fluid) be nonelectrolytic.

The cubical cell uses proximitor probes made by Bentley-Nevada Corporation. Three of these are mounted on each wall 120 degrees apart and equidistant from the centerline of the cell cavity. The probes on opposing walls are directly opposite one another. Each probe is energized by its own driver. An adjustable balancing circuit and an amplifier with an adjustable gain is included in each driver to allow the voltage output range to be matched to a specific range of gap widths. A calibration curve is then established over the range of gap widths.

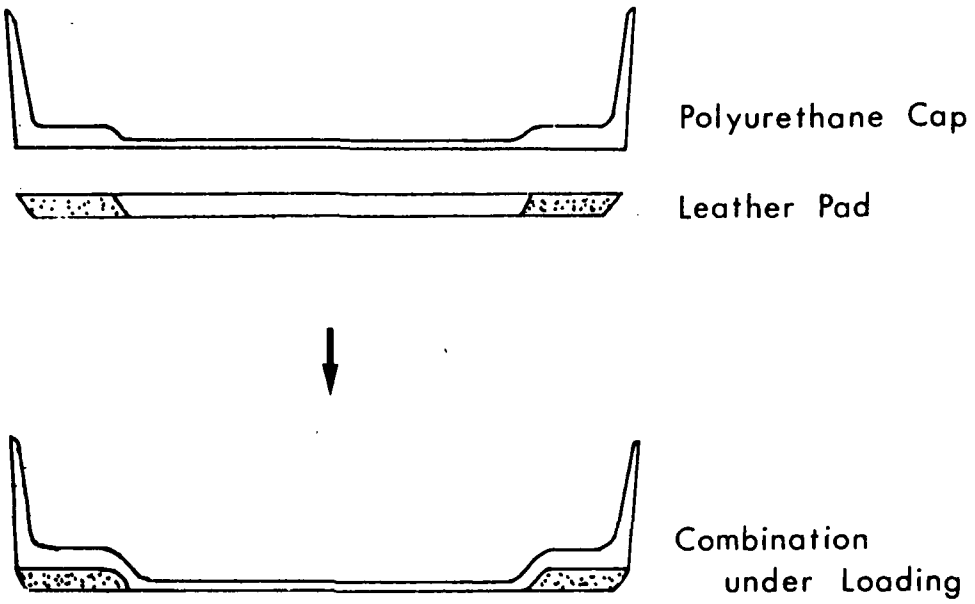

Fig. 2.5 Plastic and Leather Protective Pads

Testing in the cubical cell is performed using step-wise loading. After each stress increment is applied, the data acquisition system scans the eighteen proximitor channels and sends the voltage outputs, in digitized form, to a HP 9830A Calculator (microcomputer). The gap widths corresponding to these voltages are determined from the calibration curves, which are stored in computer memory. These gap widths are then compared to the gap widths obtained at the start of the test to get the cumulative change in gap width. By adding the changes in gap width from opposing probes and correcting for the displacements of the cubical cell itself, the specimen deformations are obtained. This additive prccess automatically eliminates rigid-body translation and rotation of the specimen from consideration.

Because the proximitor probes are mounted on the exterior walls of the cubical cell, which move in reaction to the changes in pressure in the fluid cushions, the displacements of the probes away from the specimen must be accounted for. This is done by following the stress paths prescribed in the test program with an aluminum cube as the specimen. All measured deformations in excess of those calculated for the aluminum cube (the elastic properties of which are known) are attributed to the cell and compiled into a cell calibration curve which is also stored in computer memory for reference during subsequent concrete tests.

2.3 Hydraulic System

The high-pressure hydraulic system consists of three hand-operated pumps, each with a 30,000 psi capacity, which are

interconnected such that any one pump can control the pressure on one, two, or all three axes of the cubical cell. This is shown diagramatically in Fig. 2.6. Through suitable valving, the pumping system can be operated so as to produce three totally independent principal stresses in the test specimen.

Silicone fluid was chosen as the hydraulic fluid because it is both chemically inert and nonelectrolytic, the latter being a requirement of the proximitor probes as previously mentioned. Brake fluid was previously used in the hydraulic system but it was found to cause deterioration of the polyurethane membranes and the rubber O-rings. Since switching to silicone fluid as a pressurizing medium, no deterioration has been seen and the membranes and O-rings last indefinitely.

2.4 Specimen Preparation

Although the leather pads prevent the membranes from extruding into adjacent cavities, it is still possible for the membranes to rupture by extruding into small holes on the surface of the test specimen. As a result, premature rupture of the test specimen can result as the membranes deform into these holes because the fluid pressure would be applied to the sides of the holes, tending to split the specimen in two. Therefore, care must be taken in preparing the specimens for testing.

To remove any small air voids just below the surface of the specimen and to remove any weak cement paste which may have bled to the surface during the initial set of the concrete, a circular area is sandblasted on each face. This area covers all of the face not

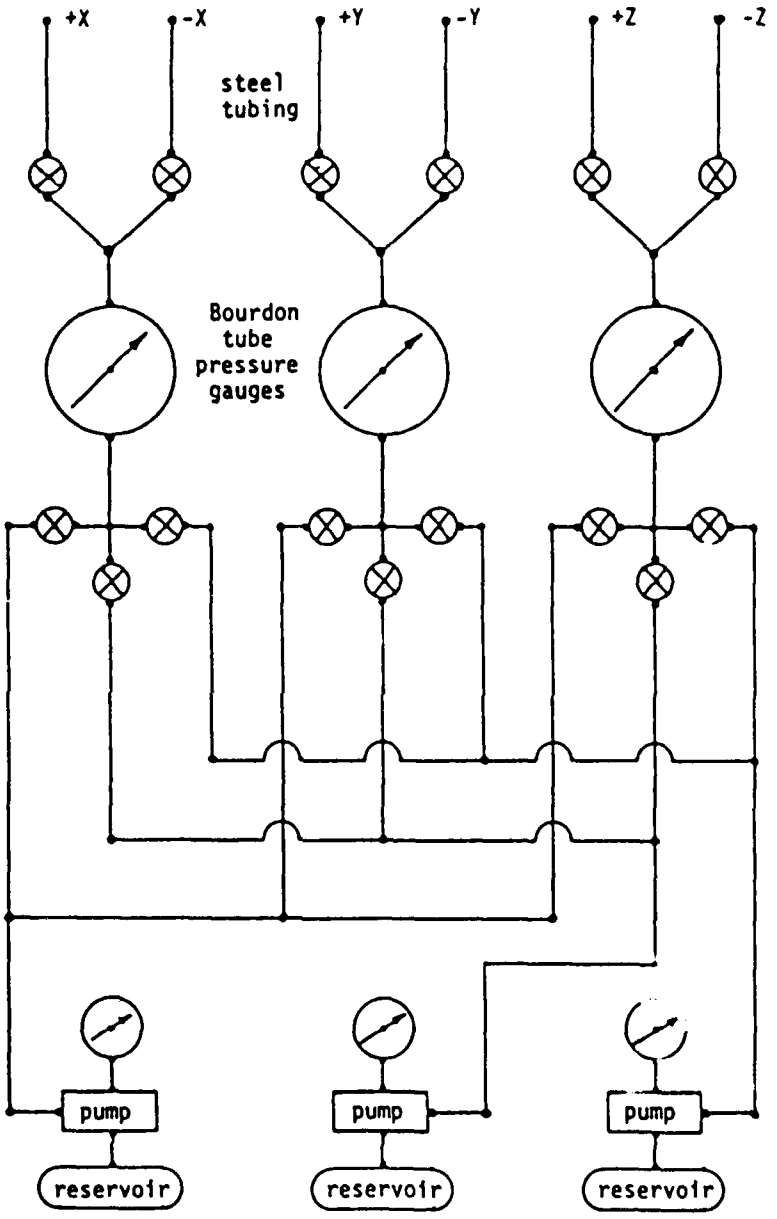

Fig. 2.6 Hydraulic System Schematic
(Egging [1981])

protected by the leather pads. The entire face is not sandblasted due to the risk of damaging the corners and edges of the specimen. These must remain intact so as not to present an even larger gap through which the membranes can extrude.

Concrete is removed to a depth of 1/16 to 1/8 inch and replaced with a plastic wood filler (Durham's Water Putty) which has properties similar to those of concrete. After the putty has dried, the cubes are sanded down to their original dimensions on a belt sander. Any holes or rough spots which appear as a result of sanding are refilled. When this second coat is dry, the cube is finished by hand-sanding with 280-grit sandpaper. A concrete cube as it appears after preparation is shown in Fig. 2.7.

Just prior to insertion into the cubical cell, the proximitor targets are glued onto the specimen. These targets are 1-inch diameter disks machined from 0.012-inch thick brass shim stock. Each disk is attached to the specimen directly in front of a proximitor probe using household rubber cement. The cement is applied in an amount just barely sufficient to hold the targets in place until the apparatus is assembled to prevent errant probe readings due to deformation of the glue layer.

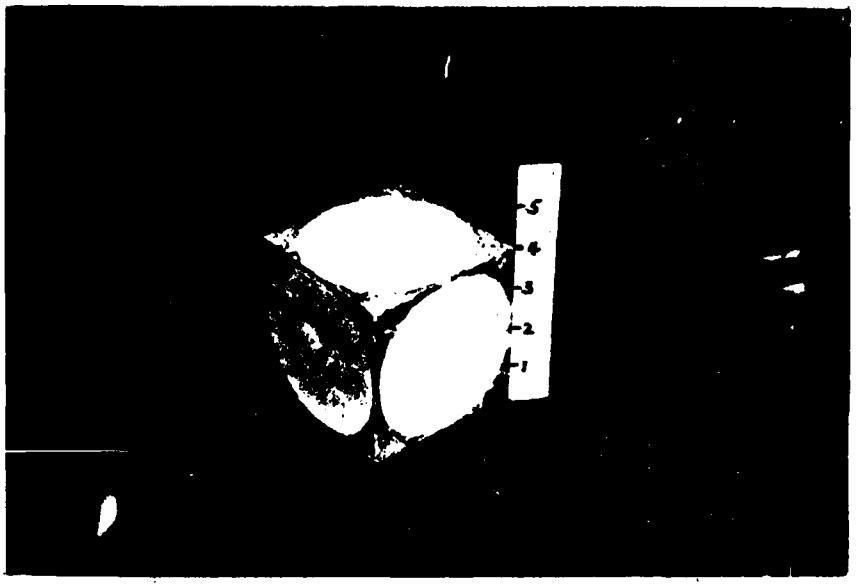

Fig. 2.7 Concrete Cube Prepared for Testing (Egging, 1971)

CHAPTER 3

TENSILE LOADING APPARATUS

3.1 Introduction

The tensile loading apparatus described in this chapter was designed on the basis of the following criteria:

1. The apparatus was to be used in conjunction with the existing fluid-cushion, cubical test cell to permit simultaneous tension-compression loading,
2. The means by which tensile loads were applied to the test specimen had to be such that boundary constraints were minimized.
3. The loading apparatus had to be capable of eliminating eccentricity in the line of action of the applied tensile loads which might develop during a test.
4. Measurement of the deformation of the specimen in the tensile direction had to be provided for.
5. Preference was to be given to an apparatus which could utilize the same test specimens as are presently used in the cubical cell (i.e., 4-inch cubes).

A design incorporating brush platens was chosen on the basis of the results of the cooperative investigation mentioned in Chapter

1 and the successful use of brush platens elsewhere (Linse and Stegbauer, 1973; Hilsdorf, 1965; Tasuji, et al., 1978). Brush platens have become particularly attractive for tensile loading since the appearance of structural adhesives capable of withstanding high tensile stresses. With these epoxies, failure in the test specimen instead of the adhesive is virtually assured.

3.2 The Brush Platens

The principle of brush platens is to reduce the lateral rigidity of a stiff loading platen by dividing it into a series of filaments (bristles) which can move independently of one another to follow the lateral deformations of the specimen to which it is attached. The bristles are rigidly affixed to a base through which attachment to a loading frame is made possible and, in essence, act as cantilevered beams.

The preference for retaining the 4-inch cubical specimens used for compressive loading in the test cell, and the fact that access to the central cavity of the cell is provided by 4.07-inch wide openings in the frame, dictated that the brush platens be exactly as wide as the specimens. If wider brushes were to be employed, they would have to be glued onto the specimen after it was placed within the cubical cell. Because the cubical cell is often used in several test programs concurrently, the length of time that the cell would be tied up while the glue was curing was judged to be unacceptable. Thus, the brushes would have to be glued to the specimen outside the cell and the entire brush-specimen system inserted just prior to testing.

Several design options were considered. Among them were a solid block of metal cut on a band saw to form bristles over a portion of its length, metal plates cut on a band saw to form "combs" which would be stacked together into a brush, and individual bristles attached to a solid base. The first option was discarded due to the anticipated difficulties in obtaining straight and vertical cuts through the 4-inch height of the metal blocks. As successive bristles were formed in the block, the loss of rigidity would have hindered the cutting process. Additionally, the amount of material removed with a saw cut would have resulted in unnecessarily wide gaps between the bristles, reducing the surface area available for gluing and increasing the nonuniformity of the applied loads.

The second option, that of stacked combs, was discarded for these same reasons, as well. Also, it would have been difficult to attach the combs together mechanically (e.g., with bolts or clamps) without exceeding the width of the brush itself.

The final option was judged to be the best and it was decided that the individual bristles would be inserted into an array of holes drilled into a solid base and held in place by mechanical means so that, in the event any one bristle was damaged, it could be easily replaced.

Each brush consists of 225 bristles arranged in a square array and held into a solid base with dowel pins as shown in Fig. 3.1. The bristles were manufactured from readily available 1/4-inch square rods of 2024-T3 aluminum. By evenly spacing 15 of these

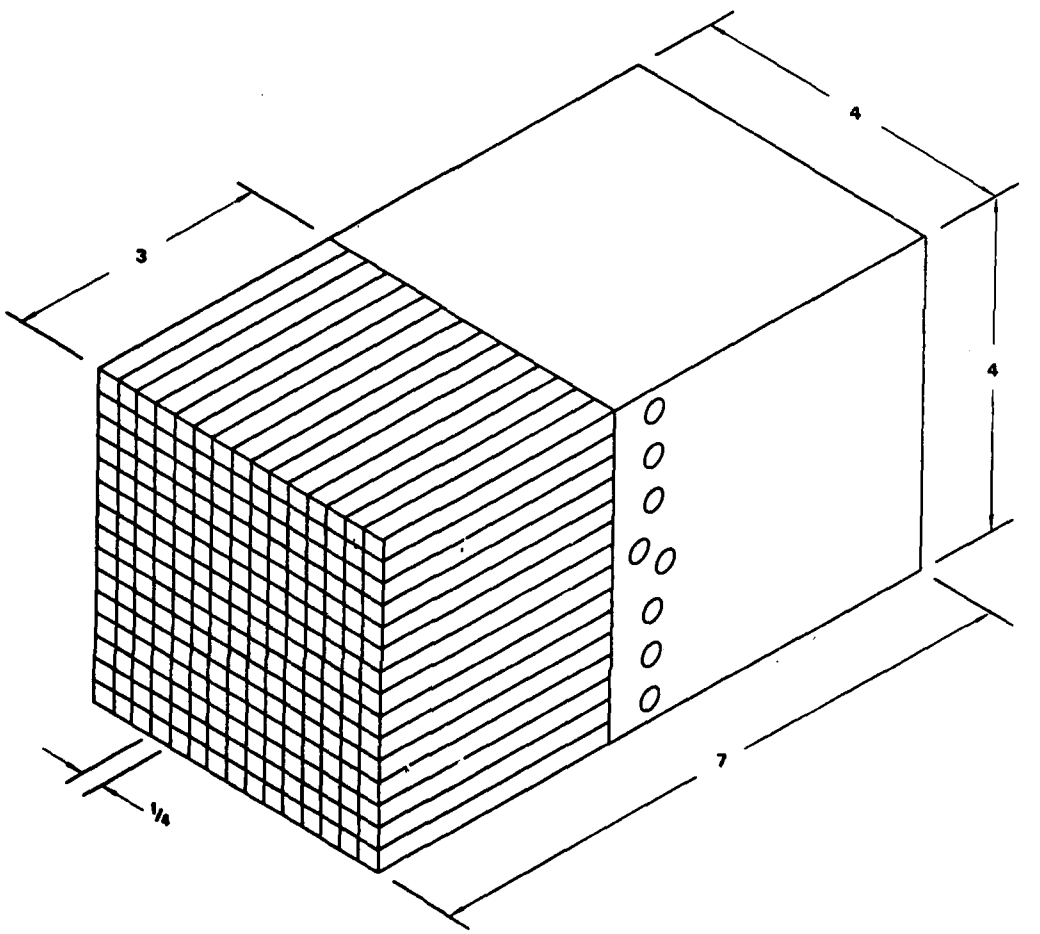

Fig. 3.1 Brush Platen

rods across the 4-inch width of the brush, a gap of 0.018 inches between bristles was provided. The resulting surface area available for gluing was 88 percent of the surface area of the specimen.

The bristles have a total length of 4 inches with one end machined to form a cylindrical stud 11/64 inch in diameter which is inserted into the base. A tapered section provides the transition from the cylindrical portion to the remainder of the bristle as shown in Fig. 3.2. The bristles were machined on a numerically-controlled lathe to ensure they would all be identical.

The bases were machined from 4-inch cubes of 7075-T6 aluminum. The holes into which the bristles are inserted exactly match the ends of the bristles, including the tapered section. This tapered section was included to provide a perfect fit of the bristles into the holes, allowing no lateral movement. A clearance fit was provided between the cylindrical studs and the corresponding holes in the base to make sure contact between the bristles and the base was made at the tapered section. Once the bristles were inserted into the base, holes were drilled transversely through the base and the cylindrical studs aligned perpendicular to the bristles to accept 1/4-inch diameter, hardened steel dowel pins. These holes are positioned between rows of bristles so that each dowel pin secures two rows of bristles.

In the event of damage to a bristle, the dowel pin could be removed to allow for replacement of the affected bristle. Once the new bristle was in place, the dowel hole would be redrilled and the dowel pin put back in. The holes are dimensioned to provide a

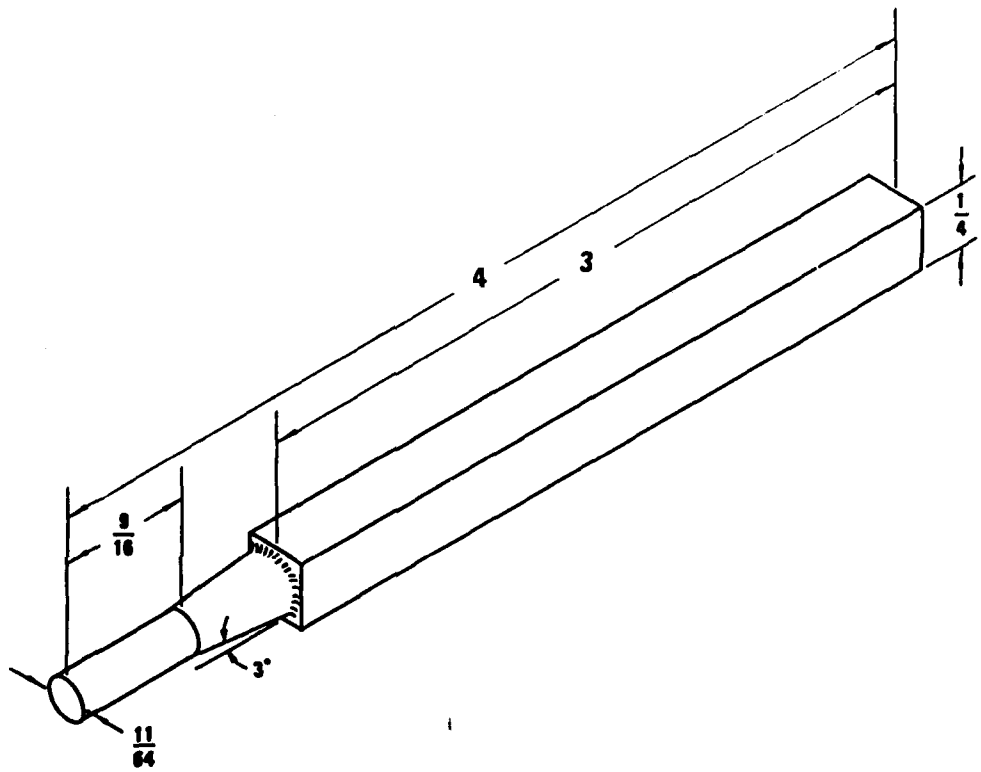

Fig. 3.2 Typical Bristle

press-fit connection between the dowel pins and the base. By drilling through the bristles in place, this fit is maintained.

An assembled brush platen is shown in Fig. 3.3.

3.3 Loading Frame

The loading system consists of hydraulic cylinders mounted on reaction frames which replace the existing walls of the cubical cell on two opposing sides. As shown in the exploded view in Fig. 3.4, the frame is composed of a pair of stand-offs capped by a plate onto which the double-acting hydraulic cylinder is mounted. The stand-offs and the mounting plate slide onto four threaded rods which screw into the existing corner bolt holes which had been provided for the walls.

The hydraulic cylinders (Squareline^{TM} S-Series Interchangeable Cylinders, manufactured by Carter Controls, Inc.) have a 4-inch bore and 1-inch stroke and are rated at 5000 psi for nonshock loading. This provides a tensile loading capacity of 50,850 lbs. which translates to a normal stress applied to the specimen of 3178 psi, thus affording a large margin of safety.

In order to eliminate the possibility of eccentric loading, each brush platen is connected to the hydraulic cylinders through a pair of opposing spherical seats. In direct-tension loading, the specimen must be allowed to translate slightly from side to side so the lines of action of the applied forces coincide. The addition of transverse compressive stresses applied through fluid cushions, however, also presents the possibility of slight

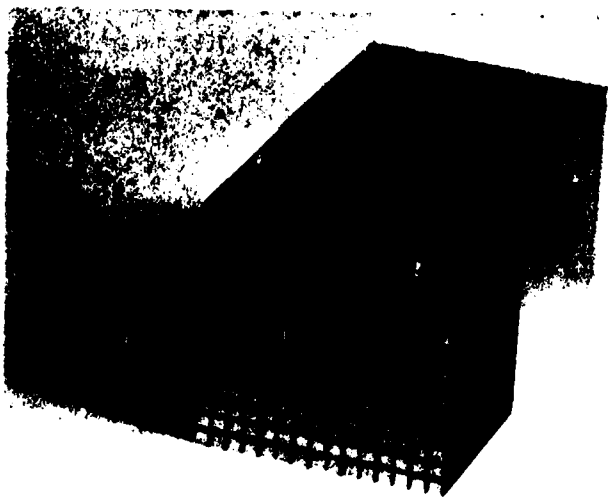

Fig. 3.3 Brush Platen

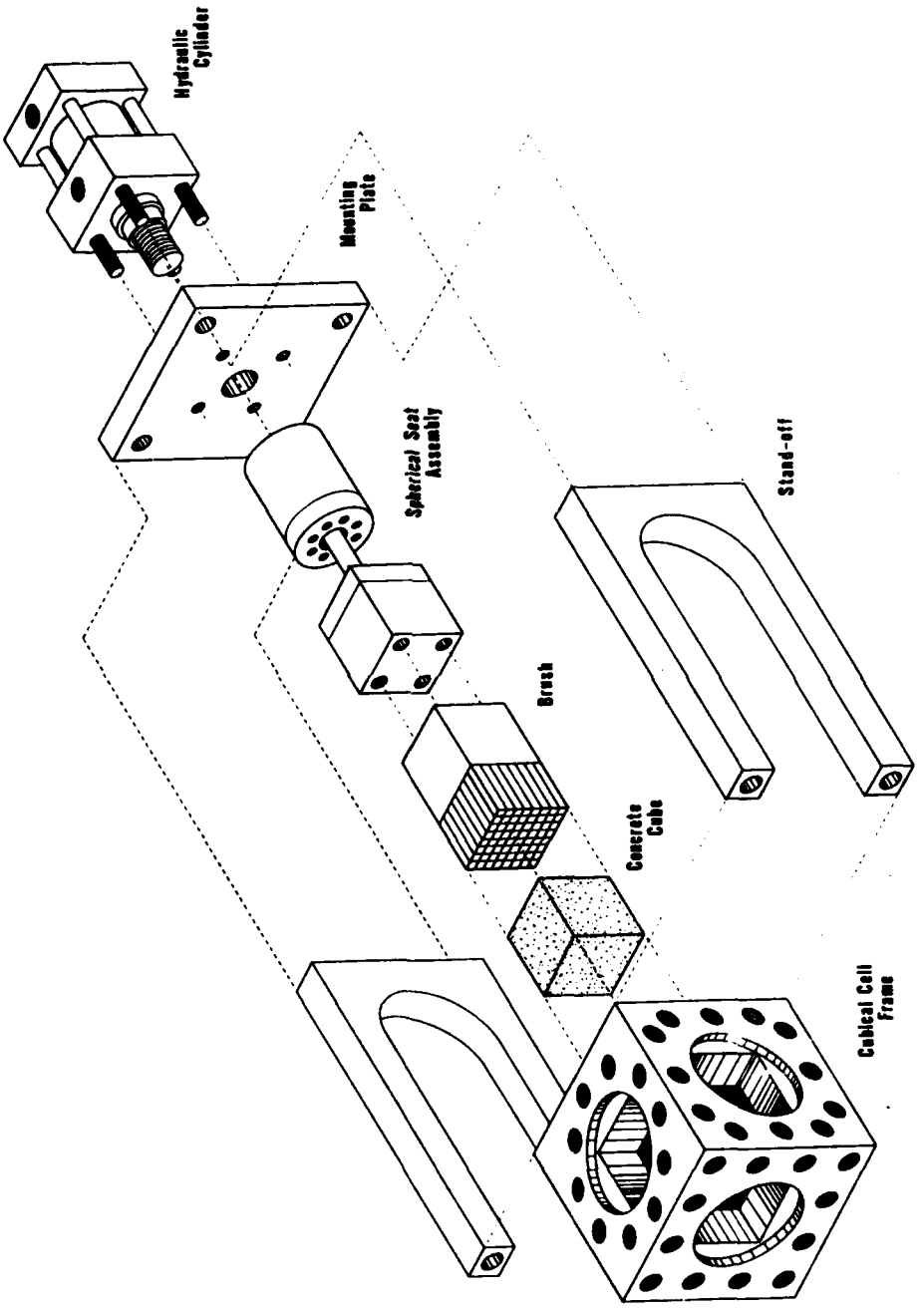

Fig. 3.4 Exploded View of Tensile Loading Apparatus

rotations of the specimen within the central cavity of the cubical cell. By using two opposing spherical seats on each side of the specimen, both translations and rotations of the specimen can be accommodated as shown in Fig. 3.5.

Each spherical seat contains four components. An exploded view of the spherical seat assembly (Fig. 3.6) shows these components. There are two different types of spherical seats which are identical in every respect except for the shape of the housing. One housing is designed to be bolted into the back of a brush platen while the other is threaded onto the piston rod of the hydraulic cylinder. These housings are machined from either 4-inch diameter or 4-inch square rods of 7075-T6 aluminum. A 2-1/4-inch diameter hole is bored into one end of the housing to accommodate the movements of the core, which has a diameter of 2 inches. The front of the core, which is also 7075-T6 aluminum, is machined to form a truncated hemisphere which seats into a matching depression in the front piece of the housing. This front piece, made from 1018 cold-rolled steel, has a tapered hole at the center through which a connection rod passes to connect the two cores together. This connection rod, 1-inch diameter and made of 1018 steel, threads into the front of each core.

The assembly is completed by two 1-inch diameter, chrome-steel ball-bearings. Each 1-inch diameter ball-bearing fits between the back of the core and the bottom of the hole in the housing. Spherical depressions in both the core and the housing hold the ball-bearing in place. The center of rotation of the

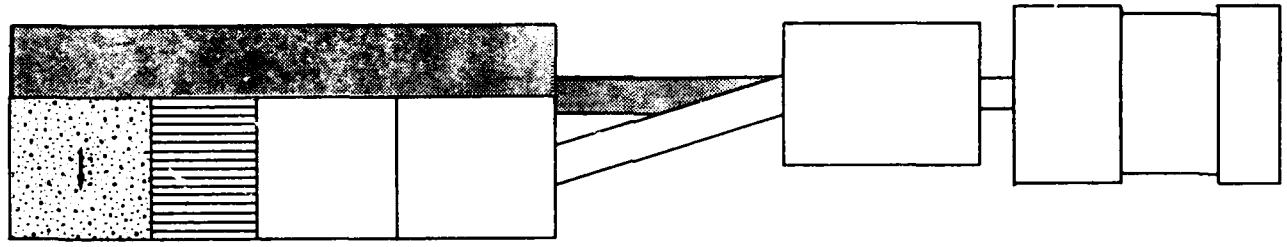

(a) Translation

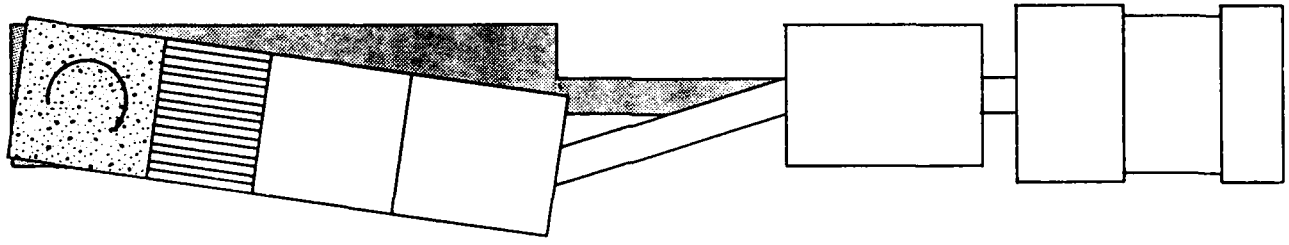

(b) Rotation

Fig. 3.5 Use of Opposing Spherical Seats to Eliminate Load Eccentricity

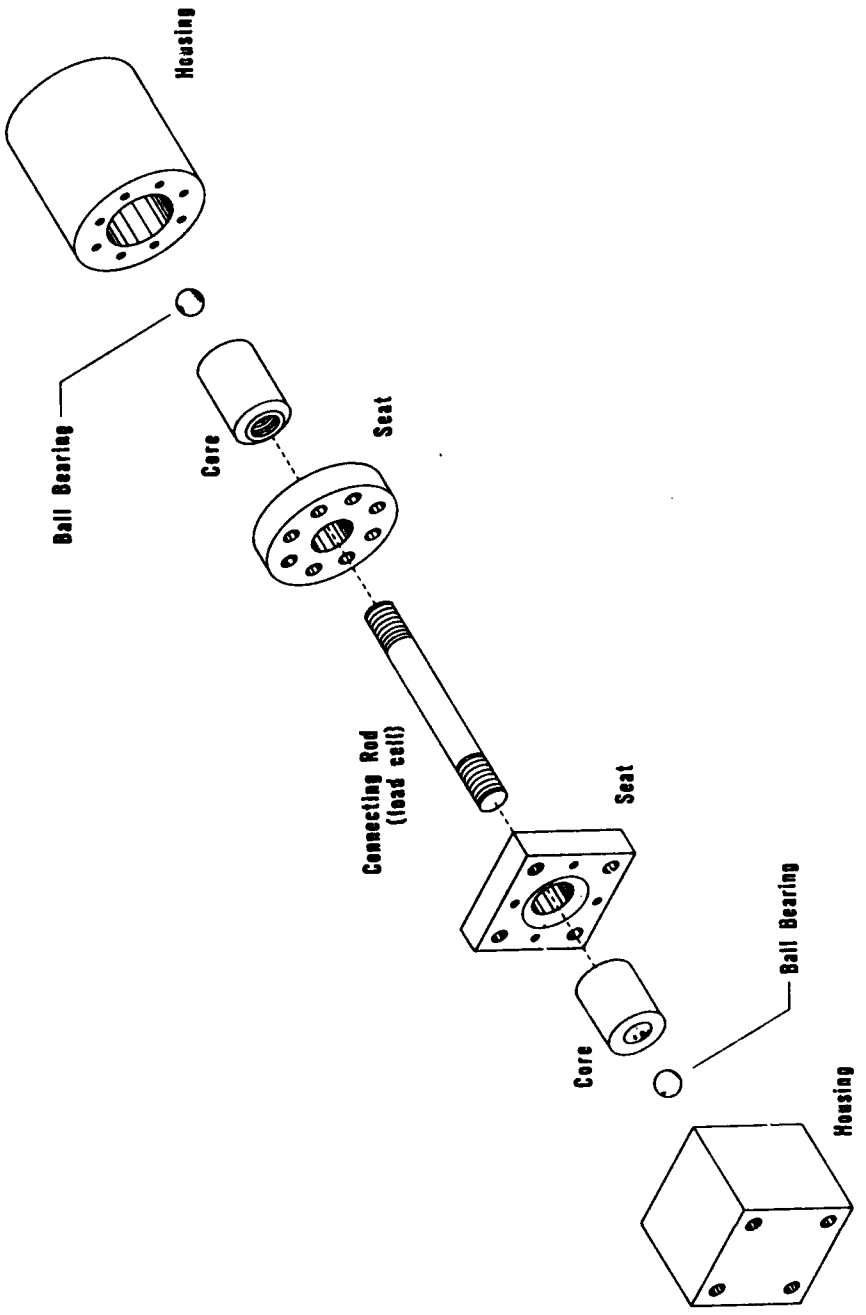

Fig. 3.6 Exploded View of Spherical Seat Assembly

spherical seats coincides exactly with the center of these ball-bearings. This permits the connecting rods to rotate freely from side to side while making the entire assembly rigid in the direction of loading. This axial rigidity was required to prevent damage to the components when the test specimen fails.

Tensile failure in brittle materials is often explosive in "soft" loading apparatuses such as this, because the strain energy built up in the reaction frame is immediately released as soon as the load sustained by the specimen begins to drop off. This sudden release of energy causes the two halves of the failed specimen to fly apart. If the cores were free to move axially within the housings, the mass momentum of the apparatus would result in a large impact force when as the cores hit the bottom of the holes in the housing. These forces would be potentially damaging to the soft aluminum core and especially to the threaded connection between the cores and the connecting rods. With the ball bearings preventing axial movement of the cores, however, the entire spherical seat assembly can move back into the hydraulic cylinder as a rigid body. The chamber behind the piston in the hydraulic cylinder is filled with hydraulic fluid. A small opening to the outside regulates the escape of this fluid, thus cushioning the apparatus in much the same way as an automotive shock absorber works. This shock absorbing capability was the reason for selecting a double-acting hydraulic cylinder.

A cross-section through the assembled housing unit is shown in Fig. 3.7. The clearance between the sides of the core and the interior wall of the housing allows the connecting rod to rotate

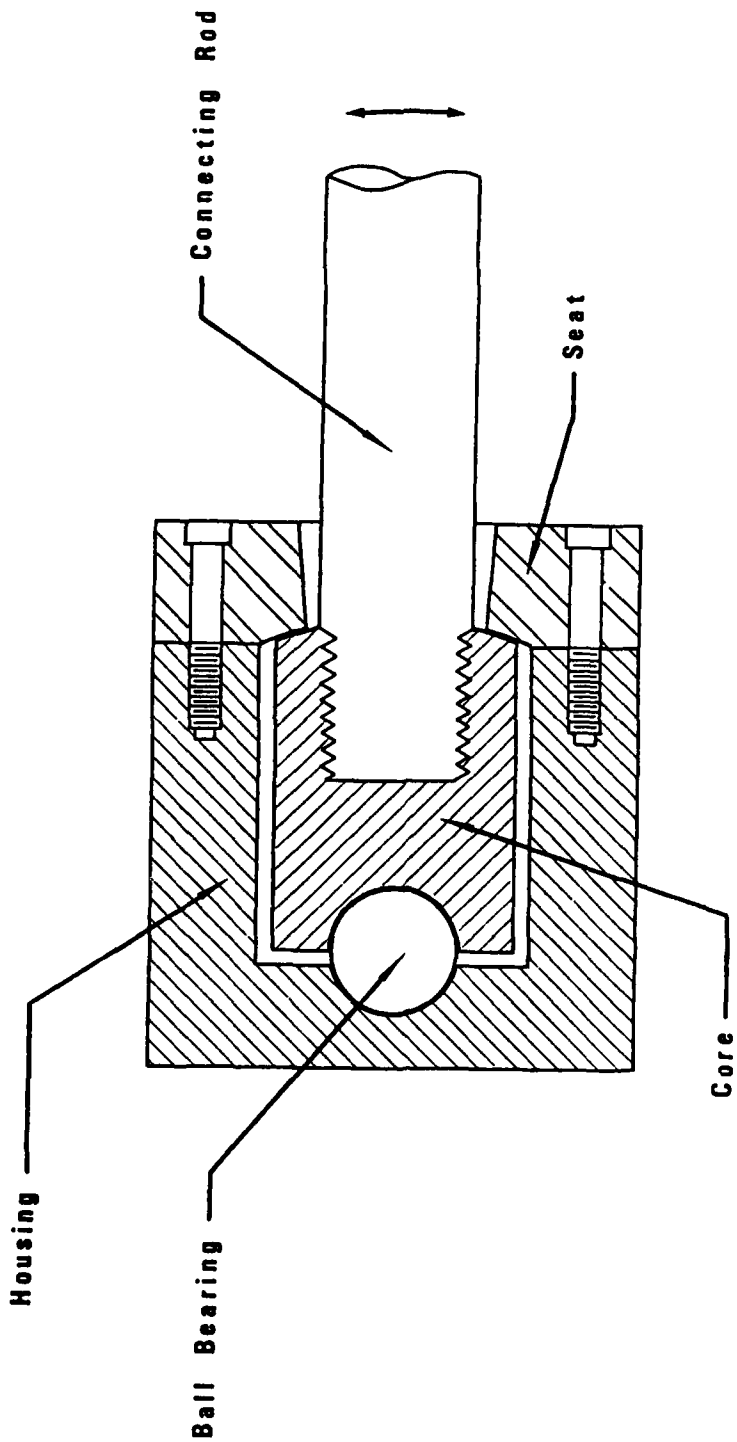

Fig. 3.7 Cross-Section Through Assembled Spherical Seat

about the ball bearing through an included angle of approximately 5 degrees. This is more than sufficient as the specimen itself can only translate 0.035 inches to either side in the central cavity of the cell and can rotate about its centroid through an angle of only 1 degree.

3.4 Load Cell

In order to provide an accurate measurement of the actual tensile stresses applied to the test specimen, the connecting rods were instrumented with strain gages. Each connecting rod is instrumented with four Micro-Measurements CEA-06-125UN strain gages. Two are positioned longitudinally and the other two transversely to eliminate bending effects.

The custom-built electronics which support these strain gages amplify the transducer signal by an amount such that the voltage output is equal to the stress in the test specimen (the force in the connecting rod divided by the 16 sq. in. surface area of the specimen). The amplifier gain is adjustable to allow precise calibration of the load cell. An external 4-1/2 digit voltmeter connects to the signal output which is switch-selectable to allow either of the two load cell voltages or the average of the two to be read. This latter function is provided by a summing amplifier set at a gain of 0.5. This, too, is adjustable for precise calibration.

Calibration of the load cells was accomplished using an MTS 100,000 lb capacity load frame to apply a tensile force to the connecting rods. The servo-controlled loading ram is connected to a

function generator to allow automatic execution of a variety of load or displacement histories.

Each connecting rod had to be calibrated separately due to the limited distance between the piston and the crosshead in the MTS load frame. First, both load cells were connected to the electronics and the voltage outputs were adjusted to read 0.000V. Each load cell, as well as the averaging circuit, is provided with a separate balancing circuit for this purpose. After the zeros were established, one of the connecting rods was placed into the load frame. The platens used for tensile loading have spherical seats into which a variety of gripping devices can be screwed. In order to simulate the loading conditions in the spherical seat assembly, the rod ends were screwed into these platens directly. This eliminated concerns that local stress concentrations induced by gripping devices might affect the strain gage readings.

Once in the load frame, the connecting rod was loaded to 20,000 lbs. This is equivalent to a 1250 psi stress in the test specimen which is slightly greater than the stresses anticipated in the test program. The amplifier corresponding to that load cell was adjusted to give a voltage output of 1.250 V. With the other load cell providing a dummy load of 0 V, the averaging amplifier was adjusted to give a 0.625 V output.

After unloading back to zero, the function generator was programmed to cycle between 0 and 20,000 lbs. At 1000 lb. intervals, loading was stopped and the voltage output was recorded. The resulting calibration curve is shown in Fig. 3.8. Although there is

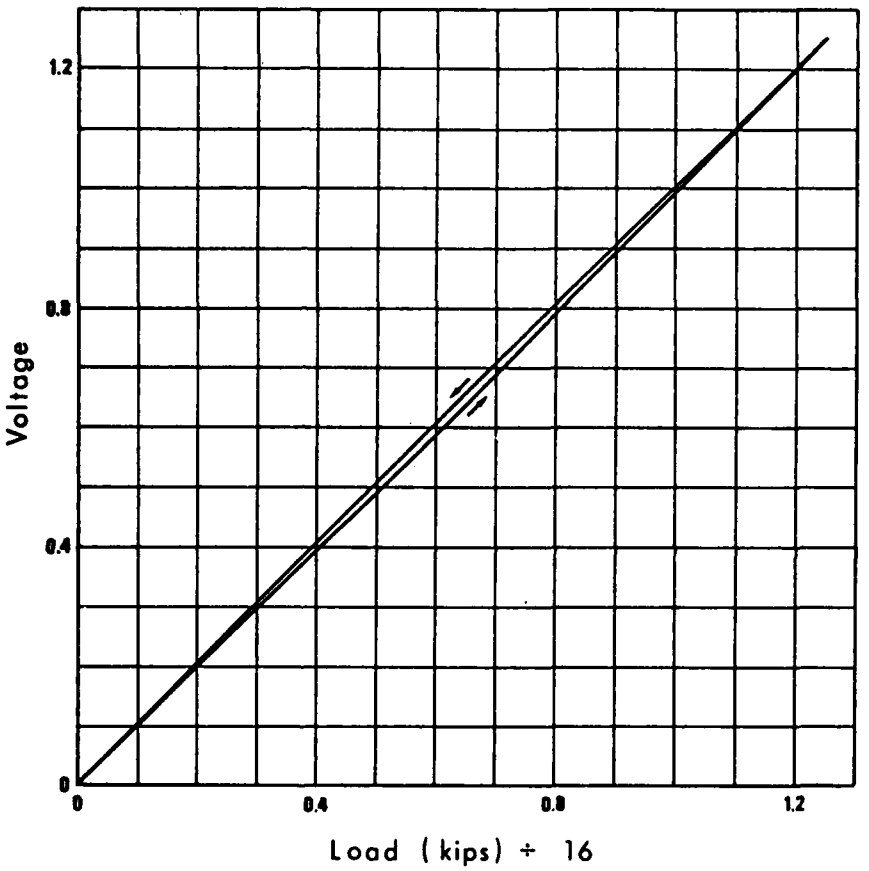

Fig. 3.8 Load Cell Calibration Curve

a slight hysteresis in this curve, the difference between the measured load and the applied load is never greater than 1.2 percent of the applied load. This accuracy is comparable to the accuracy of the Bourdon-tube gages used in conjunction with the fluid cushions.

In order to check the reliability of the load cells with repeated use, the function generator was reprogrammed to cycle between 0 and 20,000 lbs., returning to zero every 15 minutes. The connecting rod was loaded until a total of 50 cycles had been completed. Another calibration curve was established and found to be identical to the first calibration curve, indicating that the calibration would only need to be checked periodically. Since only monotonic loading was used in the test program, each test was equivalent to one cycle of loading. Therefore, the calibration was only checked at the beginning of the test program and approximately half-way through the test program. In both cases, adjustments were found to be unnecessary.

3.5 Deformation Measurements

Because the data acquisition system mentioned in Chapter 2 is built around the Bentley-Nevada proximitor drivers and can only be used with those drivers, it was decided that the deformation measurement system for the tensile loading apparatus would utilize Bentley-Nevada proximitor probes as well. This eliminated the need to build a separate data acquisition system to support the tensile loading apparatus.

The proximitor probes are suspended from an aluminum frame which bolts onto the top face of the assembled cubical cell. This

frame is shown in Fig. 3.9. The uppermost probe is suspended just above the brush platen while the two lower probes hang one to each side of the platen. As with the compression walls of the cubical cell, the probes are arranged to be 120 degrees apart and equidistant from the centerline of the tensile loading apparatus. The probes are directed away from the cell frame and point at aluminum targets attached to the sides of the brush platen as shown in Fig. 3.10. With this arrangement, the targets move away from the probes as the test progresses; thus, when the specimen splits apart at failure there is no danger of the targets colliding with the probes and damaging either the probes or the probe frame.

Because the frame is attached atop the cubical cell and remains stationary throughout a test, there is no need for calibrating the cell to correct for movements of the probes. There must be a calibration, however, to correct for the elastic deformations of the brush platen and the glue layer since deformations are measured at the back of the platen rather than at the specimen surface.

The calibration was performed by gluing a pair of brush platens to an aluminum cube and loading the cube in uniaxial tension. A typical calibration curve is shown in Fig. 3.11. The initial, nonlinear portion of the curve reflects a slight movement of the bristles as they seat themselves in the base of the brush platen. Although the curve always becomes linear above 10 psi of tensile stress in the specimen, the amount of movement which occurs prior to this varies randomly from test to test. The actual

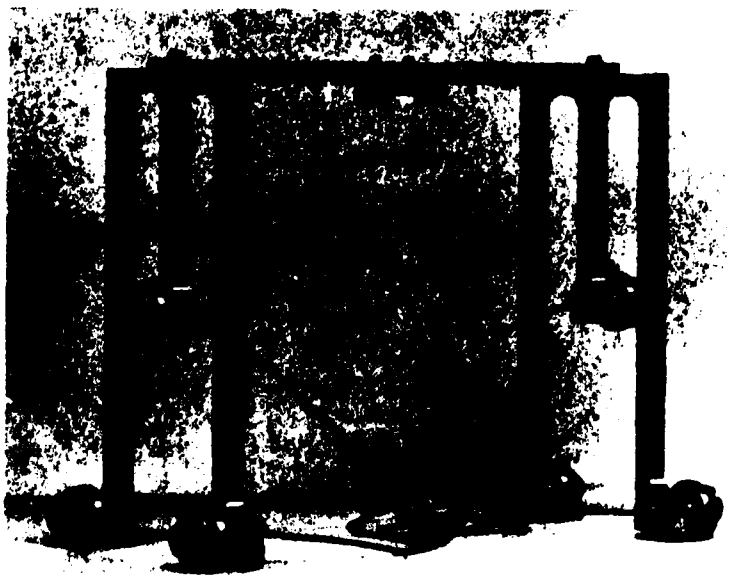

Fig. 3.9 Proximitor Probe Frame

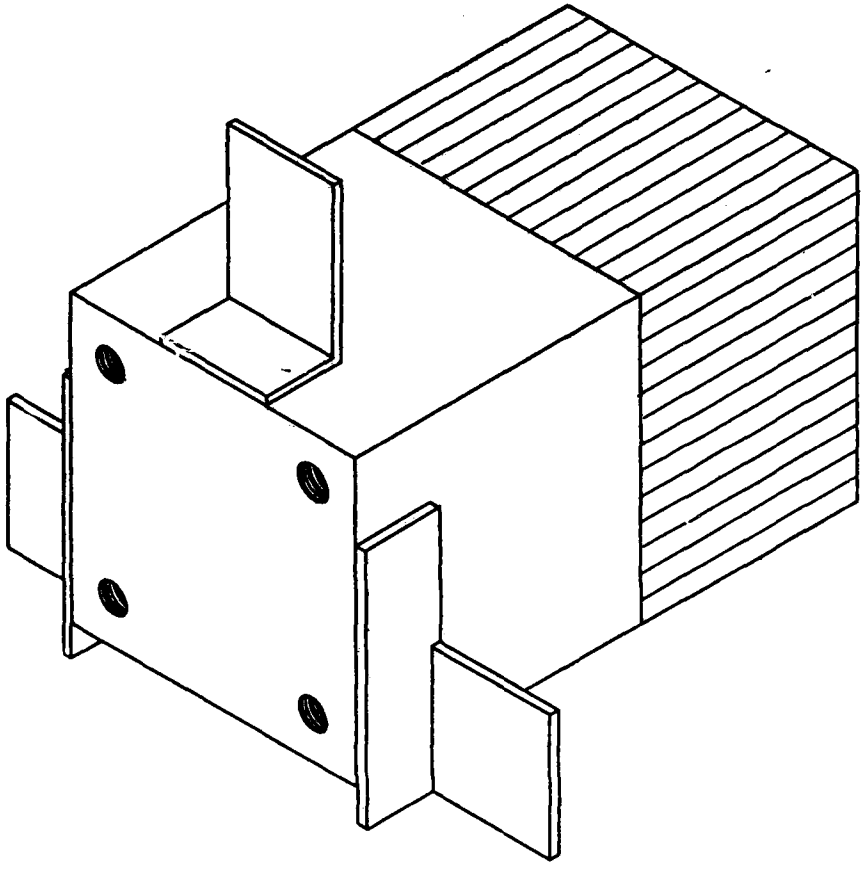

Fig. 3.10 Proximitor Probe Targets Mounted on Brush Platen

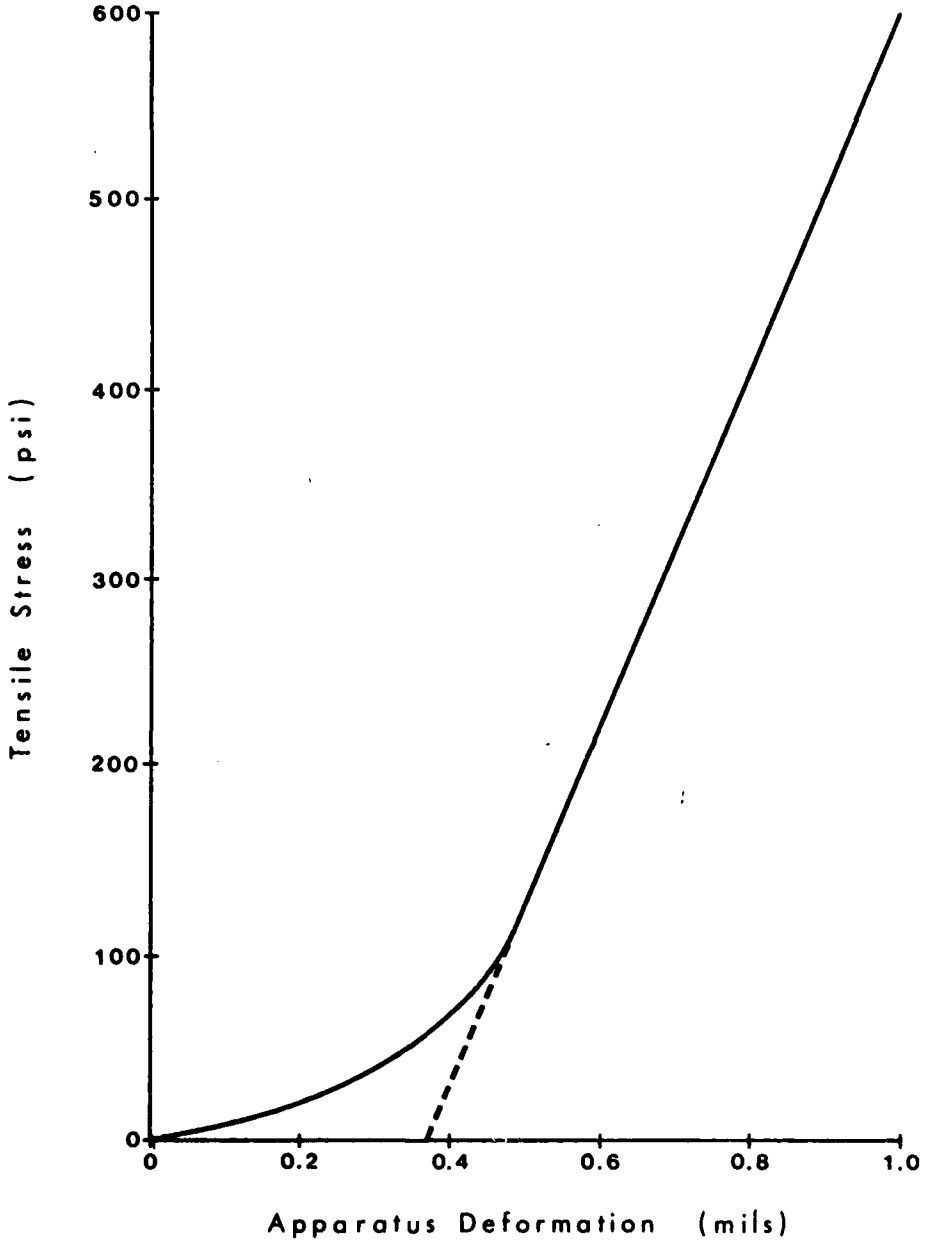

Fig. 3.11 Typical Stress-Deformation Response of Tensile Loading Apparatus

calibration curve used during testing is merely a straight line drawn through the origin. Upon completion of a test, the stress-strain data are corrected to eliminate the initial nonlinearity which appears as a result of not subtracting the true platen extension from the measured deformations. This is done by performing a linear regression analysis through the data points immediately above the 100 psi stress level and shifting the stress-strain curve so that this regression line passes through the origin. The procedure is discussed in greater detail in Chapter 6. Because the brush platens were manufactured to precise specifications and a press-fit was achieved between the dowels in the base and the bristle ends, the initial nonlinearity appears to be unavoidable and is merely a consequence of not being able to measure deformations at the specimen surface.

It should be noted that this same phenomenon is apparent in the calibrations of the compressive walls as well. Here the cause appears to be an initial seating of the walls against the Allen bolts which secure them to the frame and seating of the Allen bolts themselves in the frame. When the cubical cell is assembled, these bolts are torqued to 300 ft-lbs. to eliminate as much of this movement as possible. The level to which the bolts can be torqued is limited by the strength of the bolts which must resist not only the stresses induced by torquing but the applied stresses within the cubical cell as well. With 300 ft-lbs. of torque, failure of the bolts should occur at the same time the 30,000 psi capacity of the cell is reached. For low-pressure testing, the torque has been

increased to 400 ft-lbs with the result being that the initial slack in the system is cut approximately in half. However, some slack still exists and the amount of movement still varies randomly from test to test. Therefore, the same linear regression procedure is used in analyzing the stress-strain data generated along the compression axes.

The calibration of the proximitor probes is a function of the driver-probe-target material combination being used. Therefore, a separate calibration was needed for the tensile apparatus probes. To accomplish this, a second set of calibrating potentiometers was added to each of the proximitor drivers, in effect creating 18 additional drivers. A toggle switch provides for selection of the appropriate "driver". Because these potentiometers match the voltage output range to a preselected range of gap widths, the probe calibrations for the tensile loading apparatus could be adjusted to account for the fact that the tensile stresses, and thus the resulting deformations, would be an order of magnitude less than the compressive stresses and deformations at failure (assuming a tensile strength approximately one-tenth the compressive strength). By reducing the range of gap widths over which the probes were calibrated, the accuracy of the probe measurements was increased proportionally.

Although the proximitor probes on the compressive walls are the same regardless of the type of test being performed, a second set of potentiometers was added to the drivers for these probes as well to provide better accuracy in the measurements of the lateral

AD-A136 124 THE STRENGTH AND BEHAVIOR OF STEEL FIBER-REINFORCED CONCRETE UNDER COMBIN..(U) COLORADO UNIV AT BOULDER DEPT OF CIVIL ENVIRONMENTAL AND ARCH.. 2/4

UNCLASSIFIED R W MEIER ET AL. MAY 83 AFOSR-TR-83-0974 F/G 13/3 NL

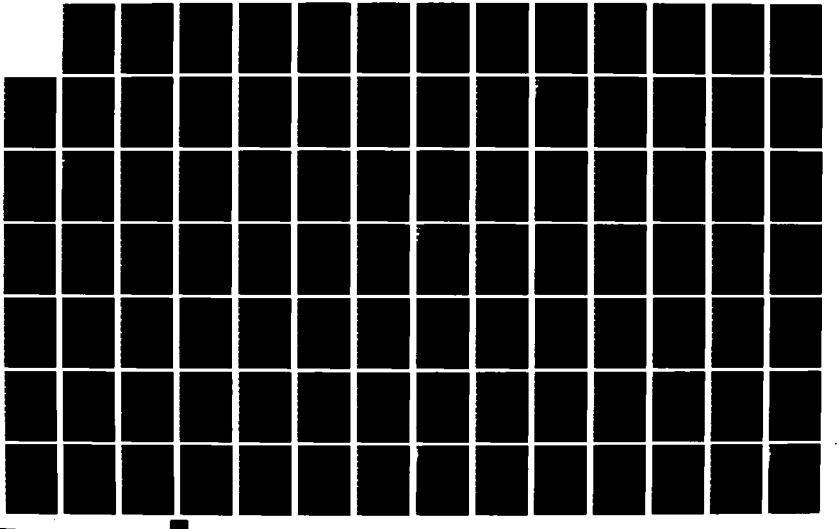

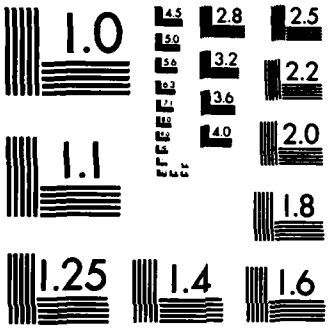

MICROCOPY RESOLUTION TEST CHART
NATIONAL BUREAU OF STANDARDS-1963-A

strains resulting from uniaxial tension loading. For compressive loading, a 0.120 inch range of gap widths was provided. For those tests in which one or more axes remained unloaded, a 0.060 inch range could be selected on those axes, effectively doubling the accuracy of the deformation measurements. The degree to which the range of gap widths can be reduced is limited by the fact that the probes are rigidly affixed to the walls of the cubical cell, while the specimen can translate a distance of 0.035 inches within the central cavity. The probe calibration must therefore be able to accommodate this movement as well as the deformations of the specimen and the displacement of the wall away from the frame under loading. A 0.060-inch range was the smallest possible range which could accommodate all of these movements.

This problem was partially eliminated in the tensile loading apparatus since the probes are accessible even after the apparatus has been assembled. The probes are connected to the frame through threaded holders which allow for adjustments in the axial direction. After the apparatus is assembled, the probe holders are screwed further into or out of the frame to bring each probe within the calibrated range. Since the calibration curves are nonlinear (a typical curve is shown in Fig. 3.12) this serves to further increase the accuracy of the deformation measurements by allowing the initial gap widths to be set such that the probes will operate in the most sensitive portion of the calibration curve throughout the test.

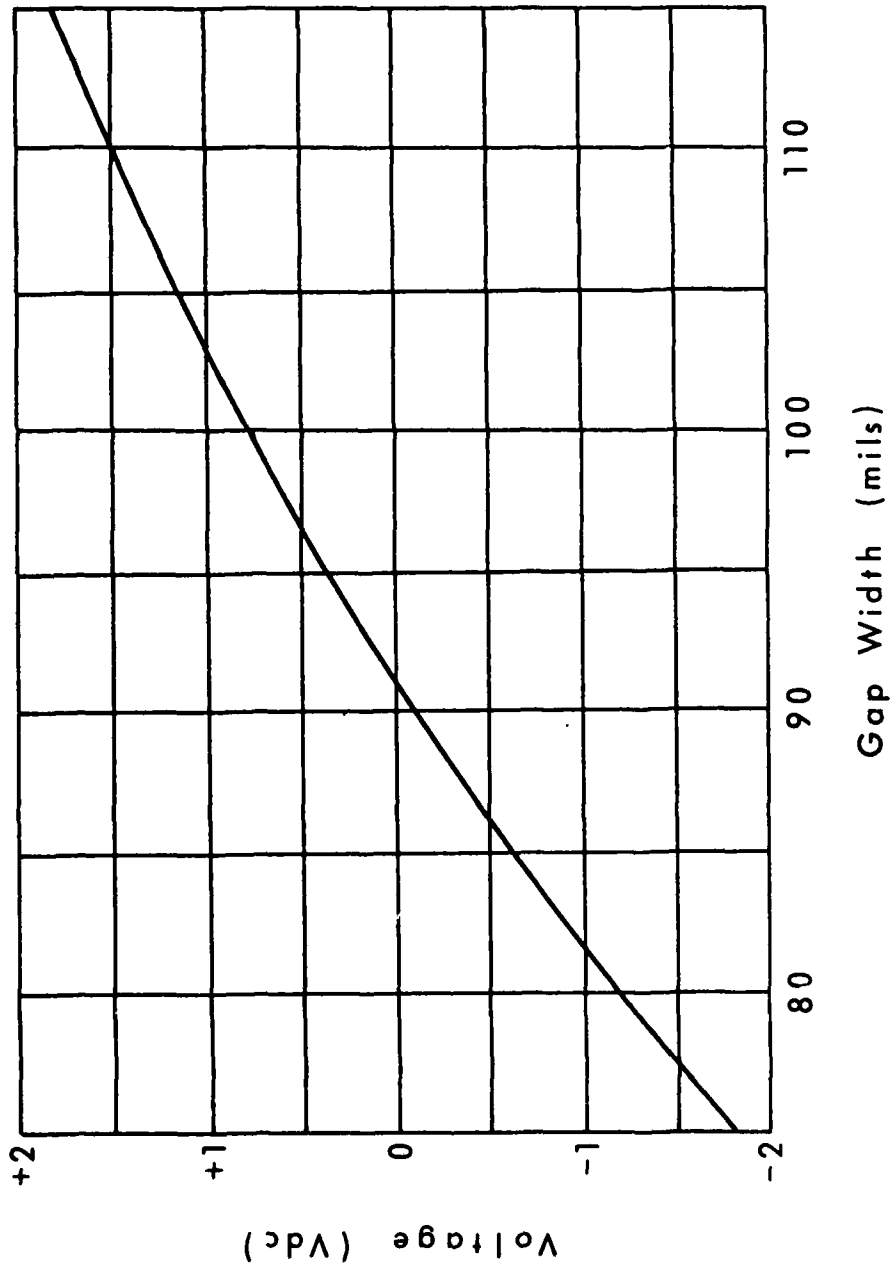

Fig. 3.12 Typical Probe Calibration Curve

3.6 Specimen Preparation and Gluing

The brush platens are glued to the specimens with a commercial structural concrete epoxy (Sikadur 31 Hi-Mod Gel, manufactured by Sika Corporation). This epoxy was chosen for its high elastic modulus (to provide a rigid structural connection), high strength, and ease of application. It has the consistency of a thick paste so it can be troweled onto the surface of the specimen.

To investigate the adhesive capabilities of the epoxy, a series of tests were conducted in which solid aluminum platens were glued to opposing faces of a concrete cube and loaded in tension in a universal testing machine. In every test, the epoxy-aluminum bond failed long before the strength of the concrete was reached. To remedy this, the surfaces of the aluminum were sandblasted to roughen the gluing surface and remove any traces of dirt or grease. This proved to be sufficient as subsequent tests resulted in failure of the concrete cubes.

Next, a way to remove the epoxy from the brush platens after each test had to be found. A first attempt involved the use of a chemical bond-breaker (Visstrip, manufactured by Oakite Corporation). To determine the suitability of this method, 1/4-inch square aluminum rods identical to those from which the bristles were made were glued onto the surface of a concrete cube. After the epoxy had fully cured, a small amount of the Visstrip was applied around the perimeter of each bristle and the cube was set aside. Every half-hour, the bristles were checked to see if the bond had loosened sufficiently to allow the bristle to be pulled off. This was

finally accomplished after 4-5 hours at which time any remaining epoxy could be removed with a putty knife. Subsequent tests using an array of bristles spaced apart by approximately the same amount as in the assembled brush platens showed that the Visstrip would penetrate between the bristles as long as the tips of the bristles remained submersed in the solvent.

A number of disadvantages of this method appeared after using the Visstrip on the actual brush platens over a number of tests. The foremost problem was that the Visstrip would soften the epoxy enough to break the bond but not enough to enable the epoxy to be removed from between the bristles. The very small size of the gaps made it difficult to get in between the bristles and after a few tests, the buildup of epoxy between the bristles had caused the brush platens to become significantly stiffer. Another problem was that repeated and prolonged exposure to the Visstrip (which is highly acidic) resulted in pitting of the aluminum.

This method was abandoned in favor of simply sandblasting the epoxy off. This had the the advantage of being fairly quick and easy, and it renewed the surface of the bristles after every test to promote optimum adhesion of the epoxy in the next application. The amount of aluminum removed by sandblasting was insignificant and dozens of tests could be performed without measurably shortening the bristles.

To prevent the glue from penetrating between the bristles, which would increase the stiffness of the brush platens in the lateral direction, the gaps between bristles were filled with a

household silicone rubber caulk to a depth of about 1/8 inch. Silicone rubber was chosen because it not only had the low stiffness required but was also chemically inert, and so would neither affect nor be affected by the epoxy.

The silicone rubber also served the purpose of preventing sand from accumulating between the bristles during the sandblasting operation. Because of its high resiliency, the rubber was unaffected by the sandblasting. As a precaution, however, the rubber was removed from between the bristles and replaced with a fresh layer approximately half-way through the test program.

Since the deformations of the glue line are included in the standard calibration of the apparatus, as mentioned in Section 3.5, it was essential to the accuracy of the strain measurements taken during a test that a good bond between the brushes and the specimens be attained and a uniform thickness of the glue line be maintained from test to test. A standard specimen preparation procedure was established as follows:

1. The specimens, which were cast in 4 x 4 x 5 inch steel molds, are cut into 4-inch cubes using a double-bladed masonry saw equipped with diamond blades. The purpose of this is to ensure that the brush platens are glued to competent concrete and to create a smooth, level surface for gluing.
2. The ends of the brush platens and the cut faces of the specimen are cleaned thoroughly with ethyl alcohol and blown dry with compressed air. This

removes any traces of dust or grease which might affect the adhesion of the epoxy.

3. The two-component epoxy is mixed according to the manufacturer's instructions and applied to the surface of the brush platen with a putty knife. Using a 5-inch broad knife, the glue is spread evenly over the surface of the brush and any excess glue is removed, leaving a glue line aproximately 0.05 inches thick.
4. A trowel with a saw-toothed edge is run across the surface once, removing slightly more than half of the remaining glue.
5. The same procedure is repeated with the specimen with care being taken to work the glue into the surface to fill any small voids. Again, the trowel is used to remove half the glue.
6. The brush platen is stood on end with the bristles pointing up and the specimen is pressed down onto the brush and rotated slightly from side to side to eliminate any air pockets in the glue. The excess glue forced out the sides is removed with a putty knife.
7. The same procedure is repeated for the other brush platen and the opposite face of the specimen. The brush platen is then pressed down onto the cube.

8. Eight 10-lb weights are stacked on top of the completed brush-specimen assembly to force out even more of the remaining glue. This amount of weight is sufficiently great in relation to the weight of the specimen itself (approximately 5 lbs.) that the additional weight of the specimen on the lower of the two glue lines will not result in a thickness different from that of the upper glue line.
9. For the first hour after the gluing is completed, the specimen is periodically checked and the glue being squeezed out by the added weight is removed with a putty knife. The glue line must be flush with the sides of the brushes and specimen to prevent any problems with inserting the specimen into the central cavity of the cubical cell. Additionally, it was discovered during preliminary testing of the apparatus that the brushes would be sheared off the specimen under transverse compressive loading if the glue line was not flush with the specimen because the fluid cushions will apply pressure to the exposed surface of the glue line in the tensile direction.
10. The glue is allowed to cure for a minimum of 16 hours with the weights in place before the specimen is placed into the cubical cell. According to the manufacturer's specifications, the epoxy achieves

75 percent of its ultimate strength in 16 hours and approaches 100 percent of its strength in 24 hours. Therefore, the specimen was not moved until 16 hours had elapsed and, regardless of when the specimen was placed into the apparatus, testing did not begin until at least 24 hours had elapsed.

By following this procedure for every test, an adequate bond between the specimen and the brush platens was always achieved and failure of the bond was eliminated. Additionally, the excellent reproducibility of the stress-strain results (which will be discussed in Chapter 5) suggests that differences in the thickness of the glue line from test to test were kept to a minimum.

CHAPTER 4

RESEARCH PROGRAM

4.1 Introduction

The primary objective of the present test program is to complement the information gathered by Egging (1981) on the strength characteristics of steel-fiber reinforced concrete (SFRC). In that research program, referred to as Phase I, a series of multiaxial compression tests were performed on SFRC specimens with a common mix design. The results of those tests were used to calibrate several analytical constitutive models for possible use in characterizing SFRC stress-strain and strength behavior.

The details of the SFRC mix design employed in both Phase I and the present investigation (Phase II) are presented in Section 4.2. The strength results of the Phase I test program are summarized in Section 4.3. The present test program is described in Section 4.4.

4.2 The SFRC Mix Design

The design of a plain concrete mix for use with steel-fiber reinforcing is governed by the need for good workability to offset the decrease in workability after the addition of fibers, the need for a good dispersion of fibers throughout the mix, and the need for an adequate paste content to coat the large surface area of the

fibers and provide the mechanical bond between the fibers and the concrete matrix . In view of these considerations, the design parameters that have generally been used for fiber-reinforced concrete fall within the following ranges:

1) low water/cement ratio (0.35-0.45)
2) cement contents from 600 to 1000 lb. per cu. yd.,
3) maximum coarse aggregate size of 3/8 inch,
4) low fineness modulus of the fine aggregate (less than 2.7, i.e., a high percentage of fines),
5) percentage of fine aggregate from 45 to 60 percent of the total aggregate; and
6) slump (before the addition of fibers) of 3 to 4 inches.

Additionally, the workability of the fibered concrete and the degree of dispersion of the fibers is affected by the aspect ratio and volume percentage of the fibers. Aspect ratios in excess of 100 tend to promote segregation or balling of the fibers and hence an inadequate dispersion of the fibers in the mix. The same is true for high volume percentages of fiber reinforcing which, in addition, decrease the workability of the fresh concrete. Volume percentages of 0.4 to 0.9 are commonly used when incorporating deformed fibers and 0.9 to 1.8 with straight fibers.

The plain concrete mix design selected by Egging (1981) is as follows:

water/cement ratio = 0.5

cement content = 770 lb/yd^3

maximum size of coarse aggregate = 3/8 in.

fineness modulus = 2.5

percentage of fine aggregate = 53% of total aggregate (by weight)

The resulting mix proportions are: C 1 : FA 1.82 : CA 1.64 : W 0.5.

The steel fibers chosen for this research program are "Dramix" fibers, manufactured by Bekaert Steel Wire Corp. These fibers are smooth, round wires with a patented hooked end to increase their resistance to pullout. A typical fiber is shown in Fig. 4.1. To prevent segregation or balling as the concrete is mixed, an artificially low aspect ratio is created by collating the fibers into clips with a water soluble glue. This glue dissolves within one minute after the addition of the fibers to the plain concrete. The clips are evenly distributed throughout the mix within this first minute, then the individual fibers are distributed as the glue dissolves.

The Dramix fibers are available in a number of length/diameter combinations providing a range of aspect ratios from 60 to 133. In a preliminary test program conducted by Egging (1981), four different fiber sizes were investigated. Based on the results of that test program, fibers with a length of 30 mm (1.18 in.) and a diameter of 0.4 mm (0.016 in.) were selected. The properties of the concrete incorporating these fibers were intermediate among the properties obtained with the other fibers, the fresh concrete had good workability, and the fibers had the shortest available length which fit comfortably within the 4-in. size of the cubical test

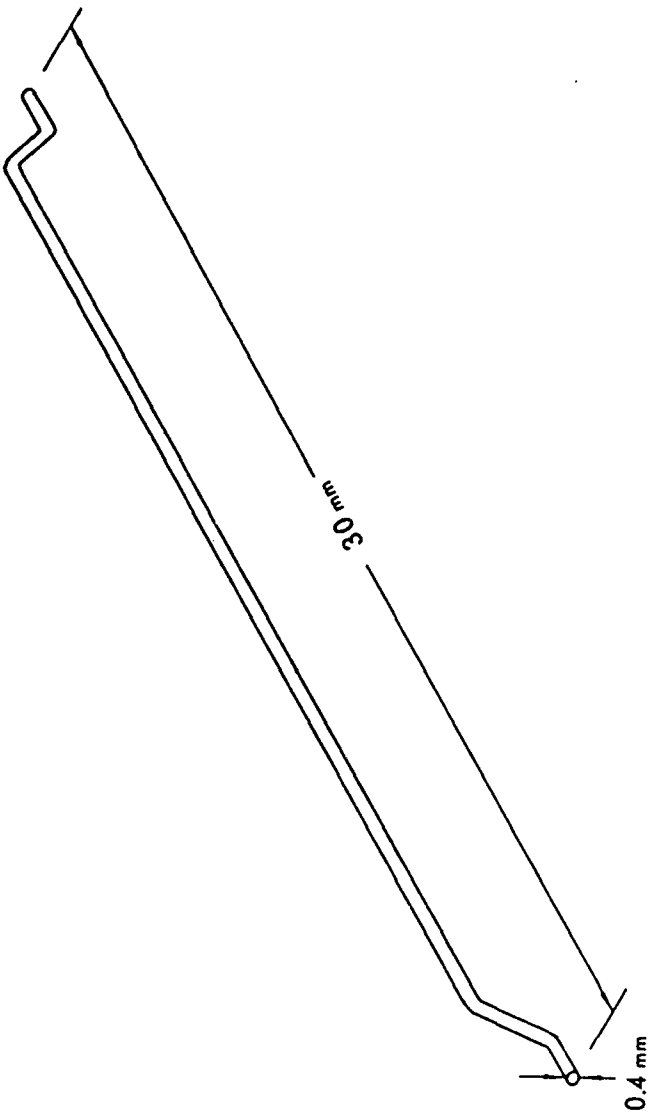

Fig. 4.1 Typical Fiber

specimen. The latter would tend to promote good dispersion and random orientation of the fibers within each test specimen.

The volume percentage of reinforcing used in this research program was 0.6% as recommended by the manufacturer. This recommendation is based on field work which indicates that with 0.6% reinforcing, no balling or segregation occurs and, with a properly designed concrete mix, good workability is achieved.

4.3 Phase I Test Results

For the final test series of Phase 1, two identical batches of SFRC were cast. These were designated Batches F1 and F2. In order to ensure similarity in strength between the two batches, strength-age curves were established using unconfined compression tests on 3x6 in. control cylinders. These curves are shown in Fig. 4.2 along with the strength-age curve for an identical mix used during the preliminary investigation into the effects of fiber size. This batch was designated P3. The unconfined compressive strengths at an age of approximately 50 days were 9305, 9035 and 9099 psi, respectively, indicating that comparable specimens had been obtained. These curves were also useful in establishing the point at which the cubical cell tests could begin, showing that no further increase in strength was to be expected beyond the age of 50 days.

The stress paths employed in the final test series consisted of hydrostatic loading to one of three levels of octahedral normal stress (σ_o = 4, 6, or 8 ksi), followed by monitonic shearing in the deviatoric plane in one of three directions, as shown in Fig. 4.3. The three directions were those of triaxial compression

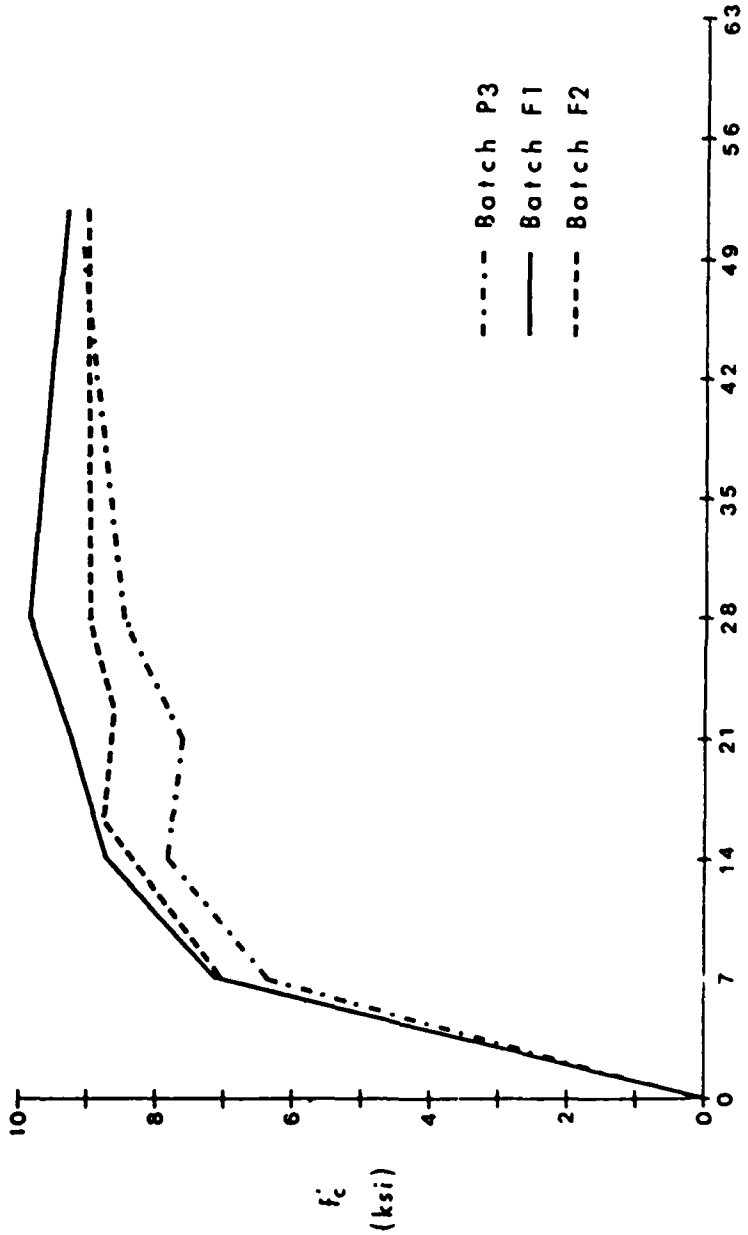

Fig. 4.2 Unconfined Compressive Strength vs. Age for Phase I FRC

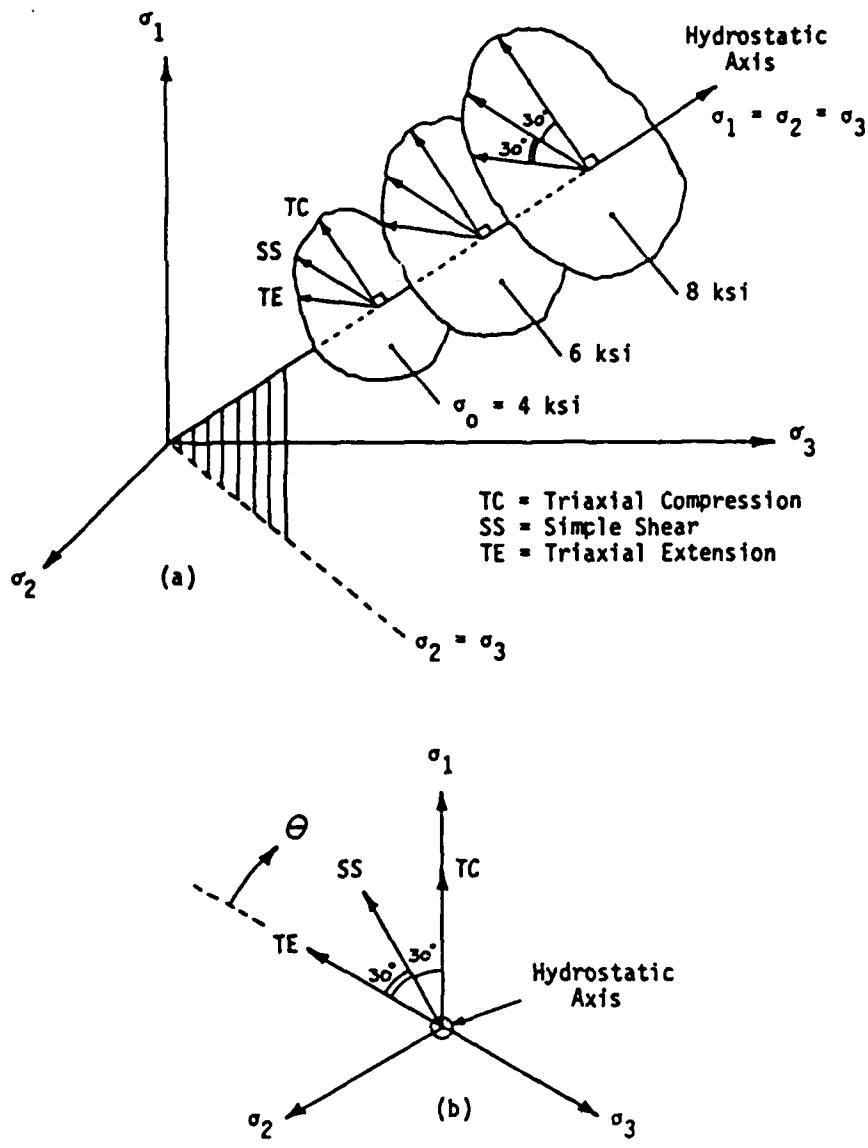

Fig. 4.3 Multiaxial Compression Stress Paths in (a) Stress Space; (b) Octahedral Plane (Egging [1981])

($\Delta\sigma_1>0$, $\Delta\sigma_2=\Delta\sigma_3=-1/2\ \Delta\sigma_1$), triaxial extension ($\Delta\sigma_1=\Delta\sigma_2>0, \Delta\sigma_3=-2\Delta\sigma_1$) and simple shear ($\Delta\sigma_1>0, \Delta\sigma_2=0, \Delta\sigma_3=-\Delta\sigma_1$), designated TC, TE and SS, respectively. These load paths are shown as a function of time in Fig. 4.4. For each stress path, a minimum of three replications was obtained. The data acquired during the tests consisted of stress-strain response curves in each of the three loading directions up to the point of failure. Because fluid-cushion loading is used, these three directions are assumed to coincide with the principal stress and strain axes.

In the Phase 1 research program, failure was defined as the point at which volume dilation of the material begins. This was determined from a plot of the volumetric strain ($\varepsilon_v=\varepsilon_1+\varepsilon_2+\varepsilon_3$) vs. the maximum principal stress as that stress level at which the slope becomes vertical, as shown in Fig. 4.5. This point, which was originally called "discontinuity" by Newman (1965), is perceived by many to be a true material property as opposed to ultimate strength (loss of continuity in the specimen or failure to sustain continued loading) which has been shown to vary with the rate at which loads are applied (Newman 1966: Rusch, 1959). This feature will be discussed in greater detail in the next section.

The stress-strain curves from all of the Phase I tests have been presented by Egging (1981) and will not be repeated here. Since the present research program is primarily concerned with the strength characteristics of the SFRC, only this feature of the constitutive behavior will be discussed. These strengths are summarized in Table 4.1.

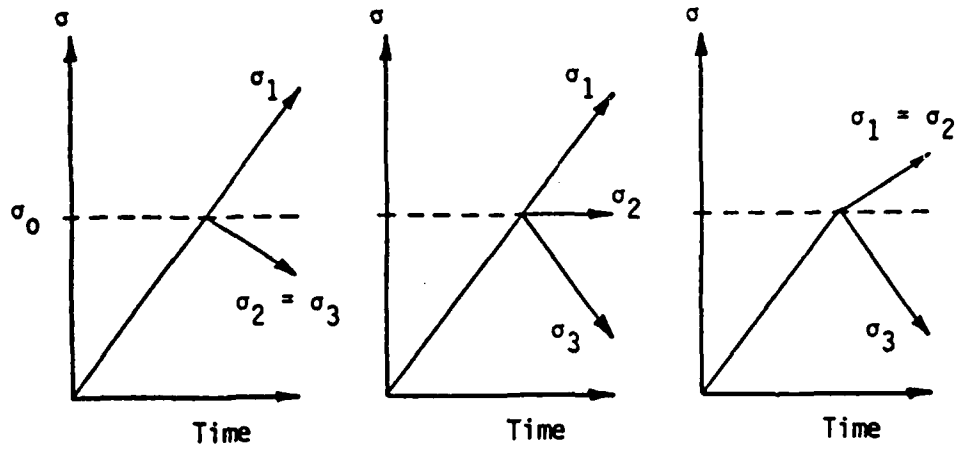

Triaxial Compression (TC)	Simple Shear (SS)	Triaxial Extension (TE)
$\Delta\sigma_1 > 0$	$\Delta\sigma_1 > 0$	$\Delta\sigma_1 > 0$
$\Delta\sigma_2 = \Delta\sigma_3 = -\frac{1}{2}\Delta\sigma_1$	$\Delta\sigma_2 = 0$, $\Delta\sigma_3 = -\Delta\sigma_1$	$\Delta\sigma_2 = \Delta\sigma_1$, $\Delta\sigma_3 = -2\Delta\sigma_1$

Fig. 4.4 Multiaxial Compression Test Load Histories (Egging [1981])

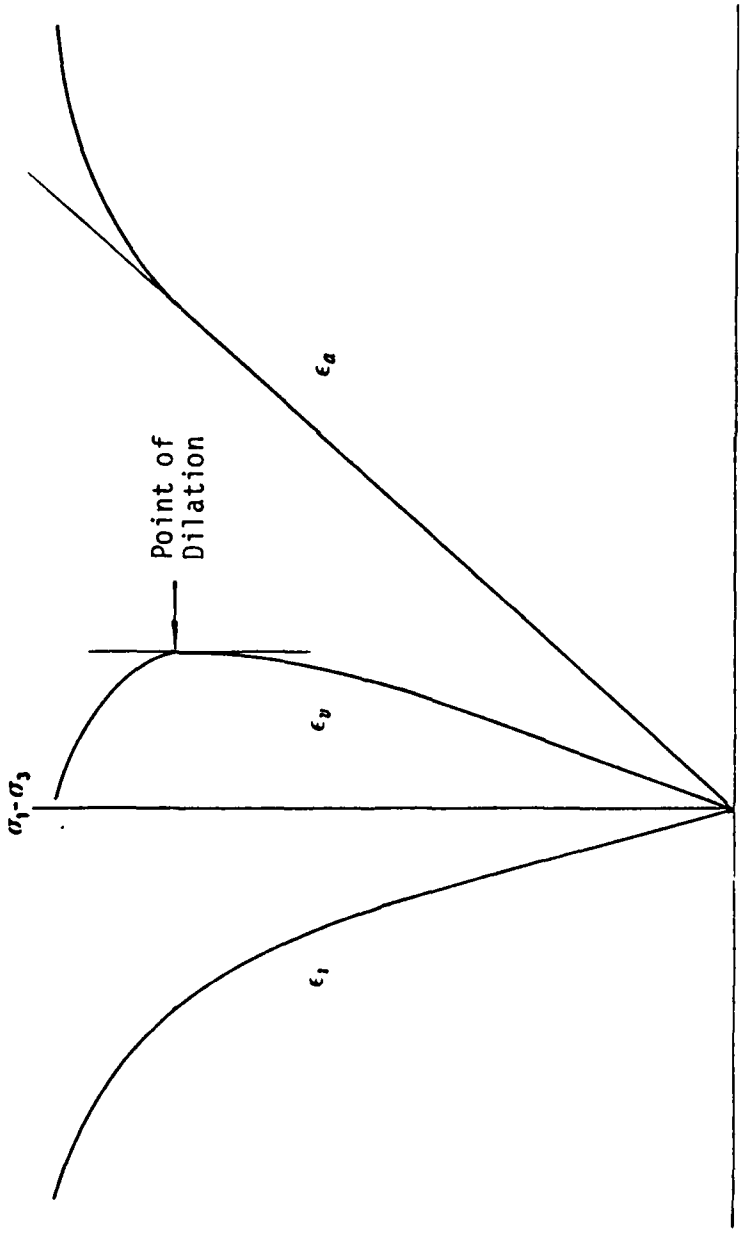

Fig. 4.5 Point of Dilation

Table 4.1

MULTIAXIAL COMPRESSION TEST RESULTS
(Egging [1981])

Load Path	Spec. No.	σ_1 (psi)	σ_2 (psi)	σ_3 (psi)	σ_o (psi)	τ_o (psi)
Triaxial Compression (TC) ($\theta=60^o$)		σ_z	σ_x	σ_y		
	F1A1	10400	800	800	4000	4525.48
	F2B2	10200	900	900	4000	4384.06
	F1B3	14000	2000	2000	6000	5656.85
	F1D6	17800	3100	3100	8000	6929.64
Simple Shear (SS) ($\theta=30^o$)		σ_z	σ_x	σ_y		
	F2B3	7900	4000	100	4000	3184.33
	F1A6	7600	4000	400	4000	2939.38
	F2D3	11600	6000	400	6000	4572.38
	F1A5	11200	6000	800	6000	4245.78
	F1B2	15000	8000	1000	8000	5715.47
Triaxial Extension (TE) ($\theta=0^o$)		σ_x	σ_y	σ_z		
	F2C2	5900	5900	200	4000	2687.00
	F2C1	5900	5900	200	4000	2687.00
	F1B1	5900	5900	200	4000	2687.00
	F2D4	8900	8900	200	6000	4101.21
	F2C5	8600	8600	800	6000	3676.95
	F1C5	8600	8600	800	6000	3676.95
	F1A2	11500	11500	1000	8000	4949.74

In Fig. 4.6, the test results are plotted in the τ_o-σ_o plane. From this plot, it can be seen that the octahedral shear stress at failure of the SFRC is dependent on both the hydrostatic stress level and the stress path. Furthermore, the relationship between strength and confining pressure appears to be linear over the range of confining pressures investigated. Unfortunately, strength data could not be obtained from some of the tests because of either brittle failure, which often occurred at a corner or on an edge of the specimen prior to volume dilation, or due to the rupture of a fluid cushion. Therefore, some of the test categories are represented by only one data point.

From Fig. 4.6, it can be inferred that the failure envelope is conical but with an irregular cross-section. This is better illustrated in Fig. 4.7 in which the octahedral shear strengths are plotted in the deviatoric planes. Here, the data points are plotted along their respective stress paths. Notice, also, from this plot that the shape of the cross-section is different in each of the deviatoric planes, becoming more rounded as the octahedral normal stress increases. This precludes the use of generalized strength formulations such as the three-dimensional Mohr-Coulomb or Drucker-Prager failure criteria.

Finally, the test results from the two axisymmetric stress paths (TC and TE) are plotted in the Rendulic Plane in Fig. 4.8. Here, the stresses correspond to the stresses along the (arbitrarily chosen) x-, y-, and z-axes of the cubical cell. In order to be consistent with the convention generally employed in the

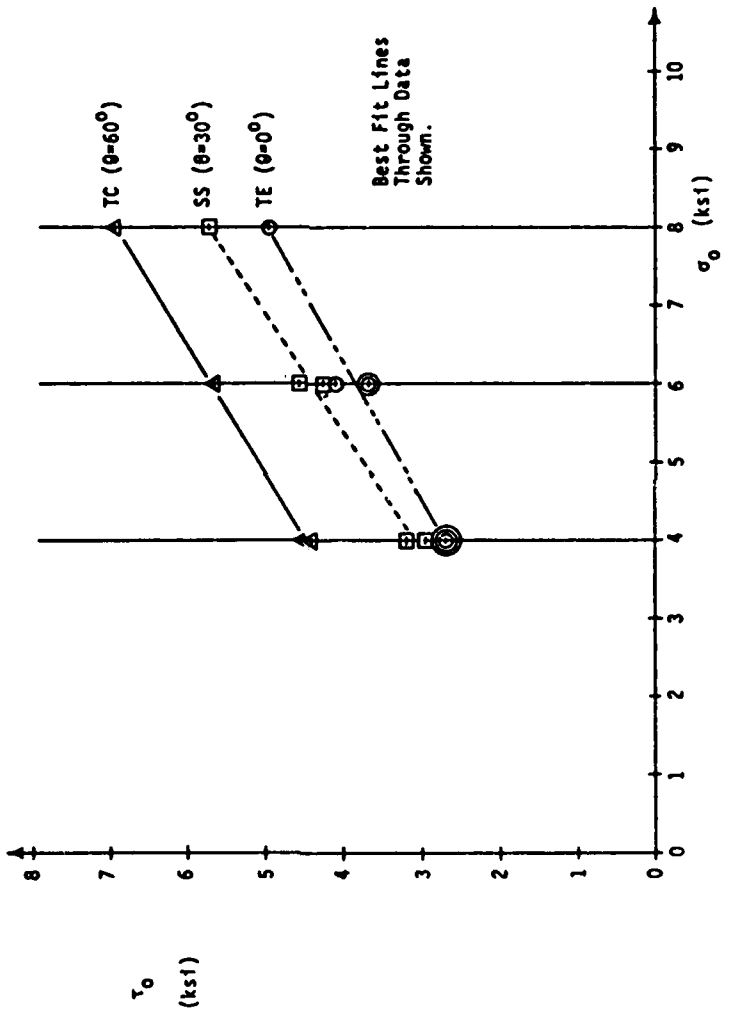

Fig. 4.6 Test Results from Phase I in τ_o-σ_o Plane (Egging [1981])

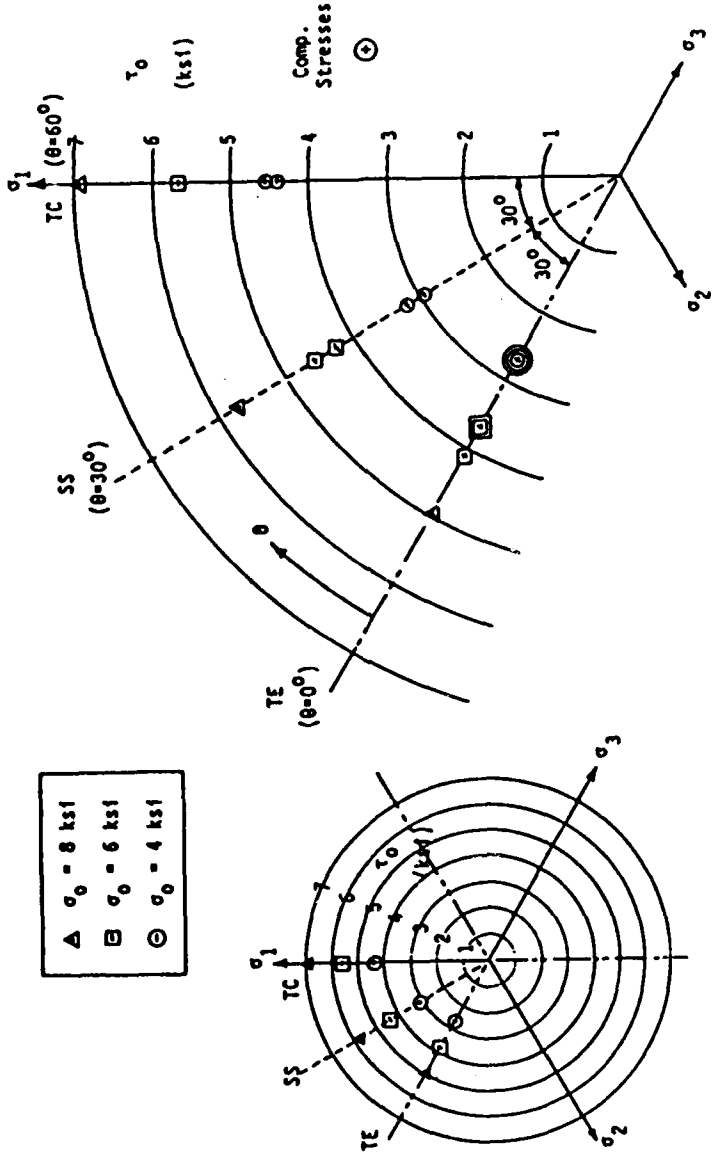

Fig. 4.7 Test Results from Phase I in Deviatoric Plane (Egging [1981])

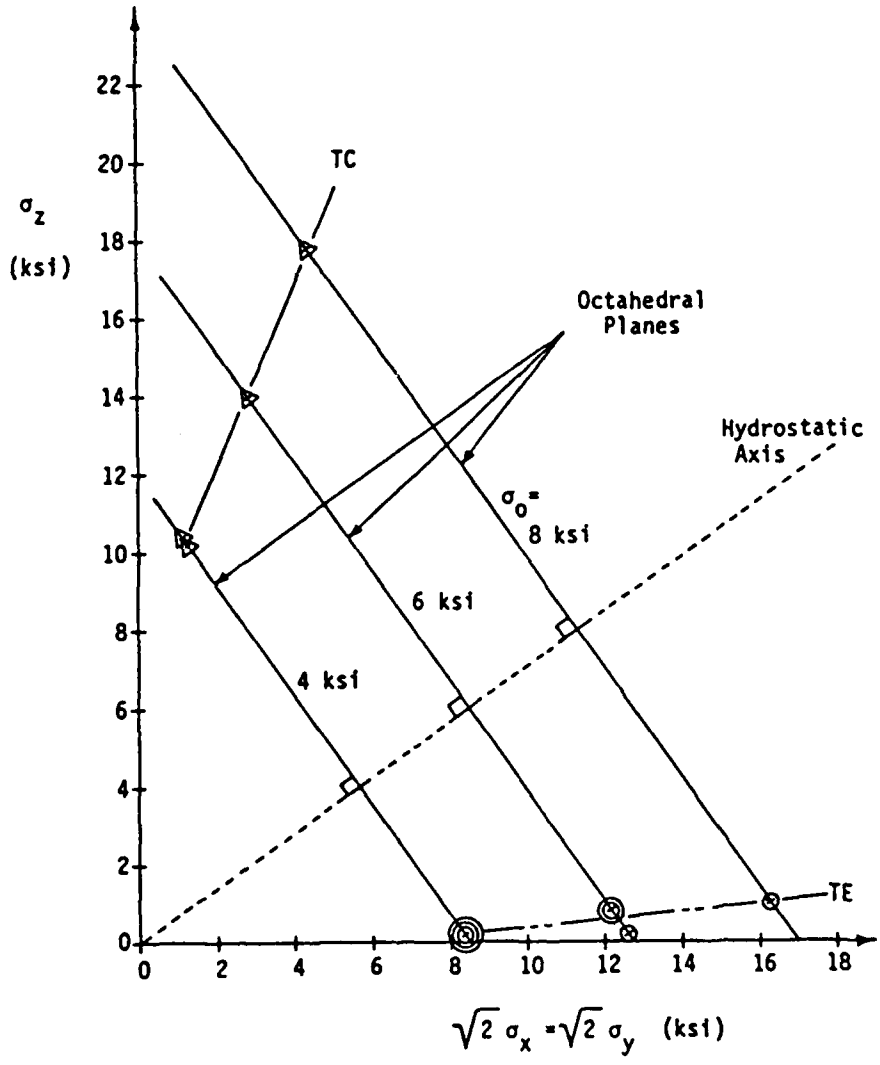

Fig. 4.8 Test Results from Phase I in Rendulic Plane (Egging [1981])

conventional cylindrical triaxial cell test, the stresses were applied such that the x- and y-axes would coincide with the lateral directions in a cylindrical specimen.

4.4 Test Program

The objective of the present test program is essentially to define the failure envelope for the SFRC in the biaxial stress plane and to use the strength data generated to refine the strength formulations derived by Egging (1981). In order to fully utilize the unique capabilities of the tensile loading apparatus when used in conjunction with the fluid-cushion cubical cell, particular attention was given to defining the failure envelope in the tension-compression quadrant.

The two failure criteria examined by Egging were those of Willam and Warnke (1974) and Lade (1981). In order to properly calibrate the Willam-Warnke model, which is described in detail in Chapter 6, the uniaxial compressive, uniaxial tensile, and equibiaxial compressive strengths are needed. None of these values were available to Egging, however, and had to be either assumed or extrapolated from his multiaxial compression test data. The uniaxial tensile strength is also required for proper calibration of the Lade model and the uniaxial compressive strength would have been useful, although not essential. Therefore, it was necessary for these parameters to be determined in the present test program.

The failure envelopes predicted from both the Willam-Warnke and the Lade models showed good agreement with the experimental data from Phase I. This is not surprising since both models were

calibrated directly from the experimental data. In order to properly investigate the validity of these models, however, the predicted failure envelopes should be compared with data other than those used in calibration. For this reason, the test program was designed to established the entire biaxial failure envelope with the exception of the small portion in the tension-tension quadrant. Stress states in this region of the biaxial plane are beyond the present capabilities.

To determine the failure envelope in the compression-compression quadrant, three stress paths were chosen in addition to uniaxial and equibiaxial compression. These paths represent proportional loading at stress ratios of $\sigma_3:\sigma_1$ = 1:10, 1:3, and 2:3. The stress ratio of 1:10 was included because the slope of the biaxial compression failure envelope changes fastest near the principal stress axes as shown in Fig. 4.9. The five compressive stress paths are shown in Fig. 4.10.

To determine the tension-compression portion of the biaxial failure envelope, six test types incorporating non-proportional loading were included in the test program. These tests involved loading in uniaxial compression to some percentage of the uniaxial compressive strength, then holding that stress constant while applying a transverse tensile stress to failure. These stress paths are shown in Fig. 4.11.

There was a number of reasons for choosing a sequential manner of loading rather than proportional loading. The first reason was to adequately investigate the shape of the envelope over

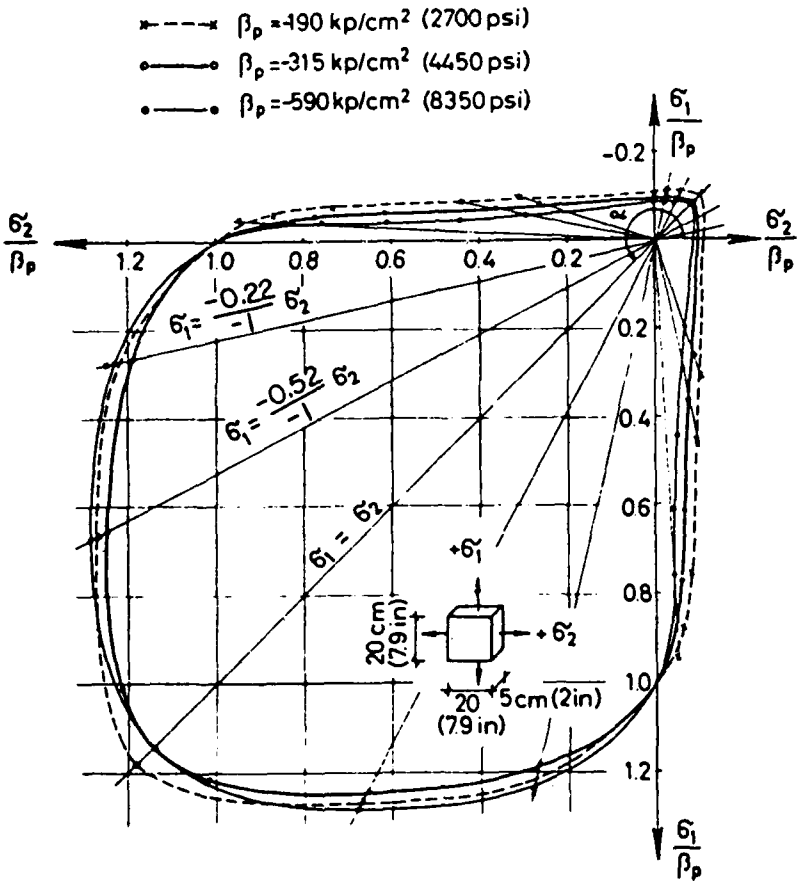

Fig. 4.9 Typical Failure Envelopes in Biaxial Plane (Kupfer, et al. [1969])

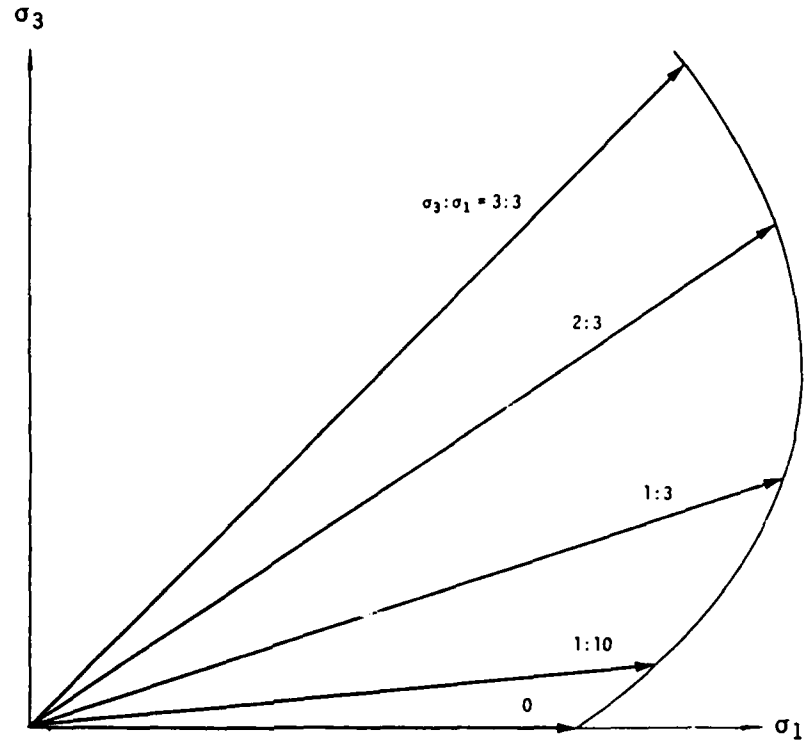

Fig. 4.10 Biaxial Compression Stress Paths

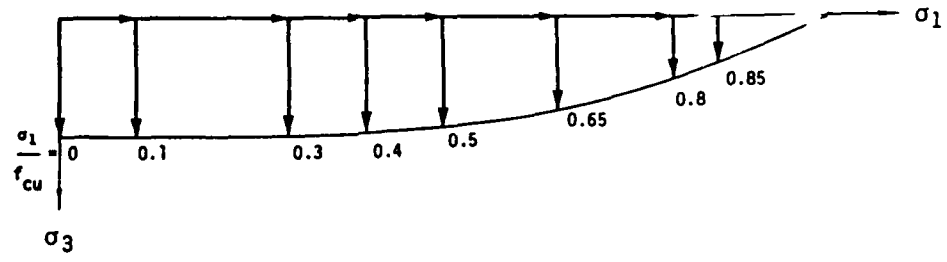

Fig. 4.11 Biaxial Tension-Compression Stress Paths

the entire tension-compression region. A number of investigations has indicated that the tension-compression failure envelope contains one or more inflection points. Vile (1965) conducted a series of biaxial tension-compression tests using direct tension specimens with a square, reduced cross-section loaded transversely in compression with concrete cubes as platens. This is shown in Figure 4.12(a). His results for both concrete and mortar specimens indicate a significant loss in tensile strength with the addition of a small transverse compressive stress (approximately one-tenth the uniaxial compressive strength), as shown in Figs. 4.12(b) and (d). The failure envelope for lightweight concrete, on the other hand, is slightly S-shaped with the greatest change in slope occurring at a stress level of 30-40 percent of the uniaxial compressive strength. This is shown in Figure 4.12(c).

McHenry and Karni (1958) used hollow cylinders loaded axially in compression with internal hydrostatic pressure providing a tensile hoop stress. Their results, shown in Fig. 4.13, are similar to those obtained by Vile for concrete and mortar.

Kupfer, et al. (1969) used brush platens to apply both tension and compression and established failure envelopes for three mixes of concrete with different compressive strengths. Each envelope was found to be slightly S-shaped as shown in Fig. 4.14.

One explanation for the shapes of these envelopes is that the mode of failure changes from tensile splitting at lower compressive stress levels to cleavage (predominantly compressive failure) at higher stress levels. Thus, the inflection in the

(a)

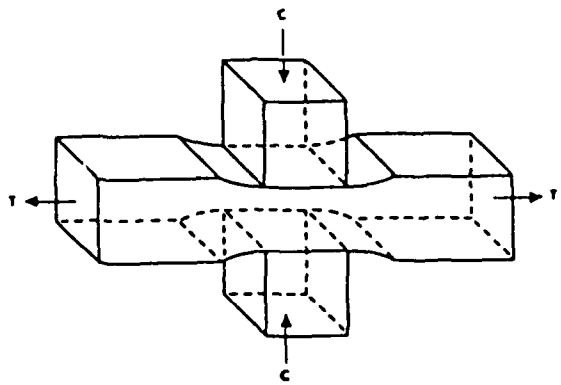

(b)

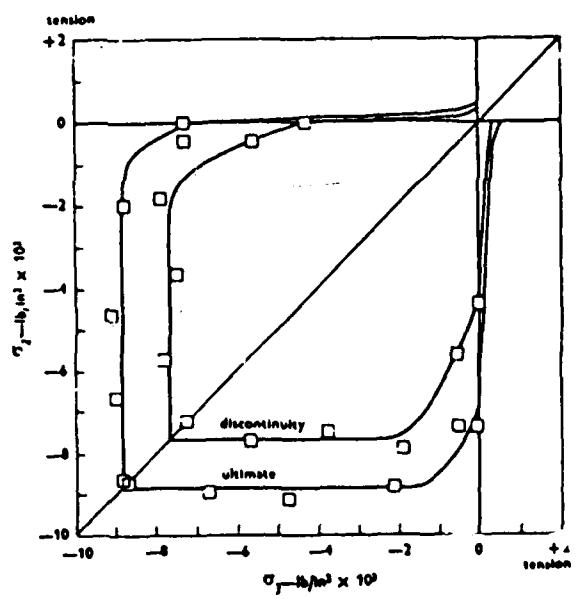

Fig. 4.12 (a) Loading Configuration;
(b) Biaxial Failure Envelope for Plain Concrete (Vile [1965])

(c)

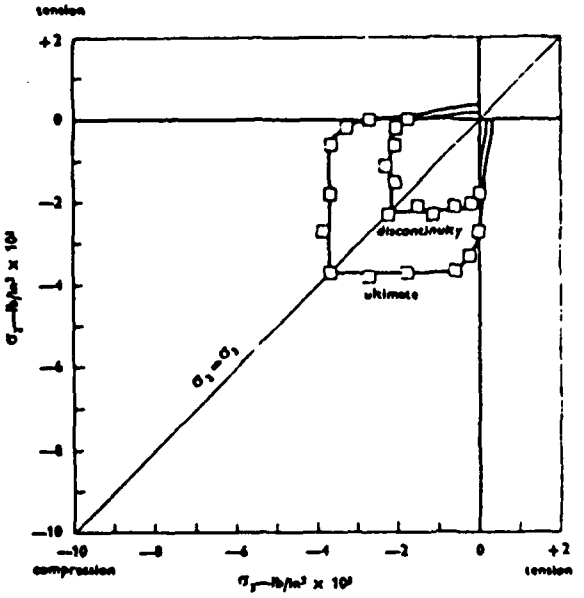

(d)

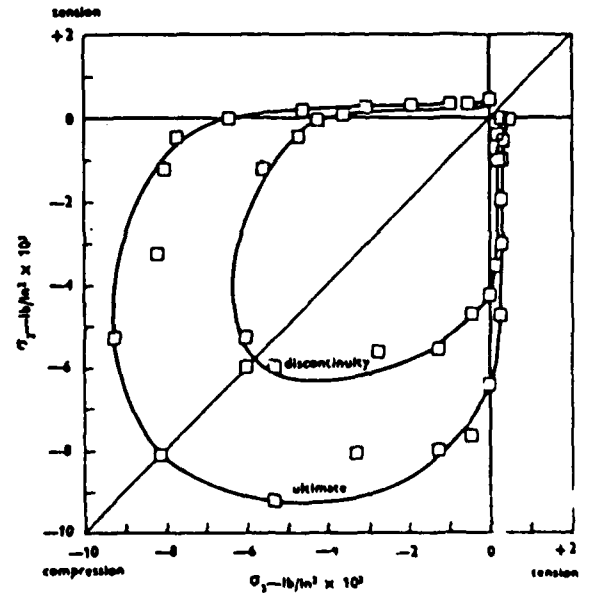

Fig. 4.12 Biaxial Failure Envelopes for
(c) Lightweight Concrete;
(d) Mortar
(Vile [1965])

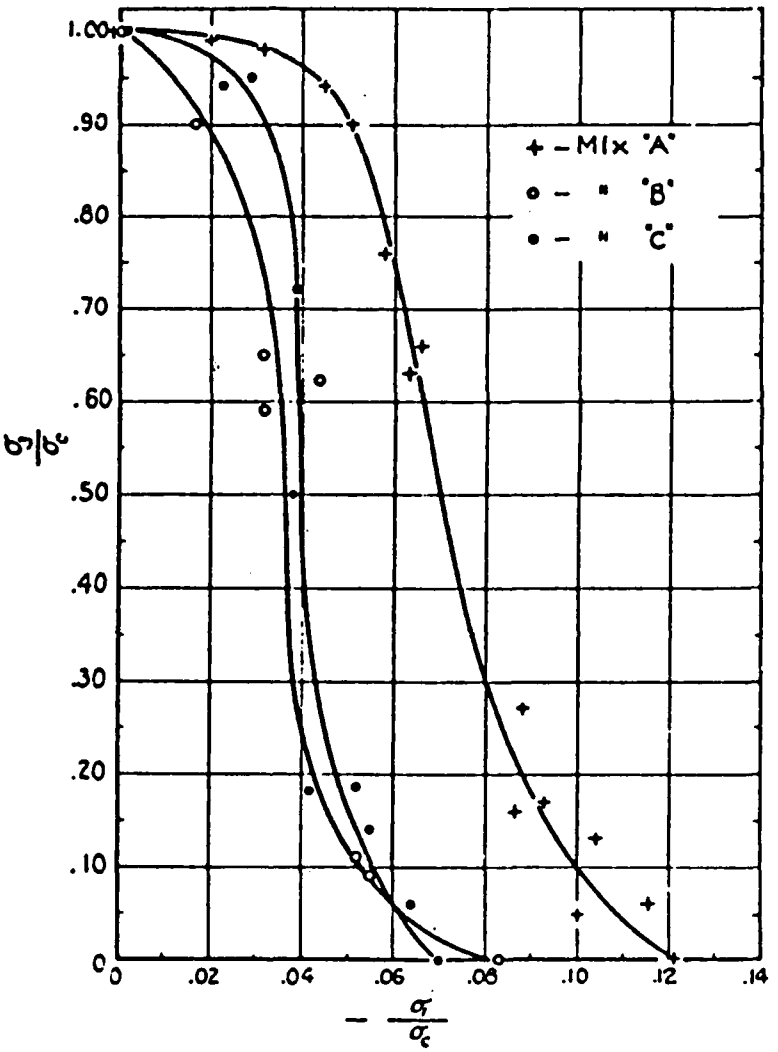

Fig. 4.13 Biaxial Tension-Compression Failure Envelopes
(McHenry and Karni [1958])

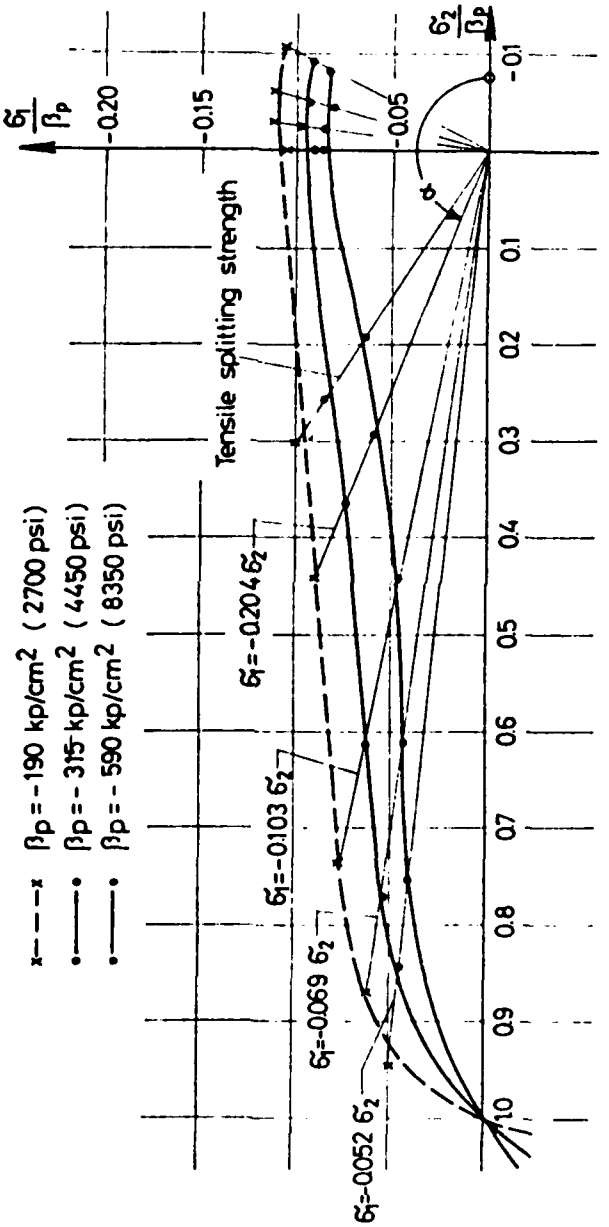

Fig. 4.14 Biaxial Tension-Compression Failure Envelopes (Kupfer, et al. [1969])

envelopes represents the transition from one mode to the other. Because the strength enhancement afforded by fiber reinforcing is greater in tension than in compression, it is reasonable to assume that the transition from tensile splitting to compressive cleavage would be even more pronounced.

In order to locate this transition, if it occurred, tests were conducted at stress levels of 10, 30, and 50 percent of the uniaxial compressive strength coinciding roughly with the stress levels at which inflection points were seen by the various investigators.

Another reason for choosing sequential loading was to study the changes in the structure of concrete under increasing compressive stress. It has been well-established that minute cracks (microcracks) exist in concrete even before it is loaded due to incomplete bonds between aggregate and cement paste and shrinkage of the cement paste during hydration (Hsu, 1963; Slate and Olsefski, 1963). As the concrete is stressed, these cracks propagate, causing a gradual deterioration of the concrete. At some critical point, these cracks coalesce and failure ensues.

The stress-strain curve for concrete in compression is reasonably linear up to a stress level of 30-60 percent of ultimate. During this initial loading, very little change in structure occurs. Above this stress level, however, the microcracks begin to grow in a stable fashion (i.e., if loading is halted, the cracks stop propagating). The initiation of crack growth has been determined experimentally using a variety of techniques. Jones (1952) used the

decrease in velocity of an ultrasonic pulse to detect the beginning of crack growth. Rusch (1959) used transducers to pick up the sounds emitted as the cracks opened up. Robinson (1965) used X-rays taken at various stress levels to follow the propagation of the cracks. Similarly, Hsu, et al. (1963) took slices from specimens loaded to different levels of stress and, using a staining technique, developed crack "maps" to indicate where crack initiation occurred as well as the paths taken by the cracks as they grew. The findings of these investigators are summarized in Table 4.2.

The results of these investigations indicate that crack propagation begins at the interfaces between coarse aggregate particles and cement paste and, once initiated, cracking proceeds along these interfaces. At this point, the cracks are localized around the individual aggregate particles.

At higher stress levels, these localized cracks are bridged by cracks running through the mortar and the cracks begin to coalesce into a failure surface. At a stress level of 75 to 90 percent of ultimate, the propagation of these cracks becomes unstable, requiring no further increase in stress to continue growing. This is the state originally called "discontinuity" by Newman (1965). The stress levels observed by the various investigators appear in Table 4.2.

From a fracture mechanics viewpoint, this state is reached when the strain energy released during crack growth exceeds the strain energy absorbed in the formation of new crack surfaces. The energy imbalance is sufficient to maintain the growth of the cracks,

TABLE 4.2

STUDIES THROUGH MICRO-CRACKING

	Investigator	Ref. No.	Load When Micro-cracks Start	Critical load
1	Hsu, Slate, Sturman and Winter	(18)	0.30 P_{ult}	0.7 to 0.9 P_{ult} direct observation
2	Krishnasawmy	(19)	0.30 P_{ult}	0.7 to 0.9 P_{ult} direct observation
3	Sturman, Shah and Winter	(20)	0.30 P_{ult}	0.7 to 0.9 P_{ult} direct observation
4	Jones	(16)	0.25 to 0.30 P_{ult} (sonic method)	-
5	L'Hermite	(17)	Cracking noise at 0.5 to 0.75 P_{ult}	sonic method
6	Rusch	(11)	Noise begins at at 0.5 P_{ult} (sonic method)	Noise increases rapidly at 0.75 P_{ult}
7	Oladapo	(21)	-	0.70 to 0.85 P_{ult} (strain distribution)

even in the absence of a stress increase. Because no further increase in stress is needed for the cracking to proceed to failure, this point is considered to be the true failure state in concrete and other brittle materials.

It is further contended that this failure point represents a true material property, identified by Glucklich (1963) as a critical strain energy release rate, whereas the ultimate strength is merely a time-dependent phenomenon. Physical separation will not coincide with the state of discontinuity if the continued application of stress occurs at a rate faster than the cracks can propagate to failure. This was shown by Rusch (1959) in a series of uniaxial compression tests performed at a variety of loading rates. These results, shown in Fig. 4.15, indicate that the long-term strength of concrete is approximately 80 percent of the ultimate strength measured during conventional short-term tests. The logical extension of this would be that under a sustained stress at or above the stress at dilation, failure will occur after a sufficient amount of time has passed. This was shown by Welch (1965).

Shah (1968) showed that the various stages of crack initiation and propagation are reflected in the shape of the stress-strain curve and, in particular, the shape of the stress-volumetric strain response. His results, shown in Fig. 4.16, indicate that the stiffening of the volumetric strain response, which begins at a stress level of approximately 50 percent of ultimate, is the result of the initiation of bond crack growth. This stiffening of the volumetric strain response continues until the stress-volumetric strain curve

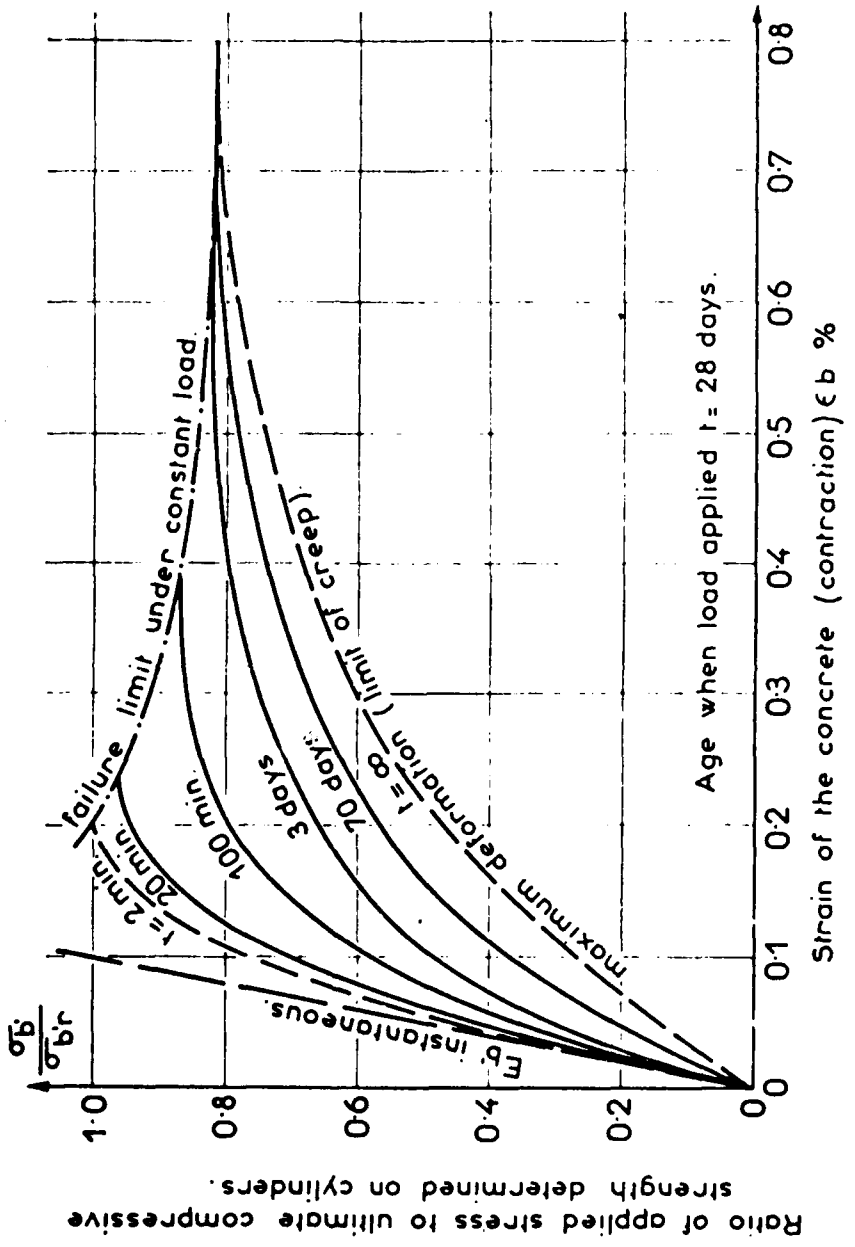

Fig. 4.15 Long-Term Strength of Concrete (Rusch [1959])

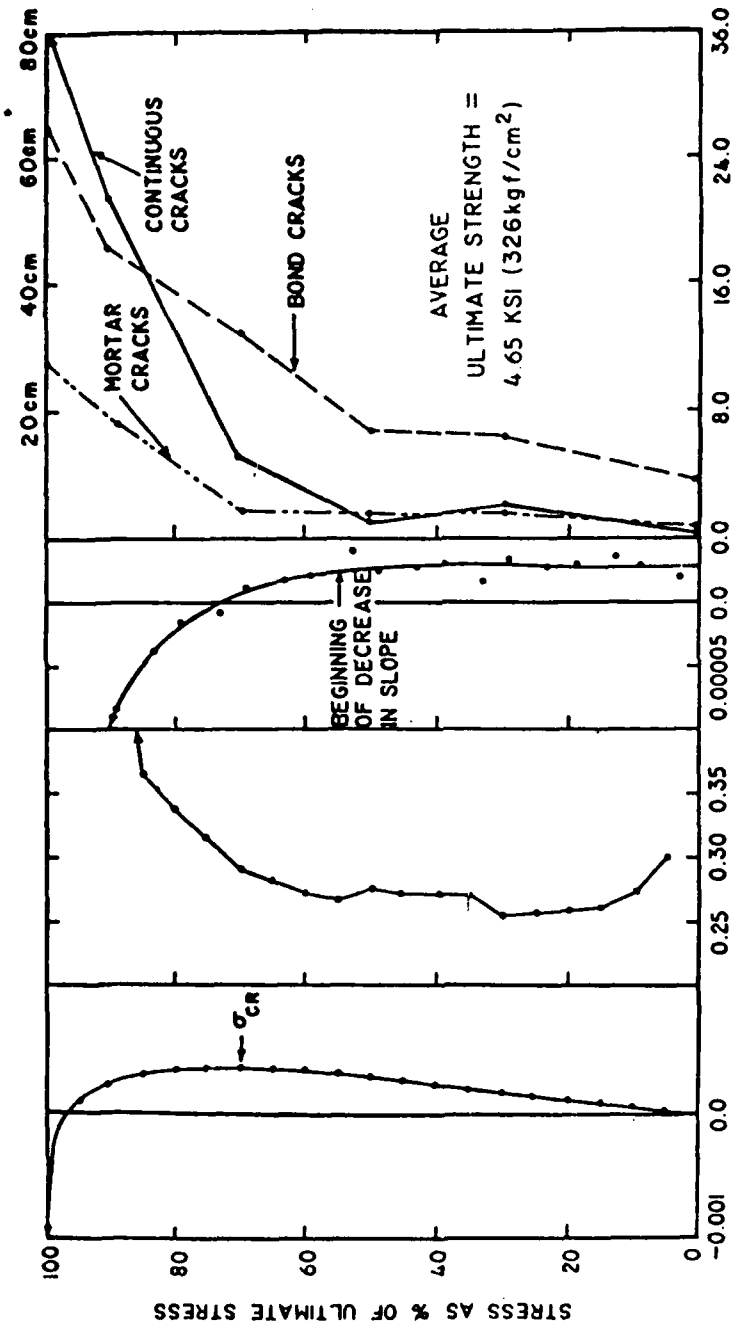

Fig. 4.16 Effect of Internal Microcracking on the Stress-Strain Behavior of Concrete (Shah [1968])

become vertical, at which point mortar cracking commences. Beyond this point, volume dilation occurs as these cracks open up and coalesce, which eventually leads to physical failure of the specimen. From this investigation and the others already mentioned, it was concluded that the point at which volume dilation begins coincides with the beginning of unstable crack propagation, and that the stress state which exists at this point represents the long-term strength of the concrete.

In order to investigate the effect of these changes in internal structure on the tensile strength of the SFRC and the reinforcing ability of the fibers, tests were also performed at stress levels of 40 and 65 percent. These stress levels more or less bracket the range of stresses at which crack initiation has been observed. Additionally, one more test category was included to involve loading to a stress level at or slightly below the point of discontinuity before applying tensile stress. From the results of the uniaxial compression tests, it was seen that dilation begins at a stress level of approximately 85 percent of ultimate. Therefore, two tests were performed with compressive loading to 80 percent of ultimate and one test was performed by loading in compression to the point at which volume dilation was observed before applying tensile stress. In this test, dilation occurred at a stress level of 85 percent, as expected.

The entire test program is summarized in Table 4.3 and Fig. 4.17. In this figure, the numbers associated with each stress path correspond to the test numbers indicated in the table.

Table 4.3

BIAXIAL TEST PROGRAM

Test Number	Test Type	Test Designation
1	Uniaxial Tension	UNIAX TEN
2	Uniaxial Compression	UNIAX COMP
3	Biaxial Compression $\sigma_2 / \sigma_1 = 1 / 3$	BIAX 1:3
4	Biaxial Compression $\sigma_2 / \sigma_1 = 2 / 3$	BIAX 2:3
5	Biaxial Compression $\sigma_2 / \sigma_1 = 3 / 3$	BIAX 3:3
6	Biaxial Tension-Compression $\sigma_1 / f_{cu} = 0.5$	0.5 F(CU)
7	Biaxial Tension-Compression @ Point of Dilation	0.8 F(CU) 0.85 F(CU)
8	Biaxial Tension-Compression $\sigma_1 / f_{cu} = 0.1$	0.1 F(CU)
9	Biaxial Tension-Compression $\sigma_1 / f_{cu} = 0.65$	0.65 F(CU)
10	Biaxial Tension-Compression $\sigma_1 / f_{cu} = 0.3$	0.3 F(CU)
11	Biaxial Compression $\sigma_2 / \sigma_1 = 1 / 10$	BIAX 1:10
12	Biaxial Tension-Compression $\sigma_1 / f_{cu} = 0.4$	0.4 F(CU)

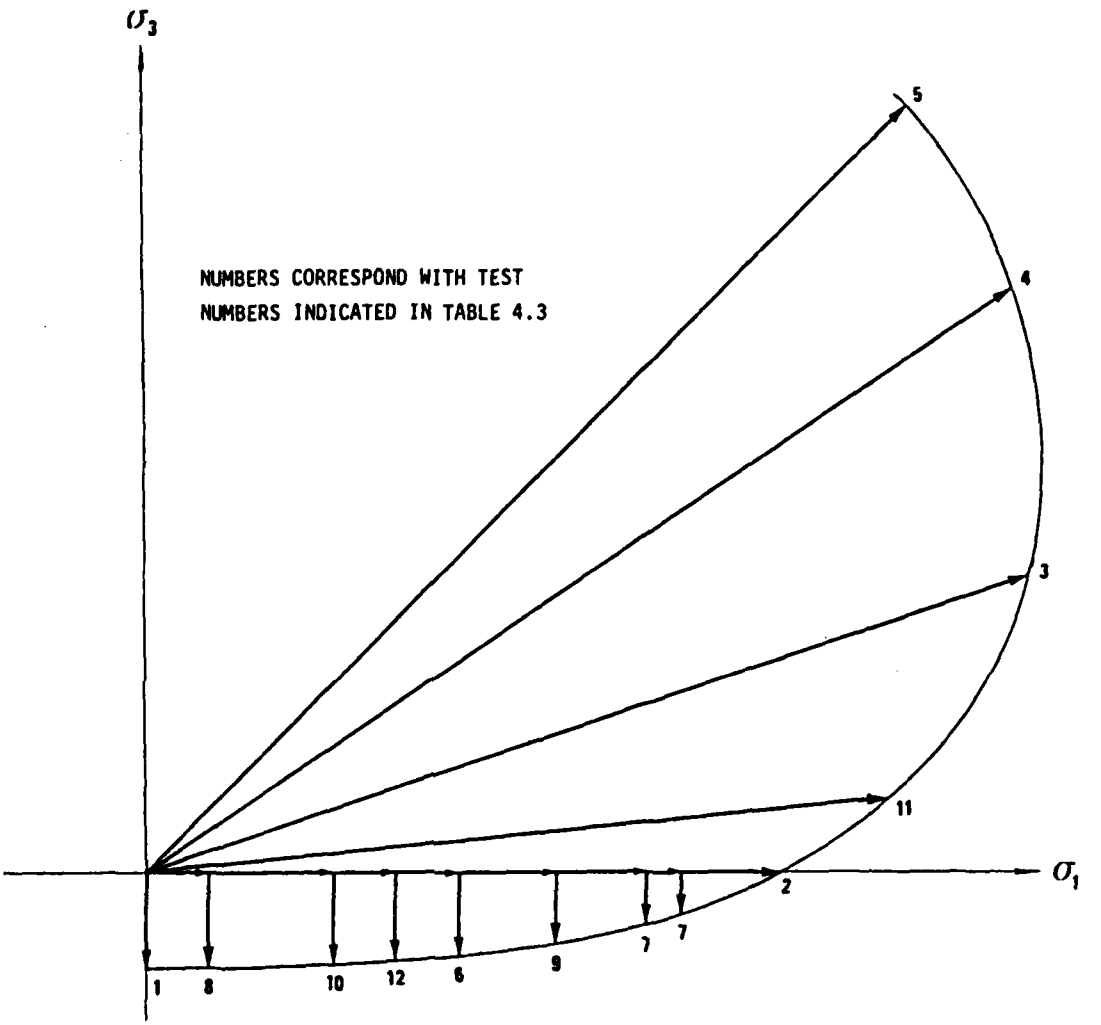

Fig. 4.17 Biaxial Stress Paths

CHAPTER 5

TEST RESULTS

5.1 Introduction

The results of the present investigation are presented in this Chapter. In Section 5.2, the results of preliminary tests on 3x6 inch control cylinders are presented and compared to the strengths of the control cylinders from Phase I. In Section 5.3, the results of both indirect and direct tension tests are discussed. The results of the uniaxial compression, biaxial tension-compression, and biaxial compression tests are presented in Sections 5.4, 5.5, and 5.6, respectively.

5.2 Strength Comparisons

For the present test program, a total of six batches of the SFRC were cast. Each batch consisted of twenty-four 5x4x4 inch "cubes" and forty-two 3x6 inch control cylinders. From the results of a preliminary series of conventional tests on the cylinders, two batches were selected for use in the final test program. These batches are designated Batches 4 and 5.

Figure 5.1 shows the strength-age curves established for Batches 4 and 5 using conventional unconfined compression tests on the 3x6 inch control cylinders. The test results from which these curves were drawn are tabulated in Table 5.1. Direct comparison of

Table 5.1

UNCONFINED COMPRESSION TEST RESULTS

BATCH	AGE (days)	f'_c (psi)			
		1	2	3	Average
4	7	6649	6543	-	6596
	14	6508	6189	-	6349
	23	7427	7679	-	7553
	28	7427	8524	8135	8029
	37	8665	8488	8241	8465
	46	8488	8488	-	8488
	54	8594	9082	8418	8698
	63	9160	9054	8630	8948
5	10	6720	6826	-	6773
	14	5765	5800	-	5783
	23	6614	6755	-	6685
	32	6366	6649	7286	6767
	40	7781	8099	8241	8040
	49	8135	8311	8347	8264
	56	8276	8397	8488	8387
	63	8559	8630	8700	8630
	154	8983	9019	-	9001

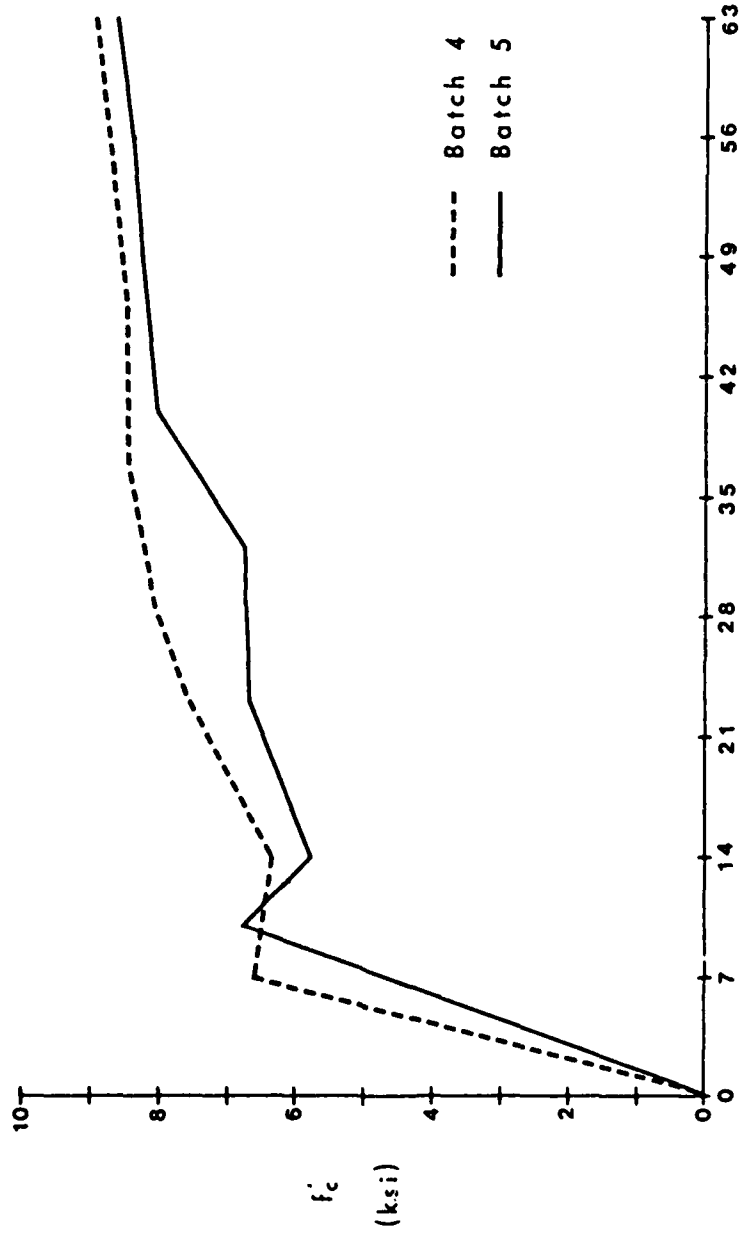

Fig. 5.1 Unconfined Compressive Strength vs. Age for Phase II FRC

these strength-age curves with the curves for Batches F1 and F2 from Phase I is not possible due to a difference in curing conditions. In Phase I, the specimens were removed from the molds the day after casting and placed in a moist room for 6 days. In the present test program, the specimens remained in the moist room until an age of 28 days had been reached. Therefore, all of the Phase I tests performed beyond an age of seven days were on essentially dry specimens whereas the preliminary tests in the present test program were performed on wet specimens up to an age of 28 days. Since the moisture conditions in a specimen have an effect on the measured strength (Bache and Nepper-Christensen, 1965), direct comparison of test results from wet and dry specimens would be misleading; however, a comparison of the final strengths can be made as all of the specimens had been out of the moist room for at least four weeks when these tests were performed.

The average unconfined compressive strengths at 63 days were 8948 and 8630 psi for Batches 4 and 5, respectively. Although these are slightly below the 9305 and 9035 psi strengths for Batches F1 and F2, the strength-age curves indicated that a slight gain in strength could still be expected. Two cylinders from Batch 5 were set aside and tested at an age of 154 days, just before the cubical cell testing commenced. The average strength of these two specimens was 9001 psi which represents a 3 percent gain in strength over that obtained after 63 days. The similarity in the strength-age curves from Batches 4 and 5 would suggest a similar increase had occurred in Batch 4. Therefore, the final strengths of Batches 4 and 5 were

on the order of 9300 and 9000 psi, respectively. These are identical to the final strengths of Batches F1 and F2 and because they are within 3 percent of each other, there is no need to adjust the strength results of the final test series to account for a difference in strength between batches.

In addition to unconfined compressive strengths, indirect (split cylinder) tensile strengths were also obtained at various ages. These results are given in Table 5.2 and Fig. 5.2. Again, a slight increase in strength beyond 63 days was noted. The final strengths are between 1100 and 1150 psi. Unfortunately, split-cylinder tests were not performed on Batch F1 or F2 specimens; however, 28-day split-cylinder strengths were obtained for Batch P3 from Phase I. The average splitting strength was 953 psi which is comparable to the 28-day strengths of Batches 4 and 5. Therefore, it can be assumed that the specimens from both Phase I and the present test program are identical.

5.3 Direct and Indirect Tension Test Results

5.3.1 Indirect Tension

As part of the preliminary test series, indirect tension (split cylinder) tests were performed using a "stiff" testing machine in order to investigate the post-peak behavior of the SFRC. The specimens used in these tests were taken from Batch 6. This batch was not chosen for the final test program because the compressive strength was about 10 percent higher than those of Batches 4 and 5; however, the split-cylinder strength was comparable to those

TABLE 5.2

INDIRECT TENSION (SPLIT CYLINDER) TEST RESULTS

BATCH	AGE (days)	f_{sp} (psi) 1	2	3	Average
4	7	9	795	-	853
	14	734	955	-	845
	23	1008	743	-	876
	28	1061	1026	-	1044
	37	1061	1088	937	1029
	46	(1335)	(1211)	(1247)	(1264)
	54	(1238)	(1185)	(1256)	(1226)
	63	1123	1114	1132	1123
5	10	899	911	-	905
	14	778	831	-	805
	23	778	893	-	836
	32	990	1025	1034	1016
	40	813	1105	1132	1017
	49	849	1061	1114	1008
	56	1026	1079	1105	1070
	154	1061	1158	-	1110

* Numbers in parentheses refer to tests performed with a different type of packing strip.

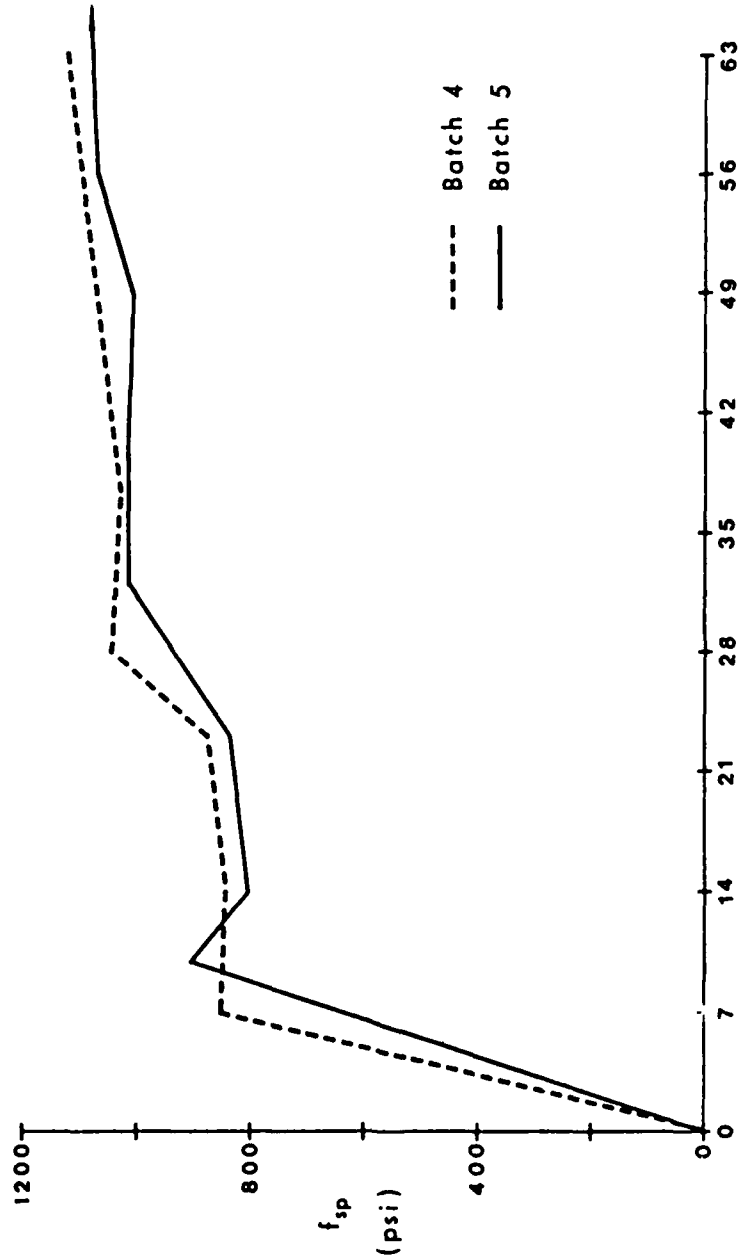

Fig. 5.2 Indirect Tensile Strength vs. Age for Phase II FRC

of Batches 4 and 5 so the results can be considered as indicative of the behavior of those batches in indirect tension.

In order to determine the influence of the fiber reinforcing, split-cylinder tests were also performed on plain concrete specimens remaining from the Phase I preliminary test program. These specimens, designated Batch P0, were of a mix identical to that used in the fibered specimens, permitting direct comparison of the plain and fibered concrete strength results.

The tests were conducted in an Instron testing machine equipped with a load-time plotter. The specimens were loaded using a constant rate of crosshead movement of 0.0165 in/min. This was found to produce a rate of increase in stress of 100-200 psi/min as specified in ASTM C-496. In order that the 20,000 lb. capacity of the Instron not be exceeded, the 3x6 in. cylinders had to be cut into halves, each being 3 in. long; therefore two test results were obtained for each cylinder. Two cylinders (four half-cylinders) were tested from each of Batches 6 and P0.

The average load vs. crosshead movement response of both the plain and the fibered specimens is shown in Figure 5.3. The scale on the vertical axis has been transformed from load to stress using Equation 1.1. In all of the plain concrete tests, the stress-crosshead movement response was linear up to the point of failure except for the initial nonlinearity at the start of the test which can be attributed to compression of the packing strips. Failure occurred in a very brittle manner. The average strength was observed to be 685 psi.

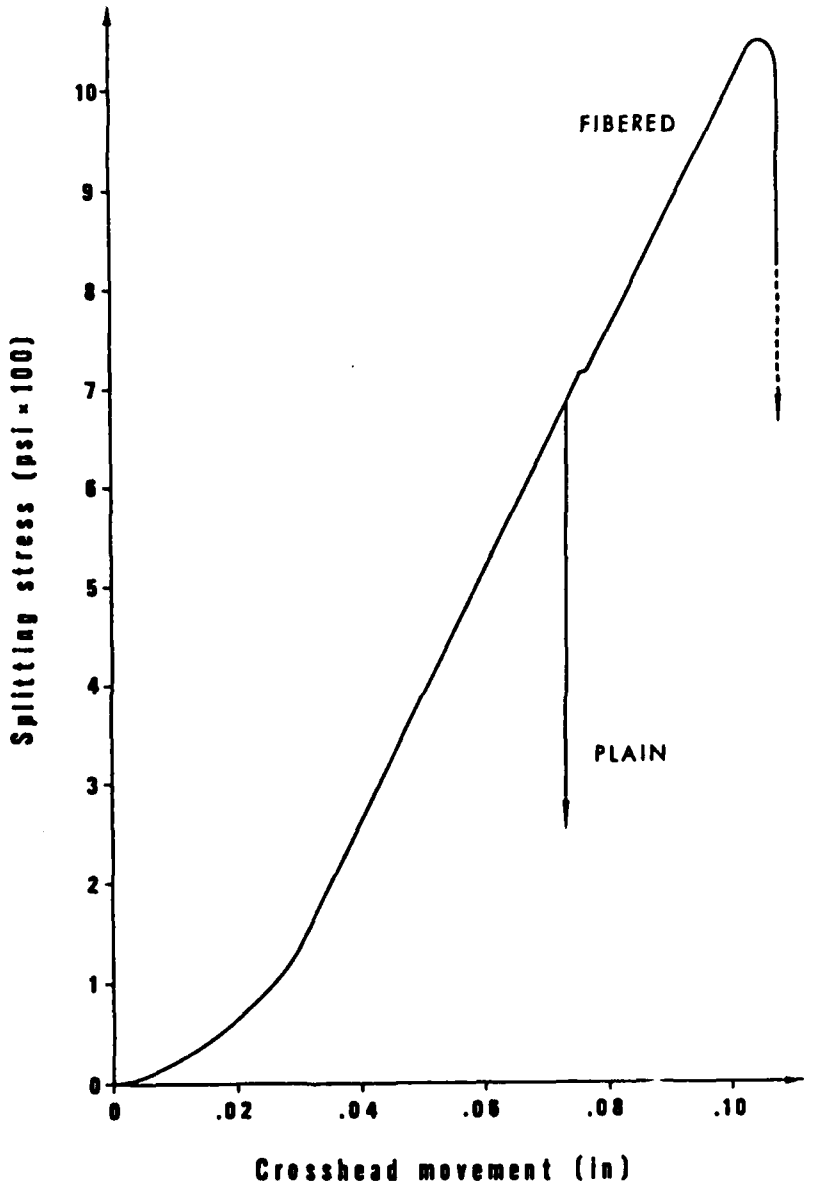

Fig. 5.3 Response of Plain and Fibered Concrete in Indirect Tension

The responses of the fibered concrete specimens were identical to those of the plain concrete specimens up to a stress level of 715 psi. At this point in the tests, a slight inflection in the load-crosshead movement curves was observed which coincided with the appearance of a vertical hairline crack on one or both ends of the specimen. In some of the tests, the inflection point could only be located through very close examination of the plots while in others it was quite obvious. There seemed to be a correlation between the difficulty in locating the inflection point and the difficulty in observing the crack at the surface of the specimen.

Immediately after the crack had formed in the specimen, the load-crosshead movement response again became quite linear. The slope of this portion of the curve is only slightly less than that observed prior to cracking. At a stress level of approximately 1000 psi, the response began to soften, indicating the onset of failure. The average stress at which the maximum load was achieved was 1050 psi, which is comparable to the strengths of Batches 4 and 5.

Unlike the plain concrete specimens, which virtually exploded at failure, the fibered specimens failed in a more ductile manner. As the load-crosshead movement curve began to drop, "popping" sounds could be heard as individual fibers broke. This continued for about five seconds, after which time approximately half of the ultimate load still remained. In most of the tests, the load began to increase at this point with a second maximum level being reached. This was accompanied by the formation of a second crack in the specimen which was parallel to the main crack and approximately

1/4 inch to one side. This is attributed to a slight movement of the specimen after the initial failure which resulted in the line of action of the applied loads being loated off to one side of the main crack. The post-peak response response is not shown in Fig. 5.3 because Equation 1.1 is invalid beyond the point of fracture.

These results confirm the findings of other investigators; namely that the fibers have ro effect on the response of the specimen up to the point at which the concrete matrix cracks, and only slightly delay the formation of this crack. Here the "stress at first cracking" in the fibered specimens is only 4 percent higher than the stress in the plain specimens at failure. This small difference could be attributed to slight strength differences between the two batches rather than the presence of fiber reinforcing. The primary effect of the fibers is to increase the ultimate strength and ductility of the specimens. The ultimate strength of the fibered concrete was 53 percent higher than that of the plain concrete strength and in addition, failure occurred in a more ductile manner.

5.3.2 Direct Tension

In the final test series performed in the cubical cell, two plain specimens remaining from the Phase I test program and five fibered specimens and were tested in uniaxial tension. Individual stress-strain curves and tabulated data are presented in the Appendix. All of the stress-strain curves presented in this chapter represent calculated average responses. To aid in evaluating and comparing the individual responses, the stress-strain traces have been drawn as smooth curves. The actual curves generated during a

test show some scatter because the magnitude of the strain increments resulting from each stress increment approaches the accuracy of the proximity deformation measurement system. This is especially true of the strain response on the unloaded axes of the specimen since the accumulated strains are quite small.

The stresses at failure in each of the seven tests are given in Table 5.3 and the average stress-strain response of both the fibered and plain concrete are shown in Fig. 5.4. Two features are readily observed from these results. First, the strengths as measured in direct tension are considerably less than the indirect splitting strengths. This was to be expected as mentioned in Chapter 1. The second, and more important, point is that the direct tensile strength of the fibered concrete was only slightly greater than that of the plain concrete. The average splitting strength of Batch PO was observed to be 685 psi compared with splitting strengths between 1100 and 1150 psi for Batches 4 and 5. This represents a strength increase of about 65 percent afforded by the fiber reinforcing. In direct tension, however, the strength increase was only ten percent. Furthermore, there was little or no increase in ductility as the tensile strains at failure were almost identical.

The discrepancy in these results can be attributed to a difference in the mode of failure and the stress distribution between the two tests. In the split-cylinder specimen, as mentioned in Chapter 1, the tensile stresses are confined to a narrow band in the vicinity of the vertical diametral plane. Outside this band,

Table 5.3

UNIAXIAL TENSION
TEST RESULTS

(Stresses in psi)

Test	Specimen	$\lvert f_t \rvert$
	FIBERED	
1A	4,H6	510
1D	4,E5	480
1E	5,E1	460
1F	4,E4	470
1G	5,E3	500
	PLAIN	
1H	0,C3	420
1J	0,D3	465

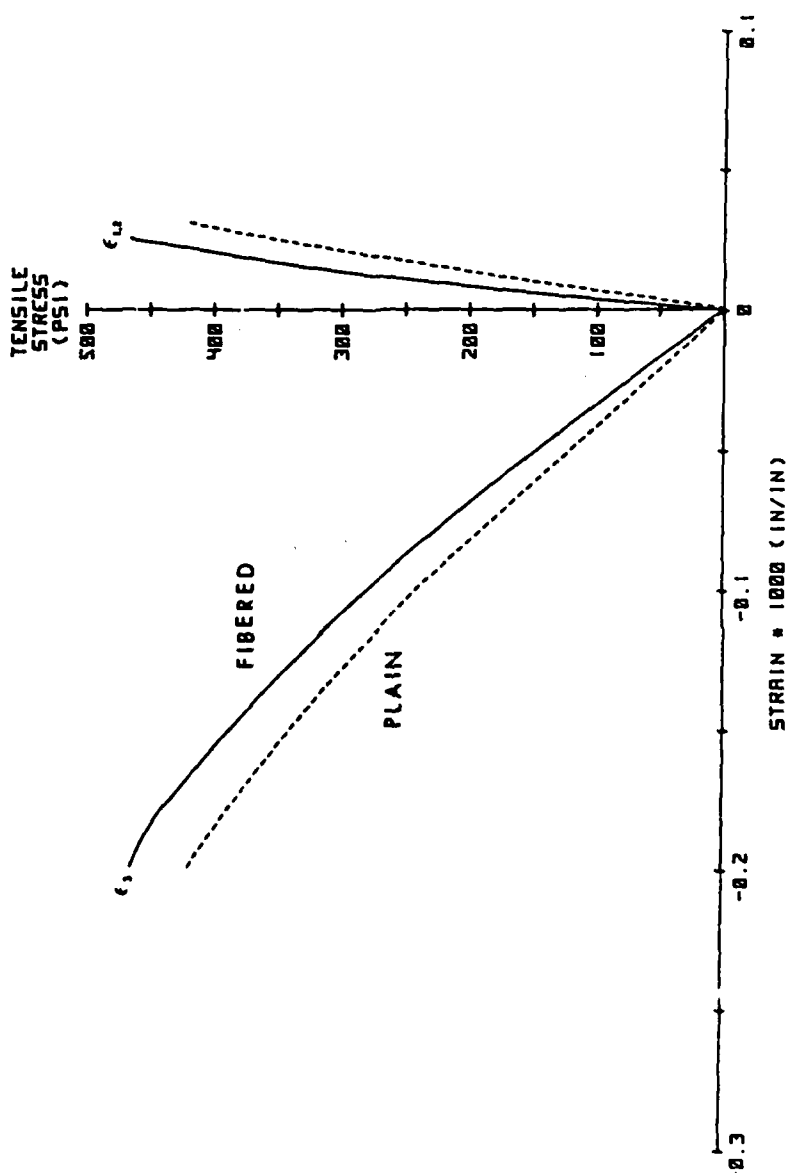

Fig. 5.4 Response of Plain and Fibered Concrete in Direct Tension

the stresses are primarily compressive and, because of the friction between the packing strips and the specimen, the stress state is most likely one of three-dimensional compression. This has two effects. First, fibers oriented perpendicular or nearly perpendicular to the splitting plane are anchored outside the region of tensile stresses; therefore, loads can be transferred through the fibers away from the splitting plane. If one assumes a uniform strain distribution along the splitting plane, a portion of the load will be transferred to the fibers because of their much greater stiffness. This is similar to the argument set forth by Romualdi and Batson (1963). The result of this is that the "stress at first cracking" of the concrete matrix is increased. The second, and probably greater, effect is that the ends of the fibers are clamped into the concrete by the compressive stress acting outside the tensile fracture zone. This prevents slipping of the fibers and allows the full tensile strength of the fibers to be developed. The measured splitting strength will essentially be the strength of the steel fibers. An example of this was seen recently in split-cylinder tests performed on specimens cast for an upcoming test program. These specimens were reinforced with the same fibers that were used in the present test program. The plain concrete specimens showed strengths less than 600 psi (compared with the 685 psi strength of Batch P0) but the specimens reinforced with 0.6 percent fibers had strengths identical to those measured in this test program, indicating that the ultimate splitting strength of the fibered concrete is rather insensitive to the strength of the concrete matrix.

In the direct tension tests carried out in the cubical apparatus, the stress distribution is uniform, thus precluding load transfer away from the failure plane. In addition, there is no transverse compressive stress to clamp the fibers in the concrete. Therefore, the mode of failure was predominantly a pulling out of fibers immediately after continuity of the concrete matrix was lost. For instance, during the tests and just prior to failure, audible sounds were emitted which could best be described as that of fibers tearing out of the concrete. Examination of the failed specimens showed that most of the fibers had been partially or fully pulled out, with the bent ends being straightened in the process. Some of the fibers were broken, most likely because they were wedged between pieces of aggregate and did not immediately pull out, but instead were overstressed as the remaining fibers ceased to resist the applied loads.

The number of fibers crossing the failure plane can be estimated from Equation 1.3.

$$n_w = 0.41\ N\ L\ /\ V \qquad (1.3)$$

The number of fibers in the specimen, N, can be found by dividing the volume of steel in each specimen (0.6 percent of the specimen volume) by the volume of each fiber. The latter can be approximated as $\pi\ d^2\ L\ /\ 4$ by assuming the fibers are straight rather than having bent ends. The result is 12.6 fibers per square inch crossing the failure plane. Since the total applied stress is transferred to the fibers when the concrete matrix cracks, each fiber must be able to resist nearly 40 lb of force (485 psi distributed among 12.6 fibers per square inch). This force is equal to a fiber stress of

approximately 50,000 psi which is less than one-third of their 170,000 psi yield strength. Therefore, failure could not possibly be attributed to yielding of the fibers. On the other hand, 40 lb of force would be sufficient to pull the fibers out of the matrix. Investigations by Robinson (1956) and deVekey and Majumdar (1968) indicated that the pullout strength of steel fibers in Portland cement concrete and cement paste is on the order of 700-1500 lb per square inch of fiber surface. For the fibers employed in this study, and assuming an average embedment length of L/4, the fibers could be expected to withstand 10-20 lb of force. Although this does not take into account the anchorage provided by the hooked ends, it does indicate the approximate magnitude of forces which could be resisted. Any increased pullout resistance afforded by the hooked ends would be partially offset by the fact that the strengths noted above were found by pulling a single fiber out of a concrete specimen while it has been observed that the resistance to pullout decreases as the number of fibers pulling out increases (Naaman and Shah, 1975). It appears that this is due to fibers oriented at slight angles to each other pulling out the wedge of concrete between them rather than pulling out of the intact concrete. The presence of significant amounts of concrete debris near the failure plane in the specimens that were tested would tend to support this assertion. Therefore, it seems reasonable that the volume percentage of fibers used in this test program was insufficient for resisting the applied loads after the concrete matrix cracked.

5.4 Uniaxial Compression

Five SFRC specimens and four plain concrete specimens were tested along the uniaxial compression stress path. Both the ultimate strengths and the stresses at the point of dilation are given in Table 5.4.

Only the ultimate strength will be used in the analysis of the test results from the present test program. This is necessitated by the absence of a point of dilation in the stress-volumetric strain curve for the biaxial tension-compression tests. Volumetric expansion began with the first application of a tensile stress increment since nonproportional loading was used in this quadrant.

In the Phase I test program, only the stresses at the point of dilation were recorded and no ultimate strength data are available. Therefore, the stress at dilation will only be used as the definition of failure when the combined data of Phase I and the present test program are analyzed. This is discussed further in Chapter 6.

The average stress-strain responses of the plain and fibered concretes are shown in Fig. 5.5. The similarity of the two responses further supports the contention that the fibers have little or no effect on the stress-strain behavior prior to tensile cracking or shear fracture of the concrete matrix. The slight difference in the initial moduli appears to be well within the statistical scatter of the test results.

Table 5.4

UNIAXIAL COMPRESSION
TEST RESULTS

(Stresses in psi)

Test	Specimen	f_{cu} †	f_{cd} ‡
	FIBERED		
2A	4,G6	7800	6800
2B	4,E6	7800	7500
2C	5,H2	8100	7000
2D	5,H4	7400	6800
2G	4,F5	7400	6800
	PLAIN		
2E	0,B4	7000	6400
2F	0,B5	6600	5600
2H	0,A5	6000	5300
2J	0,A6	6600	6000

† Ultimate Strength
‡ Point of Dilation

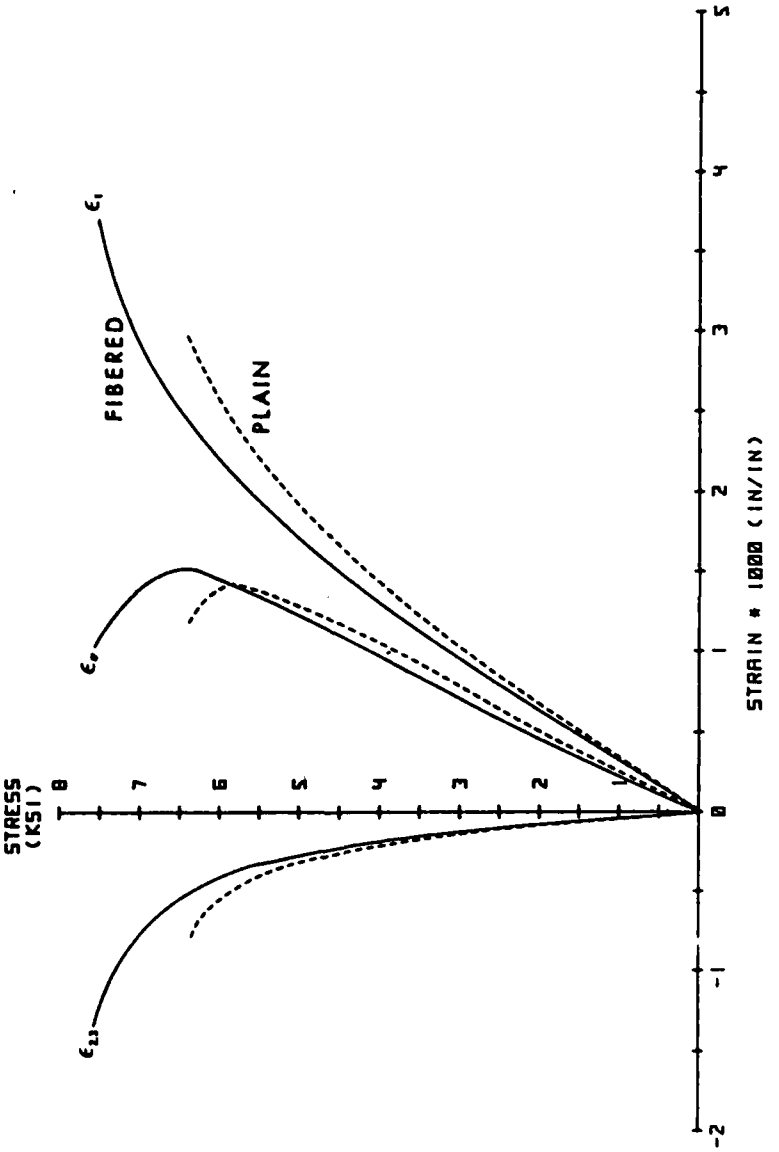

Fig. 5.5 Response of Plain and Fibered Concrete in Uniaxial Compression

The average ultimate strength of the SFRC in uniaxial compression was 7700 psi. The compressive stress levels used in the biaxial tension-compression tests were based on this value representing 100 percent of ultimate (1.0 f_{cu}).

5.5 Biaxial Tension-Compression

The strength results obtained from the biaxial tension-compression tests are given in Table 5.5. Each test category is designated by the level of compressive preloading relative to the uniaxial compressive strength. These designations will be used throughout this Chapter.

In Fig. 5.6, the strength data are plotted in the tension-compression quadrant of the biaxial stress plane. For clarity, this same data is replotted in the normalized coordinates σ_1/f_{cu} and σ_3/f_t in Fig. 5.7. The envelope which appears in this figure passes through the average strength for each test category and indicates the general trend of strength behavior. Two significant features of the strength behavior are evident in this envelope. First, it appears that the application of a compressive stress less than 30-40 percent of the uniaxial compressive strength has no effect on the measured tensile strength but it may, in fact, increase the tensile strength to a slight degree. The second feature is the inflection point in the curve at a compressive stress level near 0.5 f_{cu}. In Chapter 4, the coincidence of an inflection point and a change in the mode of failure was suggested. The validity of this supposition will be examined first.

Table 5.5

BIAXIAL TENSION-COMPRESSION
TEST RESULTS

(Stresses in psi)

σ_1/f_{cu}	Test	Specimen	σ_1	$\lvert f_t \rvert$
0.1	8A	4,E4	800	465
	8B	5,G6	800	525
0.3	10A	5,E4	2300	510
	10B	5,E5	2300	495
	10C	5,F5	2300	495
	10D	0,D5†	2300	375
	10E	0,C6†	2300	330
0.4	12A	5,F6	3100	465
	12B	5,F2	3100	465
	12C	4,F2	3100	375

† Plain Concrete

(continued)

Table 5.5 (cont.)

(Stresses in psi)

σ_1/f_{cu}	Test	Specimen	σ_1	$\lvert f_t \rvert$
0.5	6A	5,G3	3900	390
	6B	4,H2	3900	285
	6C	5,E2	3900	360
	6D	5,G5	3900	310
0.65	9A	4,H3	5000	255
	9B	4,H4	5000	315
0.8	7B	5,E6	6200	180
	7C	5,G4	6200	205
0.85#	7A	5,G2	6600	160

@ Point of Dilation

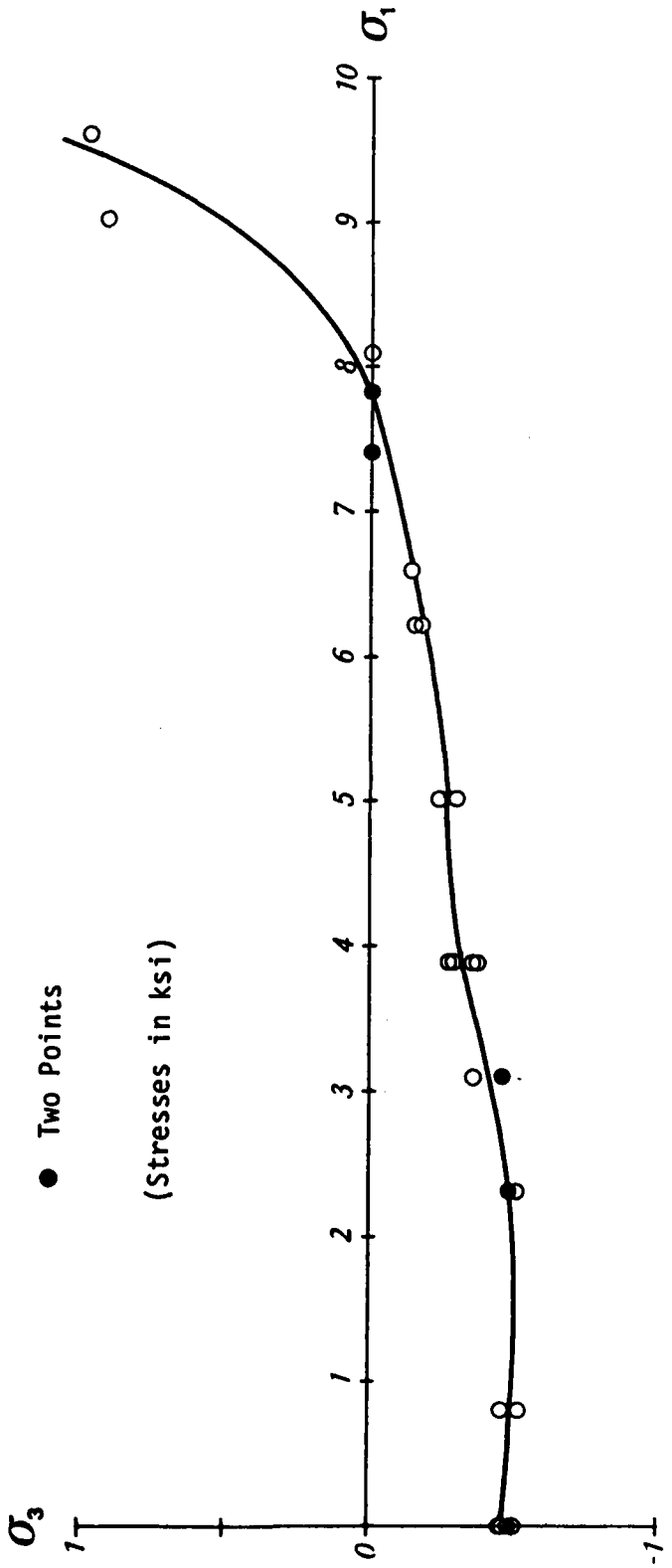

Fig. 5.6 Biaxial Tension-Compression Test Results

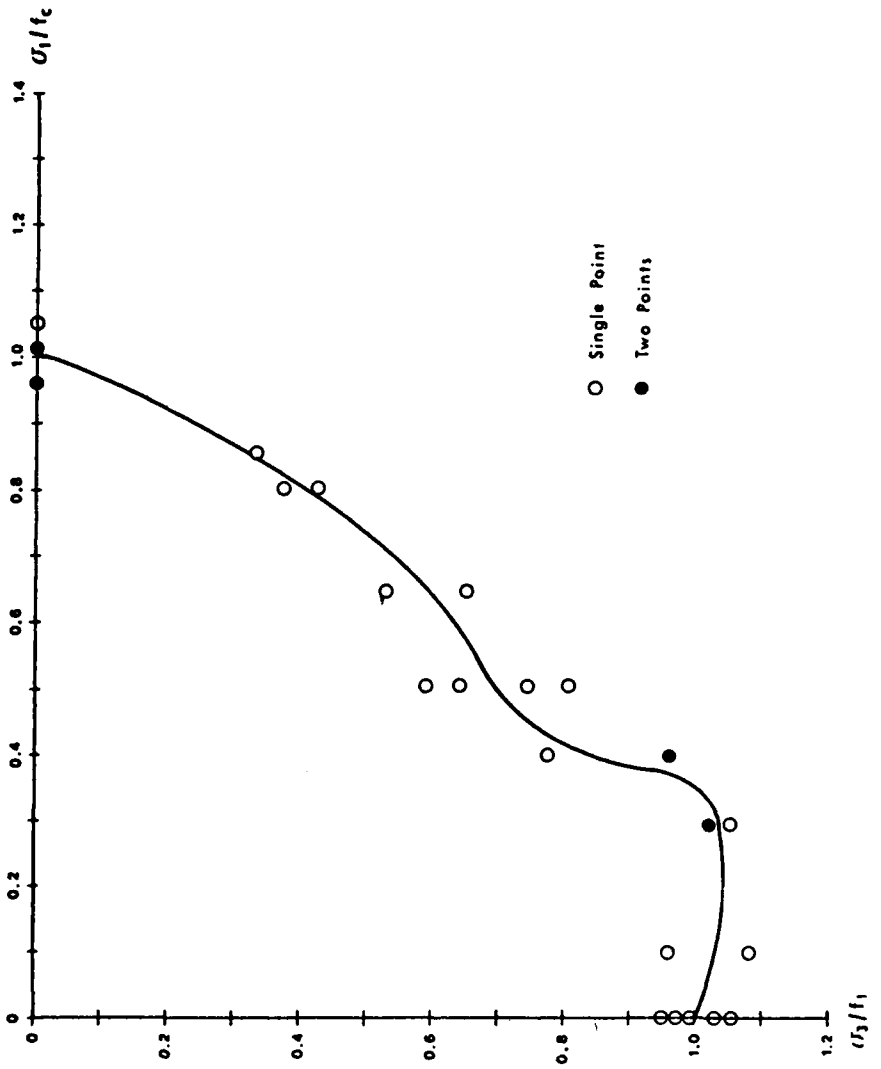

Fig. 5.7 Normalized Biaxial Tension-Compression Test Results

Figures 5.8(a)-(c) show the strain responses in the three principal stress directions to the applied tensile stress. These curves have been adjusted so as to pass through a common origin by subtracting the strains accumulated during the initial compressive loading.

Figure 5.8(a) shows the average strain responses in the direction of the applied tensile stress for different degrees of compressive preloading. The progressive softening of the strain responses with increasing compressive preloading is indicative of an increasing amount of internal damage in the form of microcrack propagation. A similar change in strain behavior is seen in Fig. 5.8(b) which shows the strain responses in the direction of the applied compressive stress. In both of these figures, a marked change in behavior is indicated at a stress level of 0.5 f_{cu}. As the compressive stress level increases from $\sigma_1/f_{cu} = 0$ through $\sigma_1/f_{cu} = 0.45$, there is a progressive increase in the strains at failure. At $\sigma_1/f_{cu} = 0.5$, however, the strains at failure decrease significantly and the strain response becomes considerably more nonlinear.

Further evidence of a change in behavior at $\sigma_1/f_{cu} = 0.5$ is seen in Fig. 5.9(c) in which the strain responses in the direction in which no loads were applied are shown. For stress levels less than 0.5 f_{cu}, the specimen contracts in this direction throughout the tensile loading. This is the expected response to a transverse tensile stress and suggests that the mode of failure is tensile splitting; that is, failure occurs on one plane oriented

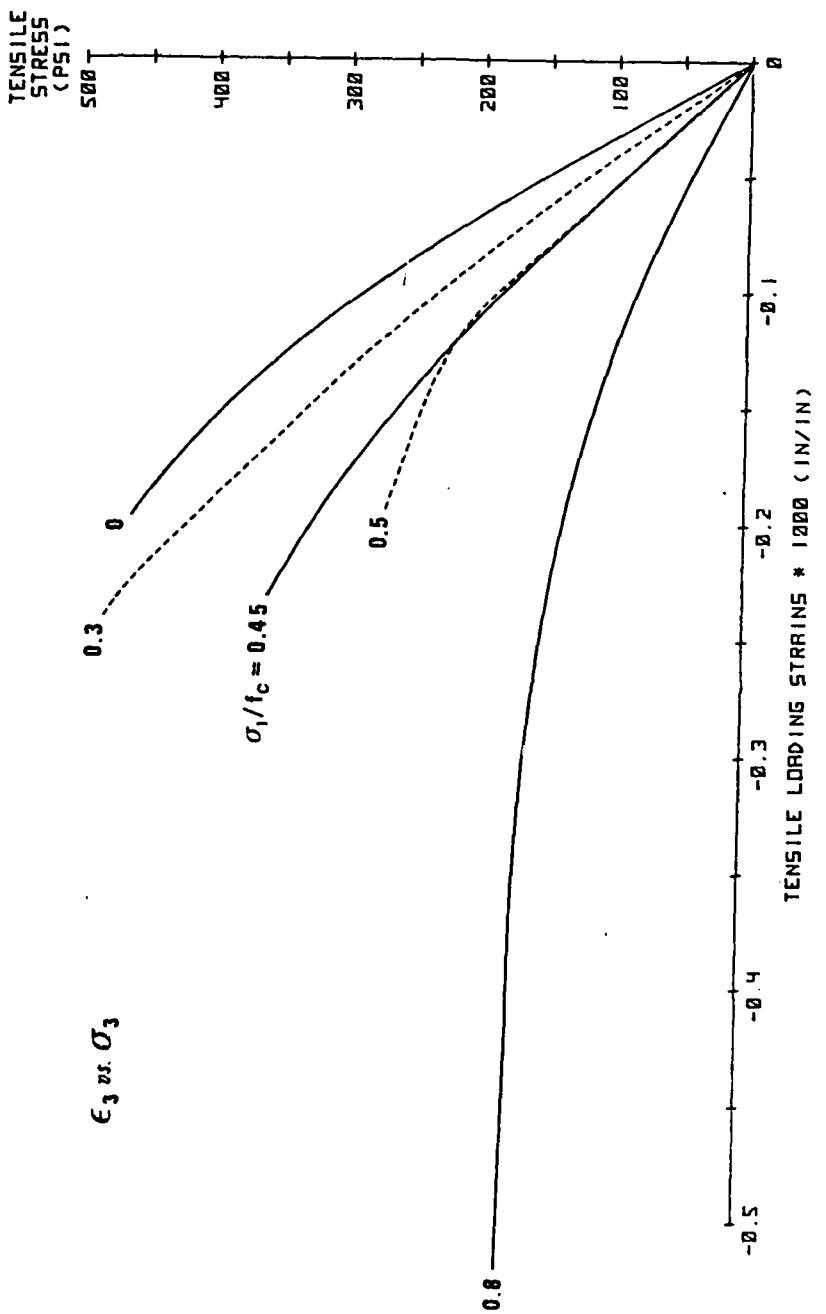

Fig. 5.8 (a) Strain Response in the Direction of Applied Tension

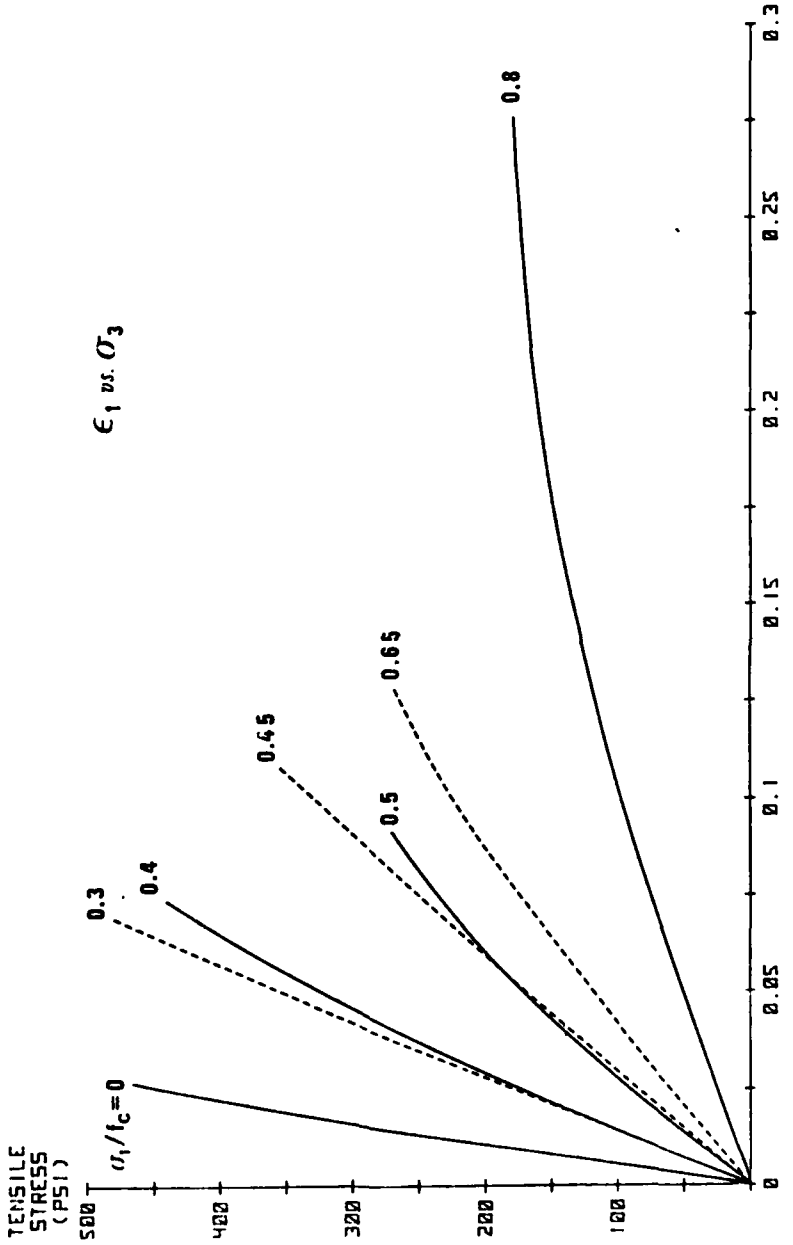

Fig. 5.8 (b) Strain Response in the Direction of Applied Compression

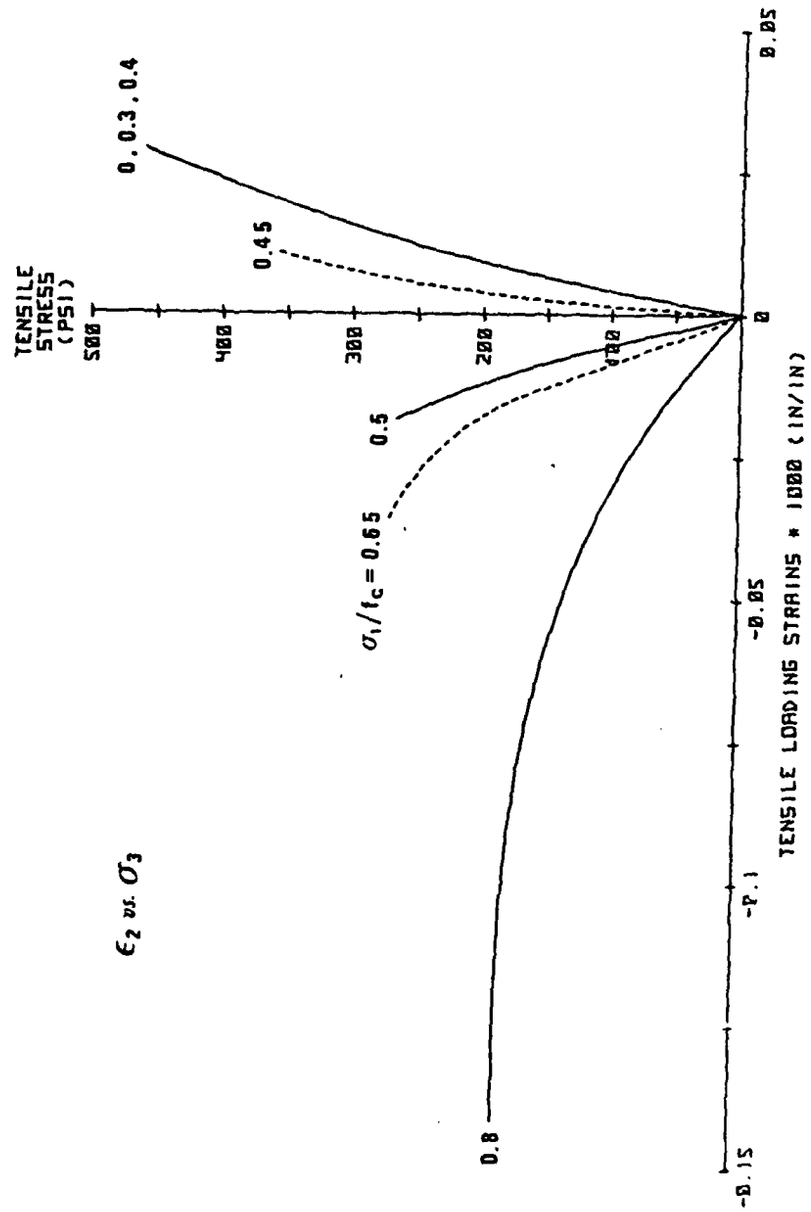

Fig. 5.8 (c) Strain Response in the Non-Loaded Direction

normal to the direction of the applied tensile stress. At compressive stress levels of 0.5 f_{cu} and above, however, the specimen expands in the non-loaded direction which suggests a cleavage mode of failure in which the microcracks propagate along many planes parallel to the direction of the applied compressive stress. This is shown in Fig. 5.9.

The inflection point in the failure envelope indicates the stress level at which this transition occurs; however, it is not caused by the transition. The appearance of these two phenomena coincide because they share a common cause. As was mentioned in Chapter 4, the microcracks which exist in the concrete prior to loading will begin to propagate when a certain amount of compressive stress has been applied. Once crack growth has been initiated, it can only be sustained by increasing the compressive stress further. In a compressive stress field, the cracks propagate along planes normal to the direction of the minor principal stress. This was first shown by Griffith (1921). Since the minor principal stress is oriented in both non-loaded directions in a uniaxial compression test, the cracks propagate along mutually perpendicular planes. As the length of these cracks increase, their widths also increase, which in turn results in expansion of the specimen in both non-loaded directions. As more cracks begin to grow and as those cracks already growing propagate further, the strain response becomes increasingly nonlinear.

In a tensile stress field, the cracks will propagate in planes perpendicular to the applied tensile stress since this is the

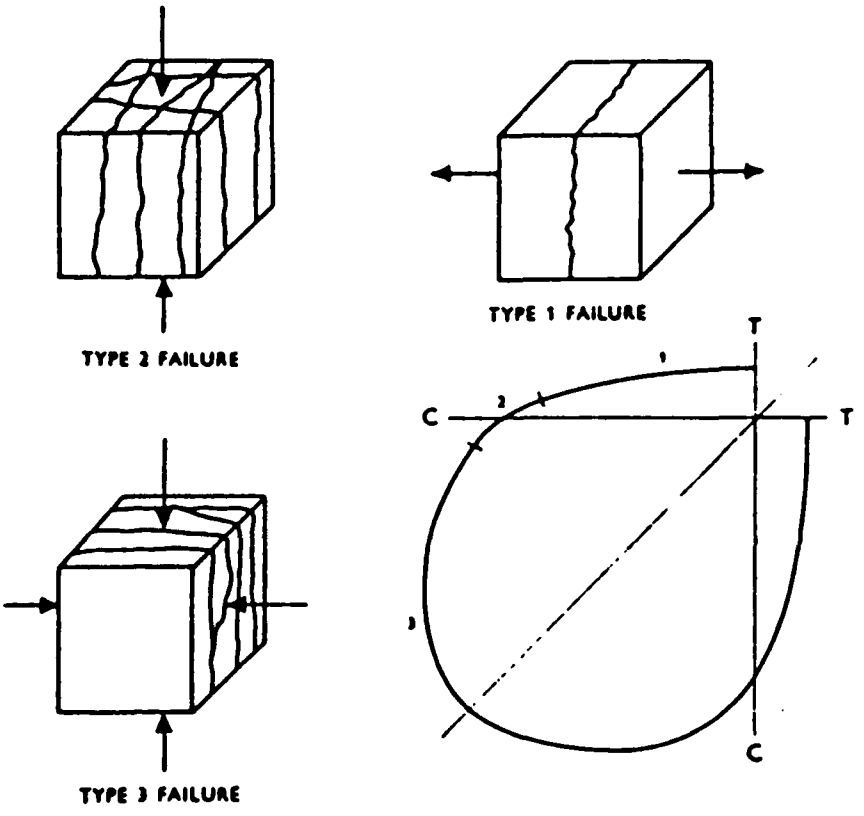

Fig. 5.9 Typical Modes of Failure under Biaxial Loading (Vile [1968])

minor principal stress direction. As these cracks grow, the cross-sectional area of the intact concrete available to resist the tensile loads decreases. Therefore, the actual tensile stress in the concrete is greater than the applied stress. This higher tensile stress causes increased crack initiation and propagation, which decreases the cross-sectional area further. As a result, the actual tensile stress increases at a much faster rate than the applied stress and unstable crack propagation commences at an applied stress level just slightly above that needed to initiate cracking. This suggests that both crack initiation and unstable crack propagation begin at compressive stress levels close to the ultimate tensile strength. Bieniawski (1961) has estimated that this stress level is 94 to 96 percent of the uniaxial strength.

With respect to biaxial tension-compression strength behavior, the above argument would suggest that compressive preloading to stress levels less than that required to initiate crack propagation would have little effect on the measured tensile strength since a tensile stress close to the ultimate strength would still have to be applied before cracking would occur. This is shown in Fig. 5.10 in which the strain response to tensile loading for the biaxial tension-compression tests at 0.1 f_{cu} is compared to the strain response for uniaxial tension. Aside from some statistical scatter, the responses are identical, indicating that no damage had resulted from the compressive preloading. This can also be seen in Fig. 5.8(c) which shows no change in the strain response until the compressive stress exceeds 0.4 f_{cu}.

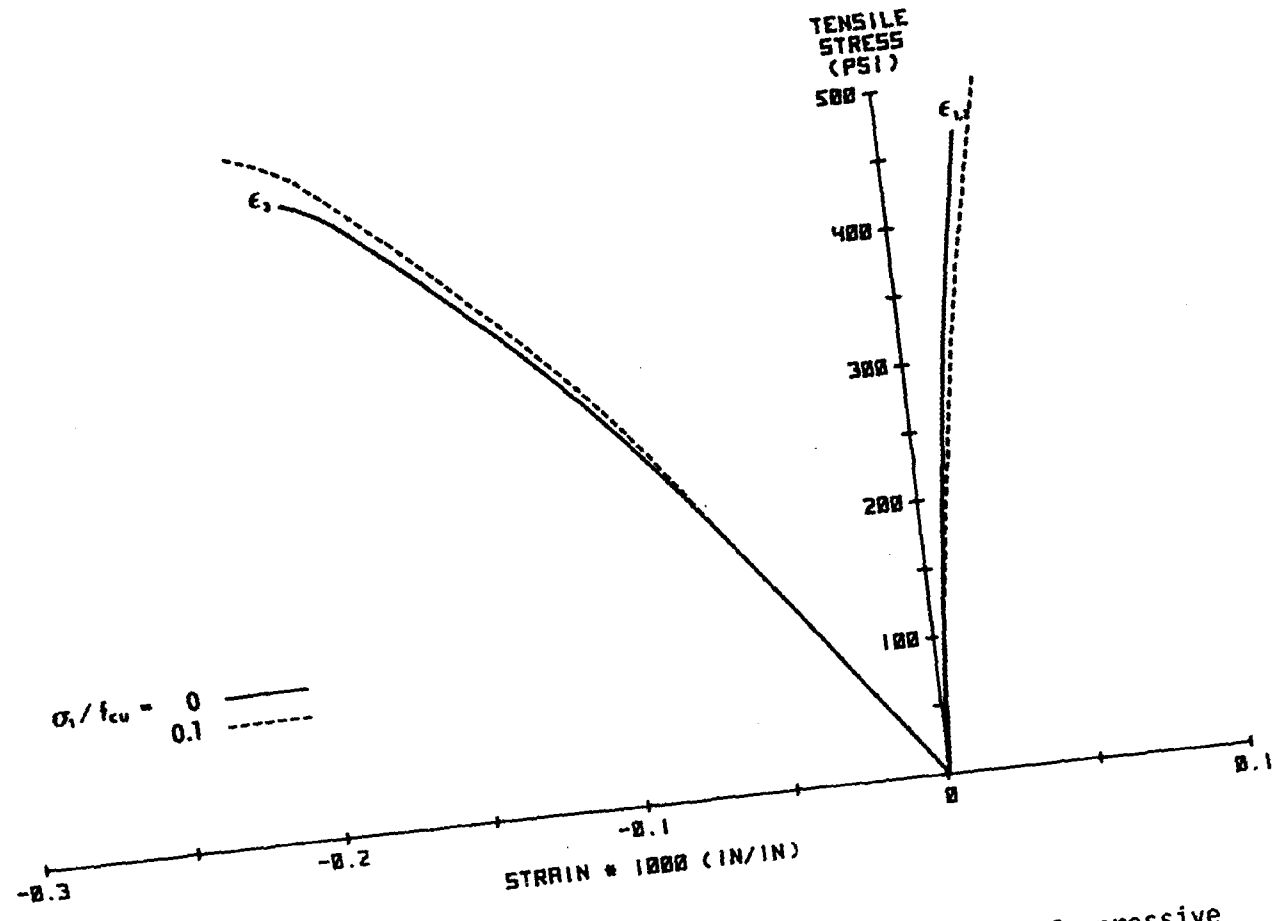

Fig. 5.10 Comparison of Strain Responses with No Transverse Compressive Stress and Small Transverse Compressive Stress

On the other hand, once cracking has begun as a result of the compressive preloading, the reduction in the cross-sectional area normal to the direction of tensile loading has the result that much less tensile stress will be required to cause failure. Thus, a sudden drop in the measured tensile strength appears once the compressive stress level required to initiate cracking has been achieved.

At sufficiently high compressive stress levels, failure will have been initiated even before the application of a tensile load. In this case, the tensile stress will only accelerate failure, not cause it. This is exemplified in Fig. 5.11 which shows the similarity between the stress-strain behavior in the biaxial tension-compression test at 0.85 f_{cu} and that resulting from uniaxial compression. It should be noted that compressive failure is suggested by the similarity in the ε_2 and ε_3 responses. Despite the fact that there is no tensile stress in the ε_2 direction, a considerable amount of expansion is taking place. The explanation for this is that the compressive stress is driving the specimen to failure. This same behavior is also seen at a compressive stress level of 0.8 f_{cu} as shown in Figs. 5.8(a) and (c). These tests represent the extreme case of cleavage failure under biaxial tension-compression loading.

On the basis of the preceding analysis, the compressive stress level required to initiate crack propagation can be found through examination of the stress-strain responses of the various tests and the failure envelope. It has already been noted that a

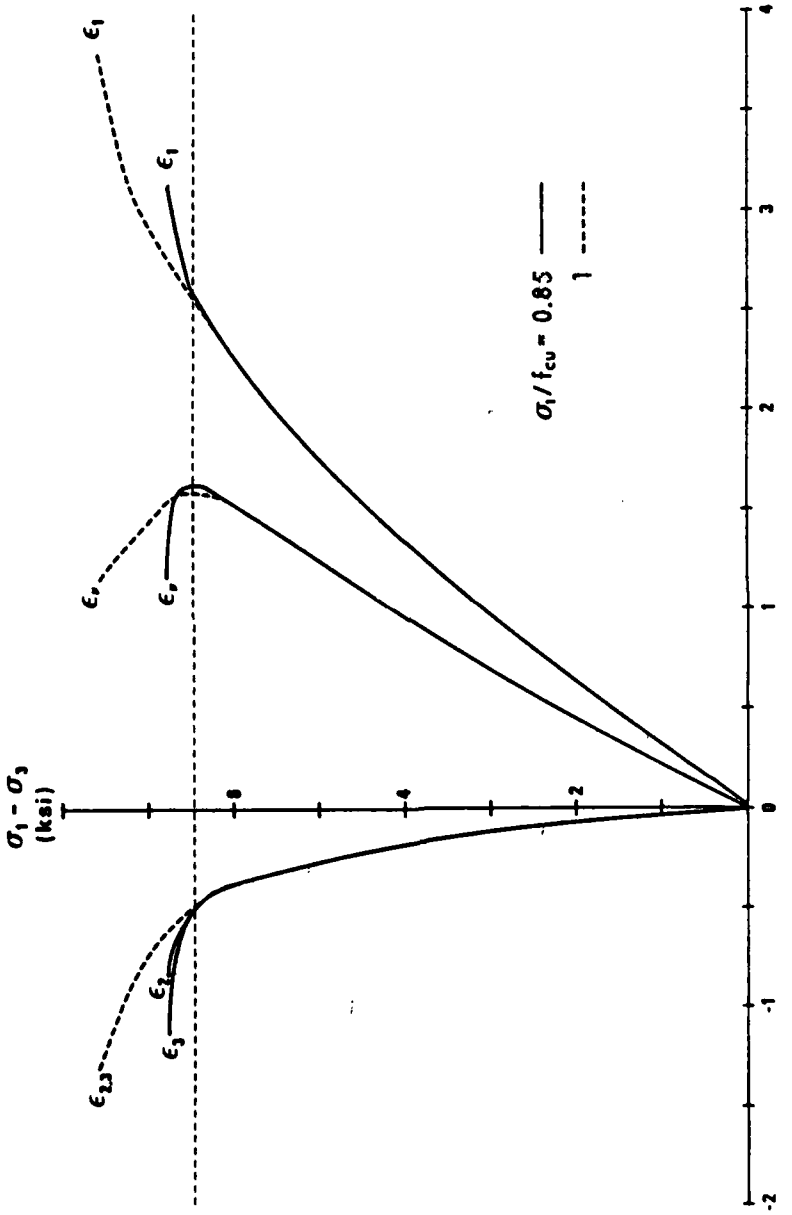

Fig. 5.11 Comparison of Strain Responses in Uniaxial Compression and Biaxial Tension-Compression with High Compressive Preloading

change in stress-strain behavior occurs at compressive stress levels between 0.4 f_{cu} and 0.5 f_{cu}. Therefore, closer examination of the test results from these two categories is warranted.

The available stress-strain response curves are presented in Figs. 5.12(a) and (b). Not every test is represented in all three directions due to inconsistencies in the recorded data, however, a sufficient amount of data exists for establishing basic trends.

The ε_1 and ε_3 responses shown in Fig. 5.12(a) can be separated into three groups. The first group consists of the two strongest specimens, 5F6 and 5F2, both of which were tested at 0.4 f_{cu}. A second group consists of the two weakest specimens, 4H2 and 5G5, both of which were tested at 0.5 f_{cu}. The strain responses of the remaining three specimens are virtually identical despite the fact that two different compressive stress levels are represented. This same grouping is evident in Fig. 5.12(b) with the exception of the response of specimen 5F6. The reason for this discrepancy is unknown.

The transition from tensile splitting to cleavage clearly occurs somewhere between 0.4 f_{cu} and 0.5 f_{cu}. For convenience, the stress level at which this transition occurs, and at which crack propagation was initiated, is assumed to be 0.45 f_{cu}. It is further assumed that specimens 5G3, 4F2, and 5E2 were at this transition stage when the tensile stresses were applied and that this is indicated by the fact that the ε_2 response curves are nearly vertical. Therefore, these three specimens will be separated from the others and categorized as having been tested at 0.45 f_{cu}. The

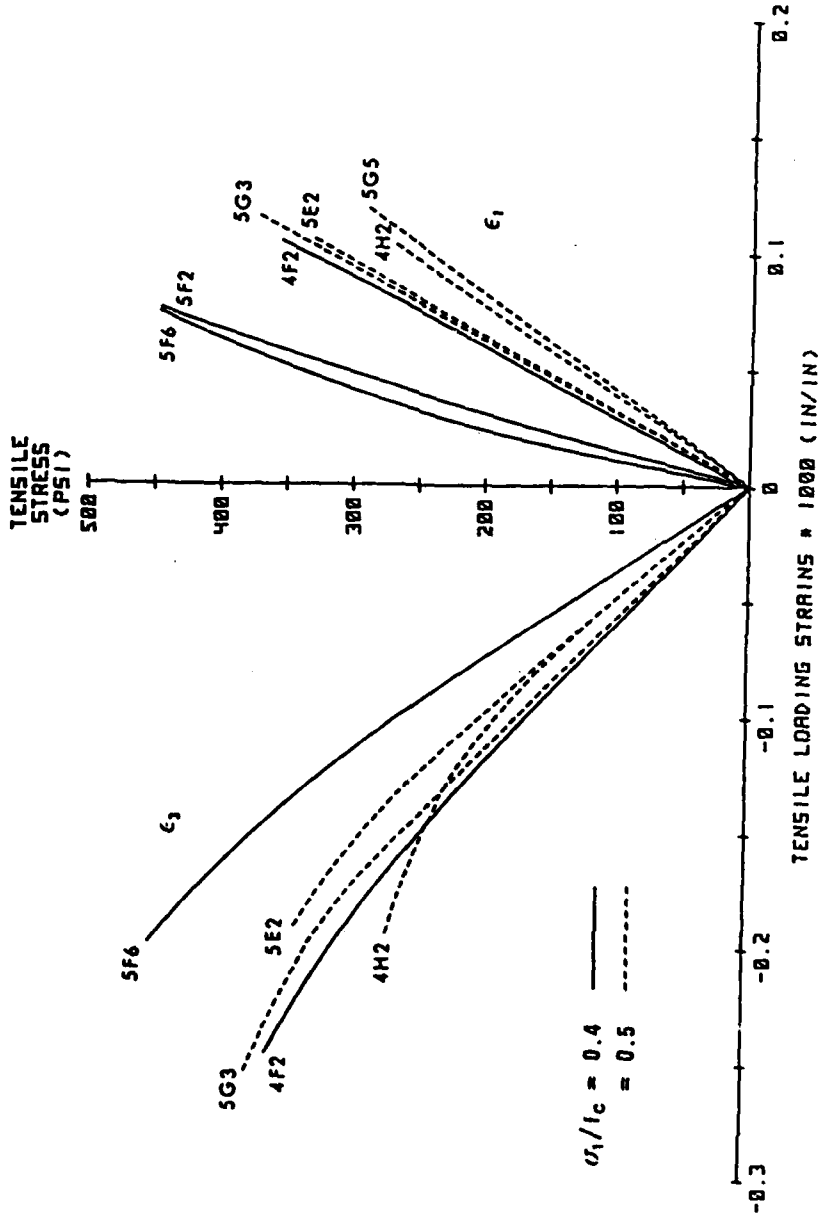

Fig. 5.12 (a) Strain Responses in the σ_1 and σ_3 Direction for Tests at 0.4 and 0.5 f_{cu}

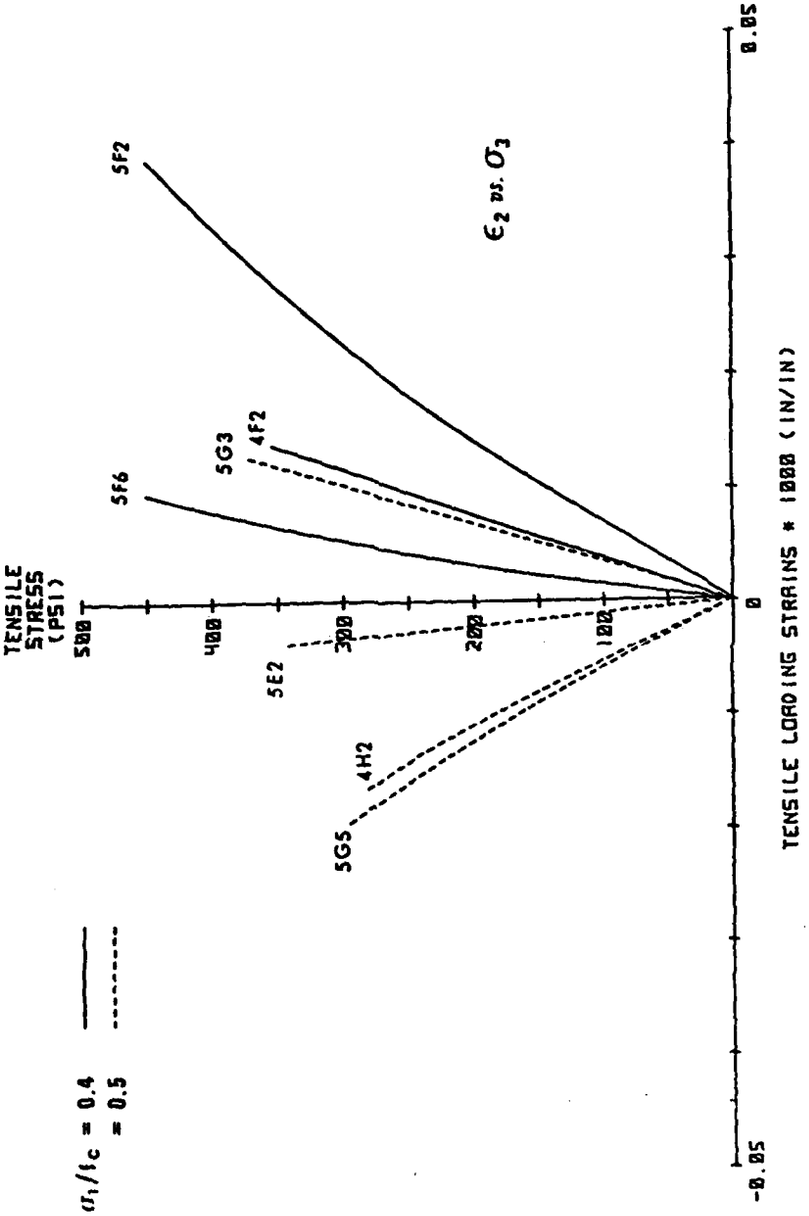

Fig. 5.12 (b) Strain Response in the σ_2 Direction for Tests at 0.4 and 0.5 f_{cu}

curves marked 0.45 in Figs. 8(a) - (c) represent the average strain responses of these three tests.

The fact that both 0.4 f_{cu} and 0.5 f_{cu} tests fall into this category can be explained in either of two ways. The first is that the stress level required for crack initiation is subjected to the same statistical variation as other concrete properties. Conversely, one could assume that the stress level 0.45 f_{cu} remains fairly constant among the specimens while the actual compressive stress of the specimens differs slightly from the computed average. Since the compressive stress level is determined on the basis of this average and because the stress-strain-strength behavior is particularly sensitive to the initiation of cracking, small deviations of the actual specimen strengths from the average would result in relatively large differences in the observed stress-strain response and the measured strength. Most likely, both of these explanations are valid to some extent.

In Fig. 5.13, the normalized strength data are replotted to include the 0.45 f_{cu} test category. The arrows indicate the positions from which the three data points have been moved. Notice that the relatively large degree of scatter at 0.4 f_{cu} and 0.5 f_{cu} is eliminated and the location of the inflection point becomes very obvious. In Fig. 5.14, the failure envelope has been adjusted to reflect these changes.

The other feature of the failure envelope mentioned at the beginning of this section is the apparent increase in tensile strength resulting from the application of small amounts of

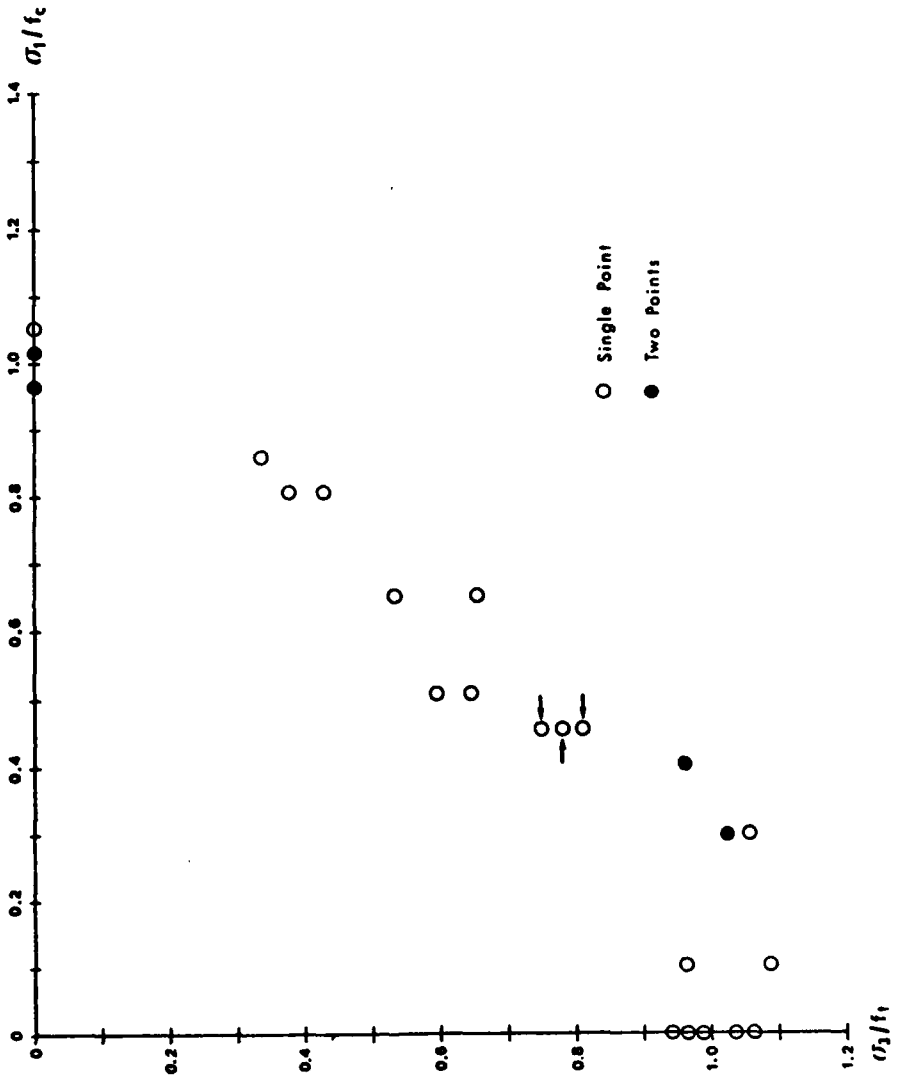

Fig. 5.13 Adjusted Biaxial Tension-Compression Failure Data

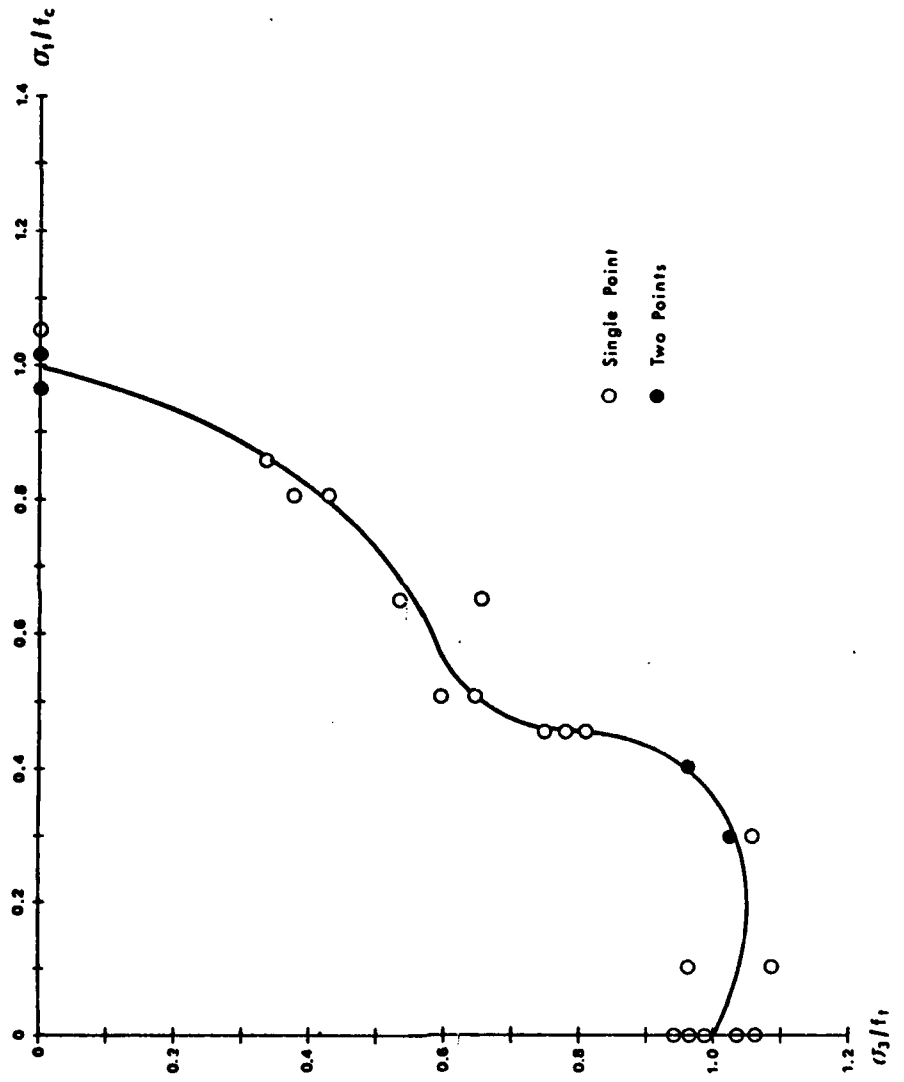

Fig. 5.14 Normalized Biaxial Tension-Compression Failure Envelope

compressive stress in the transverse direction. From the analysis just presented, a slight decrease in the tensile strength would be expected because the tensile and compressive stresses would have a combined effect on the microcracks. When the tensile stress is applied, local stress concentrations at the tips of the preexisting microcracks have already been established as a result of the compressive stress state. Therefore, less tensile stress will be required to initiate cracking. The increase in tensile strength must therefore be due to the fiber reinforcing. In Section 5.2, the rather small increase in the uniaxial tensile strength was attributed to an insufficient resistance of the fibers to pulling out of the concrete matrix. It seems reasonable that the addition of a compressive stress, and the resulting compressive strain, would have a clamping effect on the fibers, thus increasing their anchorage. With better anchorage, higher tensile stresses would be required to pull the fibers out and failure would therefore be delayed. This hypothesis was investigated by testing several plain concrete specimens at 0.3 f_{cu}. This is the test category for which the highest SFRC strengths were observed. The resulting tensile strengths were observed to be between 330 and 375 psi which, in comparison to the uniaxial tensile strength of the plain concrete, represent approximately a 20 percent loss in strength. Therefore, the fibers have a noticeable effect on the strength of the concrete in biaxial tension-compression at compressive stress levels less than that required to initiate cracking despite having very little effect in uniaxial tension.

The increased resistance to pullout afforded by the addition of a transverse compressive stress is lost once crack propagation is initiated. The findings of Shah (1968), and Hsu and coworkers (1968) show that cracks at the interface between mortar and aggregate particles are the first to begin propagating. These cracks originate in the specimen as a result of incomplete bonding of the cement paste to the aggregate as well as differential shrinkage during hydration of the cement. Similar cracks probably exist at fiber-matrix interfaces for the same reasons. The fibers oriented in a direction suitable for resisting the applied tensile loads are also oriented in the direction in which cracks will propagate under the transverse compressive stress. It seems likely that the "effective" fibers will suffer a loss in pullout resistance soon after crack propagation begins, since cracks will propagate along the fibers. The strength of the SFRC would therefore be no different than that of the plain concrete at these higher compressive stress levels.

5.6 Biaxial Compression

The strength results for the biaxial compression test categories are given in Table 5.6. Both the ultimate strength and the stresses at dilation are given for the reasons previously mentioned. These data are also plotted in the biaxial stress plane in Fig. 5.15.

The curves in Fig. 5.15 indicate plausible failure envelopes based on the two different definitions of failure. These curves have been drawn so as to conform with some commonly observed

Table 5.6

BIAXIAL COMPRESSION
TEST RESULTS

(Stresses in psi)

$\sigma_1:\sigma_3$	Test	Specimen	σ_{1_f} †	σ_{3_f} †	σ_{1_d} ††	σ_{3_d} ††
1:10	11A	5,F1	9000	900	7500	750
	11B	5,G4	9600	960	8400	840
1:3	3A	5,H6	11700	3900	9200	3067
	3B	5,E2	9900	3300	8400	2800
2:3	4A	4,G1	10800	7200	10500	7000
	4B	5,H3	9600	6400	9300	6200
3:3	5A	5,F3	9800	9800	9000	9000
	5B	4,G4	8500	8500	6300	6300

† Ultimate Strengths

†† Points of Dilation

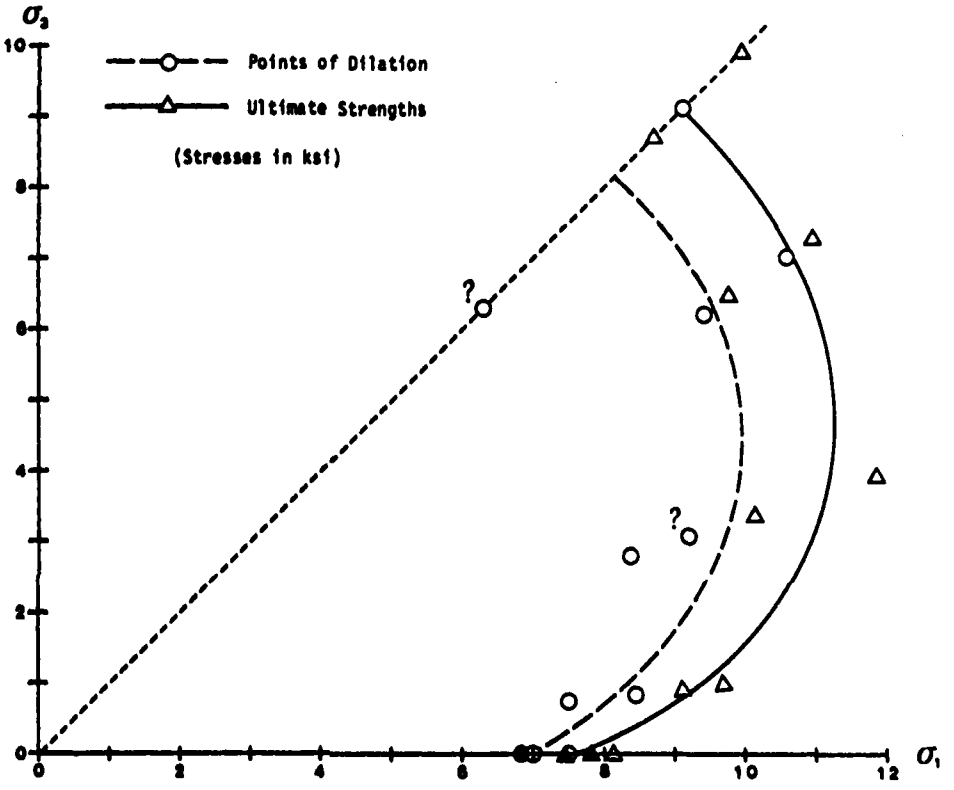

Fig. 5.15 Biaxial Compression Test Results

features (Gerstle, et al., 1978; Tasuji, et al., 1978; Kupfer, et al., 1969):

1. In the absence of boundary constraints, the failure envelope in the biaxial compression quadrant is perpendicular to the line $\sigma_1 = \sigma_2$ which is the line of symmetry.
2. The curve has a maximum extension at a stress ratio of approximately 1:2.
3. The locj of points of discontinuity (stresses at dilation) have a shape nearly identical to that of the ultimate strength envelope.

The question marks which appear next to two of the data points are to indicate that these may be inaccurate results. It is suspected that premature failure occurred as a result of stress concentrations at the surface of the specimens caused by the probe targets. Originally, a 4-inch square sheet of 0.012-inch thick brass was used as the probe target. Slits were cut in the target (Fig. 5.16) to increase its flexibility. The location of these slits could be seen in the putty on the specimen faces after a test because the edges of the target on either side of a slit were pushed into the putty slightly. This has not been a problem in the past because the putty behaved in sufficiently plastic manner that stress concentrations did not develop in the concrete. In the present test program, however, the major principal stress was applied on the cut faces of the specimen. These faces did not require sandblasting and puttying because the saw cuts were made in competent concrete. As

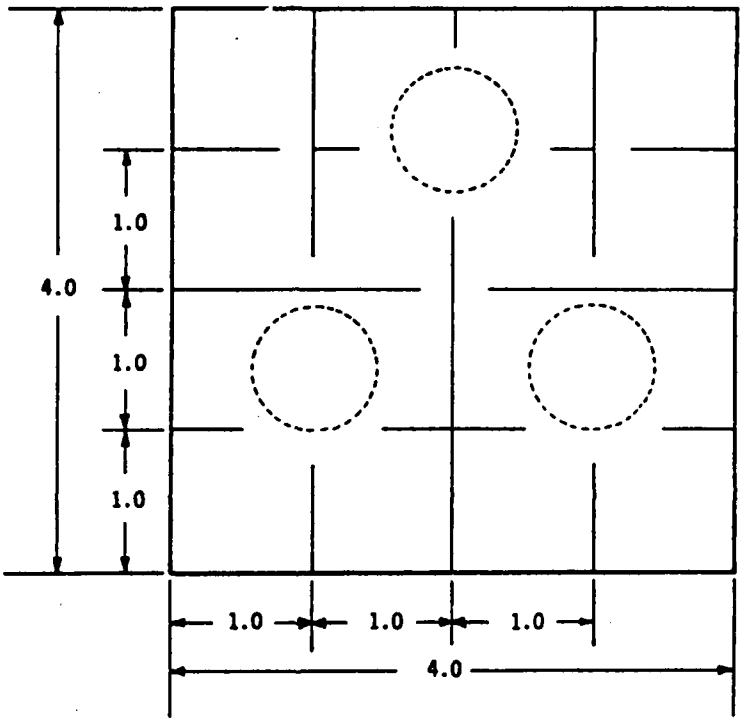

Fig. 5.16 Location of Slits in Brass Target

the edges of the target deformed into the surface of the specimen, stress concentrations resulted because the concrete was fairly brittle and could not yield enough to dissipate these stresses. In both of the tests in question, the specimen was split completely in two with the failure plane beginning at the slits 1-inch from the bottom of the specimen on one cut face and ending at the slits 1-inch from the top of the specimen on the opposing face. This indicates that failure originated at these slits due to the stress concentrations. These results precipitated the switch to brass disks as the probe targets. The fact that the stresses at dilation are inconsistent with the remaining data while the ultimate strengths agree quite well with the remaining data may be an indication of the reinforcing ability of the steel fibers in biaxial compression. Despite premature initiation of unstable crack propagation, physical failure was delayed until the ultimate strength which would have resulted in te absence of stress concentrations was achieved. This is merely a conjecture, however, as there is insufficient evidence to prove or disprove it.

Finally, the entire biaxial failure envelope is shown in Fig. 5.17. Because points of dilation were not exhibited in the tension-compression tests, only ultimate strengths are represented here.

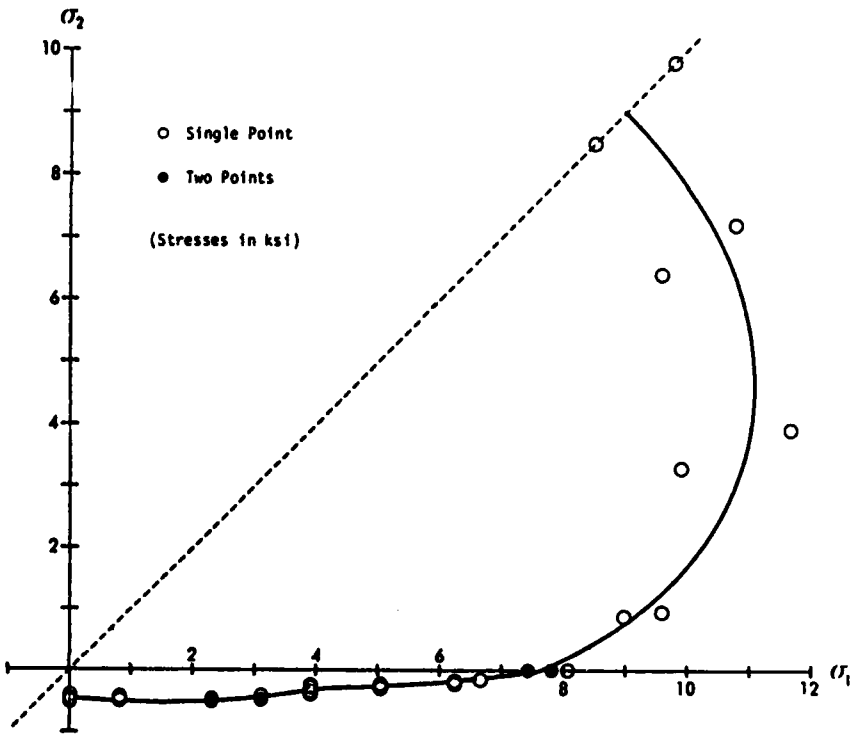

Fig. 5.17 Biaxial Failure Envelope

CHAPTER 6

ANALYTICAL STRENGTH PREDICTIONS

6.1 Introduction

In this Chapter, the two mathematical constitutive models investigated by Egging (1981) for possible use in characterizing the strength behavior of the SFRC will be discussed and the models will be calibrated using the combined strength data from the Phase I and Phase II test programs.

The Willam-Warnke model five-parameter failure criterion is presented in Section 6.2. The calibration of this model and a comparison of the predicted failure surface with the experimental data appear in Section 6.3.

The Lade three-parameter failure criterion is discussed in Section 6.4. The calibration of this model and the resulting strength predictions are presented in Section 6.5.

6.2 Willam-Warnke Five-Parameter Failure Criterion

The five-parameter failure criterion was developed by Willam and Warnke (1974) to describe the stresses at failure in concrete-type materials under multiaxial test conditions and models the main features of multiaxial concrete failure, namely the dependence of strength on both the hydrostatic stress level and the deviatoric stress path. This model describes a conical failure

surface in principal stress space with a non-circular base section and curved meridians which are centered on the hydrostatic stress axis ($\sigma_1 = \sigma_2 = \sigma_3 = \sigma_o$).

The curved meridians are approximated by second-order parabolas whose axis of symmetry is normal to the hydrostatic stress axis and located a relatively large distance from the origin. In order that the model be easily calibrated from conventional concrete tests, only the meridians for which $\sigma_1 = \sigma_2$ (TE) and $\sigma_2 = \sigma_3$ (TC) need to be specified. These can be expressed as

$$r_1 \frac{\sigma_o}{|f_{cu}|} = a_0 + a_1 \frac{\sigma_o}{|f_{cu}|} + a_2 \left(\frac{\sigma_o}{|f_{cu}|}\right)^2 ; \text{TE} \qquad (6.1)$$

$$r_2 \frac{\sigma_o}{|f_{cu}|} = b_0 + b_1 \frac{\sigma_o}{|f_{cu}|} + b_2 \left(\frac{\sigma_o}{|f_{cu}|}\right)^2 ; \text{TC} \qquad (6.2)$$

where the coefficients a_0, a_1, a_2 and b_0, b_1, b_2 are determined from test results. These parabolas and their associated nomenclature are shown in Fig. 6.1

In deviatoric cross-section (perpendicular to the hydrostatic axis) the failure surface is symmetric about the $\sigma_1 = \sigma_2$ and $\sigma_2 = \sigma_3$ axes since isotropy is assumed. Therefore, only one sextant of stress space needs to be considered. In each sextant, the trace of the failure surface is approximated by an ellipse as shown in Fig. 6.2. This ellipse, centered at point O' and having half-axes a and b, provides a smooth and convex transition between the meridians at $\theta = 0°$ (r_1) and $\theta = 60°$ (r_2).

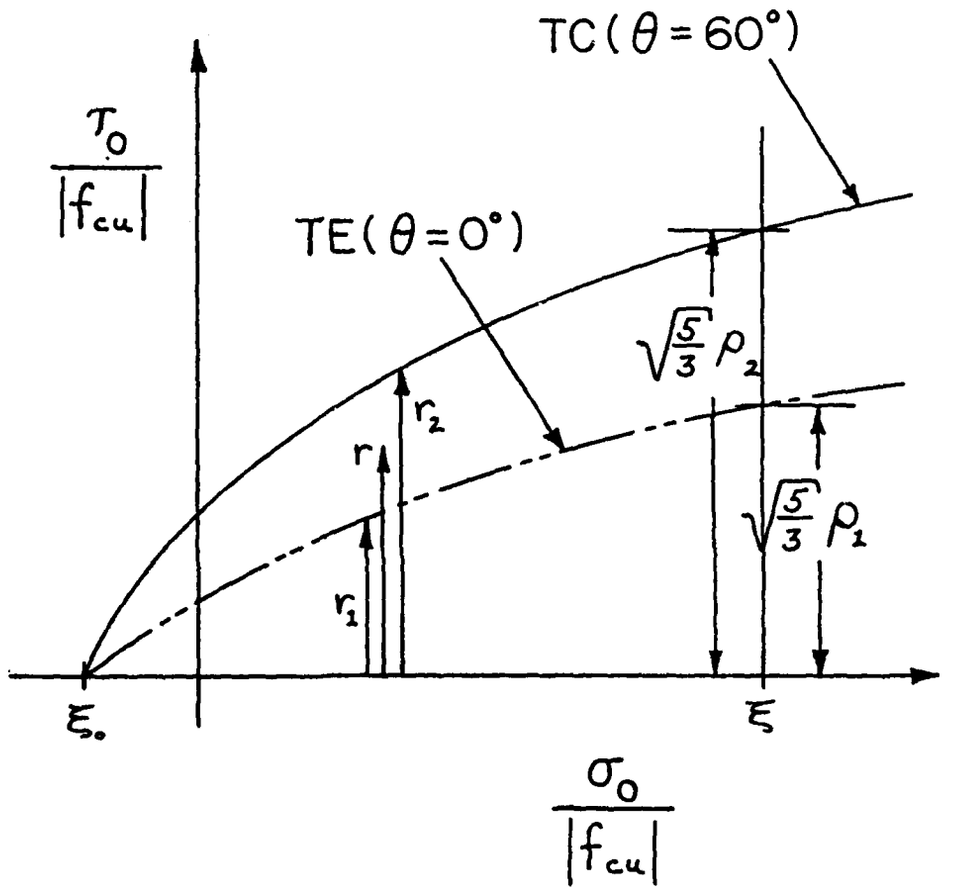

Fig. 6.1 Parabolic Meridians in Octahedral Stress Space (Egging [1981])

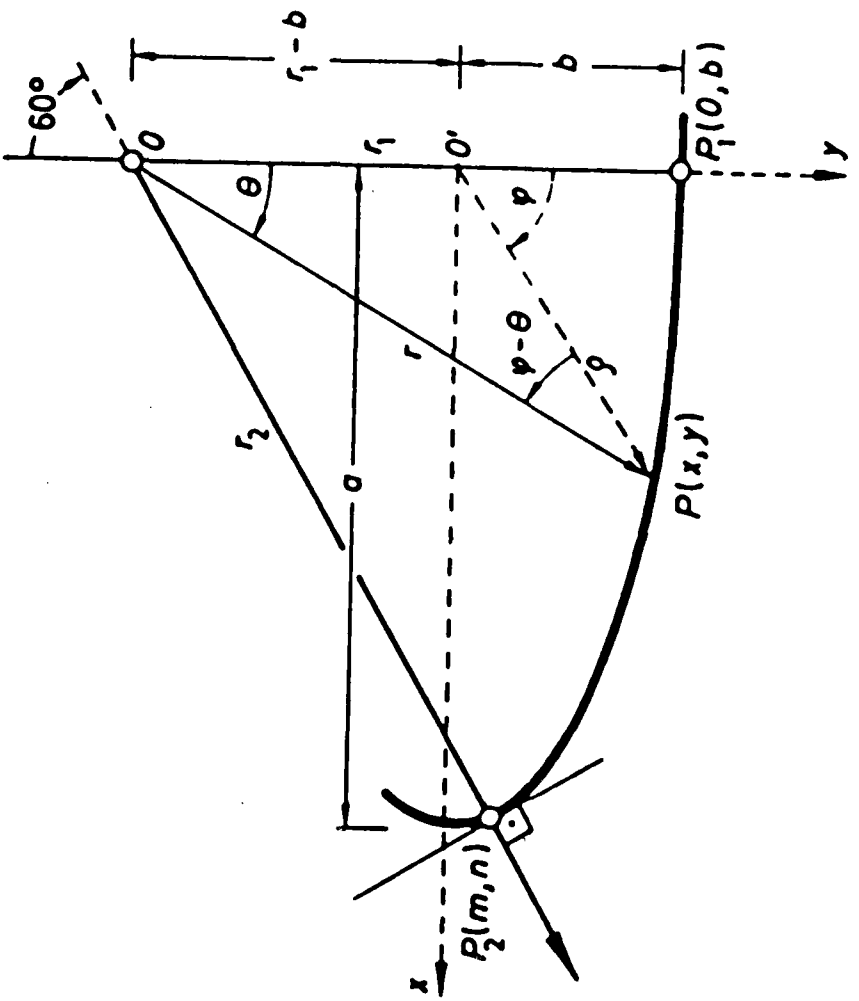

Fig. 6.2 Elliptical Approximation of Failure Surface in Deviatoric Plane (Willam and Warnke [1974])

The equation of the ellipse can be expressed in terms of the polar coordinates (r,θ) centered at the hydrostatic axis by

$$r(\sigma_o,\theta) = \{2r_2(r_2^2-r_1^2)\cos\theta + r_2(2r_1-r_2)\sqrt{4(r_2^2-r_1^2)\cos\theta + 5r_1^2 - 4r_1r_2}\} \cdot \frac{1}{4(r_2^2-r_1^2)\cos^2\theta + (r_2-2r_1)^2} \qquad (6.3)$$

where the angular measure θ can be expressed in terms of the principal stresses as

$$\cos\theta = \frac{\sigma_1 + \sigma_2 + 2\sigma_3}{\sqrt{2}\,[(\sigma_1-\sigma_2)^2 + (\sigma_2-\sigma_3)^2 + (\sigma_3-\sigma_1)^2]\,1/2^1/^2} = \frac{\sigma_2 - \sigma_3}{\sqrt{2}\,\tau_o} \qquad (6.4)$$

Equations 6.3 and 6.4, being functions of σ_o, τ_o and θ, completely describe the failure surface in octahedral stress space and the failure surface function can be written as

$$F(\sigma_o, \tau_o, \theta) = \frac{1}{r(\sigma_o,\theta)} \frac{\tau_o}{|f_{cu}|} - 1 = 0 . \qquad (6.5)$$

The complete trace of the failure surface in the deviatoric plane is shown in Fig. 6.3. The shape of the failure surface in stress space is shown in Fig. 6.4

The coefficients a_o, a_1, and a_2 describing the TE meridian $(r(\sigma_o, \theta = 0^\circ) = r_1)$ and b_o, b_1 and b_2 describing the TC

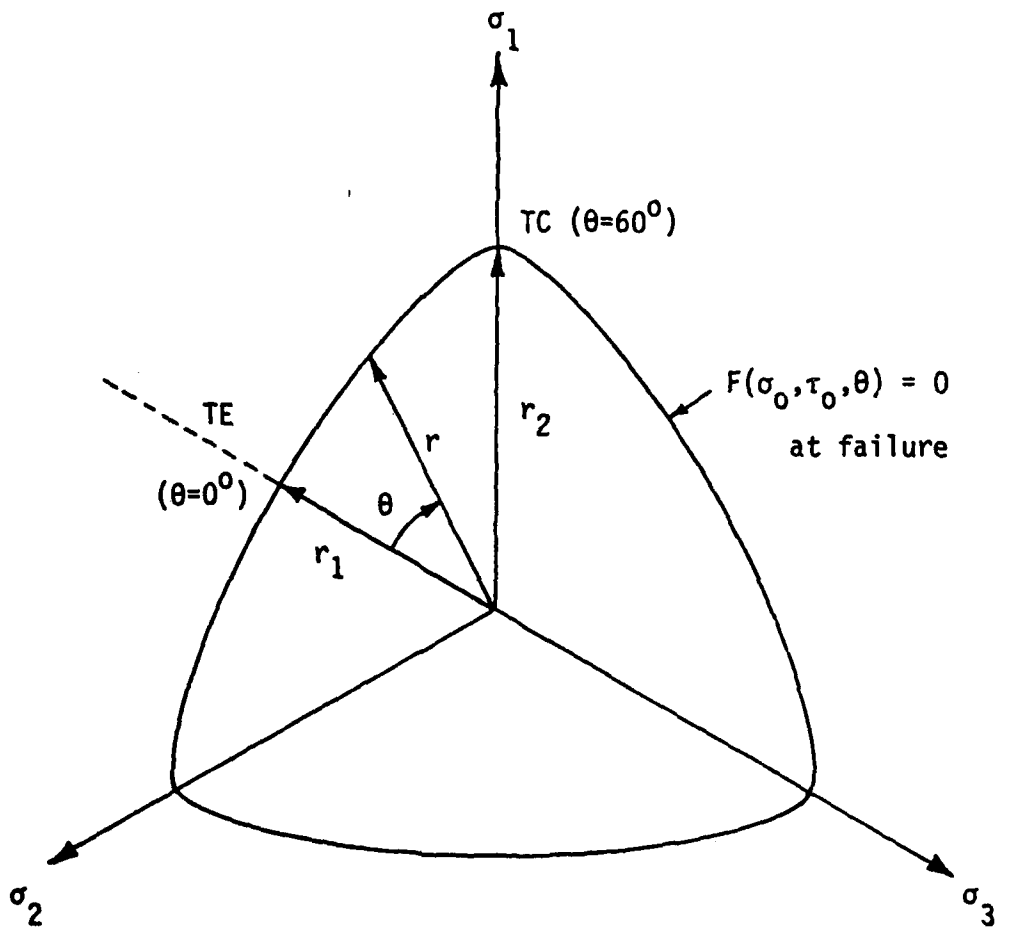

Fig. 6.3 Trace of Failure Surface in Deviatoric Plane (Egging [1981])

AD-A136 124 THE STRENGTH AND BEHAVIOR OF STEEL FIBER-REINFORCED CONCRETE UNDER COMBIN..(U) COLORADO UNIV AT BOULDER DEPT OF CIVIL ENVIRONMENTAL AND ARCH.. 3/4

UNCLASSIFIED R W MEIER ET AL. MAY 83 AFOSR-TR-83-0974 F/G 13/3 NL

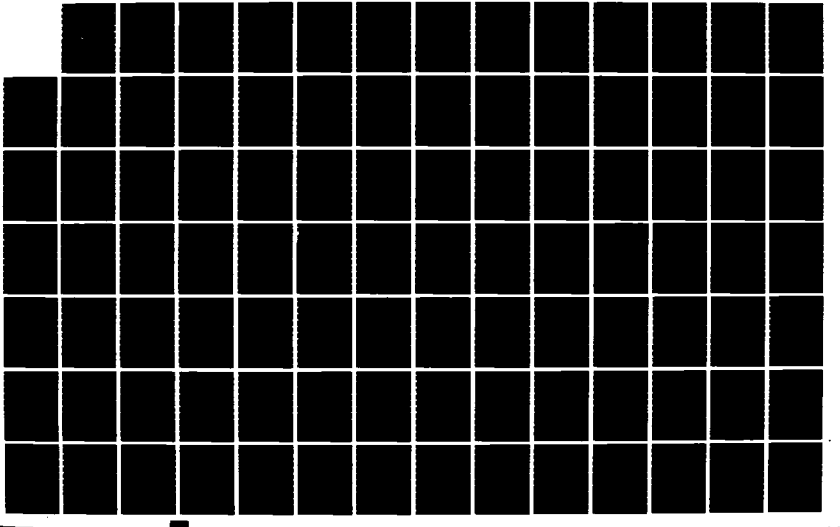

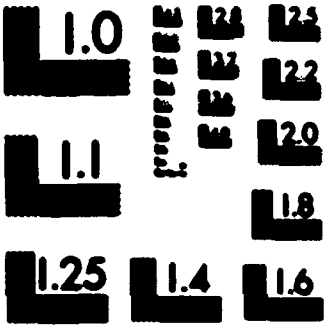

MICROCOPY RESOLUTION TEST CHART
NATIONAL BUREAU OF STANDARDS-1963-A

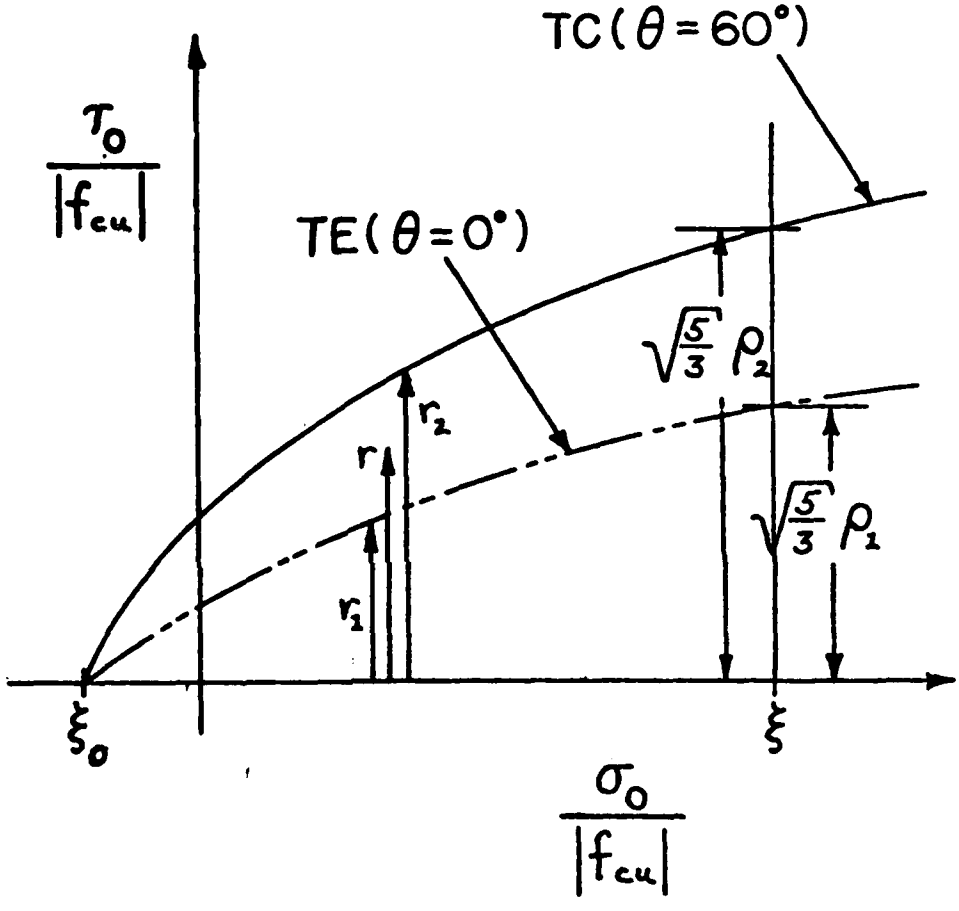

Fig. 6.4 Willam-Warnke Failure Surface in Stress Space (Willam and Warnke, 1974)

meridian ($r(\sigma_o, \theta = 60°) = r_2$) are determined from five dimensionless strength parameter ζ, ρ_1, ρ_2, α_z, and α_u, which in turn are determined from the following six strength values:

1) f_{cu} (uniaxial compressive strength)
2) f_{cb} (equi-biaxial compressive strength)
3) f_t (uniaxial compressive strength)
4) σ_o in the high compression regime
5) τ_o at θ=0° (TE) for the above σ_o
6) τ_o at θ=60° (TC) for the above σ_o

The high compression regime is approximately defined as $\sigma_o \geq f_{cu}$. This five-parameter model is an extension of the original three-parameter model developed by Willam and Warnke (1974) in which the failure surface was defined by a cone with straight meridians. The latter is only applicable in the low compression regime where the failure surface in σ_o-τ_o space can be approximated as a straight line as shown in Fig. 6.5. By reformulating the model to incorporate curved meridians which pass through the data in the high compression regime, both the low and high compression regimes can be adequately represented.

The five parameters of this model are determined as follows: for a given σ_o,

$$\xi = \frac{\sigma_o}{|f_{cu}|} \tag{6.6}$$

$$\rho_1 = \frac{\sqrt{3}}{\sqrt{5}} \frac{\tau_o}{|f_{cu}|} \text{ at } \theta = 0° \text{ (TE)} \tag{6.7}$$

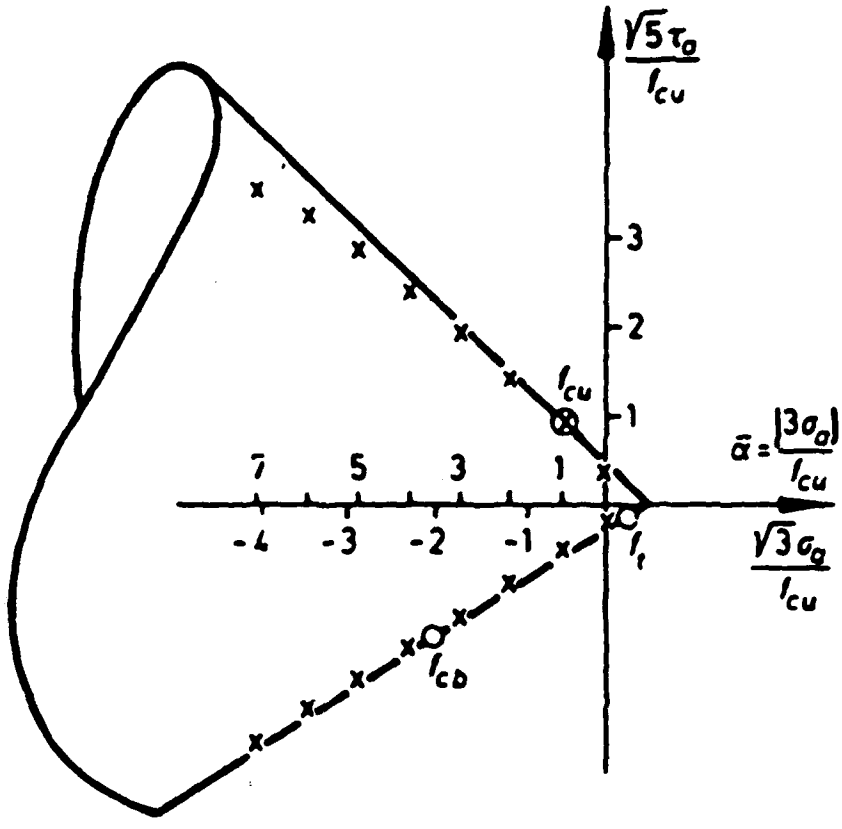

Fig. 6.5 Cone with Linear Meridians Fit to Data in the Low-Compression Regime (Willam and Warnke [1974])

$$\rho_2 = \frac{\sqrt{3}}{\sqrt{5}} \frac{\tau_o}{|f_{cu}|} \text{ at } \theta = 60^\circ \text{ (TC)} \tag{6.8}$$

and from the results of uniaxial tension and equibiaxial compression tests,

$$\alpha_z = \left|\frac{f_t}{f_{cu}}\right|$$

$$\alpha_u = \left|\frac{f_{cb}}{f_{cu}}\right| \tag{6.9}$$

From the quantities ξ, ρ_1, α_u and σ_z the coefficients of the TE meridian are calculated as

$$a_2 = \frac{\sqrt{2}\,\xi\,(\alpha_z-\alpha_u) - \sqrt{2}\,\alpha_z\alpha_u + \frac{\sqrt{5}}{\sqrt{3}}\rho_1\,(2\alpha_u+\alpha_z)}{(2\alpha_u+\alpha_z)(\xi^2 - \frac{2}{3}\,\alpha_u\,\xi + \frac{1}{3}\alpha_z\,\xi\,\frac{2}{9}\alpha_z\alpha_u)} \tag{6.10}$$

$$a_1 = \frac{1}{3}\,(\alpha_z-2\alpha_u)\,a_2 + \frac{\sqrt{2}\,(\alpha_u-\alpha_z)}{2\alpha_u+\alpha_z} \tag{6.11}$$

$$a_o = \frac{\sqrt{2}}{3}\,\alpha_u - \frac{2}{3}\,a_1\,\alpha_u - \frac{4}{9}\,a_2\alpha_u^2 \tag{6.12}$$

It is required that the TE and TC meridians intersect at a common point on the hydrostatic axis such that $r_1 = r_2 = 0$. Because

concrete has tensile strength, this point must lie in the tensile regime. If the nondimensional stress $\sigma_o/|f_{cu}|$ is set equal to some tensile value $-\xi_o$, in order that $r_1 = r_2 = 0$ it follows from equation 6.1 that

$$a_2\xi_o^2 - a_1\xi_o + a_o = 0$$

or

$$\xi_o = \frac{a_1 - \sqrt{a_1^2 - 4a_oa_2}}{2a_2} \tag{6.13}$$

where ξ_o is a positive quantity. From ξ_o and the parameters ξ and ρ_2 the coefficients of the TC meridian are calculated as

$$b_2 = \frac{\frac{\sqrt{5}}{\sqrt{3}}\rho_2\left(\xi_o + \frac{1}{3}\right) - \frac{\sqrt{2}}{3}(\xi_o + \xi)}{(\xi + \xi_o)\left(\xi - \frac{1}{3}\right)\left(\xi_o - \frac{1}{3}\right)} \tag{6.14}$$

$$b_1 = \frac{\sqrt{15}\,\rho_2 - \sqrt{2}}{3\xi - 1} - \left(\xi + \frac{1}{3}\right) b_2 \tag{6.15}$$

$$b_o = \xi_o b_1 - \xi_o^2 b_2 \tag{6.16}$$

The failure surface will be convex, as it should be, if the above determined constants satisfy the following constraints:

$$a_o,\ b_o > 0$$

$$a_1,\ b_1 \geq 0$$

$$a_2,\ b_2 \leq 0$$

and

$$\frac{r_1(\sigma_o)}{r_2(\sigma_o)} > \frac{1}{2}.$$

6.3 Calibration of the Willam-Warnke Model

Neither the uniaxial compressive strength biaxial, compressive strength nor the uniaxial tensile strength was determined during the Phase I test program. Therefore, the calibration of the Willam-Warnke model by Egging was accomplished by performing a second-order polynomial regression on the triaxial data to determine the best-fit parabolas through the TE and TC data points. Although the model, thus calibrated, fits the triaxial data almost perfectly, as shown in Figs. 6.6 and 6.7, the biaxial failure envelope predicted from the same model was totally unrealistic. This predicted biaxial envelope appears in Fig. 6.8. The reason for this can be seen in Fig. 6.9 which shows the TE and TC meridians in the Rendulic plane. Here, the TE meridian will intersect the $\sqrt{2}\,\sigma_2 = \sqrt{2}\,\sigma_3$ axis at a value equal to $\sqrt{2}\,f_{cb}$, where f_{cb} is the equibiaxial compressive strength. Similarly, the TC meridian will intersect the σ_1 axis at f_{cu}, the uniaxial compressive strength. However, the best fit through the TE data results in a value of f_{cL} much less than f_{cu}, thus causing the biaxial failure envelope to assume the shape shown in Fig. 6.8.

Although it would appear that the Willam-Warnke model is incapable of fitting both the biaxial and triaxial strengths simultaneously, it is possible that by calibrating the model with both biaxial and triaxial test results, a reasonable approximation

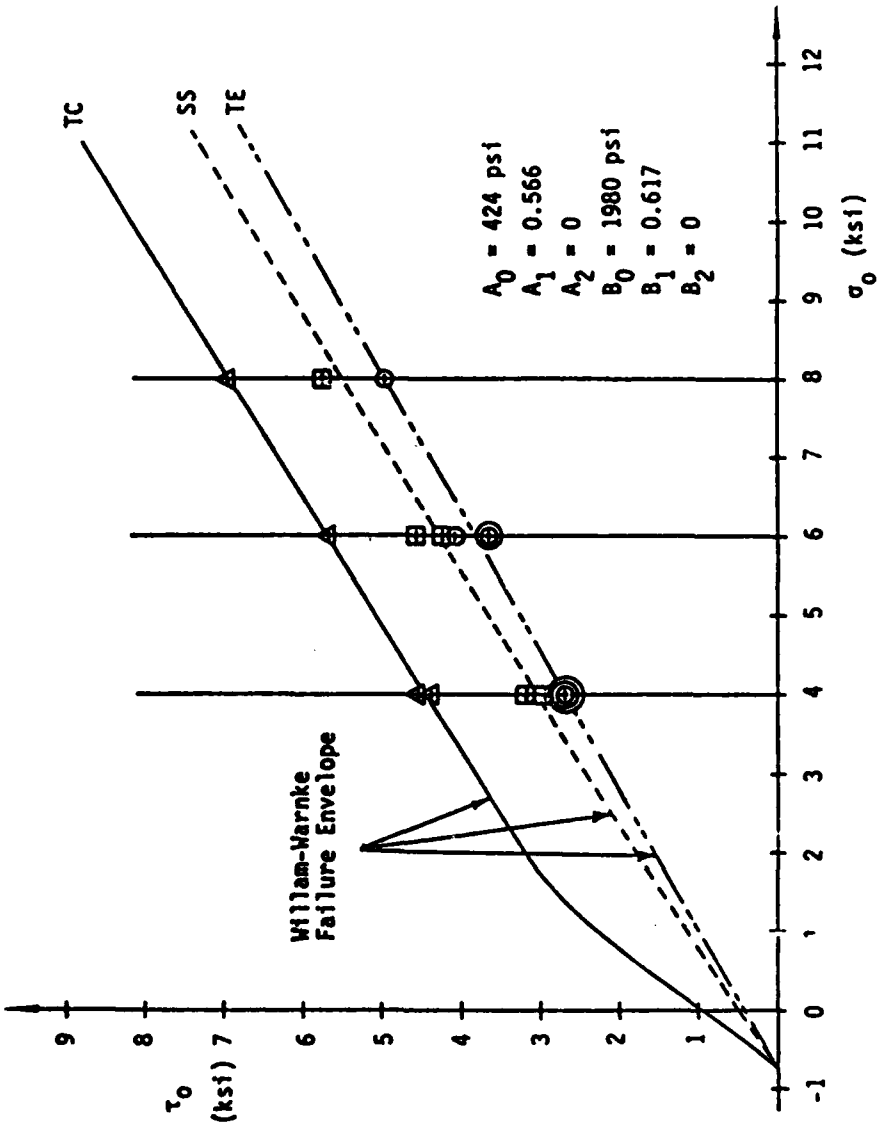

Fig. 6.6 Willam-Warnke Meridians from Phase I Data (Egging [1981])

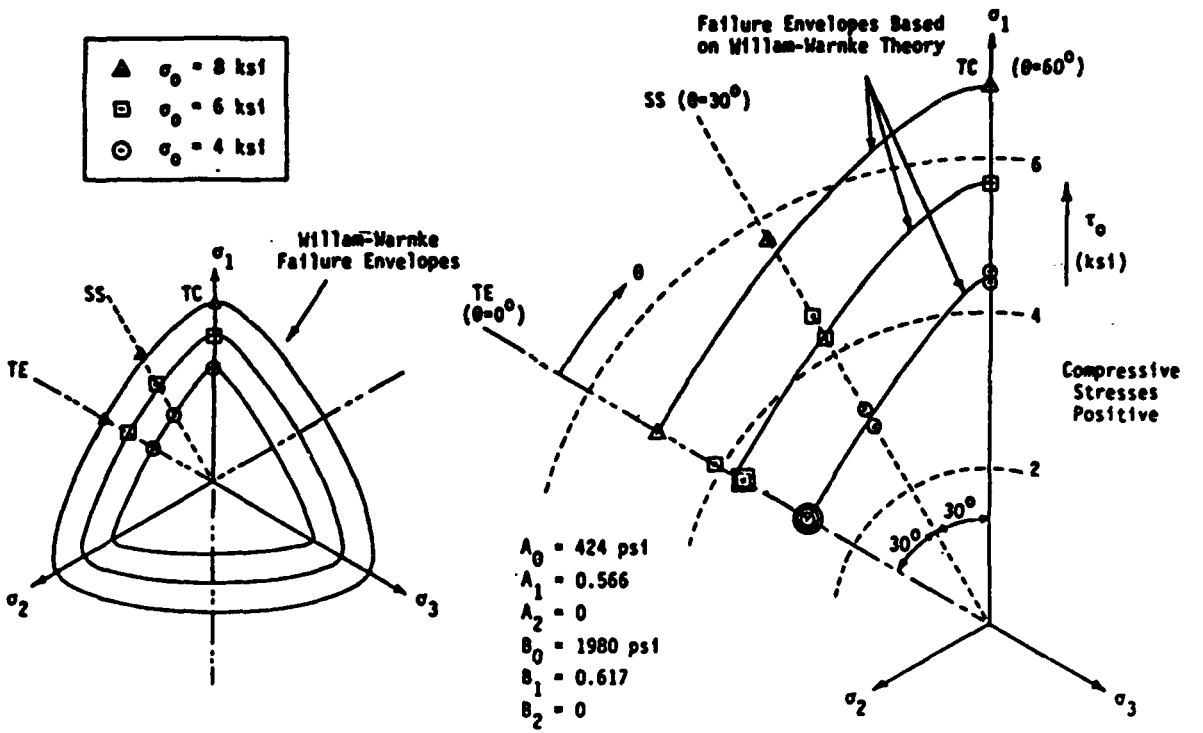

Fig. 6.7 Deviatoric Traces Predicted from the Phase I Data (Egging [1981])

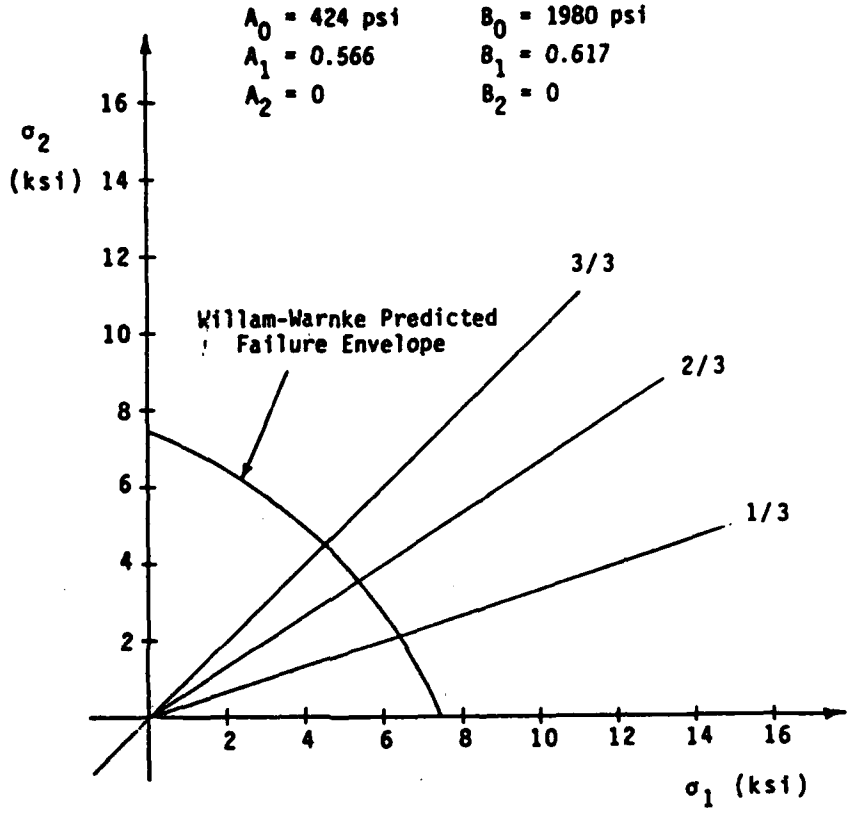

Fig. 6.8 Biaxial Failure Envelope Predicted from the Phase I Triaxial Compression Data (Egging [1981])

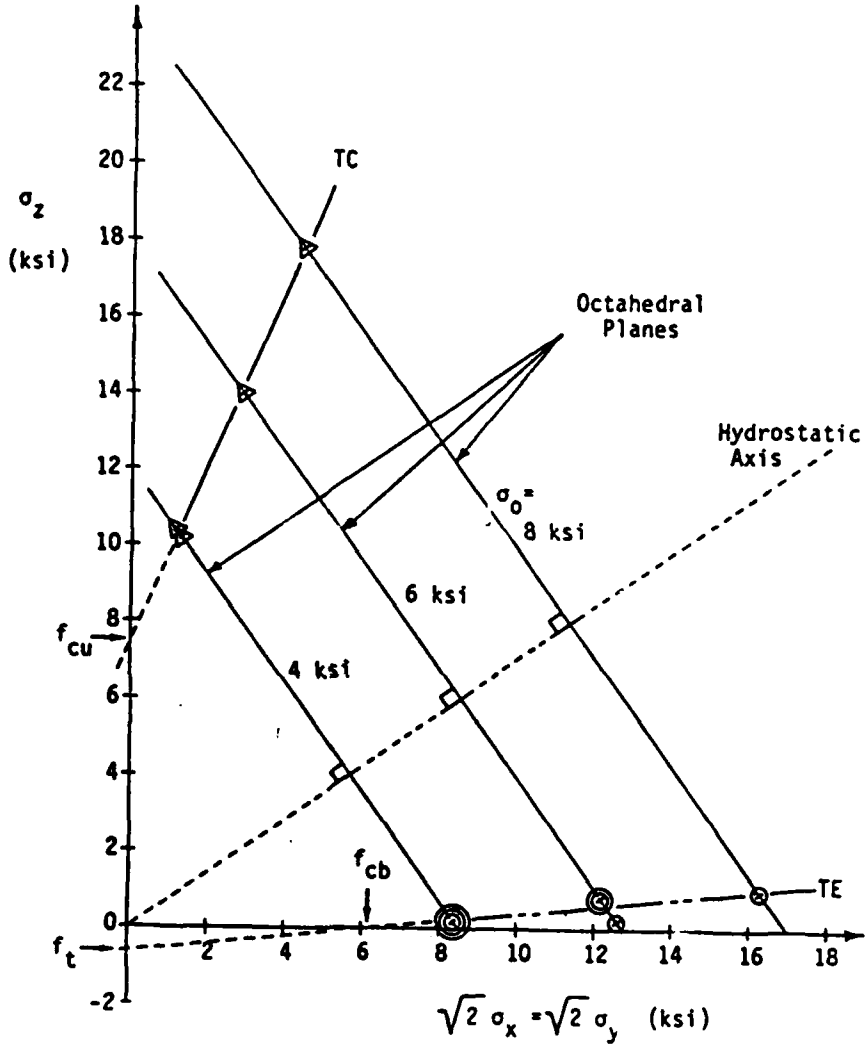

Fig. 6.9 Best Fit Through Phase I TC and TE Data in the Rendulic Plane (Egging [1981])

of both may be obtained. The TE envelope shown in Fig. 6.9 has such a shallow slope that very small changes in the best-fit parabola through that data would casue much greater changes in the predicted value of f_{cb}. Thus, a more reasonable biaxial failure envelope may be obtained without seriously affecting the fit of the model to the triaxial data. As all three of the above-mentioned strength values needed for calibrating the model were determined in the present test program, these measured strengths will be used to recalibrate the model and the resulting strength predictions will be compared to the Phase I and Phase II test results.

In order to properly calibrate the Willam-Warnke model using test results from both Phase I and Phase II, a consistent definition of failure must be used for all of the strength parameters. Because points of dilation were the only strength data recorded in Phase I, this is the definition of failure which must be used in the calibration of the model. Therefore, the resulting failure envelope will only predict the loci of stresses at dilation and cannot be compared to the biaxial tension-compression test results, for which only ultimate strength data is available.

The values selected for f_{cu}, f_{cb}, and f_t were merely the average strengths for those three test categories. Although the uniaxial tensile strength is not strictly valid, as it represents an ultimate strength, its use can be justified on the basis that the beginning of unstable crack propagation in tension, which corresonds to the point of dilation in compressive tests, occurs at a stress level very close to the ultimate strength as was mentioned in the

previous chapter. Therefore, the use of the average ultimate tensile strength is only slightly in error.

The stresses at dilation in the two equibiaxial compression tests, when plotted in the Rendulic plane, lie very close to the intersection of the σ_o = 4 ksi and σ_o = 6 ksi deviatoric planes with the $\sqrt{2}\ \sigma_2 = \sqrt{2}\ \sigma_3$ axis. Since the choice of a stress level σ_o in the high compression regime is arbitrary, and in order that the widest possible range of stress levels be represented in the calibration, the TE and TC results in the σ_o = 8 ksi deviatoric plane were chosen to represent the remaining strength values needed for calibration.

The six strength values used to calibrate the model were:

f_{cu} = 6980 psi

f_{cb} = 7650 psi

f_t = -485 psi

σ_o = 8000 psi

τ_o = at θ = 0° (TE) = 4950 psi

τ_o = at θ = 60° = (TC) 6930 psi

from which the coefficients of the parabolic meridians were calculated as

a_o	= 0.0502	b_o	= 0.0878
a_1	= 0.75	b_1	= 1.299
a_2	= -0.1527	b_2	= -0.4445

The meridians $r_1(\sigma_o)$ and $r_2(\sigma_o)$ are shown in Fig. 6.10 along with the calculated meridian $r(\sigma_o, \theta = 30°)$ which represents the SS stress paths. For all three stress paths shown, the model

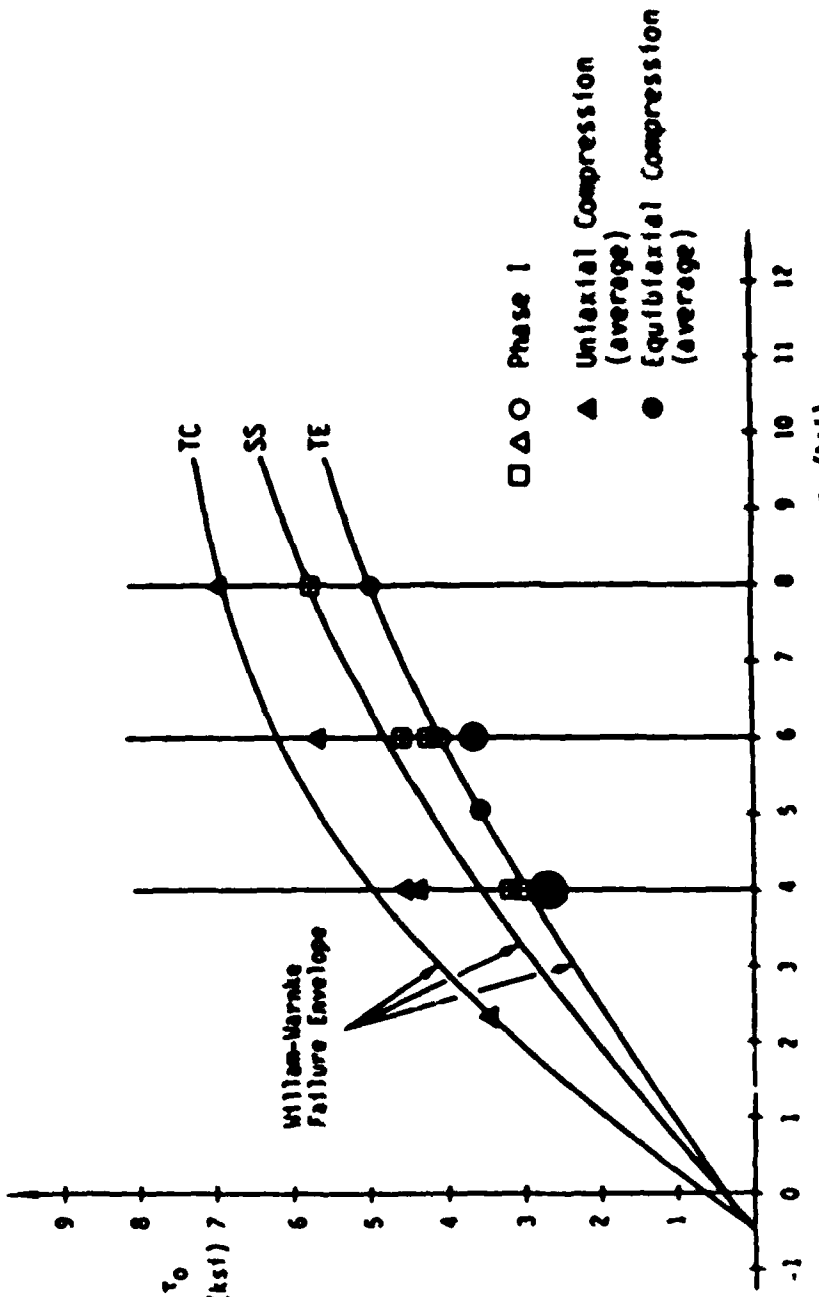

Fig. 6.10 Predicted Meridians in $\tau_o - \sigma_o$

significantly overestimates the strengths in the σ_0 = 6 ksi and σ_0 = 8 ksi deviatoric planes because the curvature of the meridians is much greater than that exhibited by the data.

The difficulty in fitting the Willam-Warnke model to this test data lies in the fact that the data exhibit nearly linear relationships between σ_0 and τ_0. In the case of the TC meridian, which shows the worst correlation to the experimental data, the problem is compounded by the fact that the parabolic meridian must not only pass through the specified data points but must also intersect the σ_0 axis at the value of $-\xi_0$ dictated by the formulation of the TE meridian. As can be seen in Fig. 6.11, the best-fit line through the data intersets the σ_0 axis at a value of σ_0 considerably less than $-\xi_0$. The excessive curvature results because the meridian must be "bent" until it passes through the proper point on the axis.

Despite the relatively poor fit to the multiaxial compression data, the model predicts a failure envelope in the biaxial plane which shows much better correlation to the data. This predicted failure envelope is shown in Fig. 6.12. Because of the relatively large scatter of the data points, it is difficult to assess the fit of the envelope from this figure. However, it was mentioned previously that the loci of points of dilation (which corresponds to the predicted failure envelope) should have essentially the same shape as the ultimate strength failure envelope. In Fig. 6.13 the Willam-Warnke prediction is shown along with the best-fit ultimate strength envelope. Here it becomes

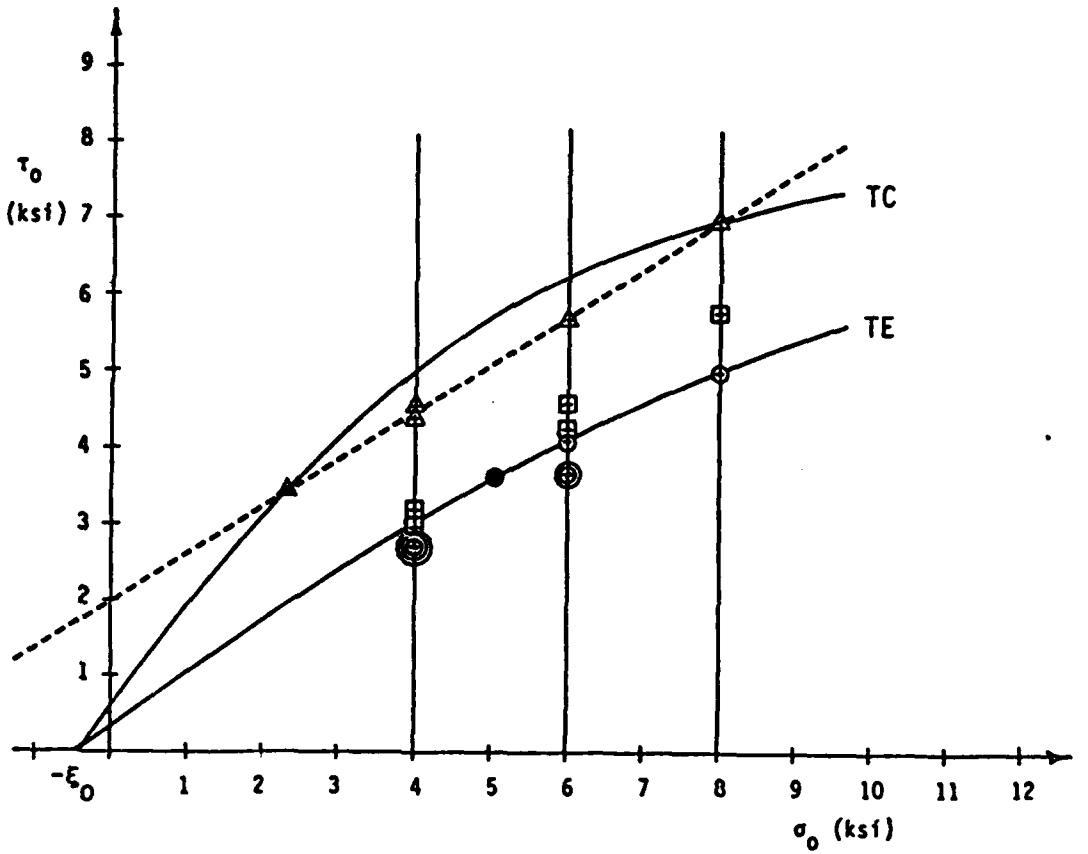

Fig. 6.11 Comparison between Best-Fit Line and Parabolic Meridian for TC Stress Paths

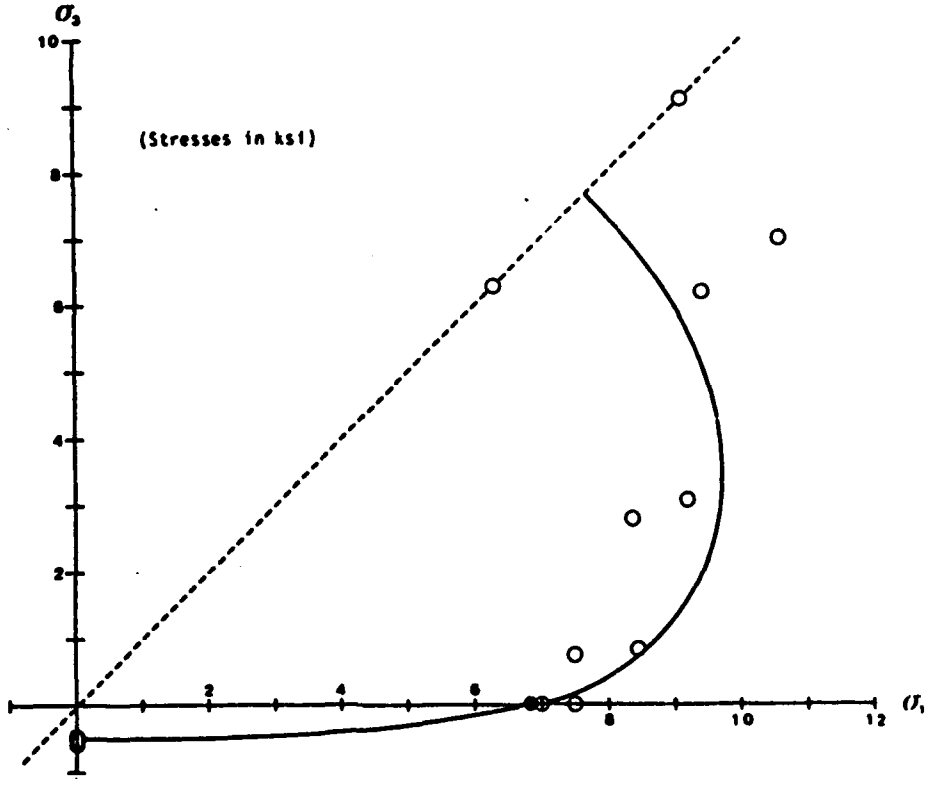

Fig. 6.12 Willam-Warnke Prediction in Biaxial Plane

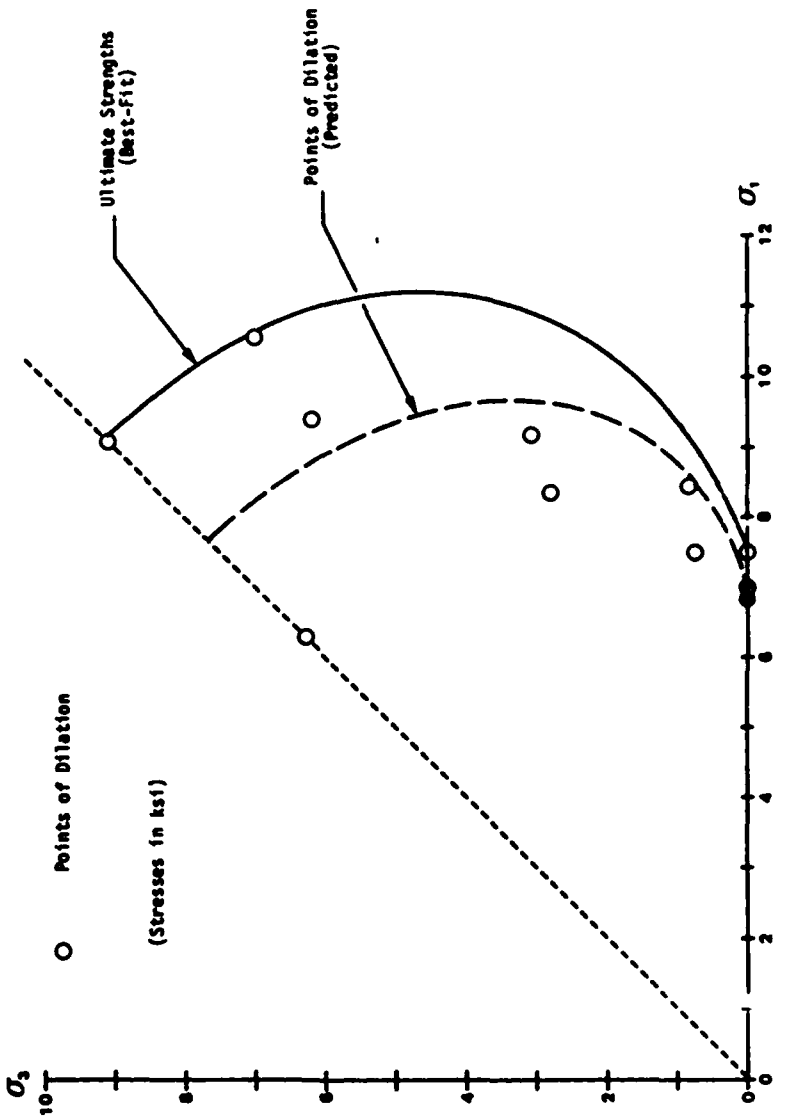

Fig. 6.13 Comparison between Best-Fit Ultimate Strength Envelope and Predicted Loci of Points of Dilation

apparent that the essential features of the failure envelope have been duplicated by the Willam-Warnke prediction.

One explanation for the considerably better fit to the biaxial data is that the shape of the deviatoric trace predicted by the model is essentially correct even though the meridians do not describe the data well. Since the biaxial failure envelope is merely the intersection of the three-dimensional failure surface with the $\sigma_3 = 0$ plane, the shape of the biaxial failure envelope is dictated, in part, by the cross-sectional shape of the failure surface. Examining Fig. 6.10, it can be seen that the predicted SS meridian passes directly through the data point at $\sigma_0 = 8$ ksi. The TC and TE meridians also pass through their respective data point in this deviatoric plane since these points were used to calibrate the model. This would suggest that the ellipse used to connect the TC and TE meridians in the deviatoric cross-sections approximates the strength behavior in the deviatoric planes fairly well. This in turn leads to a reasonable approximation of the biaxial strength behavior.

It would appear that the Willam-Warnke model does reflect some of the essential features of the strength behavior of the SFRC. A better approximation of the relationship between strength and octahedral stress might be obtained by using something other than a parabola to describe the meridians while retaining the elliptical formulations of the failure surface cross-section. However, although this might result in a convenient mathematical description of the strength behavior within the range of stresses

examined in this test program, its use for predicting stresses outside of this range would still be in question.

6.4 Lade Three-Parameter Failure Criterion for Concrete

The three-parameter failure criterion for concrete proposed by Lade (1981) is an adaptation of a general, three-dimensional failure criterion previously developed by Lade (1977) for cohesionless soils. The failure surface function is expressed in terms of the first and third invariants of stress as

$$F(\sigma) = \left(\frac{J_1^3}{J_3} - 27\right)\left(\frac{J_1}{p_a}\right)^m - \eta_1 \qquad (6.17)$$

$$= 0 \text{ for material failure}$$

where

$$J_1 = \sigma_1 + \sigma_2 + \sigma_3 \qquad (6.18)$$

$$J_3 = \sigma_1 \cdot \sigma_2 \cdot \sigma_3 \qquad (6.19)$$

m, η_1 = failure parameters

p_a = atmospheric pressure

In order for the original formulation to be applicable to concrete, allowances had to be made to account for the fact that concrete can withstand tensile stresses. This was accomplished by translating the principal stress axes through a distance $a \cdot p_a$ such that the failure envelope crosses the original σ_1 axis at a value $-f_t$ equal to the uniaxial tensile strength. This translation is shown in Fig. 6.14. Translation of the stress axes is achieved by adding a constant stress $a.p_a$ to each of the principal stresses:

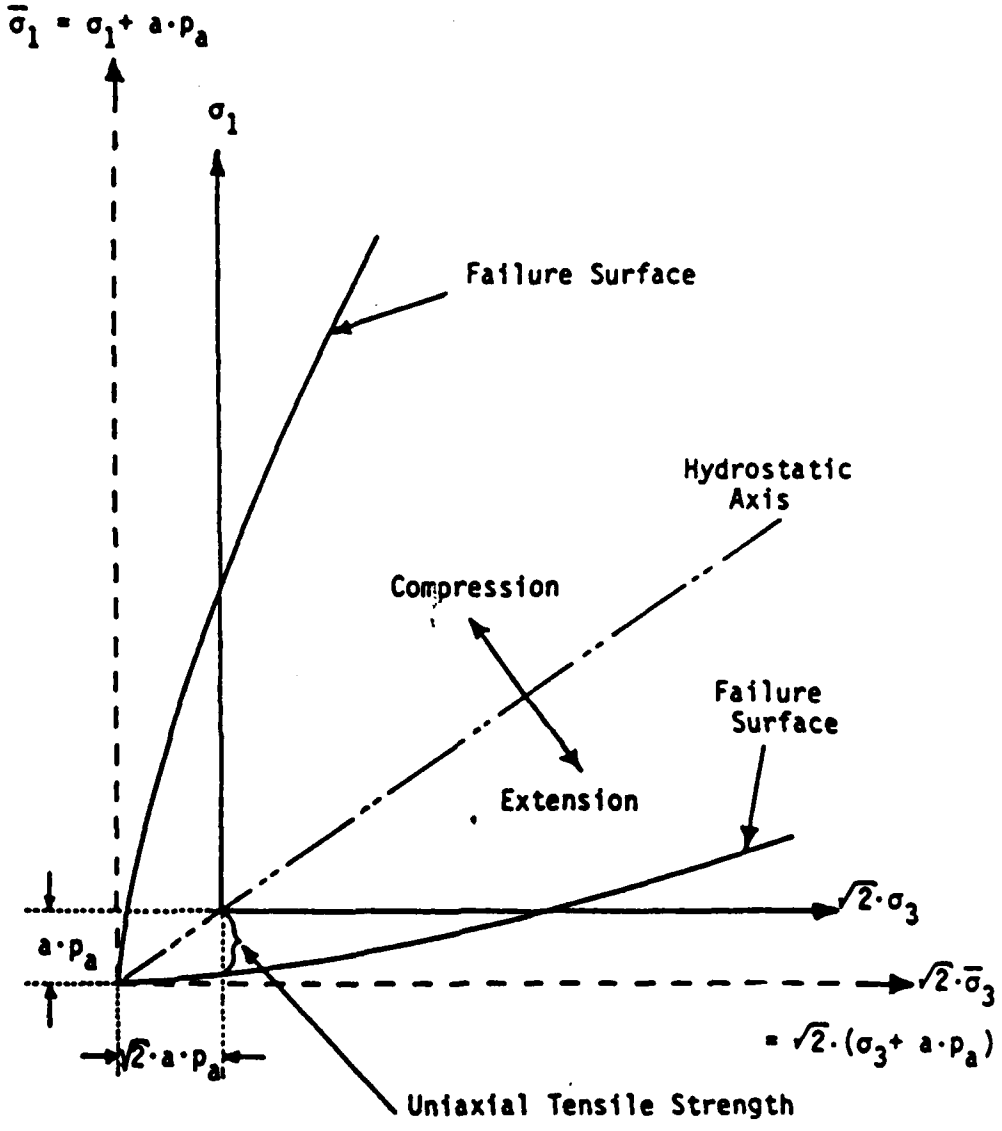

Fig. 6.14 Translation of the Principal Stress Axes to Allow for Tensile Strength (Lade [1981])

$$\bar{\sigma}_1 = \sigma_1 + a \cdot p_a$$

$$\bar{\sigma}_2 = \sigma_2 + a \cdot p_a \qquad (6.20)$$

$$\bar{\sigma}_3 = \sigma_3 + a \cdot p_a$$

The stresses $\bar{\sigma}_1$, $\bar{\sigma}_2$, and $\bar{\sigma}_3$ can be substituted directly into equations 6.18 and 6.19 in order to determine the stress invariants to be used in the failure function.

Calibration of the model to determine the parameters a, η_1, and m begins with the selection of a value for "a" such that $a \cdot p_a$ is slightly greater than the uniaxial tensile strength. From studies conducted by Lade (1981), a suitable value of "a" should lie in the range

$$1.003 \left|f_t\right| < a \cdot p_a < 1.014 \left|f\right|_t. \qquad (6.21)$$

With a first estimate of "a" selected, the stress invariants at failure, in terms of the adjusted principal stresses, are then calculated from any available failure data. This is a significant advantage of the Lade model. With the exception of uniaxial tension, no specific test types are required for calibration. The parameters η_1 and m are then determined by plotting the strength data as $(J_1^3/J_3 - 27)$ vs. (p_a/J_1) on log-log paper and finding the best-fit line through the data using regression analysis. The equation of this line is the failure function $F(\sigma)$ given in Equation 6.17. The intersection of the best-fit line with the line $(p_a/J_1) = 1$ is η_1 and the slope of the line is m. By repeating this procedure with different values of "a", the final values to be used

in the model can be determined as those for which the highest regression coefficient is obtained. An example of this fitting routine is shown in Fig. 6.15.

6.5 Calibration of the Lade Three-Parameter Model for Concrete

Because the calibration of the Lade model is not constrained to any particular type of test, a number of options was available. The first case which was studied was a calibration based on all of the Phase II test data. Since this included biaxial tension-compression tests, ultimate strength was used as the definition of failure. Such a calibration would reveal whether or not the mathematical formulation of the model reflects the essential features of biaxial strength behavior outlined in Chapter 5.

The second calibration was performed using only the biaxial compression data and, of course, the uniaxial tension results. In this way, the ability of the model to predict biaxial tension-compression tests could be examined. If a good correlation with the measured strengths could be obtained, it might eliminate the need for tension-compression testing. Because of the difficulties involved with tension-compression testing, especially with respect to the elimination of boundary effects, it would be preferable if such tests did not have to be performed.

Finally, a third calibration was performed using the multiaxial compression test results from Phase I and the biaxial compression results from the present test program. Here the stresses at dilation were used as the definition of failure as was

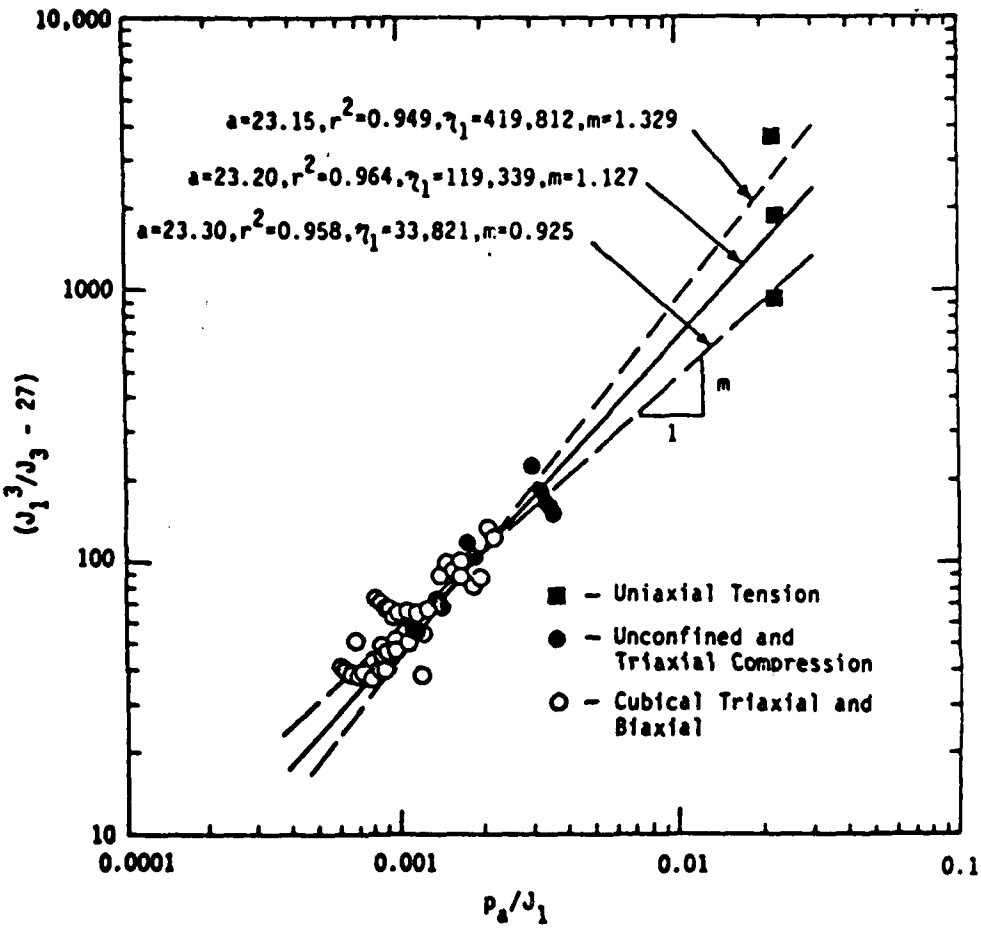

Fig. 6.15 Example of Varying the Parameter "a" to Obtain the Highest Regression Coefficient (Lade [1981])

done in the calibration of the Willam-Warnke model. As was seen in that calibration, it is difficult to predict the biaxial and multiaxial strength behavior of the SFRC simultaneously.

CASE I

Because the calibration of the Lade model is accomplished by plotting in log-log coordinates, negative values of $(J_2^3/J_3 - 27)$ and p_a/J_1 are not permitted. This presented a problem with including all of the biaxial tension-compression data in the calibration. If the average uniaxial tensile strength of -485 psi was used to determine $a \cdot p_a$, then from Equation 6.21 the value of $a \cdot p_a$ could be expected to fall within the limits 486.5 to 492 psi. Therefore, those tests in which the tensile strength exceeded -486.5 psi would have to be excluded from the calibration if all possible values of "a" were to be investigated. This category includes all of the biaxial tension-compression tests at 0.1 and 0.3 f_{cu}. In addition, the uniaxial tension test category could only be represented as an average strength since some of the data must, by definition, fall above the average. Although the former does not, in general, apply to plain concrete testing since the uniaxial tensile strength usually exceeds any biaxial tension-compression strengths, the latter applied to any calibration of the Lade model. The question which had to be reseolved was how to represent the uniaxial tension tests. If a single data point at the average strength was used, the regression analysis would be biased toward the remaining test categories which are represented by more than one data point. On the other hand, the use of multiple data points, all

at the average tensile strength, would bias the regression analysis as well.

For all of the calibrations presented here, it was decided that the uniaxial tension test category would be represented by five data points, corresponding to the five tests performed, with -485 psi strengths. Because the coefficient of variation of the uniaxial tension test results is less than 4 percent, a high degree of confidence can be had in this value of the strength. In order to accurately reflect this in the model, multiple data points were used.

The value of "a" resulting in the highest regression coefficient was found to be 33.02 which corresponds to a value of 485.4 psi for $a \cdot p_a$. This value lies outside the range of strengths suggested by Equation 6.21. At first, this was thought to be the result of using multiple data points for the uniaxial tensile strength, therefore the calibration was redone using only one data point. The highest regression coefficient again resulted from using a 33.02. Bearing in mind that $a \cdot p_a$ represents the distance by which the principal stress axes must be translated such that the failure envelope will pass through the uniaxial tension data points, its magnitude in relation to the uniaxial tensile strength depends on the slope of the failure envelope in the biaxial tension-compression quadrant. As can be seen in Fig. 6.14, $a \cdot p_a$ approaches f_t as the slope of the failure surface in the extension regime approaches the horizontal. The ratio of f_t to f_{cu} for the SFRC is only 0.06. It is therefore suggested that the range of

values cited by Lade stems from tests performed on concretes with more-commonly observed strength ratios such as 0.1 or 0.15 and that the ratio $a.p_a/|f_t|$ = 1.0008 seen here is realistic considering the very shallow slope required fo the failure envelope.

The log-log plot of the data using $a \cdot p_a$ = 33.02 is shown in Fig. 6.16. Notice that despite the use of five data points to represent the uniaxial tension tests, the best-fit regression line does not pass through those data points. This can be attributed to the fact that the majority of the biaxial tension-compression data points lie significantly below the line. The one solid circle situated above the line represents the two tests at 0.4 f_{cu} which had identical results. The circles below the line represent the tests at 0.45, 0.5, and 0.65 f_{cu}. Thus the switch from one side of the line to the other coincides with the inflection in the failure envelope which was discussed in the previous chapter. It appears that the biaxial tension-compression data, while representing only a very small portion of the failure surface, has a disproportionately large effect on the resulting model. The comression data is clustered around the line in a tight group while the tension-compression data is spread out over a much larger range of values p_a/J_1 and therefore influences the slope of the line to a greater degree. The extent of this influence will be seen in the next calibration which was performed without the tension-compression data.

The predicted failure envelope in the biaxial tension-compression quadrant is shown in Fig. 6.17. The fit to the

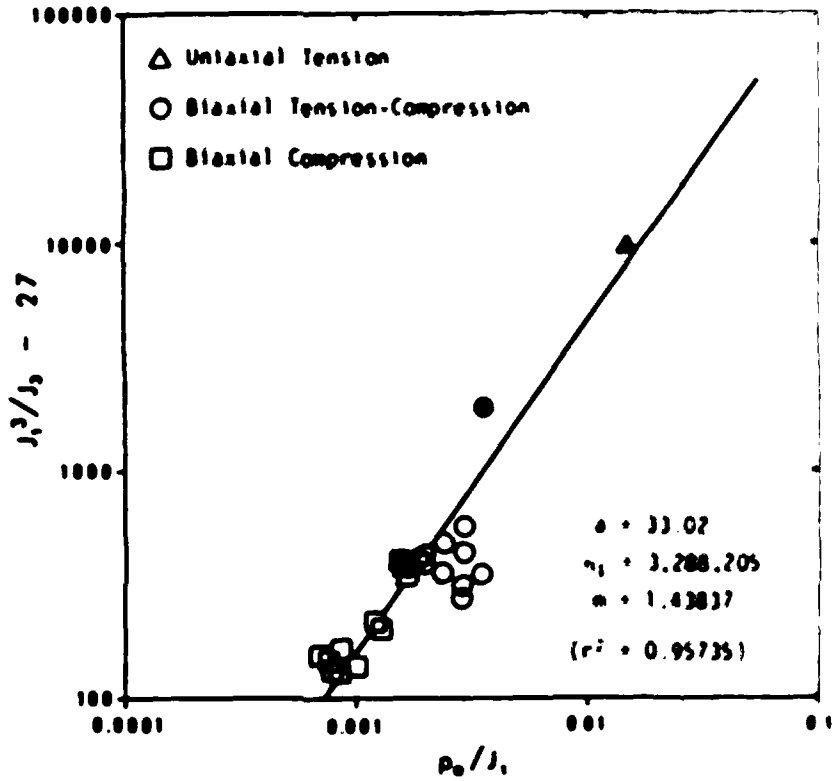

Fig. 6.16 Calibration of Lade Model from Phase II Test Results

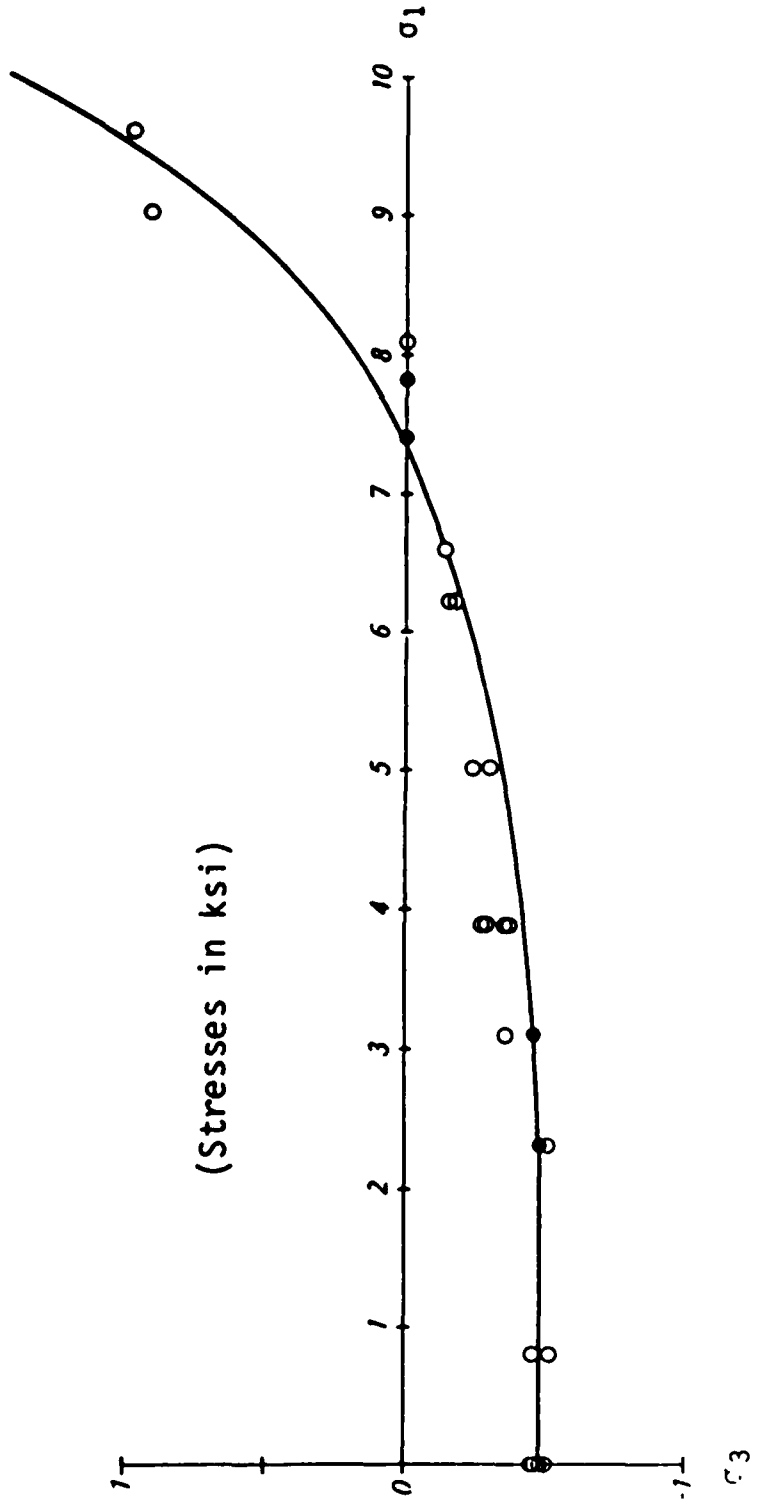

Fig. 6.17 Lade Prediction in the Tension-Compression Quadrant

data is actually quite good, given the fact that no generalized three-dimensional formulation would be capable of modeling the inflection point. In the compression quadrant, the model is slightly conservative, especially as the stress ratio σ_2/σ_1 approaches unity. The complete biaxial failure envelope is shown in Fig. 6.18.

CASE II

The second calibration, which was performed without the tension-compression data, also resulted in a value of "a" of 33.02. As can be seen in Fig. 6.19 the best-fit regression line passes exactly through the uniaxial tension data points in the absence of the tension-compression results. The predicted failure envelope in the tension-compression quadrant is shown in Fig. 6.20. At the lower ratios of σ_1/f_{cu} the fit to the data is virtually identical to that of the previous calibration. At the higher ratios, however, the model overestimates the tensile strengths to a greater extent. The entire biaxial failure envelope is shown in Fig. 6.21. Here it can be seen that the present calibration is less conservative in the compression quadrant as well although it still provides a reasonable fit to the data. One reason that the fit is no better than it is can be traced to an inherent feature of this model. Examination of the two calibrations presented here as well as calibrations from other data (Lade, 1981) shows that this model predicts a maximum value of σ_1 in biaxial compression at a stress ratio of approximately 1:3. As mentioned in Chapter 5, the maximum is more often found to occur at a stress ratio of 1:2. In this respect, the Lade model does not accurately reflect the biaxial strength behavior

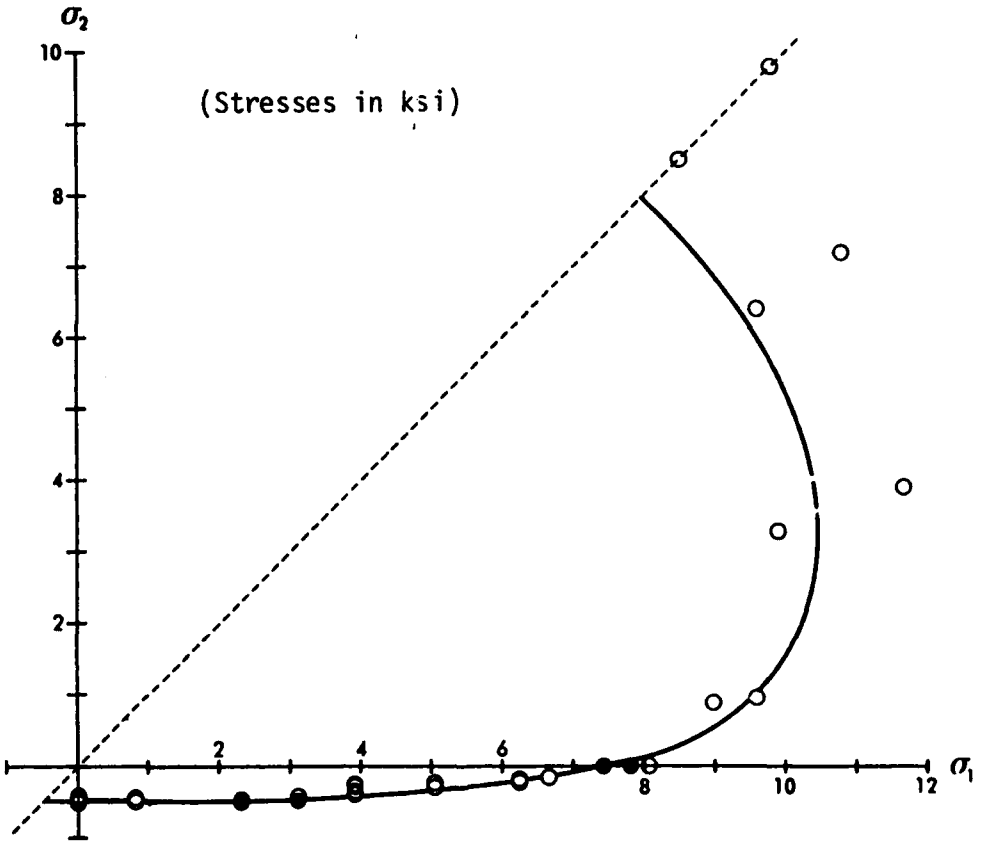

Fig. 6.18 Biaxial Failure Envelope Predicted from Lade Model

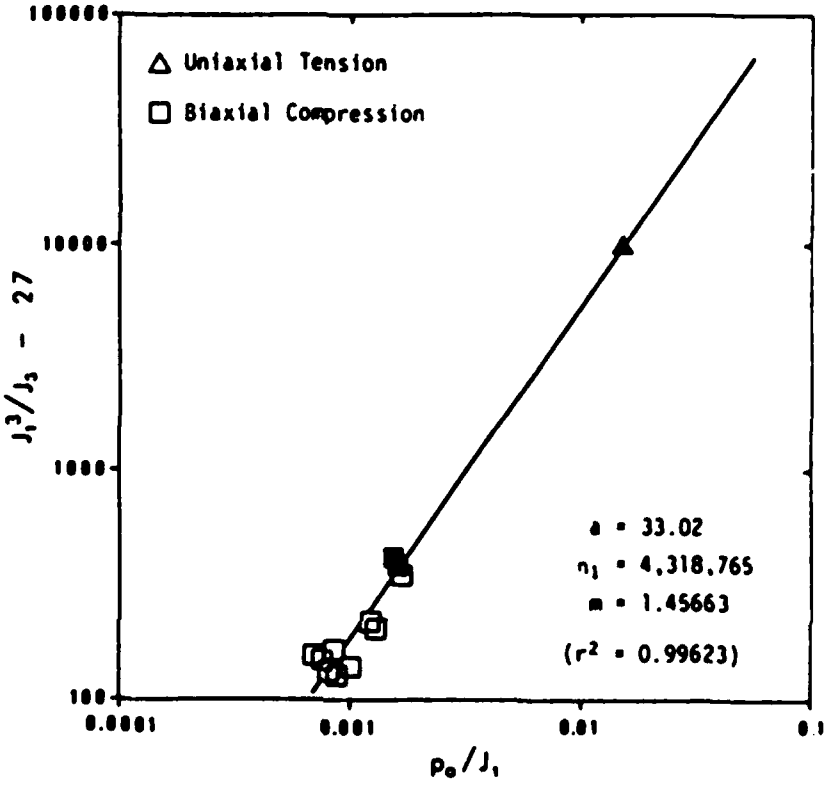

Fig. 6.19 Calibration of Lade Model from Biaxial Compression Test Results

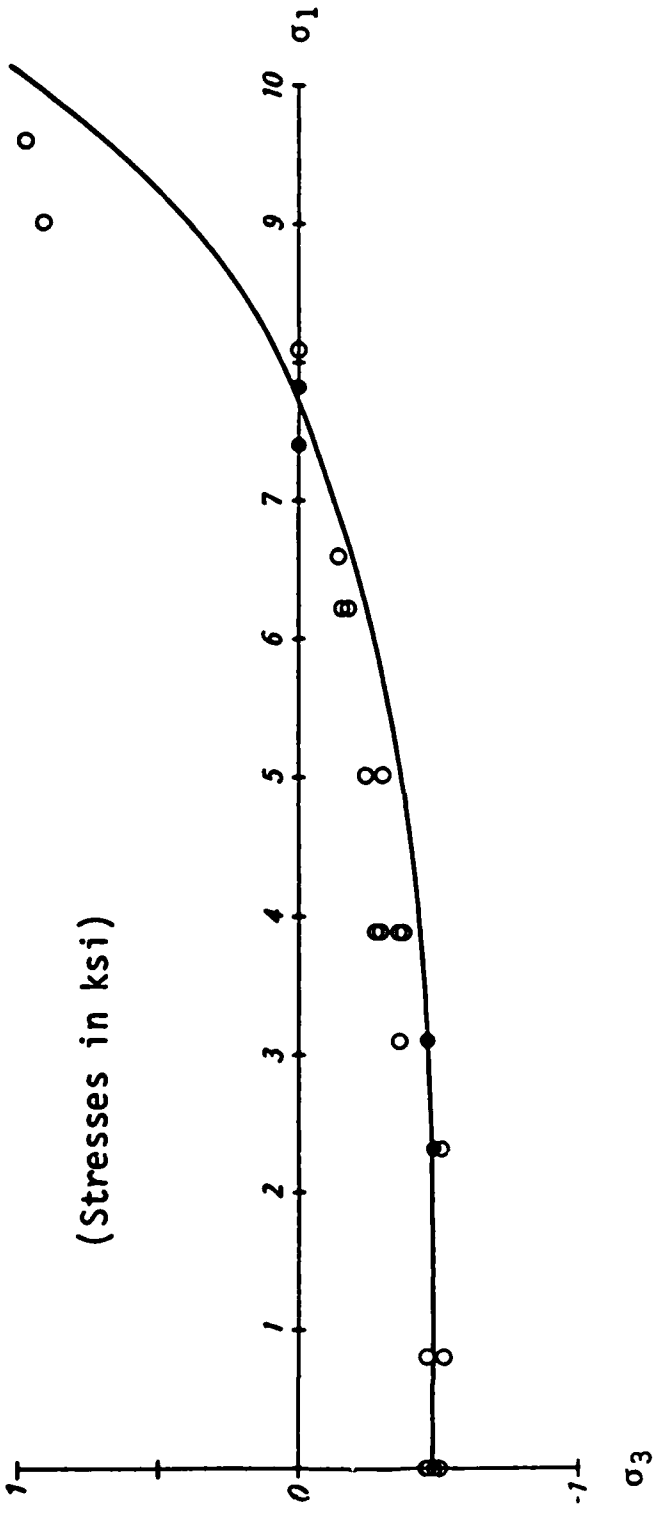

Fig. 6.20 Lade Prediction in the Tension-Compression Quadrant

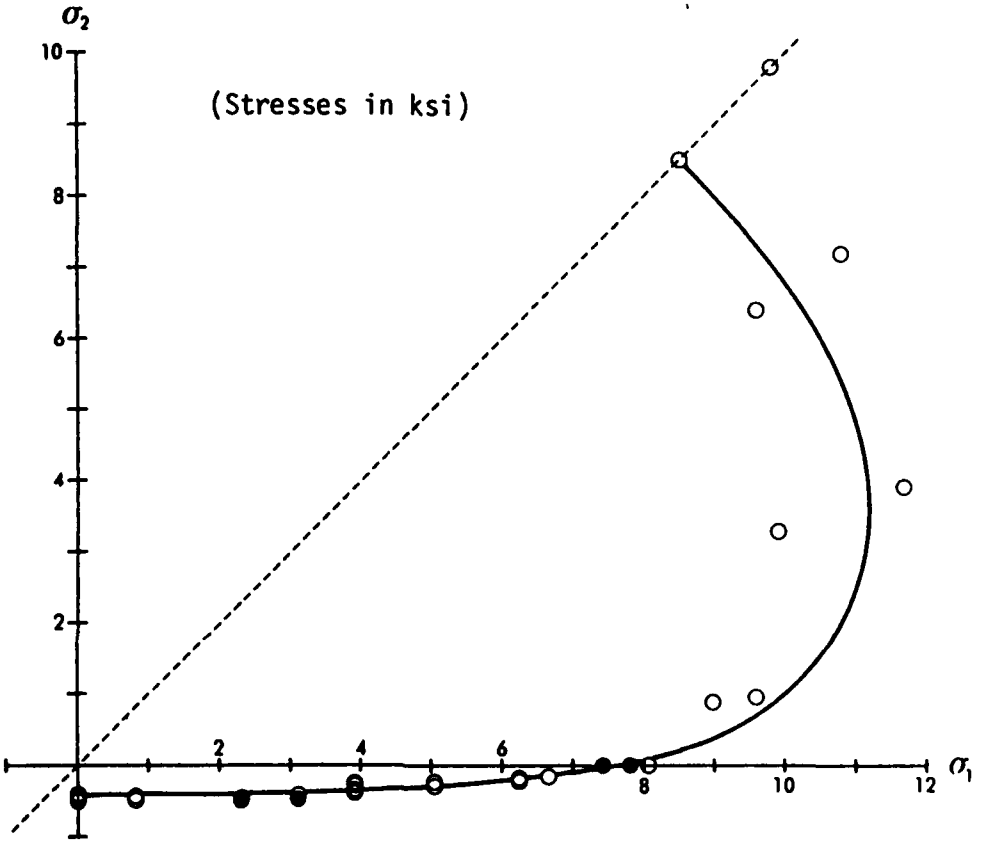

Fig. 6.21 Biaxial Failure Envelope Predicted from Lade Model

of concrete. It tends to underestimate the strengths as σ_2 approaches σ_1 and overestimate the strengths as σ_2 approaches zero.

CASE III

The third calibration was performed using the combined compression data of Phases I and II with the point of dilation as the definition of failure. Therefore, no attempt was made to comapre the resulting failure envelope to the biaxial tension-compression data.

The best-fit regression line is shown in Fig. 6.22. Notice that the multiaxial compression data is spread out along three vertical lines, each corresponding to the appropriate value $p_a/J_1 = p_a/3\sigma_o$. It is immediately obvious that the amount of scatter exhibited by the data along these lines precludes a good approximation of the multiaxial strength behavior by the model. This would be true regardless of the other data used in the calibration.

The predicted biaxial failure envelope is shown in Fig. 6.23. As with the previous calibrations, the model underestimates the strengths for stress ratios approaching unit. With the present calibration, the model predicts a maximum value of σ_1 in biaxial compression at an even lower stress ratio of approximately 1:4. In Fig. 6.24 this biaxial failure envelope is shown along with the ultimate strength envelope, which achieves a maximum value of σ_1 at a stress ratio of 1:2, to illustrate the difference in the shapes.

In Fig. 6.25 the TC and TE meridians of the predicted failure envelope are shown in the Rendulic plane. The model

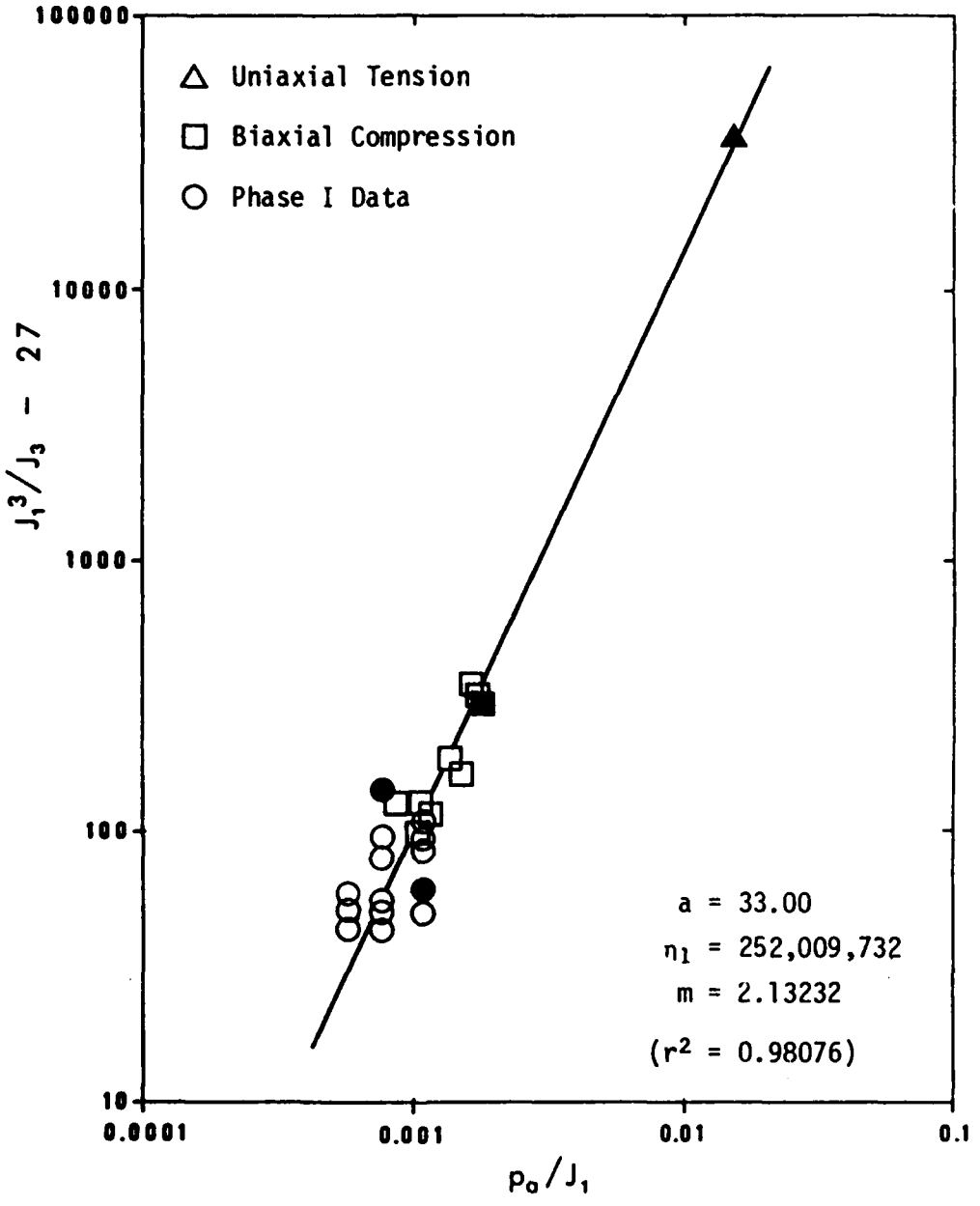

Fig. 6.22 Calibration of Lade Model from Phase I and Phase II Test Results

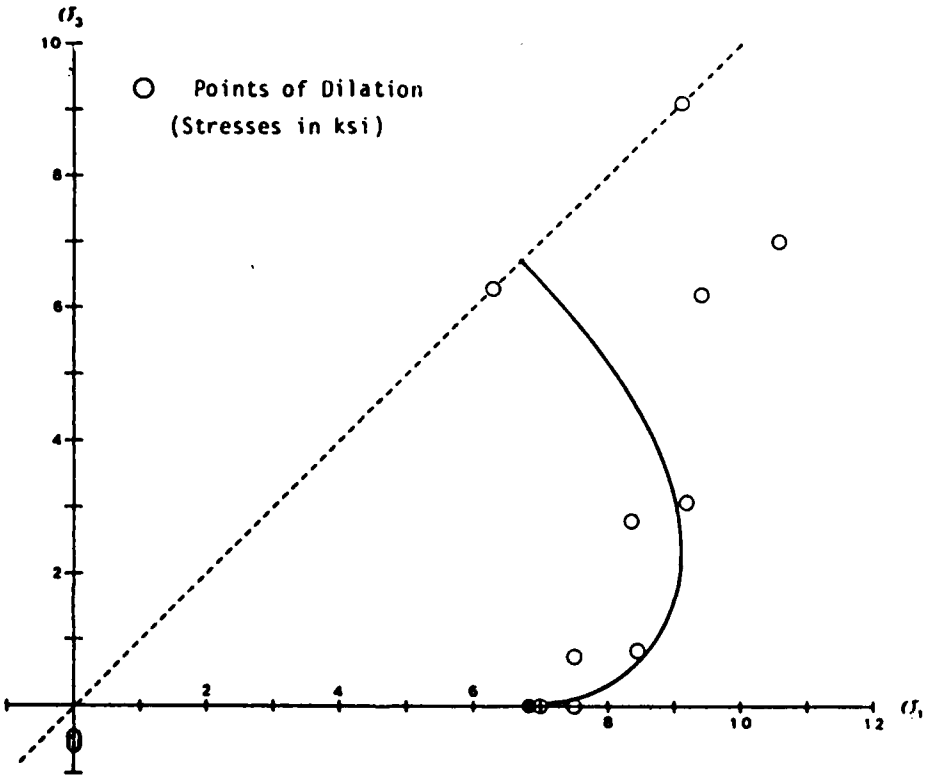

Fig. 6.23 Biaxial Failure Envelope Predicted from Lade Model

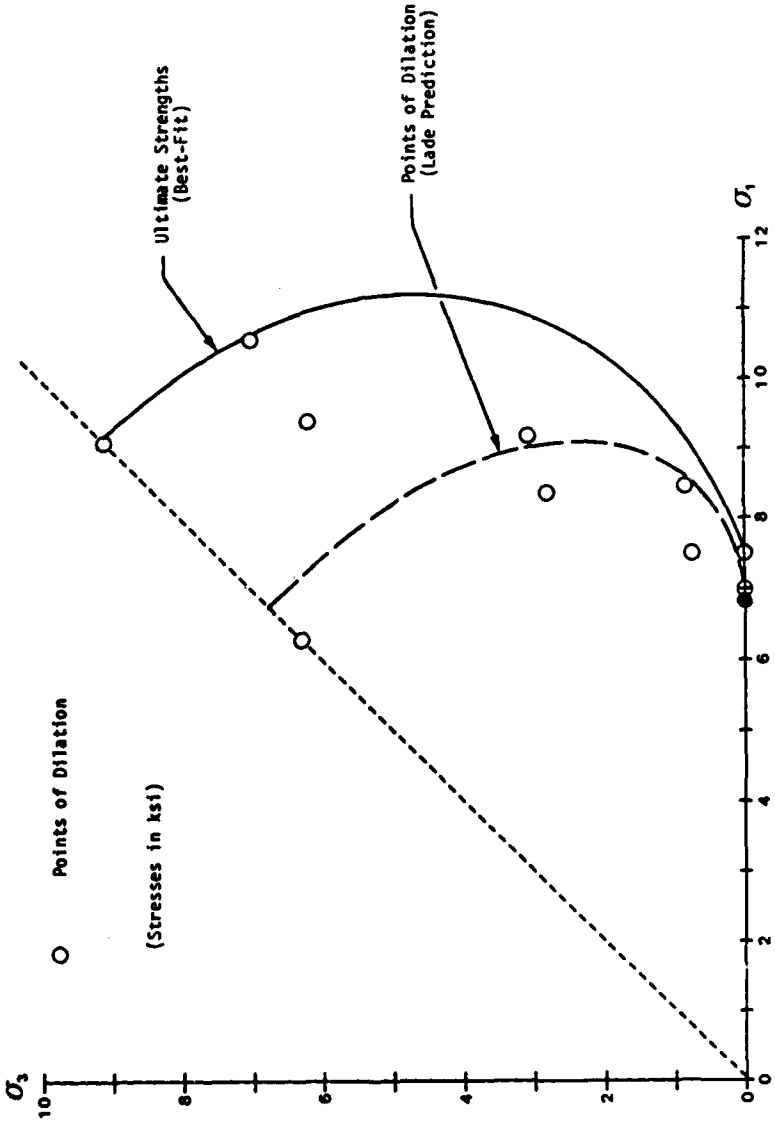

Fig. 6.24 Comparison between Best-Fit Ultimate Strength Envelope and Predicted Loci of Points of Dilation

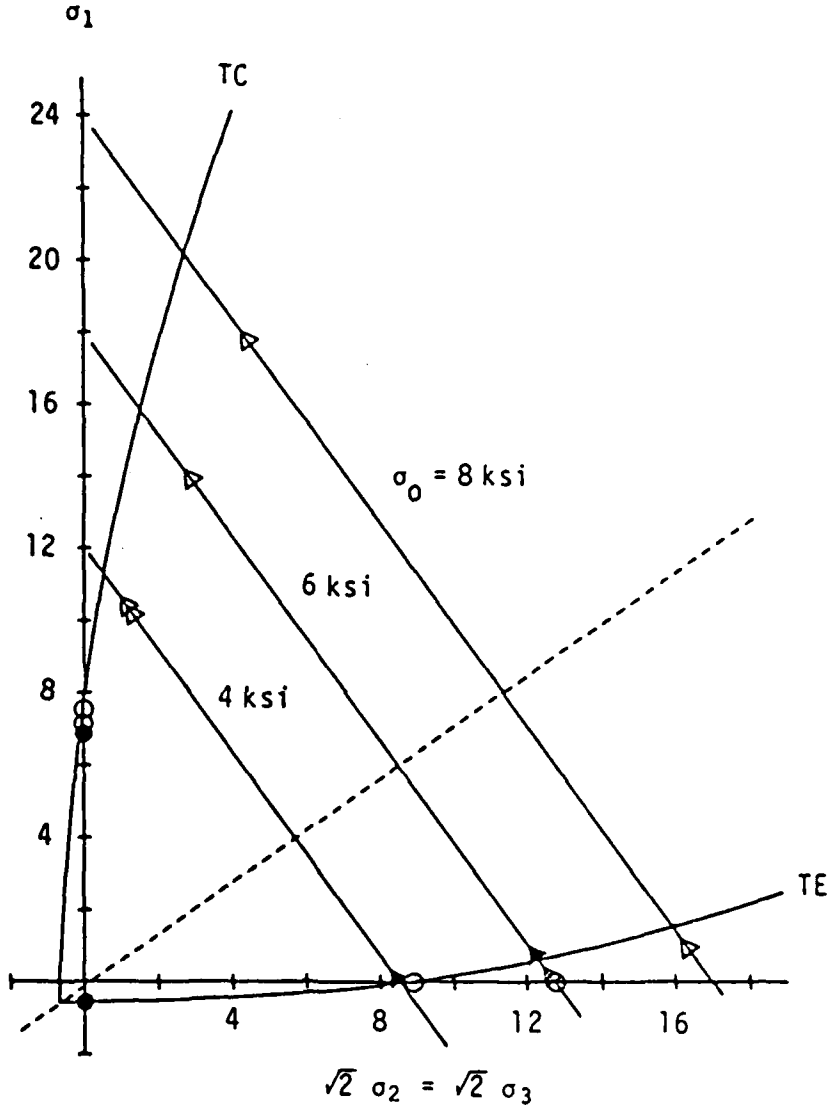

Fig. 6.25 Lade Prediction in the Rendulic Plane

significantly overestimates the strength of the SFRC when loaded along TC stress paths while underestimating the strength along the TE paths. This reflects the findings with regard to the shape of the biaxial failure envelope which can apparently be extended to three dimensions by stating that the model tends to underestimate strengths under conditions where σ_1 and σ_2 are both large in comparison to σ_3 (which describes both the TE and equibiaxial compression tests) and overestimates strengths under conditions where σ_2 and σ_3 are both small in comparison to σ_1 (corresponding to the TC and uniaxial compression tests). Since the shape of the biaxial failure envelope is related to the shape of the failure envelope in deviatoric cross-section, this is not unexpected. The reasoning is identical to that which was previously discussed with respect to the Willam-Warnke model: if the strength behavior in the biaxial plane is not adequately reflected in the model, the strength behavior in the deviatoric planes will most likely be inadequtely modeled as well because the two are related.

CHAPTER 7

CONCLUSIONS AND RECOMMENDATIONS FOR FUTURE RESEARCH

Quite a few significant findings have emerged from the research program presented here. As is often the case, just as many questions have been raised as have been answered. In this chapter, a summary of the principal findings is presented and some recommendations are made as to the direction in which future research should go in order to answer a few of these questions.

1. In the preliminary test program it was found that the split-cylinder test greatly exaggerates the influence of fiber reinforcing on tensile strength when compared to the results of direct tension testing. This has been attributed to the availability of a load transfer mechanism whereby the stresses on the incipient failure plane are transferred along the fibers to their anchorages in less highly stressed regions of the specimen. In the past, FRC research has centered on the ability of the fibers to retard the growth of microcracks and thus delay failure. As fiber reinforced concrete is applied in situations with more complex states of stress, and as better equipment becomes available to duplicate these complex stresses in the testing laboratory, this ability to shed load, at least on the small scale of the test specimen, could become very important. One of the foremost

questions concerning this phenomenon is whether or not such load transfers can occur on a structural scale. In the present test program, the size of the specimens was of the same order of magnitude as the length of the fibers and loads did not have to be transferred far to alleviate cracking. If stress redistribution attributable to the fiber reinforcing does not occur on a structural scale, these effects must be eliminated in laboratory testing. This presents yet another scale effect which must be addressed.

2. From the results of the direct tension tests, the fiber reinforcing was shown to provide very little strength enhancement due to the fact that the strength of the concrete matrix more-or-less coincided with the bond strength of the fibers . Two areas of future research are indicated here. The first should address the relationship between volume of fiber reinforcing and direct tensile strength while the other should examine the strength and distribution of fiber-matrix bonding. The latter is an area in which only a few studies have been conducted and more are clearly needed.

3. The overall strength behavior of the SFRC under biaxial tension-compression loading suggests a strong depenuence on the compressive stress level relative to the uniaxial compressive strength. It has been suggested that the sharp inflection in the tension-compression failure envelope coincides with a loss of reinforcement due to the initiation of cracking at the fiber-matrix interface. It is further hypothesized that the tensile strength of the SFRC is no different than that of the plain concrete matrix at

stress levels above 50 percent of the compressive strength. An insufficient number of plain concrete specimens were available to investigate this so this is an area which should be studied more closely. A test program involving tension-compression testing of both plain concrete specimens and specimens with varying amounts of reinforcing would contribute greatly to understanding the relationship between microcracking and reinforcing ability. It is suggested that such an investigation should also include uniaxial compressive loading to certain levels followed by sectioning to reveal the extent and location of microcracking. Although this has been heavily pursued with regard to plain concrete, little has been done in this area using fiber reinforced concrete.

4. Because the tensile loading apparatus designed and fabricated for this research program provided a capability which was heretofore unavailable, and because of the many discoveries made during the tension-compression portion of the test program, only a few specimens were made available for biaxial compression tests. Unfortunately, the amount of scatter in the biaxial compression data, most notably the stresses at dilation, leaves some ambiguity as to the shape of the failure envelope in this quadrant. Further research in this area would also be helpful. A topic of special interest is the effects of fiber reinforcing on the biaxial and multiaxial compressive strengths. A test program employing plain concrete specimens as well as specimens reinforced with different types and amounts of fibers would be necessary to determine this.

5. In Chapter 6 two mathematical models were presented and calibrated in an attempt to both model and predict the strength behavior of the SFRC. Although each model was capable of reflecting some of the essential features of the strength behavior, neither could model both the biaxial and multiaxial responses simultaneously. While it is obvious that other models could be sought out and investigated for use in describing the strength behavior of the SFRC, another important question comes to mind. Since both formulations have been shown to adequately model the strength behavior of concrete in other investigations, is there some fundamental difference in the behavior of fiber reinforced concrete under multiaxial stress states which precludes the use of these models? For example, both the Willam-Warnke and Lade criteria utilize curved meridians in stress space since this has been a commonly observed response of concrete-type materials to multiaxial compression. The combined biaxial and multiaxial compression data from Phases I and II, however, indicate an almost perfectly linear relationship between τ_o and σ_o. This is another area which should be examind further. The tensile loading apparatus and fluid cushion cubical cell would be ideal for this research because they would allow similar stress paths to be followed in deviatoric planes closer to the origin than those employed in Phase I. In the TE tests in both the 4 ksi and 6 ksi deviatoric planes, for example, the σ_1 axis had to be unloaded nearly to zero in order to achieve failure. At lower levels of octahedral stress, failure would be unattainable without the capability of applying tensile stresses.

It is at these octahedral stress levels, however, that more data is needed in order to better define the shape of the three-dimensional failure surface and to determine how and where these nearly linear meridians intersect the hydrostatic stress axis. Only after a better description of the failure surface is obtained can a model be sought out which duplicates the strength features of the SFRC and be used to reliably predict the response of the SFRC under other stress conditions.

BIBLIOGRAPHY

Abeles, P.W., Discussion on "Mechanics of Crack Arrest in Concrete," by J.P. Romualdi and G.B. Batson, Journal of the Engineering Mechanics Division, ASCE, V. 90, No. EM1, pp. 170-172 (1964).

ACI Committee 544, "State-of-the-Art Report on Fiber Reinforced Concrete," Concrete International, V. 4, No. 5, pp. 9-30 (1982).

Arredi, F., Discussion on "Correlation Between Tensile Splitting Strength and Flexural Strength of Concrete," by I. Narrow and E. Ullberg, ACI Journal, Proceedings, V. 60, No. 9, pp. 1263-1264 (1963).

Bache, H.H. and P. Nepper-Christensen, "Observations on Strength and Fracture in Lightweight and Ordinary Concrete," The Structure of Concrete and Its Behavior under Load, Proc. of an Int. Conf., Cement and Concrete Assoc., London, pp. 93-108 (1965).

Bertacchi, P. and Belloti, R., "Experimental Research on Deformation and Failure of Concrete under Triaxial Loads," Proceedings, RILEM Symposium on the Deformation and Rupture of Solids Subject to Multiaxial Stresses, V. 1, p. 37 (1972).

Broms, B.B. and S.P. Shah, Discussion on "Mechanics of Crack Arrest in Concrete," by J.P. Romualdi and G.B. Batson, Journal of the Engineering Mechanics Division, ASCE, V. 90, No. EM1, pp. 167-170 (1964).

Buckley, E.L. and N.J. Everard, "Prediction of the Modulus of Rupture of Fiber Reinforced Portland Cement Mortar and Concrete," Fiber Reinforced Concrete, Publication SP-44, American Concrete Institute, Detroit, pp. 163-176 (1974).

Chang, W.F. and R.H. Wright, Discussion on "Correlation Between Tensile Splitting Strength and Flexural Strength of Concrete," by I. Narrow and E. Ullberg, ACI Journal, Proceedings, V. 60, No. 9, pp. 1264-1266 (1963).

Chen, W-F, "Double Punch Test for Tensile Strength of Concrete," ACI Journal, Proceedings V. 67, No. 12, pp. 993-995 (1970).

Chen, W.F. and J.L. Carson, "Stress-Strain Properties of Random Wire Reinforced Concrete," ACI Journal, Proceedings, V. 68, No. 12, pp. 933-936 (1971).

Chen, W-F and R.L. Yuan, "Tensile Strength of Concrete: Double Punch Test," Journal of the Structural Division, ASCE, V. 106, No. ST8, pp. 1673-1693 (1980).

Craig, R.J., J. Decker, L. Dombrowski, R. Laurencelle, and J. Federovich, "The Inelastic Behavior of Reinforced Fibrous Concrete Members," Paper presented at the Joint ASME/ASCE Mechanics Conference, Boulder, Colorado (1981).

Craig, R.J. and R. Radici, "Steel Fibrous Reinforced Concrete Mechanical Properties," Paper presented at the Joint ASME/ASCE Mechanics Conference, Boulder, Colorado (1981).

Desayi, P. and C.S. Viswanatha, "True Ultimate Strength of Plain Concrete," RILEM Bulletin No. 36, pp. 163-173 (1967).

deVekey, R.C. and A.J. Majumdar, "Determining Bond Strength in Fiber-Reinforced Composites," Mag. Conc. Res., V. 20, No. 65, pp. 229-234 (1968).

Egging, D., "Constitutive Relations of Randomly Oriented Steel Fiber Reinforced Concrete under Multiaxial Compressive Loading," M.S. Thesis, University of Colorado, Boulder, Colorado (1981).

Endebrock, E.G. and L.A. Traina, "Static Concrete Constitutive Relations Based on Cubical Specimens," A.F.W.L. Technical Report No. AFWL-TR-72-59, Volumes I and II, Kirtland A.F.B., New Mexico (1972).

Fairhurst, C., "On the Validity of the 'Brazilian' Test for Brittle Materials," Int. Jour. Rock Mech. Mining Sci., V. 1, pp. 535-546 (1964).

Gerstle, K., D. Linse, P. Bertacchi, M. Kotosovos, H-Y Ko, J.B. Newman, P. Rossi, G. Schickert, M. Taylor, L. Traina, R. Zimmerman, and R. Bellotti, "Strength of Concrete under Multiaxial Stress States," Proceedings, Douglas McHenry International Symposium on Concrete and Concrete Structures, SP-55, American Concrete Institute, Detroit, pp. 103-132 (1978).

Glucklich, J., "Fracture of Plain Concrete," ASCE, Proceedings, V. 89, No. EM6, pp. 127-138 (1963).

Glucklich, J., "The Effect of Microcracking on the Time-Dependent Deforamtions and the Long-Term Strength of Concrete," The Structure of Concrete, Cement and Concrete Assoc., London, pp. 176-189 (1968).

Halvorsen, G.T. and C.E. Kesler, "Moment-Curvature Relationships for Concrete Beams with Plain and Deformed Steel Fibers," ACI Journal, Proceedings, V. 76, No. 6, pp. 697-706 (1979).

Heuze, F.E., "Scale Effects in the Determination of Rock Mass Strength and Deformability," Rock Mechanics, V. 12, pp. 167-192 (1980).

Hondros, G., "The Evaluation of Poisson's Ratio and the Modulus of Materials of a Low Tensile Resistance by the Brazilian (Indirect Tension) Test with Particular Reference to Concrete," Aust. J. Appl. Sci., V. 10, No. 3, pp. 243-268 (1959).

Hsu, T.T.C., "Mathematical Analysis of Shrinkage Stresses in a Model of Hardened Concrete," ACI Journal, V. 60, No. 3, pp. 371-389 (1963).

Hsu, T.T.C., F.O. Slate, G.M. Sturman, and G. Winter, "Microcracking of Plain Concrete and the Shape of the Stress-Strain Curve," ACI Journal, V. 60, No. 2, pp. 209-223 (1963).

Iyengar, K.T., Sundara Raja, K. Chandrasekhara, and K.T. Krishnaswamy, Discussion on "Correlation Between Tensile Splitting Strength and Flexural Strength of Concrete," by I. Narrow and E. Ullberg, ACI Journal, Proceedings, V. 60, No. 9, pp. 1274-1275 (1963).

Johnston, C.D. and R.A. Coleman, "Properties of Fiber Reinforced Mortar in Uniaxial Tension," Fiber Reinforced Concrete, Publication SP-44, American Concrete Institute, Detroit, pp. 177-194 (1974).

Jones, R., "A Method of Studying the Formation of Cracks in a Material Subject to Stress," British Journal of Applied Physics, V. 3, No. 7, pp. 229-233 (1952).

Jones, R., "The Development of Microcracks in Concrete," RILEM Bulletin No. 9, pp. 110-114 (1960).

Ko, H-Y and S. Sture, "Three-Dimensional Mechanical Characteristics of Anisotropic Composites," Journal of Composite Materials, V. 8, p. 178 (1974).

Komlos, K., "Strength and Deformation Properties of Concrete Reinforced with Randomly Spaced Steel and Basalt Fibers," Proceedings, RILEM Symposium on Fiber Reinforced Cement and Concrete, Construction Press, Lancaster, pp. 237-246 (1975).

Kormeling, H.A., H.W. Reinhardt, and S.P. Shah, "Static and Fatigue Properties of Concrete Beams Reinforced with Continuous Bars and with Fibers," ACI Journal, Proceedings, V. 77, No. 1, pp. 36-43 (1980).

Krenchel, H., "Fiber Reinforced Brittle Matrix Materials," Fiber Reinforced Concrete, Publication SP-44, American Concrete Institute, Detroit, pp. 45-78 (1974).

Krishnaswamy, K.T., "Microcracking of Plain Concrete under Simple Compression," Paper presented at a colloquium at Cornell Univ. (1965).

Kupfer, H., H. Hilsdorf, and H. Rusch, "Behavior of Concrete Under Biaxial Stresses," ACI Journal, V. 66, No. 9, pp. 656-666 (1969).

Kupfer, H., "Das Verhalten des Betons unter Mehrachsiger Kurzzeitbeanspruchung unter Besonderer Beruecksichtigung der Zweiachsigen Beanspruchung," Deutscher Ausschuss fuer Stahlbeton, Heft No. 229 (1973).

Lade, P.V., "Three-Parameter Failure Criterion for Concrete," Paper presented at the Joint ASME/ASCE Mechanics Conference, Boulder, Colorado, June 22-24, 1981.

L'Hermite, R., "Present Day Ideas on Concrete Technology, Part 3: The Failure of Concrete," RILEM Bulletin No. 18, pp. 27-39 (1954).

Lingham, A.B., Discussion on "Correlation Between Tensile Splitting Strength and Flexural Strength of Concrete," by I. Narrow and E. Ullberg, ACI Journal, Proceedings, V. 60, No. 9, pp. 1266-1268 (1963).

Linse, D., "Versuchanlage zur Ermittlung der Dreiachsigen Festigkeit vom Beton Mit Ersten Versuchsergebnissen," Cement and Concrete Research V. 3, No. 4 (1973).

McHenry, D. and J. Karni, "Strength of Concrete under Combined Tensile and Compressive Stress," ACI Journal, V. 54, No. 4, pp. 829-839 (1958).

Naaman, A.E. and S.P. Shah, "Bond Studies on Oriented and Aligned Steel Fibers," Proceedings, RILEM Symposium on Fiber Reinforced Cement and Concrete, pp. 171-178 (1975).

Narrow, I. and E. Ullberg, "Correlation Between Tensile Splitting Strength and Flexural Strength of Concrete," ACI Journal, Proceedings, V. 60, No. 1, pp. 27-38 (1963).

Newman, J.B., "Apparatus for Testing Concrete under Multiaxial States of Stress," Magazine of Concrete Research, V. 26, No. 89, p. 229 (1974).

Newman, K., "The Structure and Engineering Properties of Concrete," Theory of Arch Dams, Proceedings of an International Symposium, Pergamon Press, London, pp. 683-712 (1965).

Newman, K., "Concrete Control Tests as Measures of the Properties of Concrete," Proceedings of a Symposium on Concrete Quality, Cement and Concrete Assoc., London, pp. 120-138 (1966).

Oladapo, I.O., "Cracking and Failure in Plain Concrete Beams," Magazine of Concrete Research, V. 16, No. 47, pp. 103-110 (1964).

Parameswaran, V.S. and K. Rajagopalan, "Strength of Concrete Beams with Aligned or Random Steel Micro-Reinforcement," Proceedings, RILEM Symposium on Fiber Reinforced Cement and Concrete, Construction Press, Lancaster, pp. 95-104 (1975).

Parmi, S.R. and J.K.S. Rao, "On the Fracture Toughness of Fiber Reinforced Concrete," Fiber Reinforced Concrete, Publication SP-44, American Concrete Institute, Detroit, pp. 79-92 (1974).

Pratt, H.R., A.D. Black, W.S. Brown, and W.T. Brace, "The Effect of Specimen Size on the Mechanical Properties of Unjointed Diorite," Int. Jour. Rock Mech. Mining Sci., V. 9, pp. 513-529 (1972).

Rajagopalan, K., V.S. Parameswaran, and G.S. Ramaswamy, "Strength of Steel Fiber Reinforced Concrete Beams," Indian Concrete Journal V. 48, No. 1, pp. 17-24 (1974).

Ramakrishnan, V., Y. Ananthanarayana, and K.C. Gopal, "The Determination of the Tensile Strength of Concrete: A Comparison of Different Methods," Indian Concrete Journal, Vol. 41, No. 5, pp. 202-206 (1967).

Ramakrishnan, V., T. Brandshaug, W.V. Coyle, and E.K. Schrader, "A Comparative Evaluation of Concrete Reinforced with Straight Steel Fibers and Fiber with Deformed Ends Glued Together into Bundles," ACI Journal, Proceedings, V. 77, No. 3, pp. 135-143 (1980).

Ramakrishnan, V., W.V. Coyle, V. Kulandaisamy, and E.K. Schrader, "Performance Characteristics of Fiber Reinforced Concretes with Low Fiber Contents," ACI Journal, Proceedings V. 78, No. 5, pp. 388-394 (1981).

Robinson, G.S., "Methods of Detecting the Formation and Propagation of Microcracks in Concrete," The Structure of Concrete and Its Behavior under Load, Proc. of an Int. Conf., Cement and Concrete Assoc., London, pp. 131-145 (1965).

Robinson, K.D., "The Bond Strength of Galvanized Reinforcement," Technical Report TRA/220, Cement and Concrete Association, London (1956).

Romualdi, J.P. and G.B. Batson, "Mechanics of Crack Arrest in Concrete," Journal of the Engineering Mechanics Division, ASCE, V. 89, No. EM3, pp. 147-167 (1963).

Romualdi, J.P. and J.A. Mandel, "Tensile Strength of Concrete Affected by Uniformly Distributed and Closely Spaced Short Lengths of Wire Reinforcement," ACI Journal, Proceedings, V. 61, No. 6, pp. 657-672 (1964).

Rusch, H., "Physikalische Fragen der Betonprufung," Zement-Kalk-Gips, V. 12, No. 1, pp. 1-9 (1959).

Rusch, H., "Researches Towards a General Flexural Theory for Structural Concrete," ACI Journal, Vol. 57, pp. 1-28 (1960).

Schickert, G., "On the Influence of Different Load Application Techniques on the Lateral Strain and Fracture of Concrete Specimens," Cement and Concrete Research, V. 3, p. 487 (1973)

Schnutgen, B., "Some Results of Investigations on Steel Fiber Reinforced Concrete," Proceedings, RILEM Symposium on Fiber Reinforced Cement and Concrete, Construction Press, Lancaster, pp. 105-117 (1975).

Shah, S.P., "Critical Stress, Volume Change, and Microcracking of Concrete," ACI Journal, V. 65, No. 9, pp. 770-781 (1968).

Shah, S.P., "Micromechanics of Concrete and Fiber Reinforced Concrete," Structure, Solid Mechanics, and Engineering Design, Wiley and Sons, New York, pp. 367-376 (1969).

Shah, S.P. and A.E. Naaman, "Mechanical Properties of Glass and Steel Fiber Reinforced Mortar," ACI Journal, Proceedings, V. 73, No. 1, pp. 50-54 (1976).

Shah, S.P. and B.V. Rangan, Fiber Reinforced Concrete Properties," ACI Journal, Proceedings, V. 68, No. 2, pp. 126-134 (1971).

Slate, F.O. and S. Olsefski, "X-rays for Study of Internal Structure and Microcracking of Concrete," ACI Journal, V. 60, No. 5, pp. 575-587 (1963).

Snyder, M.J. and D.R. Lankard, "Factors Affecting the Flexural Strength of Steel Fibrous Concrete," ACI Journal, Proceedings, V. 69, No. 2, pp. 96-100 (1972).

Sture, S., "An Improved Multiaxial Cubical Cell and Its Application to the Testing of Anisotropic Materials," M.S. Thesis, University of Colorado, Boulder, Colorado (1973).

Sturman, G.M., S.P. Shah, and G. Winter, "Microcracking and Inelastic Behavior of Concrete," Proceedings, ASCE-ACI Int. Symposium on Flexural Mechanics of Reinforced Concrete, pp. 473-499 (1964).

Swamy, R.N. and K.A. Al-Noori, "Flexural Behavior of Fiber Concrete with Conventional Steel Reinforcement," Proceedings, RILEM Symposium on Fiber Reinforced Cement and Concrete, Construction Press, Lancaster, pp. 187-196 (1975).

Swamy, R.N. and S.A. Al-Ta'an, "Deformation and Ultimate Strength in Flexure of Reinforced Concrete Beams Made with Steel Fiber Concrete," ACI Journal, Proceedings, V. 78, No. 5, pp. 395-405 (1981).

Swamy, R.N. and H. Stavrides, "Some Properties of High Workability Steel Fiber Concrete," Proceedings, RILEM Symposium on Fiber Reinforced Cement and Concrete, Construction Press, Lancaster, pp. 197-208 (1975).

Tasuji, M.E., F.O. Slate, and A.H. Nilson, "Stress-Strain Response and Fracture of Concrete in Biaxial Loading," ACI Journal, V. 75, No. 7, pp. 306-312 (1978).

Taylor, M.A., M.K. Tai, and M.R. Ramey, "Biaxial Compressive Behavior of Fiber-Reinforced Mortar," ACI Journal, Proceedings, V. 72, No. 9 (1975).

Timoshenko, S., Theory of Elasticity, 3rd Edition, McGraw-Hill, New York, pp. 122-124 (1970).

Vile, G.W.D., "Combined Stress Testing Machine for Concrete," The Engineer, London, July 9, 1965.

Vile, G.W.D., "The Strength of Concrete under Short-Term Static Biaxial Stress," The Structure of Concrete and its Behavior Under Load, Proc. of an Int. Conf., Cement and Concrete Assoc., London, pp. 275-288 (1965).

Walkus, B.R., A. Januszkiewicz, and J. Jeruzal, "Concrete Composites with Cut Steel Fiber Reinforcement Subjected to Uniaxial Tension," ACI Journal, Proceedings, V. 76, No. 10, pp. 1079-1092 (1979).

Welch, G.B., "Factors Influencing the Tensile Strains and Flexural Failure of Plain Concrete," The Structure of Concrete and Its Behavior Under Load, Cement and Concrete Assoc., London, pp. 525-533 (1965).

Welch, G.B., "Tensile Splitting Test on Concrete Cubes and Beams," Civil Engineering (London), V. 60, No. 709, pp. 1161-1168 (1965).

Willam, K.J. and E.P. Warnke, "Constitutive Model for the Triaxial Behavior of Concrete," Concrete Structures Subjected to Triaxial Stresses, Proceedings of an IABSE Seminar, ISMES, Bergamo (1974).

Winkler, H., "Pruefanlage fuer Dreiaxiale Festigkeitsuntersuchungen an Betonprobekoerpern," Materialpruefung, V. 18, No. 4, p. 127 (1976).

Wright, P.J.F., "Comments on an Indirect Tensile Test on Concrete Cylinders," Magazine of Concrete Research, V. 7, No. 20, pp. 87-96 (1955).

Zollo, R.F., "Fibrous Concrete Flexural Testing - Developing Standardized Techniques," ACI Journal, Proceedings,V. 77, No. 5, pp. 363-368 (1980).

APPENDIX

APPENDIX

This Appendix contains the computer-generated stress-strain plots (Figs. A.1 through A.55) and tabulated stress-strain data (Tables A.1 through A.54) for each individual test and for the average response in each test category. As an aid to locating a specific figure or table, they are arranged by test category beginning with the uniaxial tension tests and proceeding counterclockwise around the biaxial plane to the equi-biaxial compression tests. (see Fig. 4.17).

The stress-strain data are plotted as ε_x, ε_y, and ε_z vs. $(\sigma_1 - \sigma_3)$ where the subscripts x, y, z correspond to the three axes of the cubical cell. Throughout the test program, the z-axis was the non-loaded axis. The x-axis was the σ_3 (tensile) axis in uniaxial tension and biaxial tension-compression tests and the σ_1 (maximum compression) axis in uniaxial compression and biaxial compression tests. For clarity, only the tensile loading portions of the biaxial tension-compression tests are plotted (with the stress-strain curves corrected to a common origin). The tabulated data include both the tensile and compressive portions of these tests.

As was mentioned in Chapter 4, most of the stress-strain data had to be corrected for the random variations in the initial apparatus response which could not be accounted for in the apparatus

calibrations. Referring to Fig. A.0, which shows a typical plot of measured strains vs. tensile stress (this could be a uniaxial tension test or the tensile loading portion of a biaxial tension-compression test), the correction was done by performing a linear regression analysis on that portion of each stress strain curve which exhibited the most-nearly linear response and correcting the strains by an amount equal to the strain-axis intercept of the best-fit line. The corrected stress-strain curves (also shown in Fig. A.0) are shown as dashed lines in the region where data was eliminated (that is, the region where random apparatus response obscured the stress-strain response of the concrete). This correction procedure was implemented in a computer program which would systematically eliminate data points from the regression analysis and select the best-fit line for which the highest regression coefficient was obtained as the basis for correcting the data. Although the example illustrated in Fig. A.0 pertains to a tensile test, this same procedure was used to correct compression data as well.

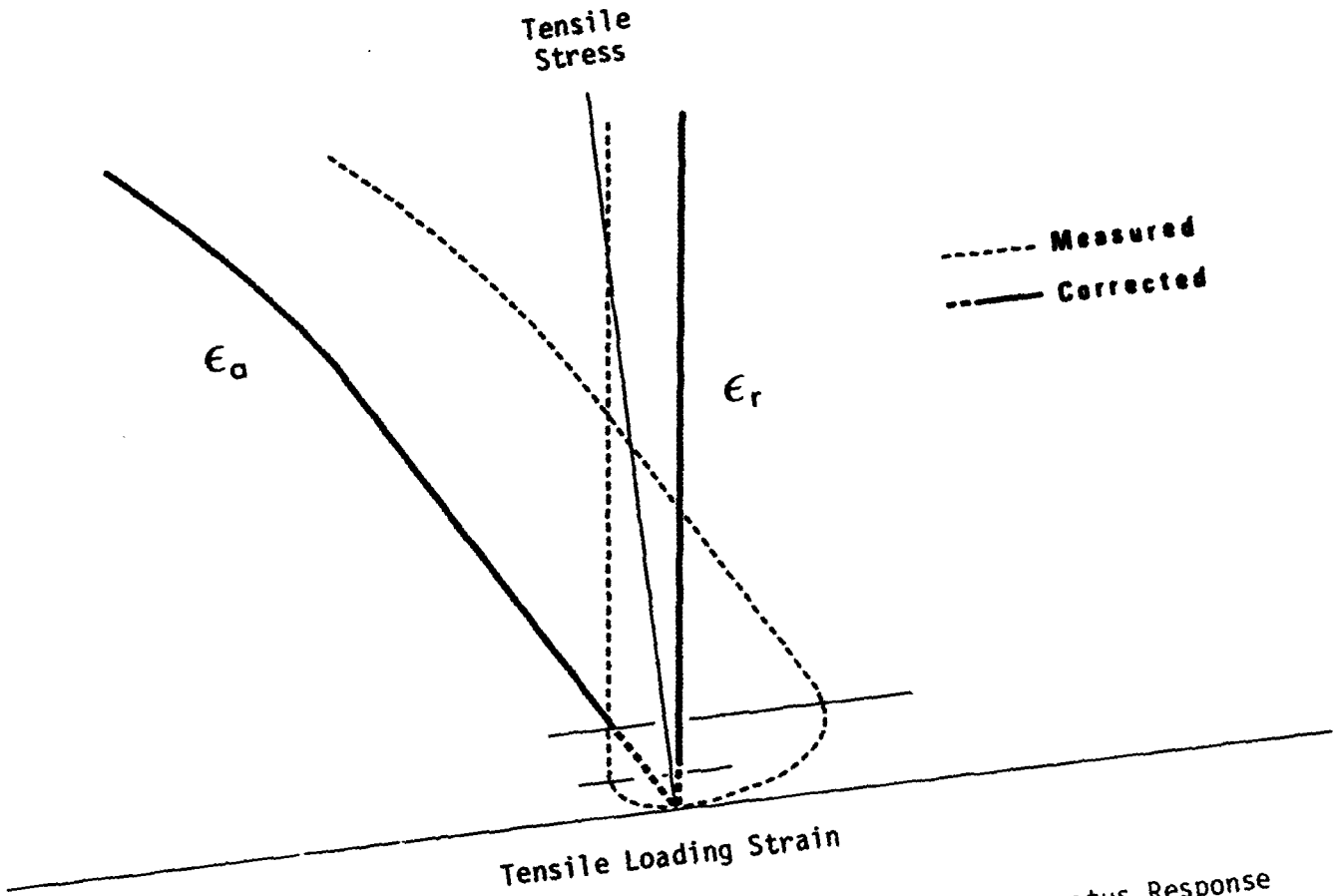

Fig. A.0 Data Correction for Random Variations in Initial Apparatus Response

Table A.1

TEST 1 ... UNIAXIAL TENSION FIBERED CONCRETE AVERAGE

STRESS - STRAIN DATA

	X-AXIS STRESS (PSI)	X-AXIS STRAIN (MILS/IN)	Y-AXIS STRESS (PSI)	Y-AXIS STRAIN (MILS/IN)	Z-AXIS STRESS (PSI)	Z-AXIS STRAIN (MILS/IN)
1	0	0.0000	0	0.0000	0	0.0000
2	10	-0.0035	0	0.0005	0	0.0005
3	20	-0.0071	0	0.0011	0	0.0011
4	30	-0.0106	0	0.0016	0	0.0016
5	45	-0.0159	0	0.0024	0	0.0024
6	60	-0.0212	0	0.0033	0	0.0033
7	75	-0.0265	0	0.0041	0	0.0041
8	90	-0.0320	0	0.0049	0	0.0049
9	105	-0.0374	0	0.0057	0	0.0057
10	120	-0.0419	0	0.0065	0	0.0065
11	135	-0.0473	0	0.0076	0	0.0076
12	150	-0.0529	0	0.0087	0	0.0087
13	165	-0.0587	0	0.0101	0	0.0101
14	180	-0.0643	0	0.0118	0	0.0118
15	195	-0.0694	0	0.0116	0	0.0116
16	210	-0.0739	0	0.0105	0	0.0105
17	225	-0.0793	0	0.0115	0	0.0115
18	240	-0.0841	0	0.0116	0	0.0116
19	255	-0.0918	0	0.0132	0	0.0132
20	270	-0.0986	0	0.0129	0	0.0129
21	285	-0.1033	0	0.0149	0	0.0149
22	300	-0.1101	0	0.0170	0	0.0170
23	315	-0.1178	0	0.0162	0	0.0162
24	330	-0.1241	0	0.0161	0	0.0161
25	345	-0.1305	0	0.0182	0	0.0182
26	360	-0.1373	0	0.0199	0	0.0199
27	375	-0.1436	0	0.0185	0	0.0185
28	390	-0.1517	0	0.0218	0	0.0218
29	405	-0.1597	0	0.0216	0	0.0216
30	420	-0.1664	0	0.0251	0	0.0251
31	435	-0.1734	0	0.0246	0	0.0246
32	450	-0.1843	0	0.0255	0	0.0255
33	465	-0.1965	0	0.0248	0	0.0248

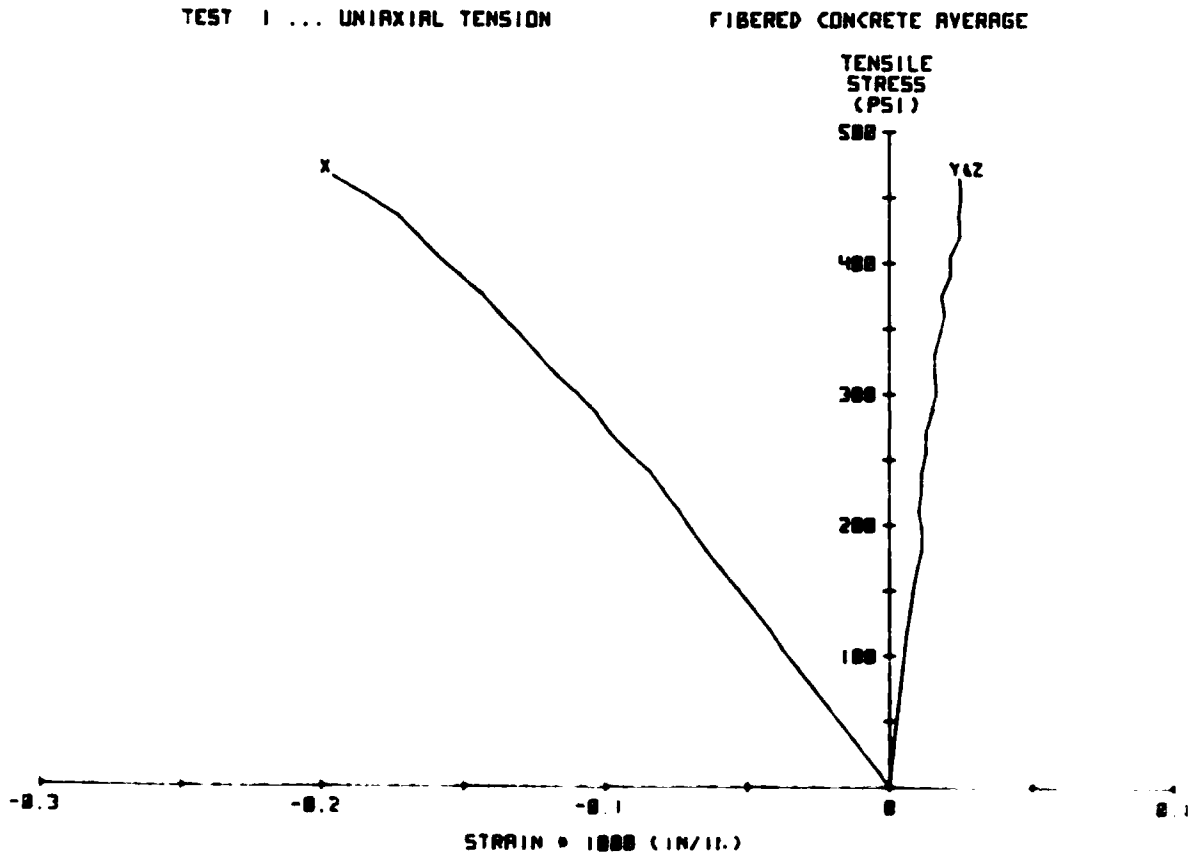

Fig. A.1 Test Results

Table A.2

TEST 1A ... UNIAX TEN SPEC 4.H6 1/12/82

STRESS - STRAIN DATA

	X-AXIS STRESS (PSI)	X-AXIS STRAIN (MILS/IN)	Y-AXIS STRESS (PSI)	Y-AXIS STRAIN (MILS/IN)	Z-AXIS STRESS (PSI)	Z-AXIS STRAIN (MILS/IN)
1	0	0.0000	0	0.0000	0	0.0000
2	10	-0.0038	0	0.0006	0	0.0005
3	20	-0.0075	0	0.0013	0	0.0009
4	30	-0.0113	0	0.0019	0	0.0014
5	45	-0.0169	0	0.0029	0	0.0021
6	60	-0.0226	0	0.0039	0	0.0028
7	75	-0.0282	0	0.0048	0	0.0035
8	90	-0.0339	0	0.0058	0	0.0041
9	105	-0.0395	0	0.0068	0	0.0048
10	120	-0.0452	0	0.0077	0	0.0055
11	135	-0.0520	0	0.0087	0	0.0080
12	150	-0.0574	0	0.0116	0	0.0088
13	165	-0.0644	0	0.0140	0	0.0105
14	180	-0.0712	0	0.0166	0	0.0123
15	195	-0.0767	0	0.0152	0	0.0123
16	210	-0.0799	0	0.0105	0	0.0114
17	225	-0.0803	0	0.0113	0	0.0133
18	240	-0.0861	0	0.0116	0	0.0116
19	255	-0.0945	0	0.0171	0	0.0078
20	270	-0.1015	0	0.0149	0	0.0075
21	285	-0.1044	0	0.0213	0	0.0085
22	300	-0.1097	0	0.0186	0	0.0116
23	315	-0.1196	0	0.0143	0	0.0095
24	330	-0.1256	0	0.0153	0	0.0079
25	345	-0.1268	0	0.0191	0	0.0116
26	360	-0.1334	0	0.0261	0	0.0144
27	375	-0.1386	0	0.0250	0	0.0143
28	390	-0.1490	0	0.0276	0	0.0192
29	405	-0.1534	0	0.0266	0	0.0203
30	420	-0.1604	0	0.0271	0	0.0271
31	435	-0.1647	0	0.0301	0	0.0229
32	450	-0.1724	0	0.0316	0	0.0251
33	465	-0.1765	0	0.0312	0	0.0211
34	480	-0.1798	0	0.0283	0	0.0197
35	495	-0.1901	0	0.0309	0	0.0232
36	510	-0.2057	0	0.0357	0	0.0276

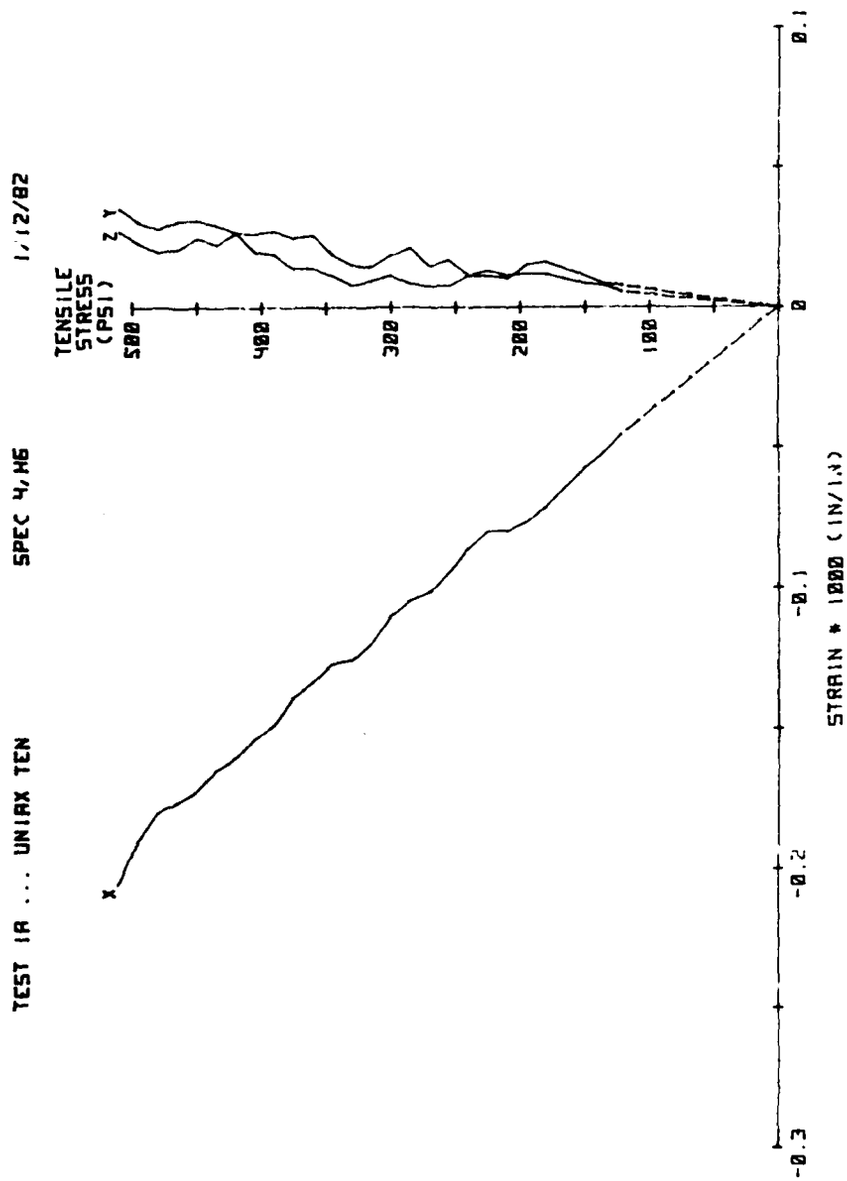

Fig. A.2 Test Results

Table A.3

TEST ID ... UNIAX TEN SPEC 4,E5 3/8/82

STRESS - STRAIN DATA

	X-AXIS STRESS (PSI)	X-AXIS STRAIN (MILS/IN)	Y-AXIS STRESS (PSI)	Y-AXIS STRAIN (MILS/IN)	Z-AXIS STRESS (PSI)	Z-AXIS STRAIN (MILS/IN)
1	0	0.0000	0		0	0.0000
2	-10	-0.0038	0		0	0.0004
3	-20	-0.0077	0		0	0.0009
4	-30	-0.0115	0		0	0.0013
5	-45	-0.0173	0		0	0.0020
6	-60	-0.0230	0		0	0.0026
7	-75	-0.0288	0		0	0.0033
8	-90	-0.0381	0		0	0.0040
9	-105	-0.0414	0		0	0.0046
10	-120	-0.0453	0		0	0.0053
11	-135	-0.0504	0		0	0.0059
12	-150	-0.0589	0		0	0.0059
13	-165	-0.0621	0		0	0.0050
14	-180	-0.0709	0		0	0.0075
15	-195	-0.0741	0		0	0.0094
16	-210	-0.0807	0		0	0.0088
17	-225	-0.0898	0		0	0.0094
18	-240	-0.0938	0		0	0.0071
19	-255	-0.1015	0		0	0.0114
20	-270	-0.1092	0		0	0.0089
21	-285	-0.1132	0		0	0.0131
22	-300	-0.1203	0		0	0.0182
23	-315	-0.1279	0		0	0.0164
24	-330	-0.1338	0		0	0.0199
25	-345	-0.1439	0		0	0.0182
26	-360	-0.1526	0		0	0.0195
27	-375	-0.1583	0		0	0.0116
28	-390	-0.1655	0		0	0.0167
29	-405	-0.1779	0		0	0.0165
30	-420	-0.1829	0		0	0.0202
31	-435	-0.1895	0		0	0.0176
32	-450	-0.2032	0		0	0.0176
33	-465	-0.2089	0		0	0.0180

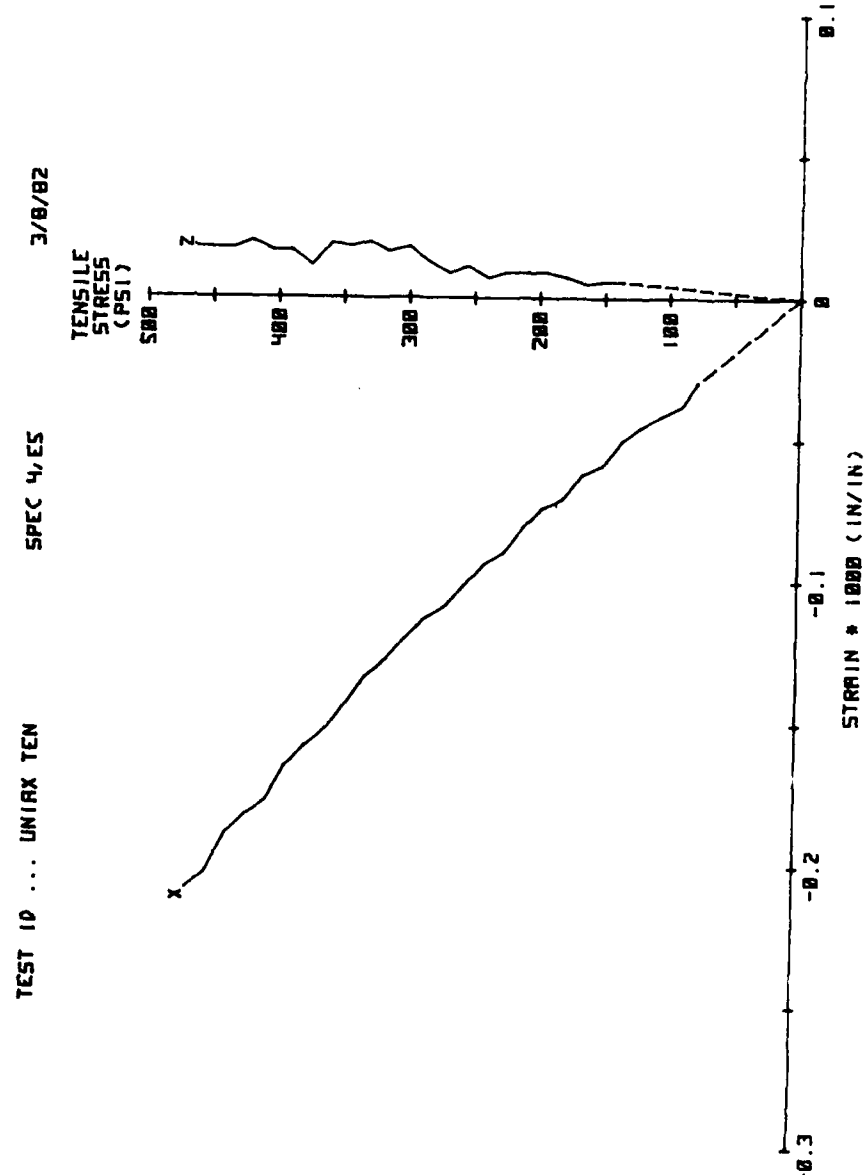

Fig. A.3 Test Results

Table A.4

TEST 1E ... UNIAX TEN SPEC 5,E1 3/10/82

STRESS - STRAIN DATA

	X-AXIS STRESS (PSI)	X-AXIS STRAIN (MILS/IN)	Y-AXIS STRESS (PSI)	Y-AXIS STRAIN (MILS/IN)	Z-AXIS STRESS (PSI)	Z-AXIS STRAIN (MILS/IN)
1	0	0.0000	0	0.0000	0	
2	-10	-0.0034	0	0.0008	0	
3	-20	-0.0068	0	0.0016	0	
4	-30	-0.0101	0	0.0024	0	
5	-45	-0.0152	0	0.0036	0	
6	-60	-0.0203	0	0.0048	0	
7	-75	-0.0254	0	0.0060	0	
8	-90	-0.0304	0	0.0072	0	
9	-105	-0.0359	0	0.0083	0	
10	-120	-0.0411	0	0.0095	0	
11	-135	-0.0464	0	0.0107	0	
12	-150	-0.0484	0	0.0120	0	
13	-165	-0.0571	0	0.0152	0	
14	-180	-0.0603	0	0.0153	0	
15	-195	-0.0651	0	0.0139	0	
16	-210	-0.0705	0	0.0147	0	
17	-225	-0.0757	0	0.0144	0	
18	-240	-0.0826	0	0.0195	0	
19	-255	-0.0929	0	0.0214	0	
20	-270	-0.1028	0	0.0227	0	
21	-285	-0.1093	0	0.0211	0	
22	-300	-0.1176	0	0.0251	0	
23	-315	-0.1248	0	0.0278	0	
24	-330	-0.1337	0	0.0258	0	
25	-345	-0.1405	0	0.0317	0	
26	-360	-0.1490	0	0.0271	0	
27	-375	-0.1569	0	0.0279	0	
28	-390	-0.1644	0	0.0312	0	
29	-405	-0.1742	0	0.0297	0	
30	-420	-0.1826	0	0.0329	0	
31	-430	-0.1891	0	0.0337	0	
32	-440	-0.1971	0	0.0365	0	
33	-450	-0.2077	0	0.0361	0	
34	-455	-0.2171	0	0.0340	0	

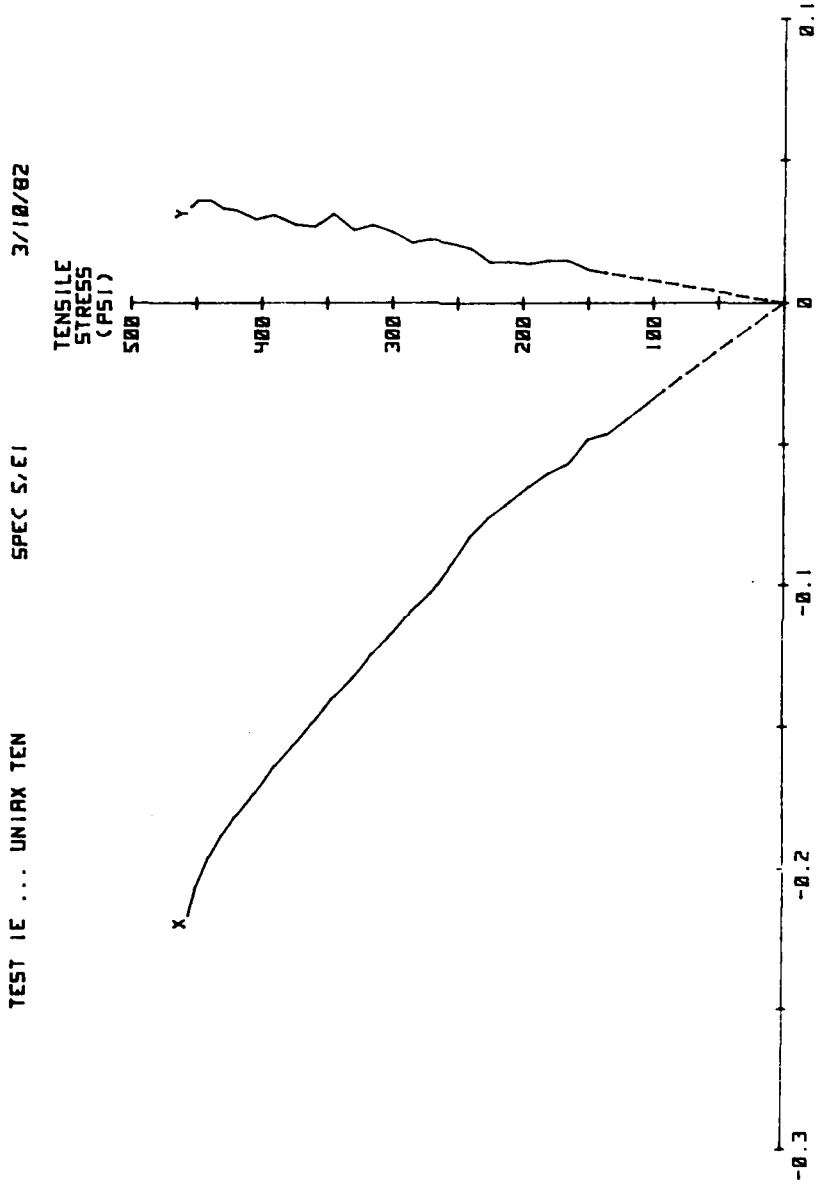

Fig. A.4 Test Results

Table A.5

TEST 1F ... UNIAX TEN SPEC 4,E3 3/14/82

STRESS - STRAIN DATA

	X-AXIS STRESS (PSI)	X-AXIS STRAIN (MILS/IN)	Y-AXIS STRESS (PSI)	Y-AXIS STRAIN (MILS/IN)	Z-AXIS STRESS (PSI)	Z-AXIS STRAIN (MILS/IN)
1	0	0.0000	0	0.0000	0	
2	-10	-0.0033	0	0.0004	0	
3	-20	-0.0065	0	0.0008	0	
4	-30	-0.0098	0	0.0012	0	
5	-45	-0.0146	0	0.0018	0	
6	-60	-0.0195	0	0.0024	0	
7	-75	-0.0244	0	0.0030	0	
8	-90	-0.0282	0	0.0036	0	
9	-105	-0.0354	0	0.0042	0	
10	-120	-0.0389	0	0.0048	0	
11	-135	-0.0431	0	0.0054	0	
12	-150	-0.0498	0	0.0060	0	
13	-165	-0.0541	0	0.0066	0	
14	-180	-0.0577	0	0.0085	0	
15	-195	-0.0645	0	0.0080	0	
16	-210	-0.0673	0	0.0079	0	
17	-225	-0.0726	0	0.0102	0	
18	-240	-0.0765	0	0.0090	0	
19	-255	-0.0811	0	0.0095	0	
20	-270	-0.0835	0	0.0113	0	
21	-285	-0.0891	0	0.0114	0	
22	-300	-0.0957	0	0.0126	0	
23	-315	-0.1016	0	0.0142	0	
24	-325	-0.1050	0	0.0143	0	
25	-335	-0.1069	0	0.0113	0	
26	-345	-0.1134	0	0.0114	0	
27	-355	-0.1149	0	0.0134	0	
28	-365	-0.1191	0	0.0112	0	
29	-375	-0.1235	0	0.0148	0	
30	-385	-0.1301	0	0.0162	0	
31	-395	-0.1312	0	0.0142	0	
32	-405	-0.1360	0	0.0157	0	
33	-415	-0.1408	0	0.0195	0	
34	-425	-0.1442	0	0.0187	0	
35	-435	-0.1491	0	0.0181	0	
36	-445	-0.1530	0	0.0180	0	
37	-455	-0.1607	0	0.0183	0	
38	-465	-0.1673	0	0.0189	0	

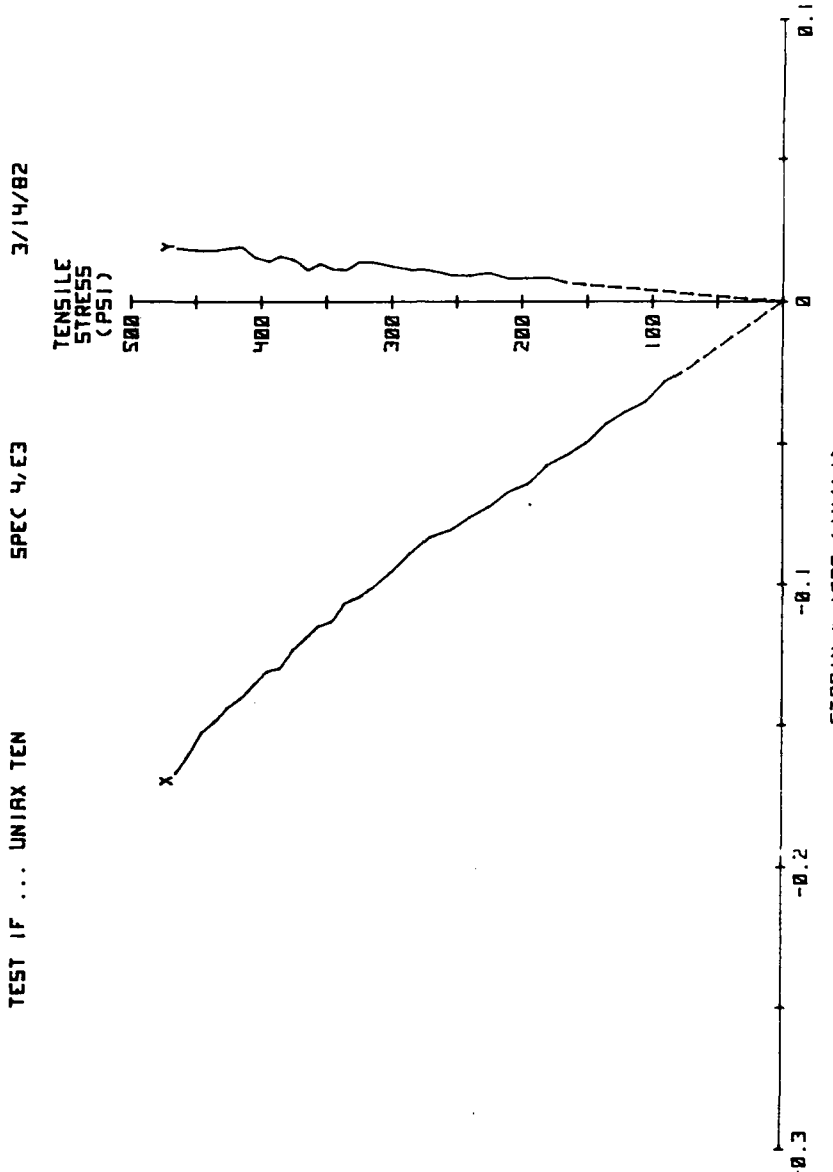

Fig. A.5 Test Results

Table A.6

TEST 1 ... UNIAXIAL TENSION PLAIN CONCRETE AVERAGE

STRESS - STRAIN DATA

	X-AXIS STRESS (PSI)	X-AXIS STRAIN (MILS/IN)	Y-AXIS STRESS (PSI)	Y-AXIS STRAIN (MILS/IN)	Z-AXIS STRESS (PSI)	Z-AXIS STRAIN (MILS/IN)
1	0	0.0000	0	0.0000	0	0.0000
2	10	-0.0041	0	0.0007	0	0.0007
3	20	-0.0083	0	0.0012	0	0.0012
4	30	-0.0126	0	0.0018	0	0.0018
5	45	-0.0190	0	0.0027	0	0.0027
6	60	-0.0254	0	0.0034	0	0.0034
7	75	-0.0318	0	0.0061	0	0.0061
8	90	-0.0382	0	0.0079	0	0.0079
9	105	-0.0446	0	0.0089	0	0.0089
10	120	-0.0528	0	0.0103	0	0.0103
11	135	-0.0582	0	0.0108	0	0.0108
12	150	-0.0633	0	0.0118	0	0.0118
13	165	-0.0698	0	0.0129	0	0.0129
14	180	-0.0757	0	0.0133	0	0.0133
15	195	-0.0829	0	0.0118	0	0.0118
16	210	-0.0891	0	0.0138	0	0.0138
17	225	-0.0955	0	0.0164	0	0.0164
18	240	-0.1039	0	0.0184	0	0.0184
19	255	-0.1104	0	0.0197	0	0.0197
20	270	-0.1161	0	0.0216	0	0.0216
21	285	-0.1228	0	0.0198	0	0.0198
22	300	-0.1303	0	0.0202	0	0.0202
23	315	-0.1358	0	0.0227	0	0.0227
24	330	-0.1443	0	0.0253	0	0.0253
25	345	-0.1521	0	0.0255	0	0.0255
26	360	-0.1601	0	0.0271	0	0.0271
27	375	-0.1691	0	0.0272	0	0.0272
28	390	-0.1781	0	0.0313	0	0.0313
29	405	-0.1895	0	0.0295	0	0.0295
30	420	-0.1968	0	0.0309	0	0.0309
31	425	-0.2058	0	0.0317	0	0.0317

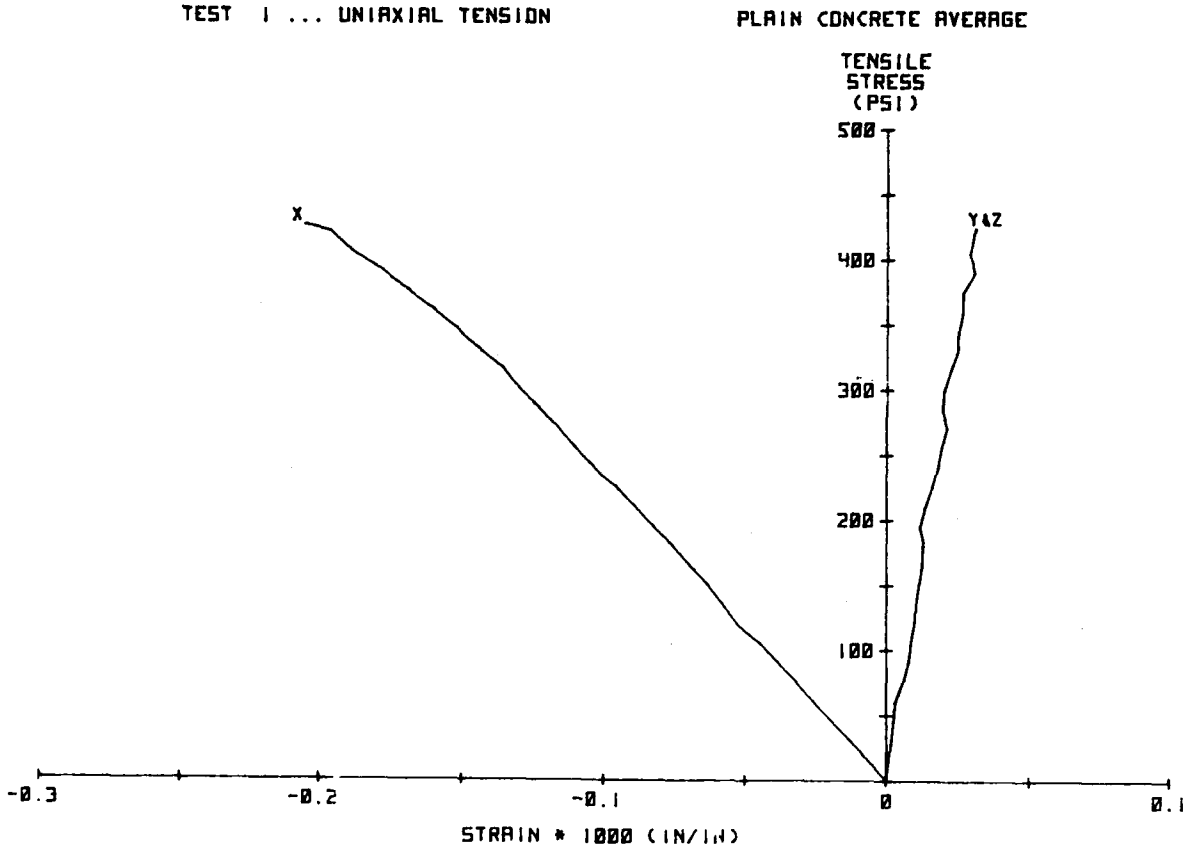

Fig. A.6 Test Results

Table A.7

TEST 1H ... UNIAX TEN SPEC 0.C3 7/3/82

STRESS - STRAIN DATA

	X-AXIS STRESS (PSI)	X-AXIS STRAIN (MILS/IN)	Y-AXIS STRESS (PSI)	Y-AXIS STRAIN (MILS/IN)	Z-AXIS STRESS (PSI)	Z-AXIS STRAIN (MILS/IN)
1	0	0.0000	0	0.0000	0	0.0000
2	10	-0.0046	0	0.0011	0	0.0018
3	20	-0.0091	0	0.0021	0	0.0036
4	30	-0.0137	0	0.0032	0	0.0053
5	45	-0.0205	0	0.0048	0	0.0080
6	60	-0.0274	0	0.0055	0	0.0069
7	75	-0.0342	0	0.0107	0	0.0125
8	90	-0.0411	0	0.0132	0	0.0170
9	105	-0.0479	0	0.0116	0	0.0221
10	120	-0.0573	0	0.0141	0	0.0253
11	135	-0.0617	0	0.0160	0	0.0251
12	150	-0.0680	0	0.0146	0	0.0302
13	165	-0.0756	0	0.0154	0	0.0336
14	180	-0.0819	0	0.0209	0	0.0296
15	195	-0.0899	0	0.0191	0	0.0290
16	210	-0.0955	0	0.0189	0	0.0341
17	225	-0.1020	0	0.0213	0	0.0378
18	240	-0.1090	0	0.0210	0	0.0421
19	255	-0.1195	0	0.0266	0	0.0448
20	270	-0.1257	0	0.0302	0	0.0488
21	285	-0.1334	0	0.0295	0	0.0495
22	300	-0.1423	0	0.0290	0	0.0495
23	315	-0.1477	0	0.0345	0	0.0565
24	330	-0.1565	0	0.0375	0	0.0590
25	345	-0.1648	0	0.0371	0	0.0607
26	360	-0.1743	0	0.0377	0	0.0665
27	375	-0.1834	0	0.0371	0	0.0661
28	390	-0.1933	0	0.0446	0	0.0739
29	405	-0.2074	0	0.0473	0	0.0712

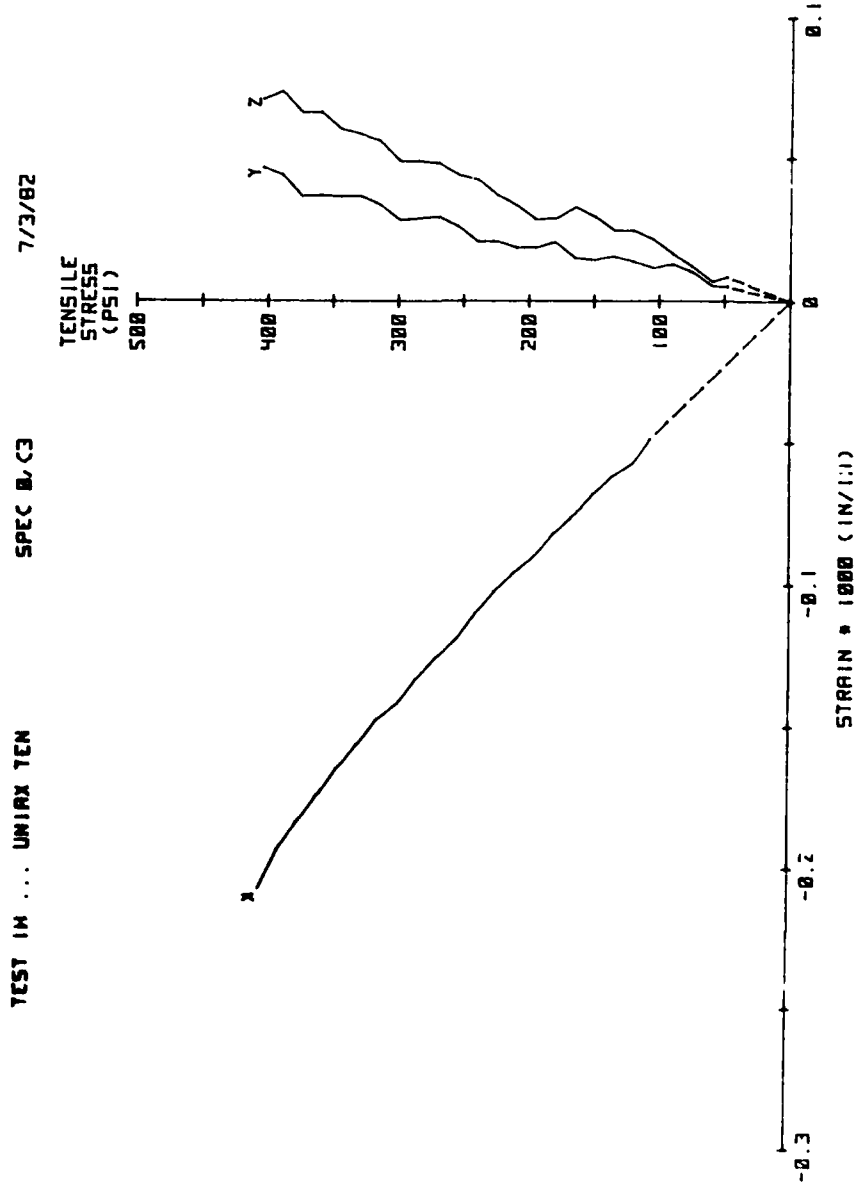

Fig. A.7 Test Results

Table A.8

TEST 1J ... UNIAX TEN SPEC 0.D3 6-25 83

STRESS - STRAIN DATA

	X-AXIS STRESS (PSI)	X-AXIS STRAIN (MILS/IN)	Y-AXIS STRESS (PSI)	Y-AXIS STRAIN (MILS/IN)	Z-AXIS STRESS (PSI)	Z-AXIS STRAIN (MILS/IN)
1	0	0.0000	0	0.0000	0	0.0000
2	20	-0.0079	0	0.0002	0	0.0000
3	30	-0.0119	0	0.0003	0	0.0001
4	45	-0.0179	0	0.0005	0	0.0001
5	60	-0.0238	0	0.0006	0	0.0001
6	75	-0.0298	0	0.0008	0	0.0001
7	90	-0.0358	0	0.0009	0	0.0002
8	105	-0.0417	0	0.0011	0	0.0002
9	120	-0.0488	0	0.0012	0	0.0002
10	135	-0.0552	0	0.0014	0	0.0002
11	150	-0.0589	0	0.0015	0	0.0003
12	165	-0.0645	0	0.0017	0	0.0003
13	180	-0.0699	0	-0.0007	0	0.0015
14	195	-0.0762	0	-0.0005	0	-0.0007
15	210	-0.0831	0	0.0016	0	-0.0001
16	225	-0.0894	0	0.0055	0	0.0004
17	240	-0.0984	0	0.0075	0	0.0015
18	255	-0.1018	0	0.0040	0	0.0027
19	270	-0.1069	0	0.0039	0	0.0031
20	285	-0.1127	0	0.0006	0	-0.0010
21	300	-0.1186	0	0.0037	0	-0.0020
22	315	-0.1243	0	-0.0000	0	-0.0006
23	330	-0.1325	0	0.0039	0	0.0004
24	345	-0.1398	0	0.0019	0	0.0019
25	360	-0.1464	0	0.0041	0	-0.0006
26	375	-0.1551	0	0.0039	0	0.0012
27	390	-0.1634	0	0.0062	0	0.0002
28	405	-0.1720	0	0.0012	0	-0.0022
29	420	-0.1822	0	0.0023	0	0.0036
30	435	-0.1961	0	0.0060	0	-0.0003
31	450	-0.2087	0	0.0060	0	0.0021

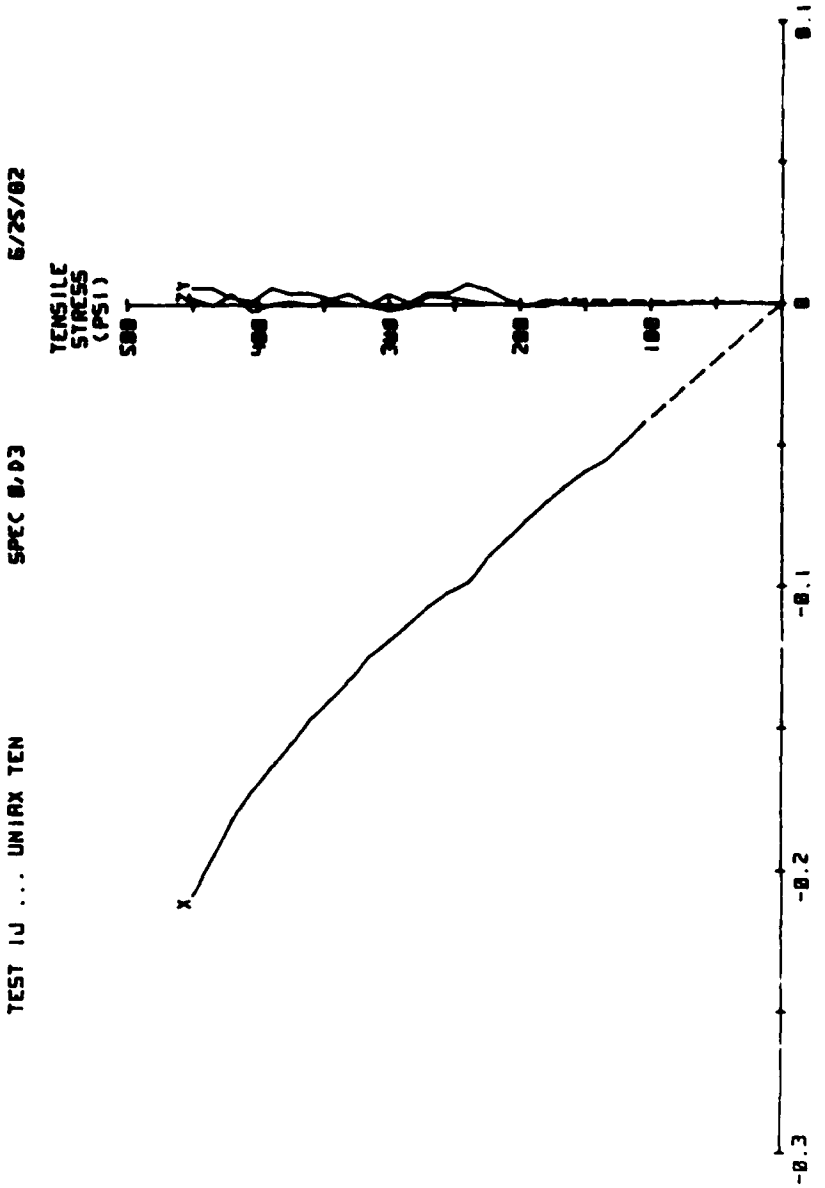

Fig. A.8 Test Results

Table A.9

TEST 8B ... 0.1 F(CU) SPEC 5.G6 8/5 82

TENSILE LOADING
STRESS - STRAIN DATA

	X-AXIS STRESS (PSI)	X-AXIS STRAIN (MILS/IN)	Y-AXIS STRESS (PSI)	Y-AXIS STRAIN (MILS/IN)	Z-AXIS STRESS (PSI)	Z-AXIS STRAIN (MILS/IN)
1	0	0.0000	0	0.0000	0	0.0000
2	-10	-0.0044	0	0.0007	0	0.0003
3	-20	-0.0106	0	0.0085	0	-0.0029
4	-30	-0.0118	0	0.0083	0	-0.0019
5	-45	-0.0189	0	0.0093	0	-0.0019
6	-60	-0.0200	0	0.0052	0	0.0045
7	-75	-0.0270	0	0.0098	0	0.0034
8	-90	-0.0307	0	0.0070	0	0.0069
9	-105	-0.0370	0	0.0090	0	0.0064
10	-120	-0.0395	0	0.0113	0	-0.0011
11	-135	-0.0471	0	0.0085	0	0.0044
12	-150	-0.0519	0	0.0073	0	0.0030
13	-165	-0.0567	0	0.0093	0	0.0087
14	-180	-0.0625	0	0.0122	0	0.0086
15	-195	-0.0658	0	0.0093	0	0.0021
16	-210	-0.0756	0	0.0117	0	0.0071
17	-225	-0.0808	0	0.0123	0	0.0076
18	-240	-0.0833	0	0.0145	0	0.0057
19	-255	-0.0915	0	0.0213	0	0.0076
20	-270	-0.0952	0	0.0178	0	0.0087
21	-285	-0.1007	0	0.0208	0	0.0052
22	-300	-0.1070	0	0.0215	0	0.0104
23	-315	-0.1136	0	0.0229	0	0.0092
24	-330	-0.1179	0	0.0212	0	0.0096
25	-345	-0.1249	0	0.0240	0	0.0116
26	-360	-0.1332	0	0.0235	0	0.0097
27	-375	-0.1402	0	0.0270	0	0.0098
28	-390	-0.1449	0	0.0298	0	0.0086
29	-405	-0.1511	0	0.0263	0	0.0159
30	-420	-0.1595	0	0.0265	0	0.0101
31	-435	-0.1656	0	0.0313	0	0.0110
32	-450	-0.1718	0	0.0326	0	0.0115
33	-465	-0.1788	0	0.0362	0	0.0135
34	-480	-0.1872	0	0.0335	0	0.0122
35	-495	-0.1974	0	0.0381	0	0.0127
36	-510	-0.2122	0	0.0418	0	0.0184

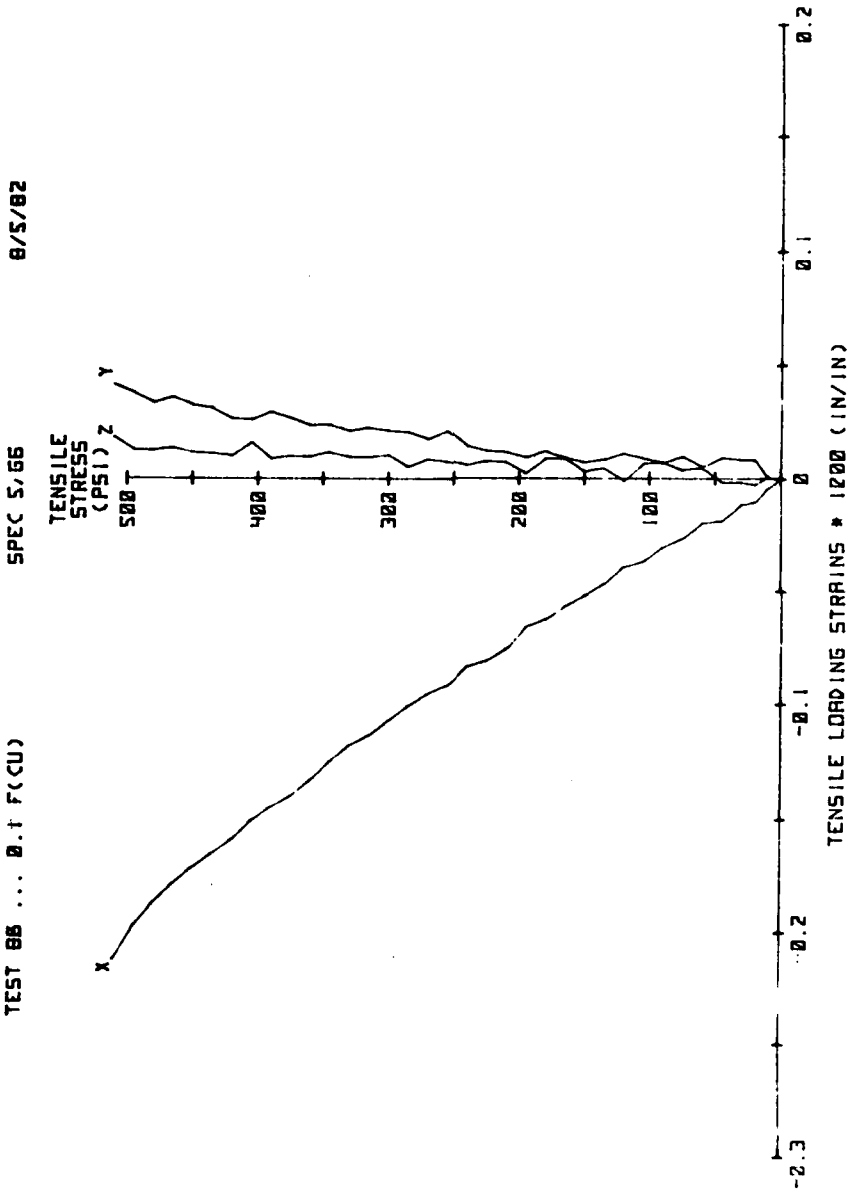

Fig. A.9 Test Results

Table A.10

TEST 10 ... 0.3 F(CU) BIAXIAL T/C FIBERED CONCRETE AVERAGE

STRESS - STRAIN DATA

	X-AXIS STRESS (PSI)	X-AXIS STRAIN (MILS/IN)	Y-AXIS STRESS (PSI)	Y-AXIS STRAIN (MILS/IN)	Z-AXIS STRESS (PSI)	Z-AXIS STRAIN (MILS/IN)
1	0	0.0000	0	0.0000	0	0.0000
2	0	-0.0100	200	0.0568	0	-0.0100
3	0	-0.0189	400	0.1195	0	-0.0189
4	0	-0.0266	600	0.1759	0	-0.0266
5	0	-0.0385	900	0.2658	0	-0.0385
6	0	-0.0520	1200	0.3514	0	-0.0520
7	0	-0.0673	1500	0.4305	0	-0.0673
8	0	-0.0799	1800	0.5200	0	-0.0799
9	0	-0.0926	2050	0.6009	0	-0.0926
10	0	-0.0985	2200	0.6429	0	-0.0985
11	0	-0.1030	2300	0.6760	0	-0.1030
12	-10	-0.1077	2300	0.6811	0	-0.1016
13	-20	-0.1114	2300	0.6810	0	-0.1047
14	-30	-0.1145	2300	0.6787	0	-0.0991
15	-45	-0.1204	2300	0.6862	0	-0.0979
16	-60	-0.1232	2300	0.6817	0	-0.1006
17	-75	-0.1312	2300	0.6867	0	-0.0961
18	-90	-0.1368	2300	0.6887	0	-0.0995
19	-105	-0.1433	2300	0.6903	0	-0.0963
20	-120	-0.1487	2300	0.6978	0	-0.0957
21	-135	-0.1555	2300	0.6939	0	-0.0930
22	-150	-0.1624	2300	0.6971	0	-0.0918
23	-165	-0.1698	2300	0.6995	0	-0.0923
24	-180	-0.1764	2300	0.7028	0	-0.0878
25	-195	-0.1843	2300	0.7007	0	-0.0909
26	-210	-0.1914	2300	0.7044	0	-0.0919
27	-225	-0.1964	2300	0.7043	0	-0.0898
28	-240	-0.2064	2300	0.7060	0	-0.0881
29	-255	-0.2142	2300	0.7106	0	-.0882
30	-270	-0.2219	2300	0.7150	0	-0.0873
31	-285	-0.2306	2300	0.7190	0	-0.0885
32	-300	-0.2378	2300	0.7205	0	-0.0896
33	-315	-0.2448	2300	0.7203	0	-0.0870
34	-330	-0.2522	2300	0.7243	0	-0.0855
35	-345	-0.2622	2300	0.7245	0	-0.0840
36	-360	-0.2716	2300	0.7302	0	-0.0815
37	-375	-0.2810	2300	0.7340	0	-0.0783
38	-390	-0.2880	2300	0.7377	0	-0.0764
39	-405	-0.2970	2300	0.7382	0	-0.0772
40	-420	-0.3033	2300	0.7418	0	-0.0720
41	-435	-0.3123	2300	0.7378	0	-0.0763
42	-450	-0.3201	2300	0.7398	0	-0.0730
43	-465	-0.3286	2300	0.7395	0	-0.0742
44	-480	-0.3428	2300	0.7433	0	-0.0724

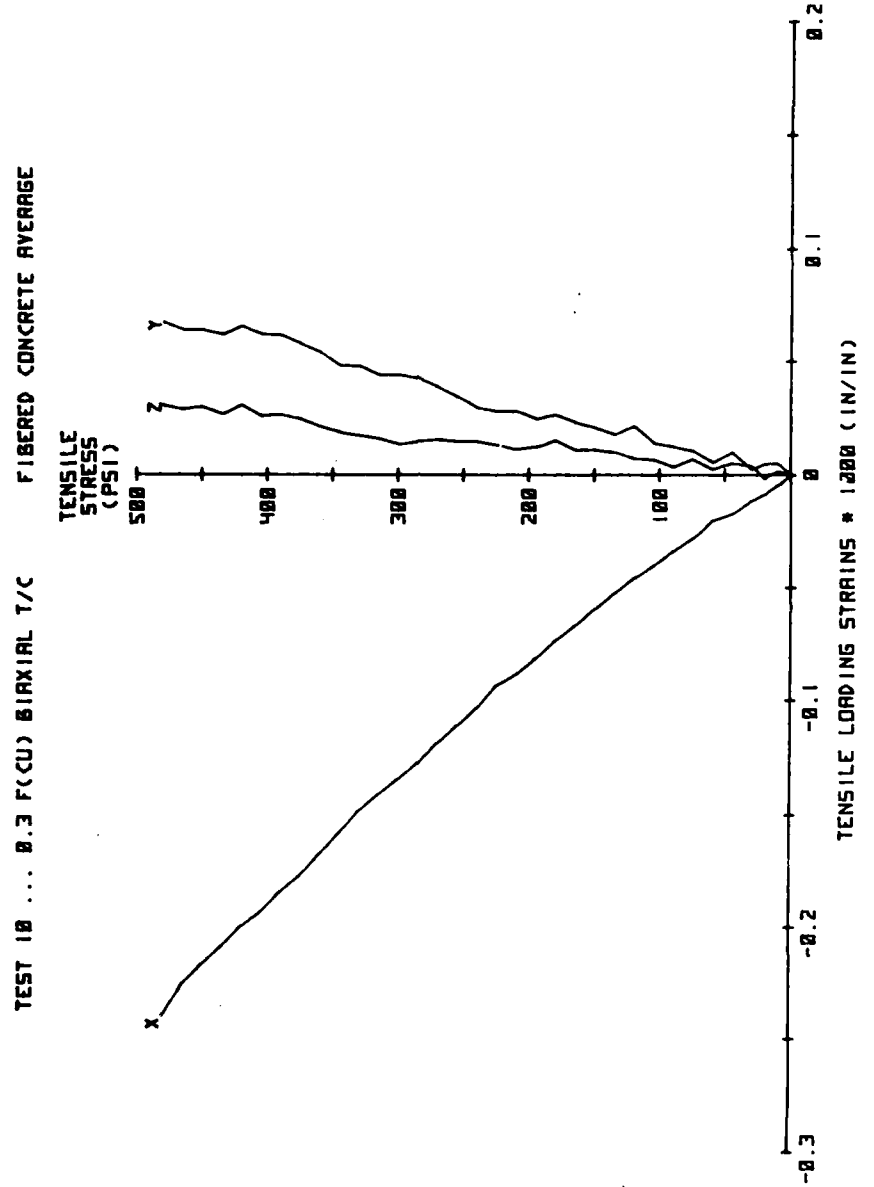

Fig. A.10 Test Results

Table A.11

TEST 10A... 0.3 F(CU) SPEC 5,E4 7/21/82

STRESS - STRAIN DATA

	X-AXIS STRESS (PSI)	X-AXIS STRAIN (MILS/IN)	Y-AXIS STRESS (PSI)	Y-AXIS STRAIN (MILS/IN)	Z-AXIS STRESS (PSI)	Z-AXIS STRAIN (MILS/IN)
1	0	0.0000	0	0.0000	0	0.0000
2	0	-0.0129	200	0.0541	0	-0.0074
3	0	-0.0231	400	0.1082	0	-0.0148
4	0	-0.0280	600	0.1608	0	-0.0200
5	0	-0.0339	900	0.2396	0	-0.0327
6	0	-0.0440	1200	0.3332	0	-0.0456
7	0	-0.0578	1500	0.4034	0	-0.0585
8	0	-0.0731	1800	0.4847	0	-0.0686
9	0	-0.0962	2100	0.5729	0	-0.0794
10	0	-0.0972	2200	0.5933	0	-0.0828
11	0	-0.1065	2300	0.6191	0	-0.0797
12	-10	-0.1088	2300	0.6219	0	-0.0768
13	-20	-0.1140	2300	0.6246	0	-0.0796
14	-30	-0.1187	2300	0.6304	0	-0.0753
15	-45	-0.1250	2300	0.6329	0	-0.0714
16	-60	-0.1248	2300	0.6260	0	-0.0738
17	-75	-0.1276	2300	0.6279	0	-0.0728
18	-90	-0.1326	2300	0.6257	0	-0.0766
19	-105	-0.1391	2300	0.6294	0	-0.0796
20	-120	-0.1439	2300	0.6347	0	-0.0733
21	-135	-0.1515	2300	0.6307	0	-0.0716
22	-150	-0.1568	2300	0.6392	0	-0.0753
23	-165	-0.1627	2300	0.6449	0	-0.0690
24	-180	-0.1651	2300	0.6502	0	-0.0626
25	-195	-0.1709	2300	0.6467	0	-0.0673
26	-210	-0.1746	2300	0.6423	0	-0.0737
27	-225	-0.1790	2300	0.6554	0	-0.0698
28	-240	-0.1839	2300	0.6521	0	-0.0644
29	-255	-0.1946	2300	0.6616	0	-0.0665
30	-270	-0.1994	2300	0.6610	0	-0.0653
31	-285	-0.2073	2300	0.6670	0	-0.0630
32	-300	-0.2111	2300	0.6677	0	-0.0636
33	-315	-0.2171	2300	0.6657	0	-0.0589
34	-330	-0.2209	2300	0.6674	0	-0.0575
35	-345	-0.2276	2300	0.6713	0	-0.0593
36	-360	-0.2357	2300	0.6806	0	-0.0569
37	-375	-0.2441	2300	0.6856	0	-0.0503
38	-390	-0.2488	2300	0.6872	0	-0.0483
39	-405	-0.2559	2300	0.6824	0	-0.0460
40	-420	-0.2610	2300	0.6851	0	-0.0496
41	-435	-0.2674	2300	0.6828	0	-0.0551
42	-450	-0.2753	2300	0.6822	0	-0.0507
43	-465	-0.2822	2300	0.6804	0	-0.0542
44	-480	-0.2900	2300	0.6831	0	-0.0566
45	-495	-0.3015	2300	0.6819	0	-0.0549

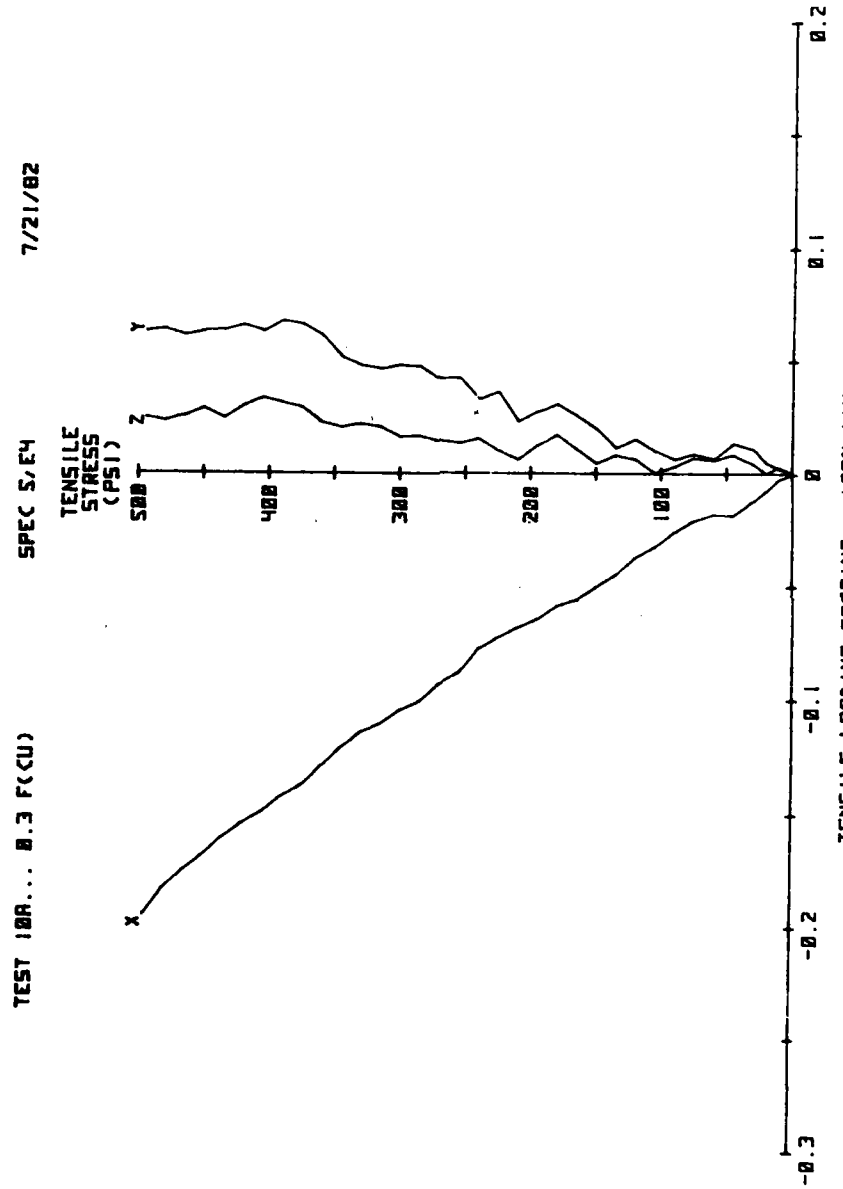

Fig. A.11 Test Results

Table A.12

TEST 10B... 0.3 F(CU) SPEC 5,E5 7/29/82

STRESS - STRAIN DATA

	X-AXIS STRESS (PSI)	X-AXIS STRAIN (MILS/IN)	Y-AXIS STRESS (PSI)	Y-AXIS STRAIN (MILS/IN)	Z-AXIS STRESS (PSI)	Z-AXIS STRAIN (MILS/IN)
1	0	0.0000	0	0.0000	0	0.0000
2	0	-0.0082	200	0.0517	0	-0.0096
3	0	-0.0164	400	0.1233	0	-0.0192
4	0	-0.0245	600	0.1762	0	-0.0288
5	0	-0.0368	900	0.2660	0	-0.0418
6	0	-0.0452	1200	0.3465	0	-0.0579
7	0	-0.0619	1500	0.4252	0	-0.0720
8	0	-0.0734	1800	0.5184	0	-0.0878
9	0	-0.0809	2000	0.5797	0	-0.0991
10	0	-0.0898	2200	0.6460	0	-0.1031
11	0	-0.0949	2300	0.6847	0	-0.1090
12	-10	-0.1056	2300	0.6915	0	-0.1076
13	-20	-0.1091	2300	0.6873	0	-0.1074
14	-30	-0.1115	2300	0.6843	0	-0.1015
15	-45	-0.1145	2300	0.6939	0	-0.1034
16	-60	-0.1195	2300	0.6914	0	-0.1042
17	-75	-0.1256	2300	0.6918	0	-0.1081
18	-90	-0.1302	2300	0.6983	0	-0.1103
19	-105	-0.1364	2300	0.6960	0	-0.1060
20	-120	-0.1425	2300	0.7041	0	-0.1098
21	-135	-0.1522	2300	0.7042	0	-0.1071
22	-150	-0.1582	2300	0.6995	0	-0.1043
23	-165	-0.1636	2300	0.7013	0	-0.1053
24	-180	-0.1685	2300	0.7045	0	-0.1048
25	-195	-0.1745	2300	0.7092	0	-0.1064
26	-210	-0.1839	2300	0.7181	0	-0.1045
27	-225	-0.1918	2300	0.7118	0	-0.1036
28	-240	-0.2026	2300	0.7176	0	-0.1066
29	-255	-0.2103	2300	0.7168	0	-0.1053
30	-270	-0.2190	2300	0.7220	0	-0.1036
31	-285	-0.2263	2300	0.7292	0	-0.1032
32	-300	-0.2359	2300	0.7243	0	-0.0991
33	-315	-0.2440	2300	0.7266	0	-0.1026
34	-330	-0.2521	2300	0.7247	0	-0.1033
35	-345	-0.2613	2300	0.7215	0	-0.1033
36	-360	-0.2705	2300	0.7278	0	-0.1017
37	-375	-0.2802	2300	0.7303	0	-0.1021
38	-390	-0.2896	2300	0.7355	0	-0.0968
39	-405	-0.2972	2300	0.7349	0	-0.0951
40	-420	-0.3078	2300	0.7439	0	-0.0932
41	-435	-0.3175	2300	0.7389	0	-0.0959
42	-450	-0.3271	2300	0.7365	0	-0.0938
43	-465	-0.3378	2300	0.7451	0	-0.0953
44	-480	-0.3564	2300	0.7465	0	-0.0969

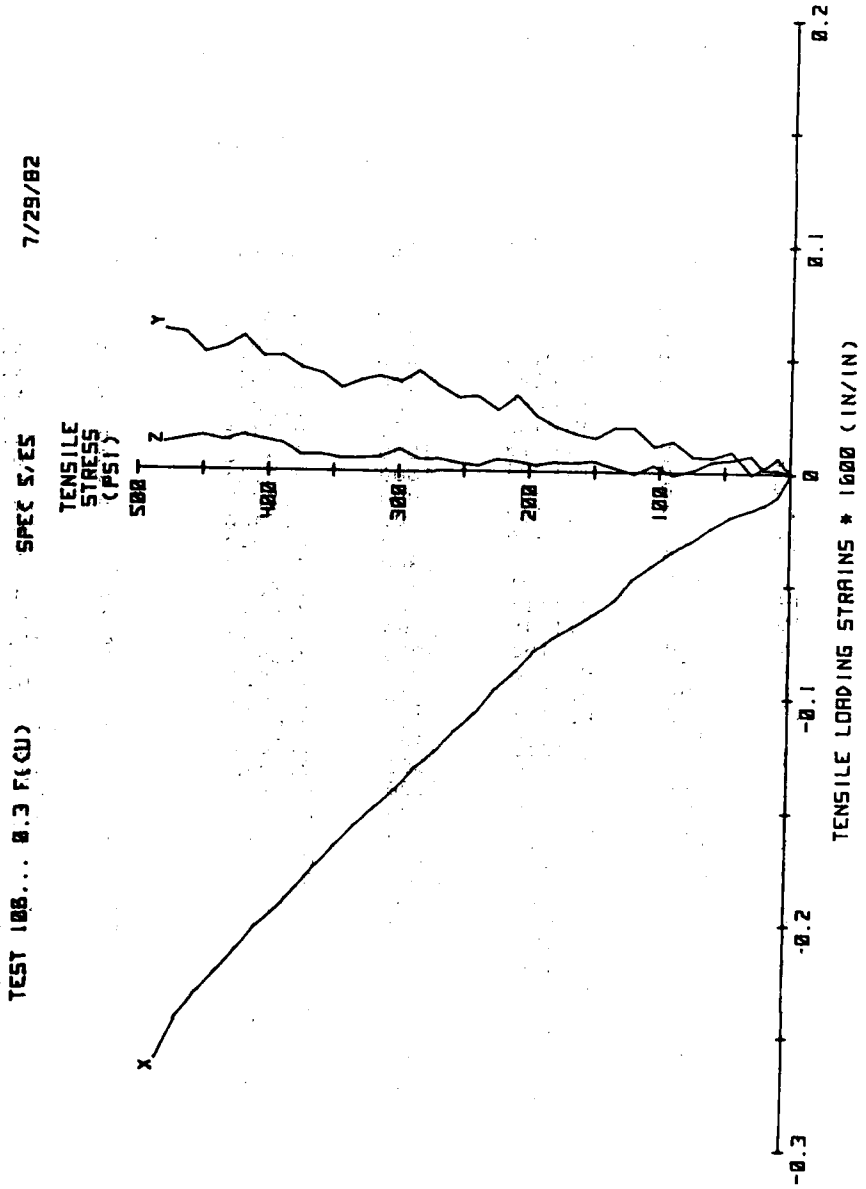

Fig. A.12 Test Results

Table A.13

TEST 10C... 0.3 F(CU) SPEC 5,F5 8/7/82

STRESS - STRAIN DATA

	X-AXIS STRESS (PSI)	X-AXIS STRAIN (MILS/IN)	Y-AXIS STRESS (PSI)	Y-AXIS STRAIN (MILS/IN)	Z-AXIS STRESS (PSI)	Z-AXIS STRAIN (MILS/IN)
1	0	0.0000	0	0.0000	0	0.0000
2	0	-0.0133	200	0.0623	0	-0.0090
3	0	-0.0224	400	0.1246	0	-0.0029
4	0	-0.0334	600	0.1883	0	-0.0036
5	0	-0.0483	900	0.2892	0	-0.0088
6	0	-0.0671	1200	0.3721	0	-0.0062
7	0	-0.0881	1500	0.4606	0	0.0178
8	0	-0.0981	1800	0.5547	0	-0.0264
9	0	-0.1106	2050	0.6478	0	-0.0221
10	0	-0.1251	2200	0.6871	0	-0.0234
11	0	-0.1336	2300	0.7217	0	-0.0079
12	-10	-0.1394	2300	0.7274	0	-0.0086
13	-20	-0.1426	2300	0.7278	0	-0.0115
14	-30	-0.1453	2300	0.7225	0	-0.0056
15	-45	-0.1521	2300	0.7311	0	-0.0042
16	-60	-0.1554	2300	0.7268	0	-0.0078
17	-75	-0.1662	2300	0.7350	0	0.0014
18	-90	-0.1723	2300	0.7369	0	-0.0023
19	-105	-0.1789	2300	0.7392	0	0.0030
20	-120	-0.1844	2300	0.7472	0	0.0031
21	-135	-0.1897	2300	0.7419	0	0.0063
22	-150	-0.1975	2300	0.7460	0	0.0087
23	-165	-0.2064	2300	0.7473	0	0.0058
24	-180	-0.2153	2300	0.7499	0	0.0111
25	-195	-0.2248	2300	0.7457	0	0.0080
26	-210	-0.2323	2300	0.7505	0	0.0079
27	-225	-0.2364	2300	0.7475	0	0.0098
28	-240	-0.2482	2300	0.7496	0	0.0119
29	-255	-0.2549	2300	0.7545	0	0.0122
30	-270	-0.2633	2300	0.7605	0	0.0126
31	-285	-0.2729	2300	0.7624	0	0.0093
32	-300	-0.2805	2300	0.7669	0	0.0060
33	-315	-0.2874	2300	0.7664	0	0.0101
34	-330	-0.2959	2300	0.7737	0	0.0126
35	-345	-0.3076	2300	0.7738	0	0.0160
36	-360	-0.3177	2300	0.7777	0	0.0189
37	-375	-0.3273	2300	0.7816	0	0.0222
38	-390	-0.3342	2300	0.7855	0	0.0227
39	-405	-0.3418	2300	0.7886	0	0.0196
40	-420	-0.3496	2300	0.7904	0	0.0296
41	-435	-0.3595	2300	0.7860	0	0.0251
42	-450	-0.3664	2300	0.7910	0	0.0285
43	-465	-0.3748	2300	0.7877	0	0.0284
44	-480	-0.3898	2300	0.7929	0	0.0333

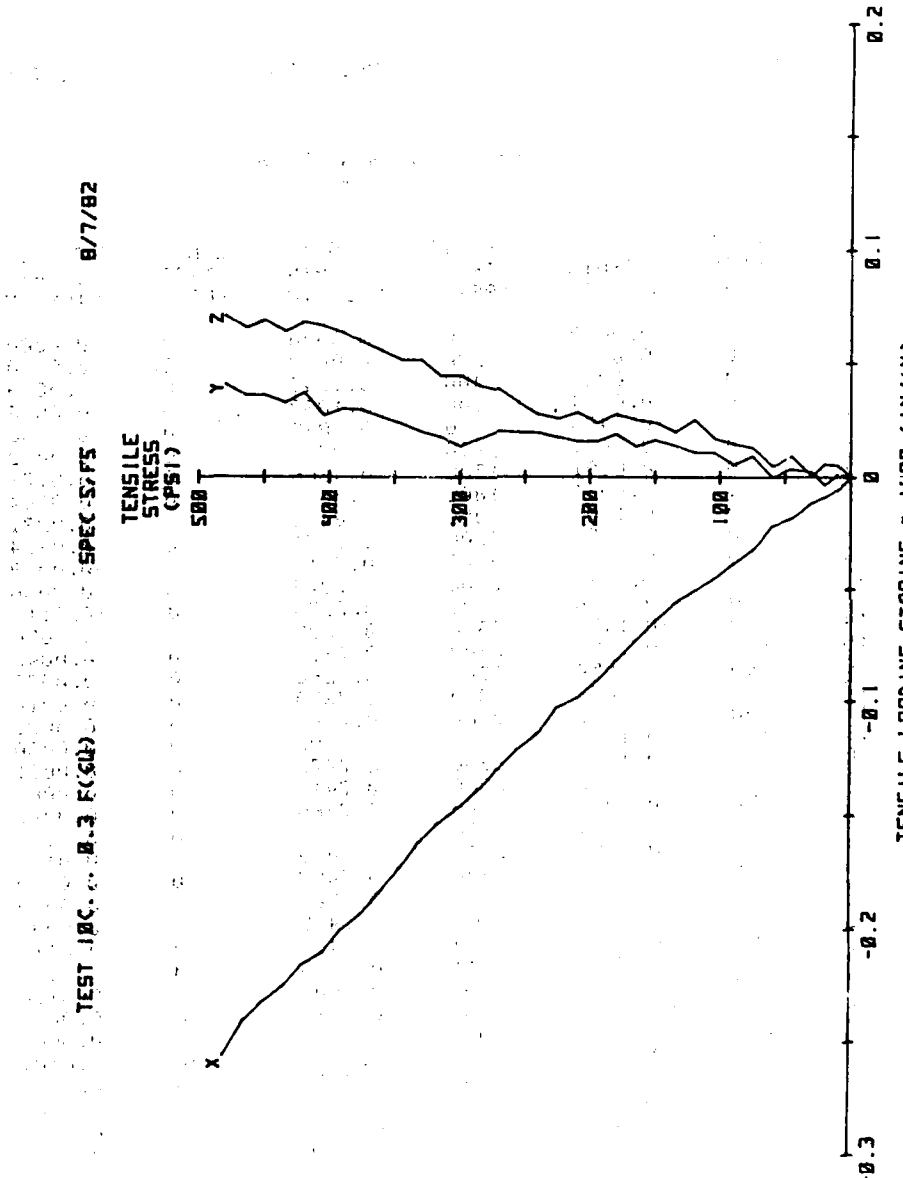

Fig. A.13 Test Results

Table A.14

TEST 10 ... 0.3 F(CU) BIAXIAL T/C PLAIN CONCRETE AVERAGE

STRESS - STRAIN DATA

	X-AXIS STRESS (PSI)	X-AXIS STRAIN (MILS/IN)	Y-AXIS STRESS (PSI)	Y-AXIS STRAIN (MILS/IN)	Z-AXIS STRESS (PSI)	Z-AXIS STRAIN (MILS/IN)
1	0	0.0000	0	0.0000	0	0.0000
2	0	-0.0060	200	0.0722	0	-0.0060
3	0	-0.0127	400	0.1469	0	-0.0127
4	0	-0.0222	600	0.2193	0	-0.0222
5	0	-0.0329	900	0.3324	0	-0.0329
6	0	-0.0420	1200	0.4426	0	-0.0420
7	0	-0.0507	1500	0.5479	0	-0.0507
8	0	-0.0609	1700	0.6264	0	-0.0609
9	0	-0.0648	1900	0.6930	0	-0.0648
10	0	-0.0694	2000	0.7359	0	-0.0694
11	-10	-0.0728	2000	0.7378	0	-0.0698
12	-20	-0.0758	2000	0.7399	0	-0.0694
13	-30	-0.0798	2000	0.7420	0	-0.0690
14	-45	-0.0833	2000	0.7444	0	-0.0688
15	-60	-0.0878	2000	0.7473	0	-0.0666
16	-75	-0.0937	2000	0.7526	0	-0.0669
17	-90	-0.0994	2000	0.7557	0	-0.0630
18	-105	-0.1004	2000	0.7602	0	-0.0618
19	-120	-0.1032	2000	0.7599	0	-0.0638
20	-135	-0.1083	2000	0.7651	0	-0.0641
21	-150	-0.1150	2000	0.7703	0	-0.0681
22	-165	-0.1179	2000	0.7705	0	-0.0634
23	-180	-0.1217	2000	0.7773	0	-0.0657
24	-195	-0.1253	2000	0.7778	0	-0.0637
25	-210	-0.1310	2000	0.7793	0	-0.0690
26	-225	-0.1409	2000	0.7810	0	-0.0628
27	-240	-0.1460	2000	0.7814	0	-0.0635
28	-255	-0.1534	2000	0.7864	0	-0.0618
29	-270	-0.1598	2000	0.7896	0	-0.0571
30	-285	-0.1685	2000	0.7918	0	-0.0562
31	-300	-0.1790	2000	0.7986	0	-0.0588
32	-315	-0.1925	2000	0.8080	0	-0.0597
33	-330	-0.2045	2000	0.8095	0	-0.0579

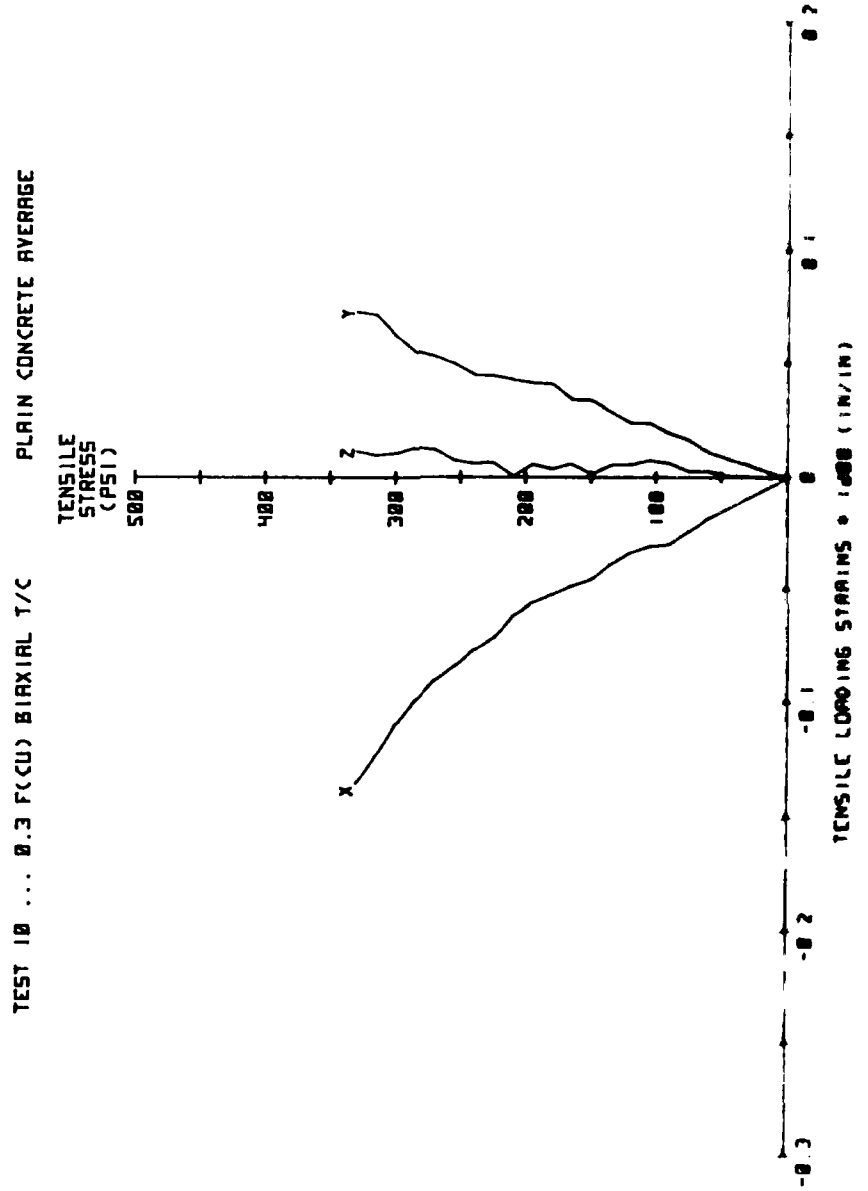

Fig. A.14 Test Results

Table A.15

TEST 10D... 0.3 F(CU) SPEC 0,D5 8/11/82

STRESS - STRAIN DATA

	X-AXIS STRESS (PSI)	X-AXIS STRAIN (MILS/IN)	Y-AXIS STRESS (PSI)	Y-AXIS STRAIN (MILS/IN)	Z-AXIS STRESS (PSI)	Z-AXIS STRAIN (MILS/IN)
1	0	0.0000	0	0.0000	0	0.0000
2	0	0.0032	200	0.0668	0	-0.0060
3	0	-0.0091	400	0.1384	0	-0.0121
4	0	-0.0186	600	0.2112	0	-0.0184
5	0	-0.0313	900	0.3124	0	-0.0224
6	0	-0.0234	1200	0.4092	0	-0.0399
7	0	-0.0360	1500	0.5172	0	-0.0421
8	0	-0.0351	1700	0.5966	0	-0.0641
9	0	-0.0442	1900	0.6509	0	-0.0526
10	0	-0.0457	2000	0.6917	0	-0.0560
11	-10	-0.0487	2000	0.6937	0	-0.0556
12	-20	-0.0517	2000	0.6957	0	-0.0551
13	-30	-0.0547	2000	0.6989	0	-0.0546
14	-45	-0.0592	2000	0.6990	0	-0.0539
15	-60	-0.0659	2000	0.7014	0	-0.0578
16	-75	-0.0697	2000	0.7085	0	-0.0514
17	-90	-0.0753	2000	0.7113	0	-0.0480
18	-105	-0.0764	2000	0.7126	0	-0.0475
19	-120	-0.0792	2000	0.7138	0	-0.0459
20	-135	-0.0842	2000	0.7187	0	-0.0474
21	-150	-0.0910	2000	0.7237	0	-0.0519
22	-165	-0.0939	2000	0.7264	0	-0.0509
23	-180	-0.0976	2000	0.7327	0	-0.0491
24	-195	-0.1012	2000	0.7310	0	-0.0474
25	-210	-0.1070	2000	0.7300	0	-0.0544
26	-225	-0.1169	2000	0.7340	0	-0.0411
27	-240	-0.1220	2000	0.7350	0	-0.0476
28	-255	-0.1294	2000	0.7382	0	-0.0481
29	-270	-0.1357	2000	0.7384	0	-0.0376
30	-285	-0.1445	2000	0.7438	0	-0.0402
31	-300	-0.1550	2000	0.7441	0	-0.0472
32	-315	-0.1685	2000	0.7582	0	-0.0412
33	-330	-0.1805	2000	0.7629	0	-0.0369
34	-345	-0.1972	2000	0.7612	0	-0.0378
35	-360	-0.2362	2000	0.7664	0	-0.0390

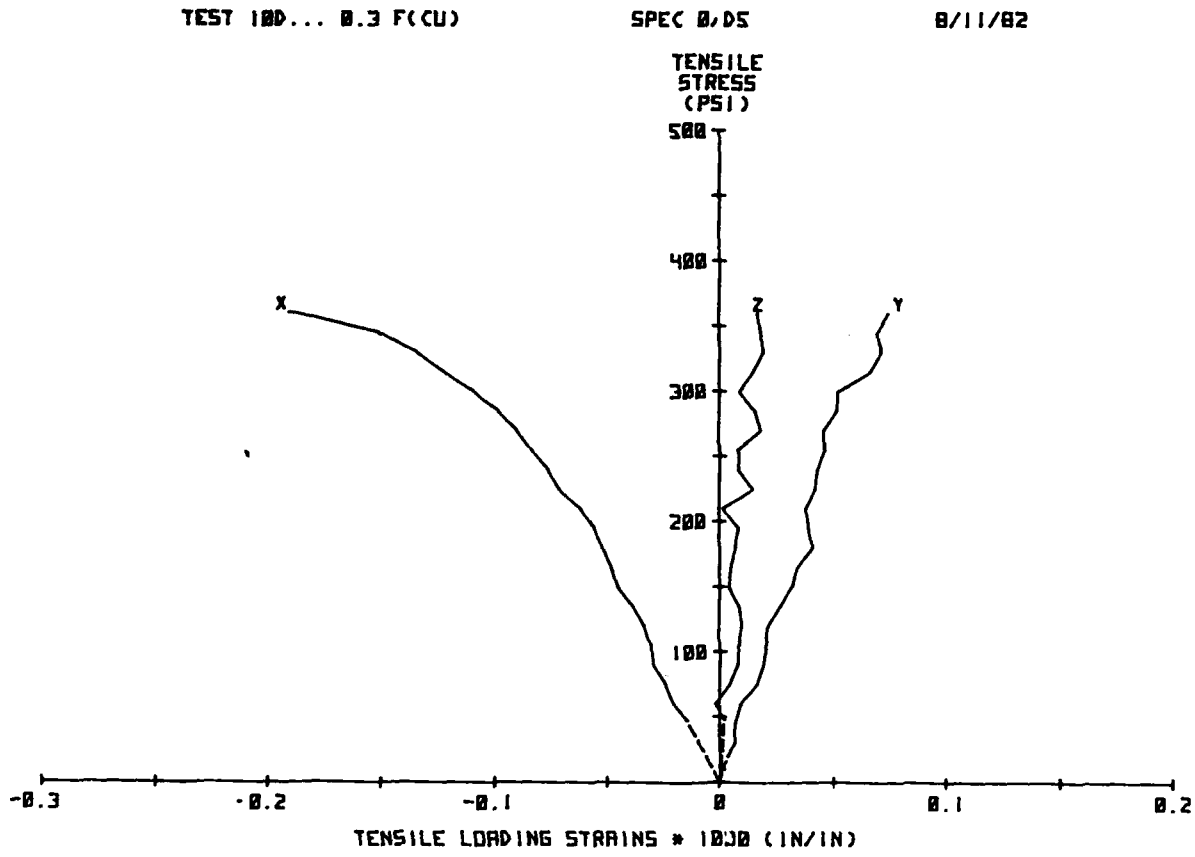

Fig. A.15 Test Results

Table A.16

TEST 10E... 0.3 F(CU) SPEC 0.06 8/12.82

STRESS - STRAIN DATA

	X-AXIS STRESS (PSI)	X-AXIS STRAIN (MILS/IN)	Y-AXIS STRESS (PSI)	Y-AXIS STRAIN (MILS/IN)	Z-AXIS STRESS (PSI)	Z-AXIS STRAIN (MILS/IN)
1	0	0.0000	0	0.0000	0	0.0000
2	0	-0.0028	200	0.0777	0	-0.0105
3	0	-0.0152	400	0.1553	0	-0.0220
4	0	-0.0166	600	0.2275	0	-0.0308
5	0	-0.0136	900	0.3523	0	-0.0470
6	0	-0.0159	1200	0.4760	0	-0.0647
7	0	-0.0265	1500	0.5786	0	-0.0758
8	0	-0.0348	1700	0.6562	0	-0.0855
9	0	-0.0444	1900	0.7350	0	-0.0994
10	0	-0.0454	2000	0.7800	0	-0.1085
11	-10	-0.0545	2000	0.7823	0	-0.1082
12	-20	-0.0640	2000	0.7846	0	-0.1079
13	-30	-0.0738	2000	0.7869	0	-0.1101
14	-45	-0.0819	2000	0.7903	0	-0.1079
15	-60	-0.0936	2000	0.7937	0	-0.1042
16	-75	-0.1112	2000	0.7971	0	-0.1066
17	-90	-0.1260	2000	0.7988	0	-0.1023
18	-105	-0.1430	2000	0.8083	0	-0.1002
19	-120	-0.1597	2000	0.8065	0	-0.1061
20	-135	-0.1746	2000	0.8120	0	-0.1051
21	-150	-0.1897	2000	0.8173	0	-0.1086
22	-165	-0.1953	2000	0.8151	0	-0.1001
23	-180	-0.2087	2000	0.8224	0	-0.1066
24	-195	-0.2240	2000	0.8249	0	-0.1042
25	-210	-0.2408	2000	0.8289	0	-0.1078
26	-225	-0.2520	2000	0.8283	0	-0.1088
27	-240	-0.2621	2000	0.8283	0	-0.1036
28	-255	-0.2758	2000	0.8350	0	-0.0997
29	-270	-0.2884	2000	0.8413	0	-0.1008
30	-285	-0.3034	2000	0.8403	0	-0.0964
31	-300	-0.3187	2000	0.8536	0	-0.0946
32	-315	-0.3393	2000	0.8582	0	-0.1024

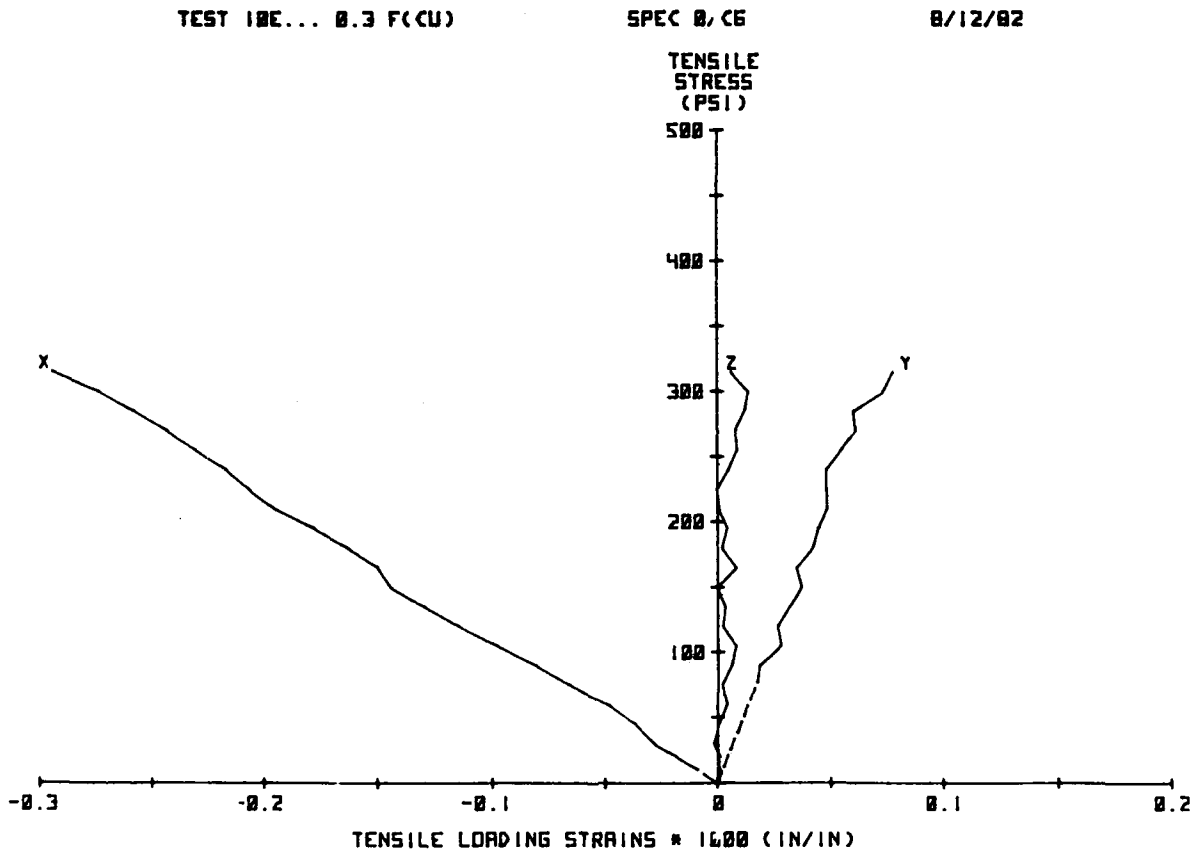

Fig. A.16 Test Results

Table A.17

TEST 12 ... 0.4 F(CU) BIAXIAL T/C AVERAGE

STRESS - STRAIN DATA

	X-AXIS STRESS (PSI)	X-AXIS STRAIN (MILS/IN)	Y-AXIS STRESS (PSI)	Y-AXIS STRAIN (MILS/IN)	Z-AXIS STRESS (PSI)	Z-AXIS STRAIN (MILS/IN)
1	0	0.0000	0	0.0000	0	0.0000
2	0	-0.0067	200	0.0506	0	-0.0067
3	0	-0.0198	400	0.1154	0	-0.0198
4	0	-0.0238	600	0.1726	0	-0.0238
5	0	-0.0362	900	0.2389	0	-0.0362
6	0	-0.0490	1200	0.3162	0	-0.0490
7	0	-0.0589	1500	0.3834	0	-0.0589
8	0	-0.0756	1900	0.4965	0	-0.0756
9	0	-0.0941	2300	0.6136	0	-0.0941
10	0	-0.1073	2700	0.7375	0	-0.1073
11	0	-0.1183	2900	0.8083	0	-0.1183
12	0	-0.1235	3000	0.8513	0	-0.1235
13	0	-0.1256	3100	0.8768	0	-0.1256
14	-10	-0.1296	3100	0.8758	0	-0.1253
15	-20	-0.1331	3100	0.8796	0	-0.1238
16	-30	-0.1375	3100	0.8799	0	-0.1249
17	-45	-0.1418	3100	0.8877	0	-0.1236
18	-60	-0.1482	3100	0.8870	0	-0.1233
19	-75	-0.1530	3100	0.8875	0	-0.1233
20	-90	-0.1601	3100	0.8954	0	-0.1187
21	-105	-0.1659	3100	0.8957	0	-0.1201
22	-120	-0.1693	3100	0.8985	0	-0.1166
23	-135	-0.1760	3100	0.8989	0	-0.1197
24	-150	-0.1809	3100	0.9001	0	-0.1198
25	-165	-0.1881	3100	0.9022	0	-0.1160
26	-180	-0.1951	3100	0.9049	0	-0.1173
27	-195	-0.1989	3100	0.9114	0	-0.1167
28	-210	-0.2032	3100	0.9088	0	-0.1176
29	-225	-0.2095	3100	0.9083	0	-0.1132
30	-240	-0.2151	3100	0.9122	0	-0.1156
31	-255	-0.2220	3100	0.9128	0	-0.1162
32	-270	-0.2324	3100	0.9133	0	-0.1113
33	-285	-0.2364	3100	0.9154	0	-0.1103
34	-300	-0.2439	3100	0.9155	0	-0.1107
35	-315	-0.2498	3100	0.9272	0	-0.1092
36	-330	-0.2543	3100	0.9257	0	-0.1095
37	-345	-0.2634	3100	0.9277	0	-0.1100
38	-360	-0.2695	3100	0.9365	0	-0.1064
39	-375	-0.2780	3100	0.9408	0	-0.1068
40	-390	-0.2847	3100	0.9428	0	-0.1028
41	-405	-0.2931	3100	0.9428	0	-0.0999
42	-420	-0.3017	3100	0.9427	0	-0.0994
43	-435	-0.3130	3100	0.9432	0	-0.0962
44	-450	-0.3247	3100	0.9491	0	-0.0924

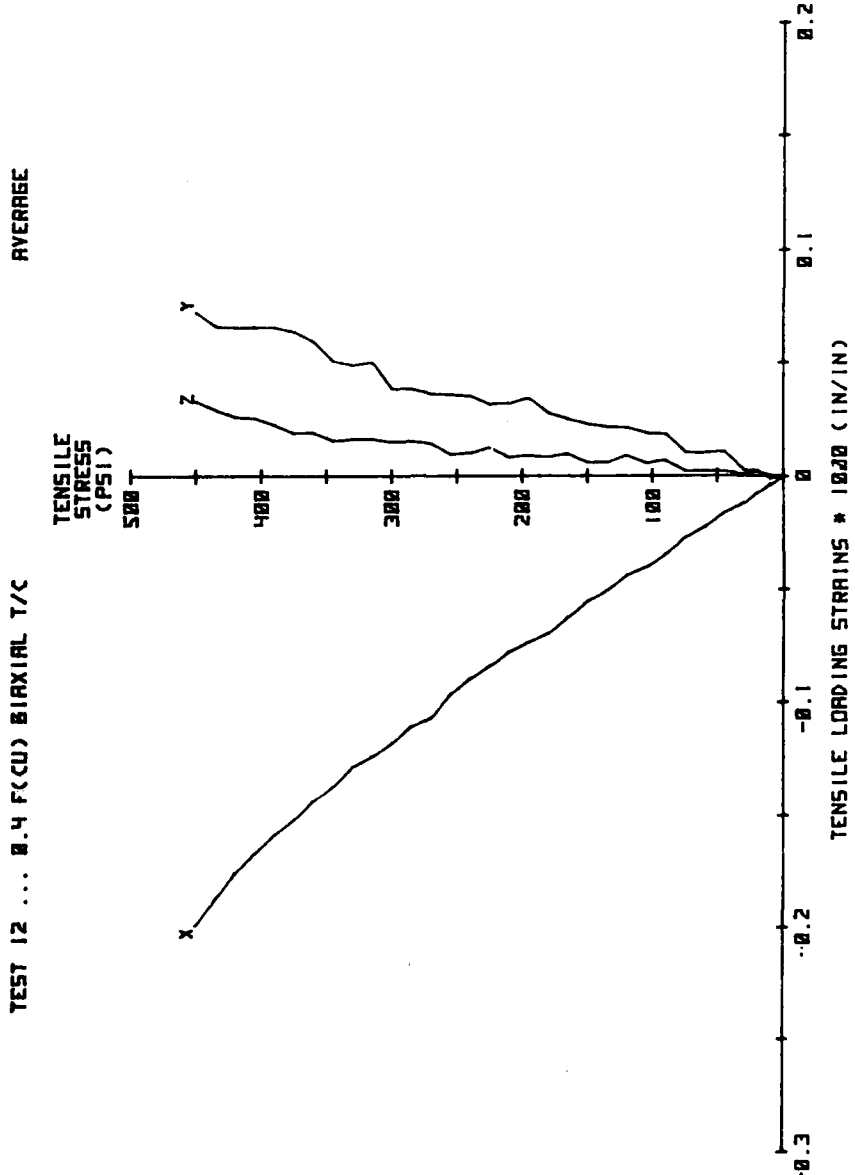

Fig. A.17 Test Results

Table A.18

TEST 12A... 0.4 F(CU) SPEC 5,F2 8/8/82

STRESS - STRAIN DATA

	X-AXIS STRESS (PSI)	X-AXIS STRAIN (MILS/IN)	Y-AXIS STRESS (PSI)	Y-AXIS STRAIN (MILS/IN)	Z-AXIS STRESS (PSI)	Z-AXIS STRAIN (MILS/IN)
1	0	0.0000	0	0.0000	0	0.0000
2	0	-0.0097	200	0.0461	0	-0.0060
3	0	-0.0194	400	0.1016	0	-0.0145
4	0	-0.0296	600	0.1689	0	-0.0117
5	0	-0.0504	900	0.2259	0	-0.0258
6	0	-0.0582	1200	0.3012	0	-0.0380
7	0	-0.0680	1500	0.3540	0	-0.0443
8	0	-0.0854	1900	0.4636	0	-0.0608
9	0	-0.1118	2300	0.5732	0	-0.0725
10	0	-0.1297	2700	0.6929	0	-0.0793
11	0	-0.1408	2900	0.7677	0	-0.0868
12	0	-0.1491	3000	0.8186	0	-0.0909
13	0	-0.1524	3100	0.8547	0	-0.0874
14	-10	-0.1540	3100	0.8511	0	-0.0871
15	-20	-0.1556	3100	0.8572	0	-0.0811
16	-30	-0.1572	3100	0.8561	0	-0.0842
17	-45	-0.1596	3100	0.8683	0	-0.0846
18	-60	-0.1620	3100	0.8631	0	-0.0874
19	-75	-0.1622	3100	0.8654	0	-0.0796
20	-90	-0.1697	3100	0.8760	0	-0.0752
21	-105	-0.1701	3100	0.8736	0	-0.0784
22	-120	-0.1705	3100	0.8786	0	-0.0745
23	-135	-0.1740	3100	0.8803	0	-0.0751
24	-150	-0.1758	3100	0.8803	0	-0.0780
25	-165	-0.1788	3100	0.8845	0	-0.0754
26	-180	-0.1821	3100	0.8836	0	-0.0777
27	-195	-0.1821	3100	0.8868	0	-0.0746
28	-210	-0.1858	3100	0.8838	0	-0.0728
29	-225	-0.1870	3100	0.8821	0	-0.0671
30	-240	-0.1897	3100	0.8873	0	-0.0699
31	-255	-0.1956	3100	0.8889	0	-0.0724
32	-270	-0.1988	3100	0.8860	0	-0.0620
33	-285	-0.2002	3100	0.8855	0	-0.0638
34	-300	-0.2023	3100	0.8886	0	-0.0630
35	-315	-0.2073	3100	0.9073	0	-0.0602
36	-330	-0.2108	3100	0.9050	0	-0.0606
37	-345	-0.2161	3100	0.8990	0	-0.0626
38	-360	-0.2194	3100	0.9168	0	-0.0544
39	-375	-0.2280	3100	0.9190	0	-0.0533
40	-390	-0.2317	3100	0.9200	0	-0.0490
41	-405	-0.2402	3100	0.9198	0	-0.0431
42	-420	-0.2548	3100	0.9198	0	-0.0300
43	-435	-0.2656	3100	0.9220	0	-0.0209
44	-450	-0.2799	3100	0.9283	0	-0.0136

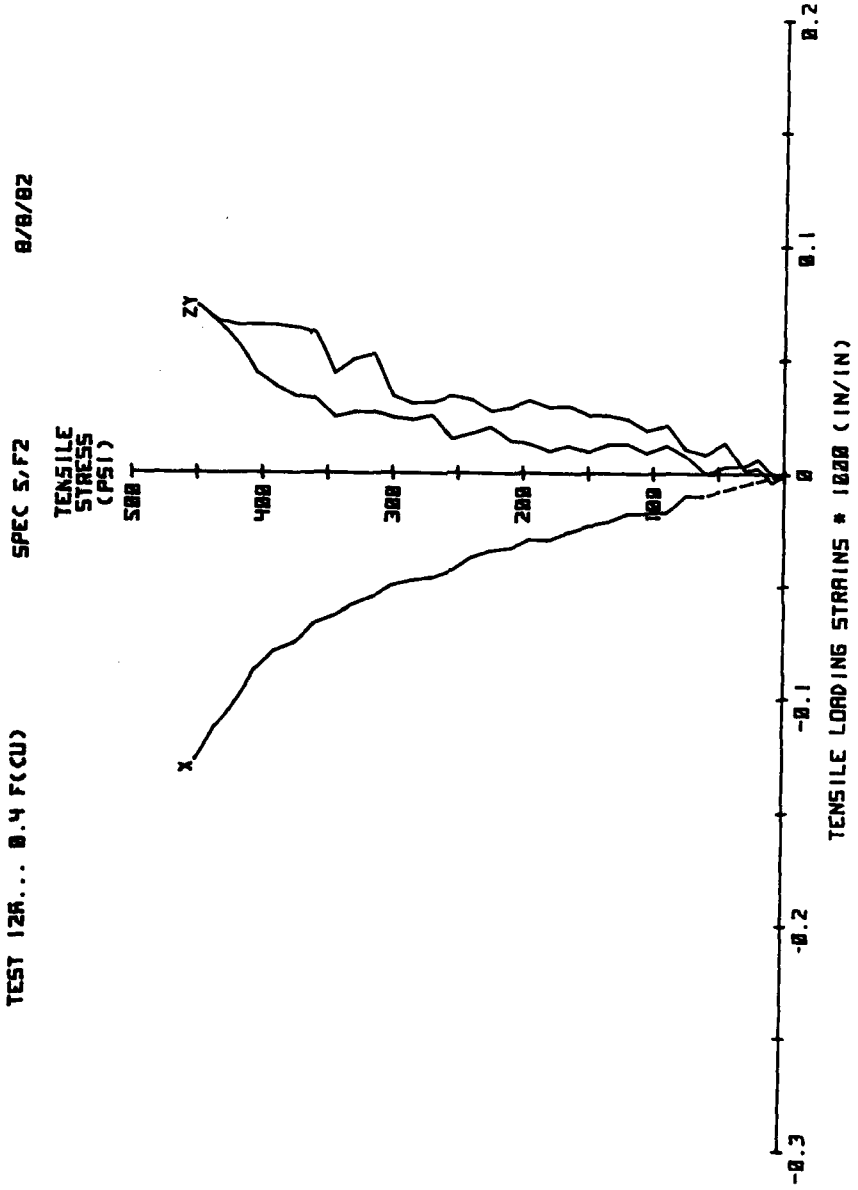

Fig. A.18 Test Results

Table A.19

TEST 12B... 0.4 F(CU) SPEC 5,F6 8/9/82

STRESS - STRAIN DATA

	X-AXIS STRESS (PSI)	X-AXIS STRAIN (MILS/IN)	Y-AXIS STRESS (PSI)	Y-AXIS STRAIN (MILS/IN)	Z-AXIS STRESS (PSI)	Z-AXIS STRAIN (MILS/IN)
1	0	0.0000	0	0.0000	0	0.0000
2	0	-0.0093	200	0.0555	0	-0.0079
3	0	-0.0233	400	0.1296	0	-0.0281
4	0	-0.0293	600	0.1767	0	-0.0309
5	0	-0.0419	900	0.2522	0	-0.0331
6	0	-0.0548	1200	0.3316	0	-0.0511
7	0	-0.0702	1500	0.4132	0	-0.0595
8	0	-0.0871	1900	0.5298	0	-0.0754
9	0	-0.1054	2300	0.6544	0	-0.0931
10	0	-0.1240	2700	0.7824	0	-0.1023
11	0	-0.1356	2900	0.8493	0	-0.1162
12	0	-0.1412	3000	0.8843	0	-0.1190
13	0	-0.1441	3100	0.8993	0	-0.1249
14	-10	-0.1480	3100	0.8977	0	-0.1241
15	-20	-0.1515	3100	0.8961	0	-0.1272
16	-30	-0.1560	3100	0.8945	0	-0.1262
17	-45	-0.1603	3100	0.9076	0	-0.1232
18	-60	-0.1666	3100	0.9113	0	-0.1198
19	-75	-0.1714	3100	0.9100	0	-0.1275
20	-90	-0.1786	3100	0.9152	0	-0.1227
21	-105	-0.1843	3100	0.9182	0	-0.1225
22	-120	-0.1877	3100	0.9188	0	-0.1194
23	-135	-0.1944	3100	0.9178	0	-0.1249
24	-150	-0.1994	3100	0.9203	0	-0.1223
25	-165	-0.2065	3100	0.9203	0	-0.1172
26	-180	-0.2135	3100	0.9266	0	-0.1175
27	-195	-0.2173	3100	0.9364	0	-0.1193
28	-210	-0.2216	3100	0.9342	0	-0.1230
29	-225	-0.2280	3100	0.9348	0	-0.1200
30	-240	-0.2336	3100	0.9374	0	-0.1219
31	-255	-0.2404	3100	0.9371	0	-0.1207
32	-270	-0.2508	3100	0.9410	0	-0.1212
33	-285	-0.2548	3100	0.9456	0	-0.1174
34	-300	-0.2623	3100	0.9427	0	-0.1191
35	-315	-0.2682	3100	0.9475	0	-0.1188
36	-330	-0.2727	3100	0.9468	0	-0.1189
37	-345	-0.2819	3100	0.9569	0	-0.1180
38	-360	-0.2879	3100	0.9566	0	-0.1191
39	-375	-0.2965	3100	0.9630	0	-0.1208
40	-390	-0.3031	3100	0.9660	0	-0.1173
41	-405	-0.3115	3100	0.9661	0	-0.1173
42	-420	-0.3202	3100	0.9659	0	-0.1130
43	-435	-0.3314	3100	0.9647	0	-0.1157
44	-450	-0.3432	3100	0.9703	0	-0.1153

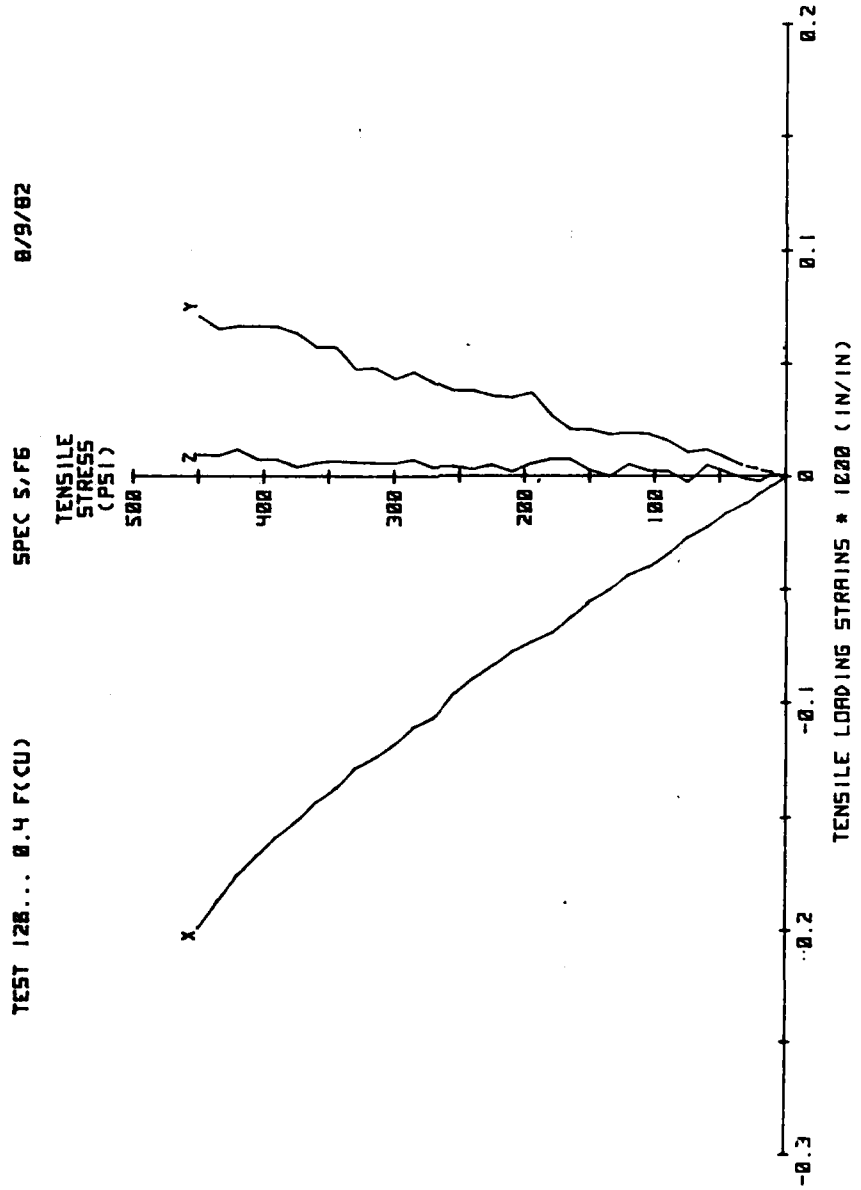

Fig. A.19 Test Results

Table A.20

TEST 12C... 0.4 F(CU) SPEC 4,F2 8/16/82

STRESS - STRAIN DATA

	X-AXIS STRESS (PSI)	X-AXIS STRAIN (MILS/IN)	Y-AXIS STRESS (PSI)	Y-AXIS STRAIN (MILS/IN)	Z-AXIS STRESS (PSI)	Z-AXIS STRAIN (MILS/IN)
1	0	0.0000	0	0.0000	0	0.0000
2	0	-0.0118	200	0.0653	0	-0.0109
3	0	-0.0236	400	0.1307	0	-0.0219
4	0	-0.0354	600	0.1960	0	-0.0328
5	0	-0.0514	900	0.2946	0	-0.0488
6	0	-0.0636	1200	0.3947	0	-0.0665
7	0	-0.0962	1500	0.4929	0	-0.0832
8	0	-0.1186	1900	0.6171	0	-0.1032
9	0	-0.1327	2300	0.7444	0	-0.1234
10	0	-0.1600	2700	0.8841	0	-0.1484
11	0	-0.1715	2900	0.9371	0	-0.1603
12	0	-0.1762	3000	0.9897	0	-0.1638
13	0	-0.1810	3100	1.0170	0	-0.1697
14	-10	-0.1871	3100	1.0199	0	-0.1693
15	-20	-0.1931	3100	1.0229	0	-0.1689
16	-30	-0.1982	3100	1.0259	0	-0.1685
17	-45	-0.2062	3100	1.0303	0	-0.1679
18	-60	-0.2195	3100	1.0348	0	-0.1673
19	-75	-0.2270	3100	1.0393	0	-0.1667
20	-90	-0.2364	3100	1.0437	0	-0.1662
21	-105	-0.2434	3100	1.0482	0	-0.1656
22	-120	-0.2531	3100	1.0527	0	-0.1653
23	-135	-0.2605	3100	1.0563	0	-0.1638
24	-150	-0.2715	3100	1.0615	0	-0.1651
25	-165	-0.2808	3100	1.0619	0	-0.1662
26	-180	-0.2908	3100	1.0725	0	-0.1611
27	-195	-0.3007	3100	1.0715	0	-0.1622
28	-210	-0.3086	3100	1.0769	0	-0.1560
29	-225	-0.3165	3100	1.0840	0	-0.1627
30	-240	-0.3249	3100	1.0949	0	-0.1595
31	-255	-0.3350	3100	1.0999	0	-0.1611
32	-270	-0.3454	3100	1.0997	0	-0.1571
33	-285	-0.3579	3100	1.1040	0	-0.1592
34	-300	-0.3674	3100	1.1057	0	-0.1592
35	-315	-0.3794	3100	1.1076	0	-0.1572
36	-330	-0.3936	3100	1.1114	0	-0.1579
37	-345	-0.4090	3100	1.1205	0	-0.1565
38	-360	-0.4276	3100	1.1217	0	-0.1546

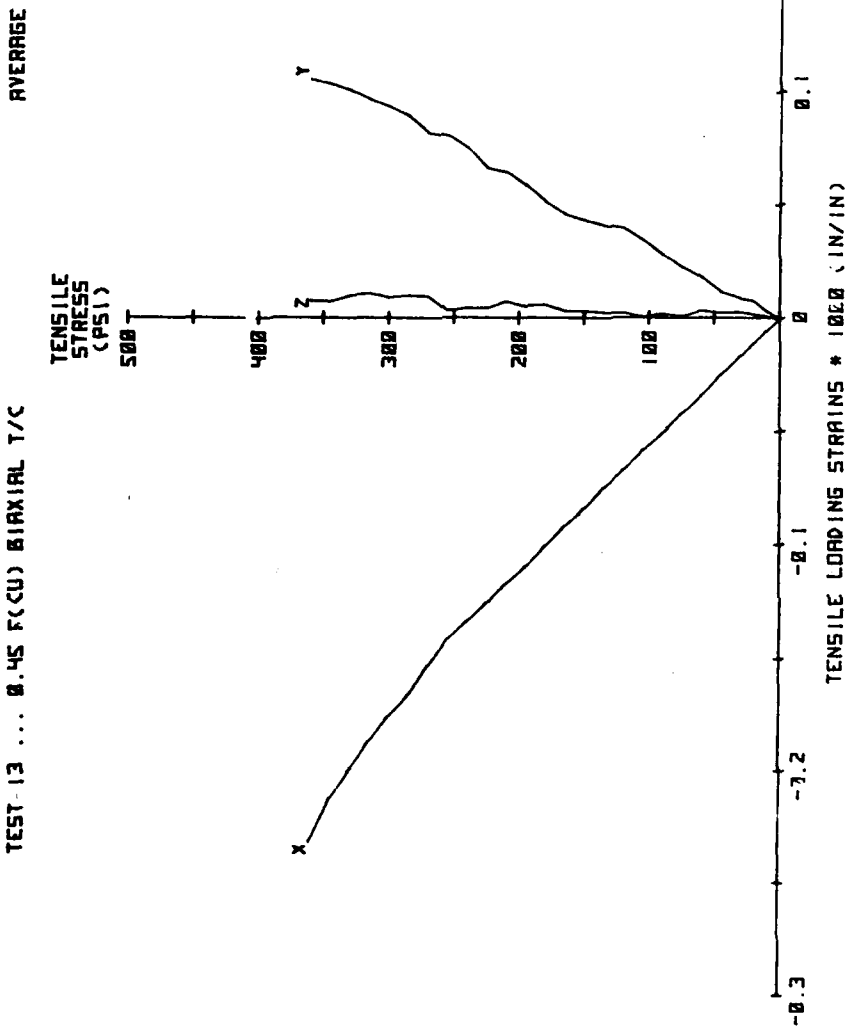

Fig. A.20 Test Results

AD-A136 124 THE STRENGTH AND BEHAVIOR OF STEEL FIBER-REINFORCED CONCRETE UNDER COMBIN..(U) COLORADO UNIV AT BOULDER DEPT OF CIVIL ENVIRONMENTAL AND ARCH.. 4/4

UNCLASSIFIED R W MEIER ET AL. MAY 83 AFOSR-TR-83-0974 F/G 13/3 NL

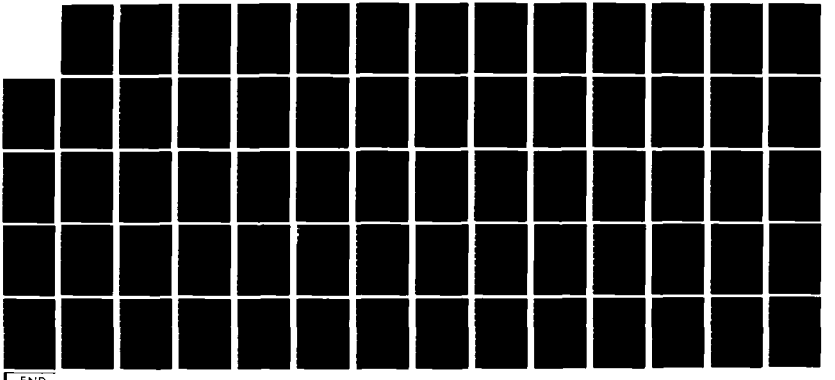

END

FILMED
1-84
DTIC

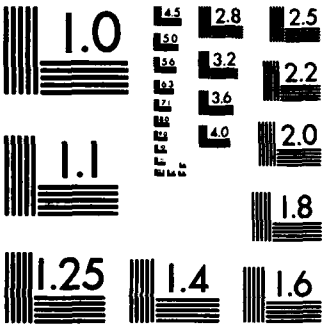

MICROCOPY RESOLUTION TEST CHART
NATIONAL BUREAU OF STANDARDS-1963-A

Table A.21

TEST 6 ... 0.5 F(CU) BIAXIAL T/C AVERAGE

STRESS - STRAIN DATA

	X-AXIS STRESS (PSI)	X-AXIS STRAIN (MILS/IN)	Y-AXIS STRESS (PSI)	Y-AXIS STRAIN (MILS/IN)	Z-AXIS STRESS (PSI)	Z-AXIS STRAIN (MILS/IN)
1	0	0.0000	0	0.0000	0	0.0000
2	0	-0.0113	200	0.0592	0	-0.0113
3	0	-0.0197	400	0.1171	0	-0.0197
4	0	-0.0282	600	0.1654	0	-0.0282
5	0	-0.0429	900	0.2320	0	-0.0429
6	0	-0.0578	1200	0.2987	0	-0.0578
7	0	-0.0775	1600	0.3946	0	-0.0775
8	0	-0.0980	2000	0.5023	0	-0.0980
9	0	-0.1254	2500	0.6418	0	-0.1254
10	0	-0.1434	3000	0.8097	0	-0.1434
11	0	-0.1612	3400	0.9339	0	-0.1612
12	0	-0.1763	3700	1.0447	0	-0.1763
13	0	-0.1855	3800	1.0779	0	-0.1855
14	0	-0.1958	3900	1.1153	0	-0.1958
15	-10	-0.2043	3900	1.1177	0	-0.1948
16	-20	-0.2057	3900	1.1229	0	-0.1957
17	-30	-0.2111	3900	1.1264	0	-0.1956
18	-45	-0.2187	3900	1.1279	0	-0.2017
19	-60	-0.2247	3900	1.1349	0	-0.1993
20	-75	-0.2323	3900	1.1411	0	-0.2033
21	-90	-0.2410	3900	1.1422	0	-0.2057
22	-105	-0.2466	3900	1.1425	0	-0.2017
23	-120	-0.2559	3900	1.1515	0	-0.2013
24	-135	-0.2629	3900	1.1548	0	-0.2028
25	-150	-0.2702	3900	1.1588	0	-0.2073
26	-165	-0.2818	3900	1.1605	0	-0.2064
27	-180	-0.2902	3900	1.1727	0	-0.2040
28	-195	-0.2981	3900	1.1741	0	-0.2086
29	-210	-0.3105	3900	1.1795	0	-0.2066
30	-225	-0.3217	3900	1.1845	0	-0.2105
31	-240	-0.3366	3900	1.1945	0	-0.2087
32	-255	-0.3604	3900	1.1976	0	-0.2096
33	-270	-0.3867	3900	1.2070	0	-0.2172

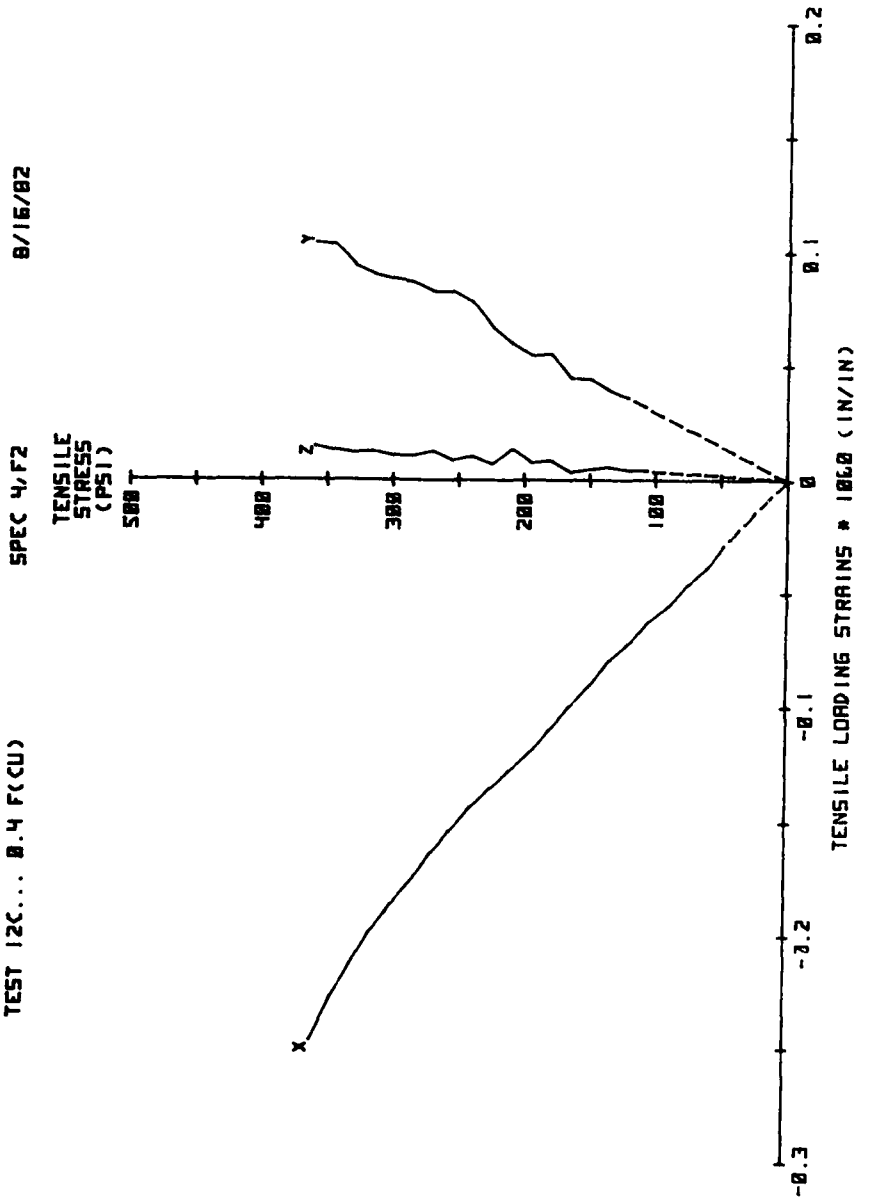

Fig. A.21 Test Results

Table A.22

TEST 6A ... 0.5 F(CU) SPEC 5,G3 7/7/82

STRESS - STRAIN DATA

	X-AXIS STRESS (PSI)	X-AXIS STRAIN (MILS/IN)	Y-AXIS STRESS (PSI)	Y-AXIS STRAIN (MILS/IN)	Z-AXIS STRESS (PSI)	Z-AXIS STRAIN (MILS/IN)
1	0	0.0000	0	0.0000	0	0.0000
2	0	-0.0092	200	0.0572	0	-0.0076
3	0	-0.0296	400	0.1144	0	-0.0274
4	0	-0.0356	600	0.1716	0	-0.0228
5	0	-0.0434	900	0.2575	0	-0.0351
6	0	-0.0525	1200	0.3478	0	-0.0489
7	0	-0.0760	1600	0.4589	0	-0.0613
8	0	-0.0944	2000	0.5750	0	-0.0715
9	0	-0.1097	2400	0.6830	0	-0.0896
10	0	-0.1187	2800	0.7924	0	-0.1053
11	0	-0.1511	3200	0.9016	0	-0.1237
12	0	-0.1620	3500	1.0028	0	-0.1311
13	0	-0.1723	3700	1.0740	0	-0.1448
14	0	-0.1802	3800	1.0905	0	-0.1489
15	0	-0.1904	3900	1.1248	0	-0.1556
16	-10	-0.1962	3900	1.1278	0	-0.1552
17	-20	-0.2021	3900	1.1329	0	-0.1529
18	-30	-0.2079	3900	1.1353	0	-0.1502
19	-45	-0.2166	3900	1.1342	0	-0.1524
20	-60	-0.2254	3900	1.1349	0	-0.1513
21	-75	-0.2341	3900	1.1458	0	-0.1543
22	-90	-0.2428	3900	1.1523	0	-0.1543
23	-105	-0.2516	3900	1.1649	0	-0.1567
24	-120	-0.2603	3900	1.1640	0	-0.1532
25	-135	-0.2690	3900	1.1661	0	-0.1562
26	-150	-0.2778	3900	1.1648	0	-0.1504
27	-165	-0.2865	3900	1.1740	0	-0.1504
28	-180	-0.2954	3900	1.1765	0	-0.1468
29	-195	-0.3049	3900	1.1892	0	-0.1483
30	-210	-0.3115	3900	1.1930	0	-0.1445
31	-225	-0.3208	3900	1.1884	0	-0.1493
32	-240	-0.3307	3900	1.2044	0	-0.1458
33	-255	-0.3387	3900	1.2075	0	-0.1478
34	-270	-0.3480	3900	1.2021	0	-0.1440
35	-285	-0.3591	3900	1.2075	0	-0.1460
36	-300	-0.3696	3900	1.2141	0	-0.1487
37	-315	-0.3790	3900	1.2179	0	-0.1436
38	-330	-0.3922	3900	1.2295	0	-0.1398
39	-345	-0.4075	3900	1.2319	0	-0.1427
40	-360	-0.4219	3900	1.2349	0	-0.1405
41	-375	-0.4454	3900	1.2407	0	-0.1444

Table A.23

TEST 6B ... 0.5 F(CU) SPEC 4,H2 7/30/82

STRESS - STRAIN DATA

	X-AXIS STRESS (PSI)	X-AXIS STRAIN (MILS/IN)	Y-AXIS STRESS (PSI)	Y-AXIS STRAIN (MILS/IN)	Z-AXIS STRESS (PSI)	Z-AXIS STRAIN (MILS/IN)
1	0	0.0000	0	0.0000	0	0.0000
2	0	-0.0089	200	0.0513	0	-0.0107
3	0	-0.0178	400	0.1235	0	-0.0215
4	0	-0.0268	600	0.1646	0	-0.0339
5	0	-0.0405	900	0.2321	0	-0.0551
6	0	-0.0600	1200	0.3052	0	-0.0614
7	0	-0.0731	1600	0.4112	0	-0.0819
8	0	-0.0852	2000	0.5387	0	-0.1023
9	0	-0.1095	2500	0.6946	0	-0.1347
10	0	-0.1234	3000	0.8855	0	-0.1610
11	0	-0.1457	3400	1.0248	0	-0.1836
12	0	-0.1670	3700	1.1488	0	-0.1998
13	0	-0.1735	3800	1.1982	0	-0.2053
14	0	-0.1823	3900	1.2403	0	-0.2154
15	-10	-0.1872	3900	1.2471	0	-0.2151
16	-20	-0.1922	3900	1.2473	0	-0.2180
17	-30	-0.1976	3900	1.2518	0	-0.2138
18	-45	-0.2052	3900	1.2566	0	-0.2218
19	-60	-0.2111	3900	1.2590	0	-0.2180
20	-75	-0.2187	3900	1.2693	0	-0.2204
21	-90	-0.2275	3900	1.2711	0	-0.2241
22	-105	-0.2331	3900	1.2716	0	-0.2217
23	-120	-0.2424	3900	1.2779	0	-0.2227
24	-135	-0.2494	3900	1.2832	0	-0.2251
25	-150	-0.2567	3900	1.2905	0	-0.2253
26	-165	-0.2683	3900	1.2916	0	-0.2221
27	-180	-0.2767	3900	1.3039	0	-0.2224
28	-195	-0.2846	3900	1.3053	0	-0.2283
29	-210	-0.2970	3900	1.3113	0	-0.2276
30	-225	-0.3082	3900	1.3161	0	-0.2319
31	-240	-0.3230	3900	1.3240	0	-0.2288
32	-255	-0.3468	3900	1.3252	0	-0.2285
33	-270	-0.3732	3900	1.3351	0	-0.2363

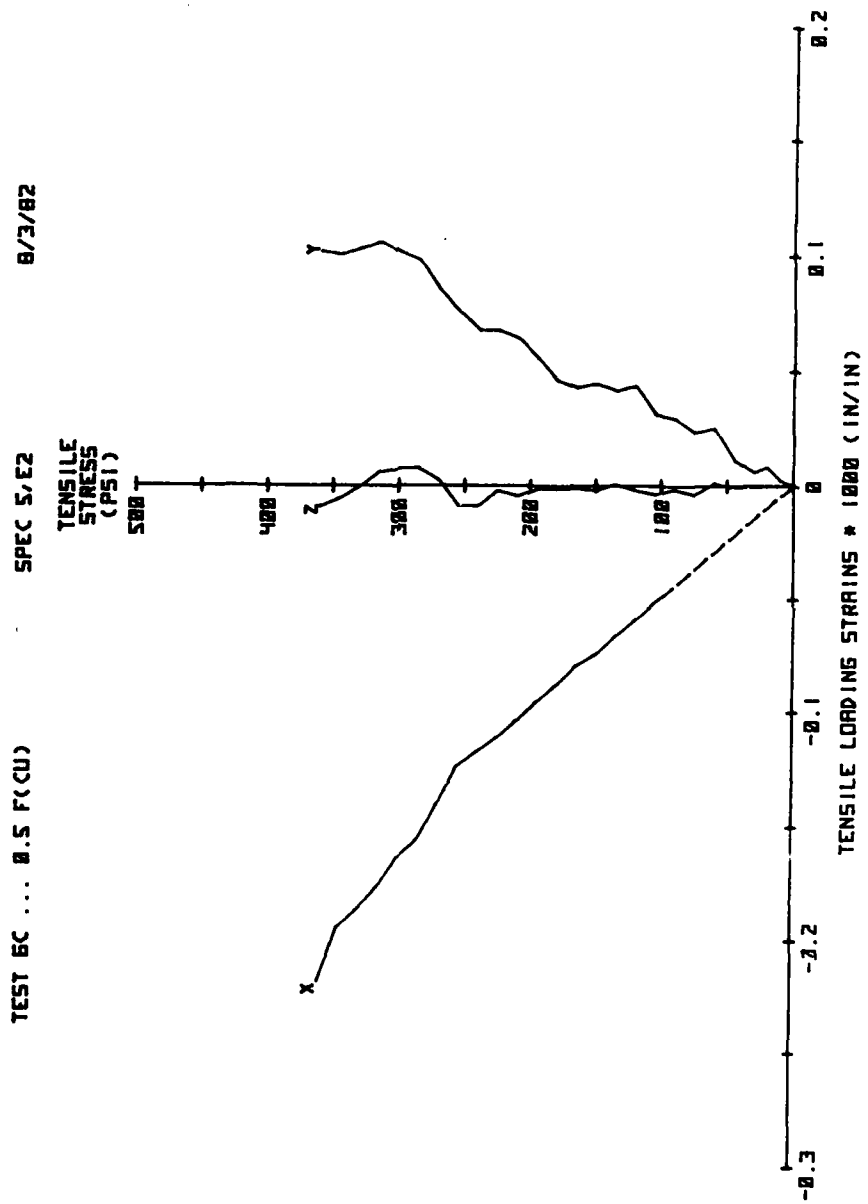

Fig. A.23 Test Results

Table A.24

TEST 6C ... 0.5 F(CU) SPEC 5,E2 8/3/82

STRESS - STRAIN DATA

	X-AXIS STRESS (PSI)	X-AXIS STRAIN (MILS/IN)	Y-AXIS STRESS (PSI)	Y-AXIS STRAIN (MILS/IN)	Z-AXIS STRESS (PSI)	Z-AXIS STRAIN (MILS/IN)
1	0	0.0000	0	0.0000	0	0.0000
2	0	-0.0094	200	0.0614	0	-0.0136
3	0	-0.0188	400	0.1227	0	-0.0257
4	0	-0.0282	600	0.1841	0	-0.0362
5	0	-0.0408	900	0.2762	0	-0.0525
6	0	-0.0596	1200	0.3735	0	-0.0722
7	0	-0.0747	1600	0.4873	0	-0.0796
8	0	-0.0942	2000	0.6127	0	-0.0983
9	0	-0.1113	2400	0.7281	0	-0.1154
10	0	-0.1315	2800	0.8668	0	-0.1367
11	0	-0.1491	3200	1.0056	0	-0.1688
12	0	-0.1645	3500	1.1175	0	-0.1882
13	0	-0.1721	3700	1.1750	0	-0.2087
14	0	-0.1774	3800	1.2180	0	-0.2224
15	0	-0.1873	3900	1.2546	0	-0.2278
16	-10	-0.1922	3900	1.2574	0	-0.2280
17	-20	-0.1971	3900	1.2630	0	-0.2281
18	-30	-0.2020	3900	1.2610	0	-0.2283
19	-45	-0.2094	3900	1.2659	0	-0.2285
20	-60	-0.2167	3900	1.2798	0	-0.2265
21	-75	-0.2240	3900	1.2781	0	-0.2317
22	-90	-0.2314	3900	1.2843	0	-0.2294
23	-105	-0.2384	3900	1.2862	0	-0.2317
24	-120	-0.2462	3900	1.2985	0	-0.2298
25	-135	-0.2534	3900	1.2963	0	-0.2271
26	-150	-0.2615	3900	1.2995	0	-0.2299
27	-165	-0.2668	3900	1.2976	0	-0.2291
28	-180	-0.2752	3900	1.3008	0	-0.2291
29	-195	-0.2826	3900	1.3106	0	-0.2295
30	-210	-0.2912	3900	1.3191	0	-0.2324
31	-225	-0.2985	3900	1.3225	0	-0.2300
32	-240	-0.3047	3900	1.3224	0	-0.2368
33	-255	-0.3110	3900	1.3305	0	-0.2367
34	-270	-0.3279	3900	1.3402	0	-0.2252
35	-285	-0.3436	3900	1.3531	0	-0.2200
36	-300	-0.3512	3900	1.3566	0	-0.2206
37	-315	-0.3644	3900	1.3608	0	-0.2217
38	-330	-0.3739	3900	1.3580	0	-0.2281
39	-345	-0.3817	3900	1.3553	0	-0.2336
40	-360	-0.4056	3900	1.3567	0	-0.2371

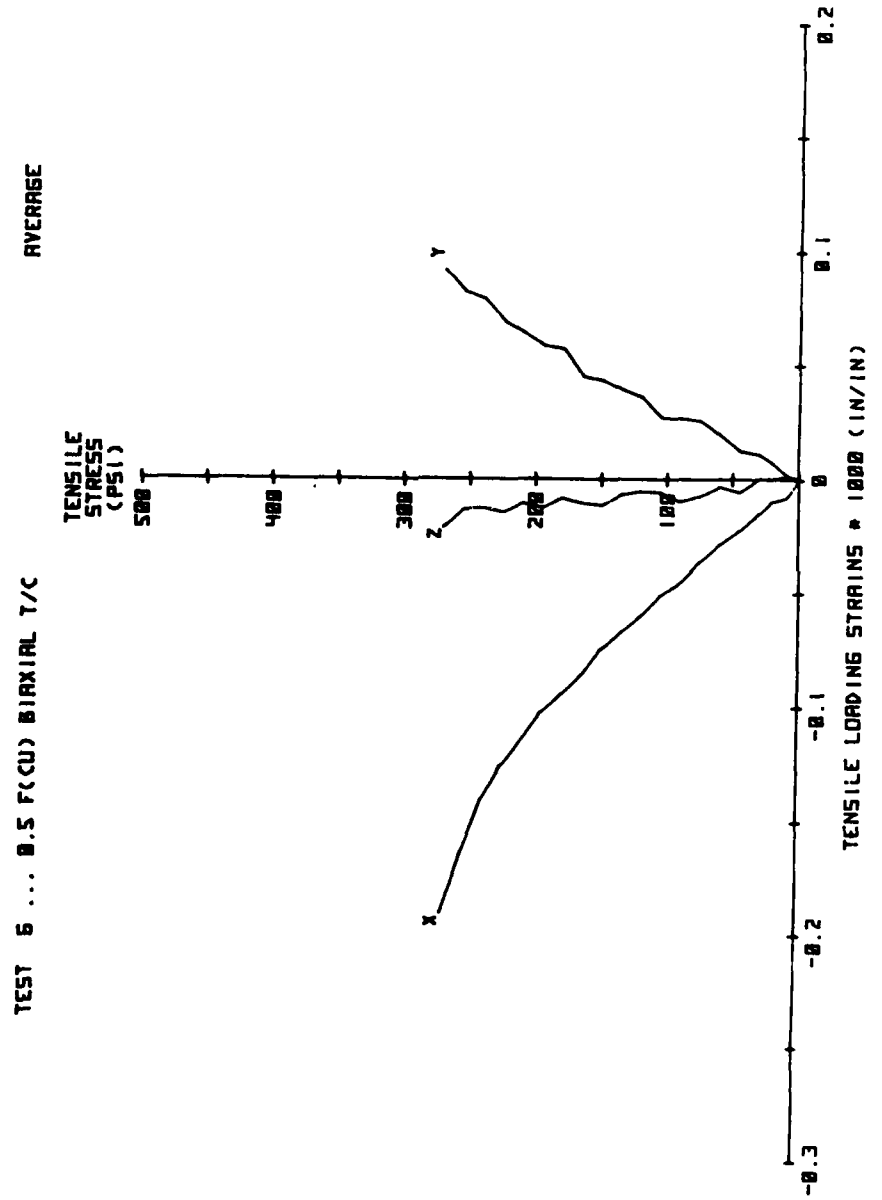

Fig. A.24 Test Results

Table A.25

TEST 6D ... 0.5 F(CU) SPEC 5;G5 3/31/82

STRESS - STRAIN DATA

	X-AXIS STRESS (PSI)	X-AXIS STRAIN (MILS/IN)	Y-AXIS STRESS (PSI)	Y-AXIS STRAIN (MILS/IN)	Z-AXIS STRESS (PSI)	Z-AXIS STRAIN (MILS/IN)
1	0	0.0000	0	0.0000	0	0.0000
2	0	-0.0084	200	0.0455	0	-0.0185
3	0	-0.0193	400	0.0890	0	-0.0213
4	0	-0.0291	600	0.1446	0	-0.0242
5	0	-0.0437	900	0.2102	0	-0.0338
6	0	-0.0650	1200	0.2707	0	0.0459
7	0	-0.0925	1600	0.3564	0	-0.0637
8	0	-0.1214	2000	0.4443	0	-0.0844
9	0	-0.1537	2400	0.5393	0	-0.0985
10	0	-0.1658	2800	0.6519	0	-0.1123
11	0	-0.1770	3200	0.7727	0	-0.1263
12	0	-0.1847	3500	0.8458	0	-0.1390
13	0	-0.1965	3700	0.9189	0	-0.1432
14	0	-0.2058	3800	0.9361	0	-0.1588
15	0	-0.2205	3900	0.9686	0	-0.1663
16	-10	-0.2328	3900	0.9674	0	-0.1646
17	-20	-0.2432	3900	0.9769	0	-0.1636
18	-30	-0.2564	3900	0.9794	0	-0.1675
19	-45	-0.2276	3900	0.9776	0	-0.1717
20	-60	-0.2422	3900	0.9892	0	-0.1707
21	-75	-0.2567	3900	0.9912	0	-0.1762
22	-90	-0.2700	3900	0.9917	0	-0.1773
23	-105	-0.2937	3900	0.9918	0	-0.1717
24	-120	-0.3094	3900	1.0034	0	-0.1700
25	-135	-0.3217	3900	1.0047	0	-0.1705
26	-150	-0.3362	3900	1.0055	0	-0.1795
27	-165	-0.3558	3900	1.0077	0	-0.1808
28	-180	-0.3296	3900	1.0198	0	-0.1757
29	-195	-0.3482	3900	1.0212	0	-0.1790
30	-210	-0.3222	3900	1.0260	0	-0.1757
31	-225	-0.3470	3900	1.0313	0	-0.1792
32	-240	-0.3729	3900	1.0433	0	-0.1787
33	-255	-0.4012	3900	1.0483	0	-0.1808
34	-270	-0.4285	3900	1.0573	0	-0.1883
35	-285	-0.4584	3900	1.0587	0	-0.1839
36	-300	-0.4718	3900	1.0706	0	-0.1849

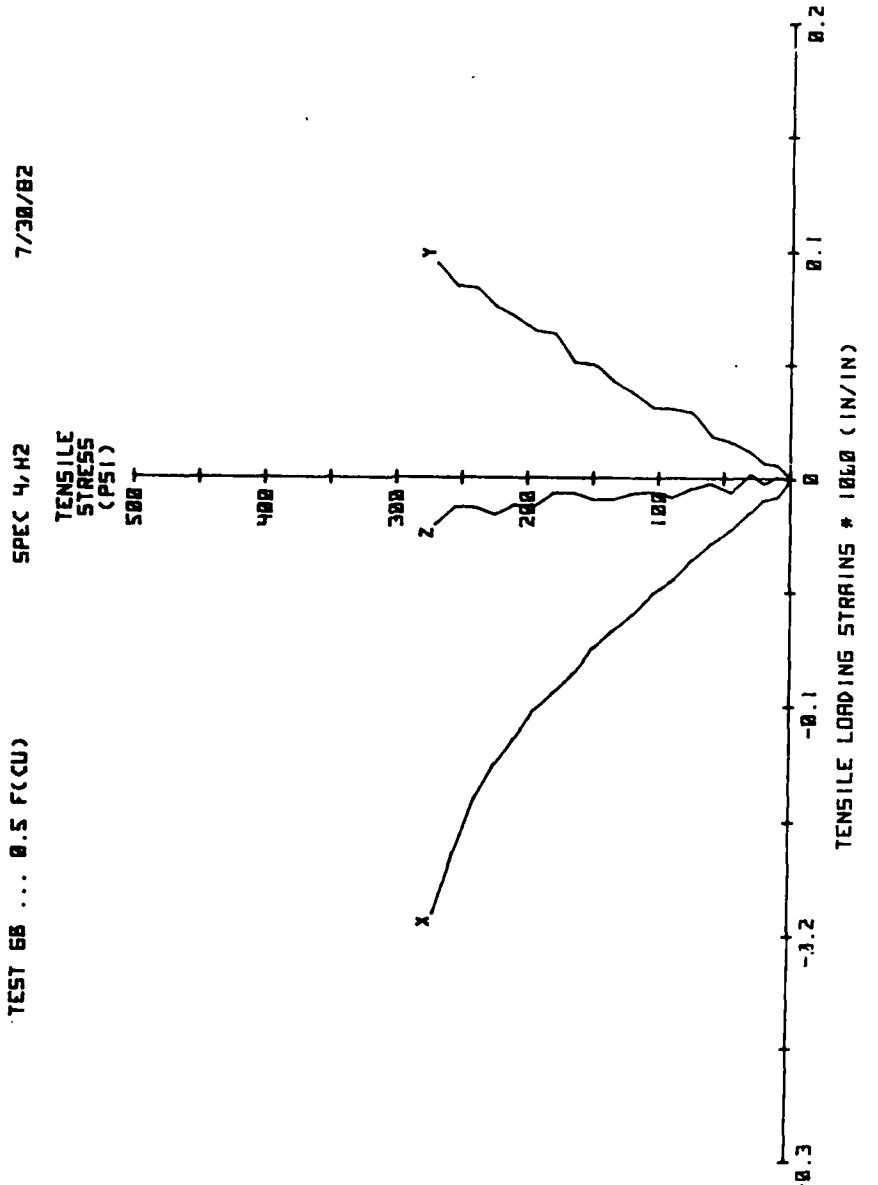

Fig. A.25 Test Results

Table A.26

TEST 9 ... 0.65 F(CU) BIAXIAL T/C AVERAGE

STRESS - STRAIN DATA

	X-AXIS STRESS (PSI)	X-AXIS STRAIN (MILS/IN)	Y-AXIS STRESS (PSI)	Y-AXIS STRAIN (MILS/IN)	Z-AXIS STRESS (PSI)	Z-AXIS STRAIN (MILS/IN)
1	0	0.0000	0	0.0000	0	0.0000
2	0	-0.0112	200	0.0541	0	-0.0112
3	0	-0.0229	400	0.1262	0	-0.0229
4	0	-0.0346	600	0.1787	0	-0.0346
5	0	-0.0522	900	0.2608	0	-0.0522
6	0	-0.0740	1200	0.3425	0	-0.0740
7	0	-0.0935	1500	0.4224	0	-0.0935
8	0	-0.1080	1800	0.5117	0	-0.1080
9	0	-0.1297	2200	0.6298	0	-0.1297
10	0	-0.1502	2600	0.7524	0	-0.1502
11	0	-0.1722	3000	0.8753	0	-0.1722
12	0	-0.1980	3500	1.0359	0	-0.1980
13	0	-0.2306	4000	1.2070	0	-0.2306
14	0	-0.2555	4400	1.3717	0	-0.2555
15	0	-0.2752	4700	1.4840	0	-0.2752
16	0	-0.2903	4900	1.5720	0	-0.2903
17	0	-0.3032	5000	1.6191	0	-0.3032
18	-10	-0.3070	5000	1.6240	0	-0.3025
19	-20	-0.3104	5000	1.6283	0	-0.3036
20	-30	-0.3139	5000	1.6326	0	-0.3046
21	-45	-0.3190	5000	1.6389	0	-0.3089
22	-60	-0.3227	5000	1.6471	0	-0.3082
23	-75	-0.3311	5000	1.6538	0	-0.3098
24	-90	-0.3351	5000	1.6610	0	-0.3126
25	-105	-0.3395	5000	1.6680	0	-0.3144
26	-120	-0.3448	5000	1.6734	0	-0.3134
27	-135	-0.3498	5000	1.6758	0	-0.3144
28	-150	-0.3545	5000	1.6825	0	-0.3155
29	-165	-0.3607	5000	1.6880	0	-0.3170
30	-180	-0.3669	5000	1.6946	0	-0.3163
31	-195	-0.3726	5000	1.7039	0	-0.3209
32	-210	-0.3839	5000	1.7070	0	-0.3222
33	-225	-0.4003	5000	1.7189	0	-0.3260
34	-240	-0.4138	5000	1.7318	0	-0.3278
35	-270	-0.4785	5000	1.7464	0	-0.3379

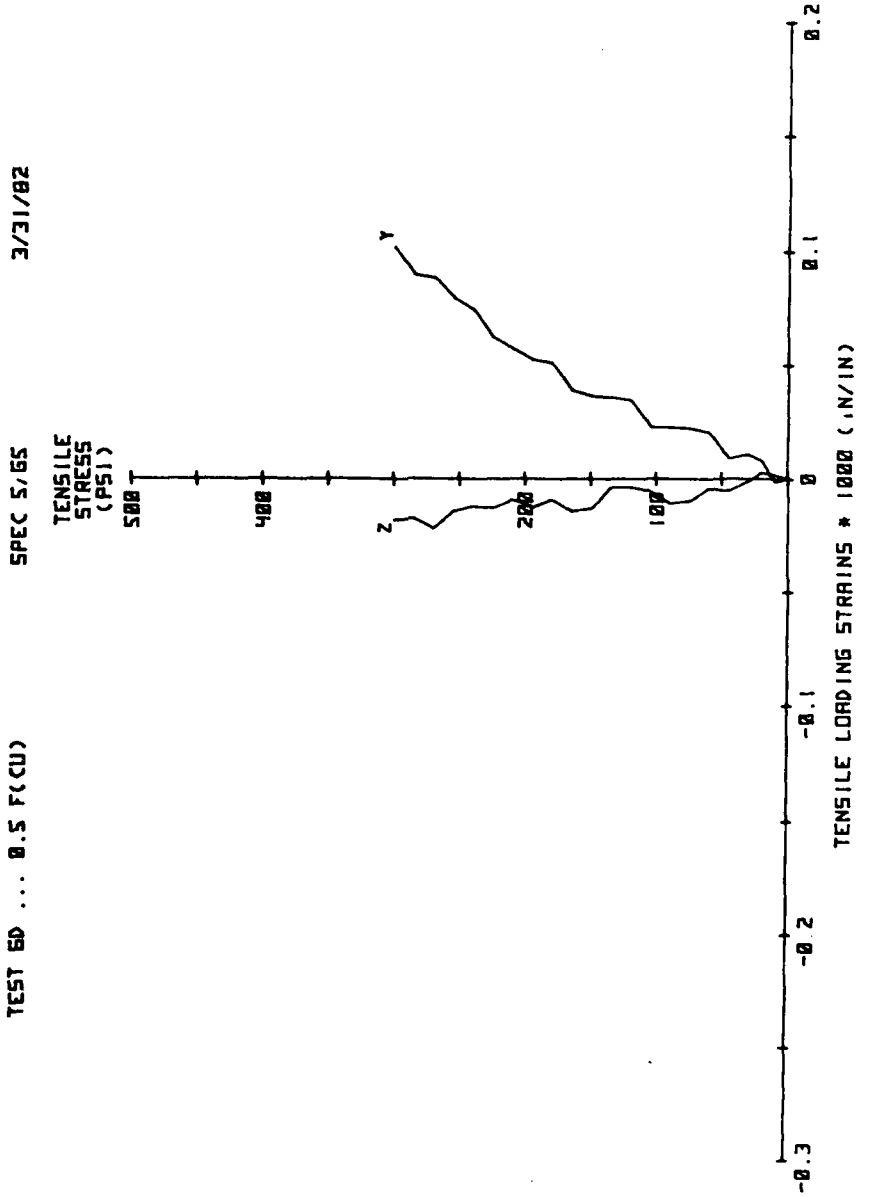

Fig. A.26 Test Results

Table A.27

TEST 9A ... 0.65 F(CU) SPEC 4,H3 7/26/82

STRESS - STRAIN DATA

	X-AXIS STRESS (PSI)	X-AXIS STRAIN (MILS/IN)	Y-AXIS STRESS (PSI)	Y-AXIS STRAIN (MILS/IN)	Z-AXIS STRESS (PSI)	Z-AXIS STRAIN (MILS/IN)
1	0	0.0000	0	0.0000	0	0.0000
2	0	-0.0114	200	0.0947	0	-0.0146
3	0	-0.0227	400	0.1275	0	-0.0291
4	0	-0.0341	600	0.1706	0	-0.0437
5	0	-0.0512	900	0.2417	0	-0.0656
6	0	-0.0937	1200	0.3102	0	-0.0887
7	0	-0.1050	1500	0.3780	0	-0.1129
8	0	-0.1138	1800	0.4654	0	-0.1331
9	0	-0.1277	2200	0.5775	0	-0.1649
10	0	-0.1426	2600	0.6990	0	-0.1872
11	0	-0.1640	3000	0.8229	0	-0.2097
12	0	-0.1897	3500	0.9920	0	-0.2458
13	0	-0.2220	4000	1.1672	0	0.2890
14	0	-0.2486	4400	1.3295	0	-0.3209
15	0	-0.2699	4700	1.4376	0	-0.3466
16	0	-0.2900	4900	1.5223	0	-0.3633
17	0	-0.3050	5000	1.5712	0	-0.3795
18	-10	-0.3082	5000	1.5763	0	-0.3813
19	-20	-0.3114	5000	1.5813	0	-0.3831
20	-30	-0.3147	5000	1.5864	0	-0.3849
21	-45	-0.3195	5000	1.5940	0	-0.3873
22	-60	-0.3213	5000	1.6016	0	-0.3889
23	-75	-0.3291	5000	1.6076	0	-0.3934
24	-90	-0.3340	5000	1.6164	0	-0.3964
25	-105	-0.3401	5000	1.6238	0	-0.3980
26	-120	-0.3431	5000	1.6326	0	-0.4012
27	-135	-0.3484	5000	1.6393	0	-0.4033
28	-150	-0.3529	5000	1.6482	0	-0.4060
29	-165	-0.3581	5000	1.6545	0	-0.4111
30	-180	-0.3638	5000	1.6616	0	-0.4085
31	-195	-0.3732	5000	1.6792	0	-0.4163
32	-210	-0.3871	5000	1.6842	0	-0.4149
33	-225	-0.4097	5000	1.6986	0	-0.4236
34	-240	-0.4929	5000	1.7105	0	-0.4390

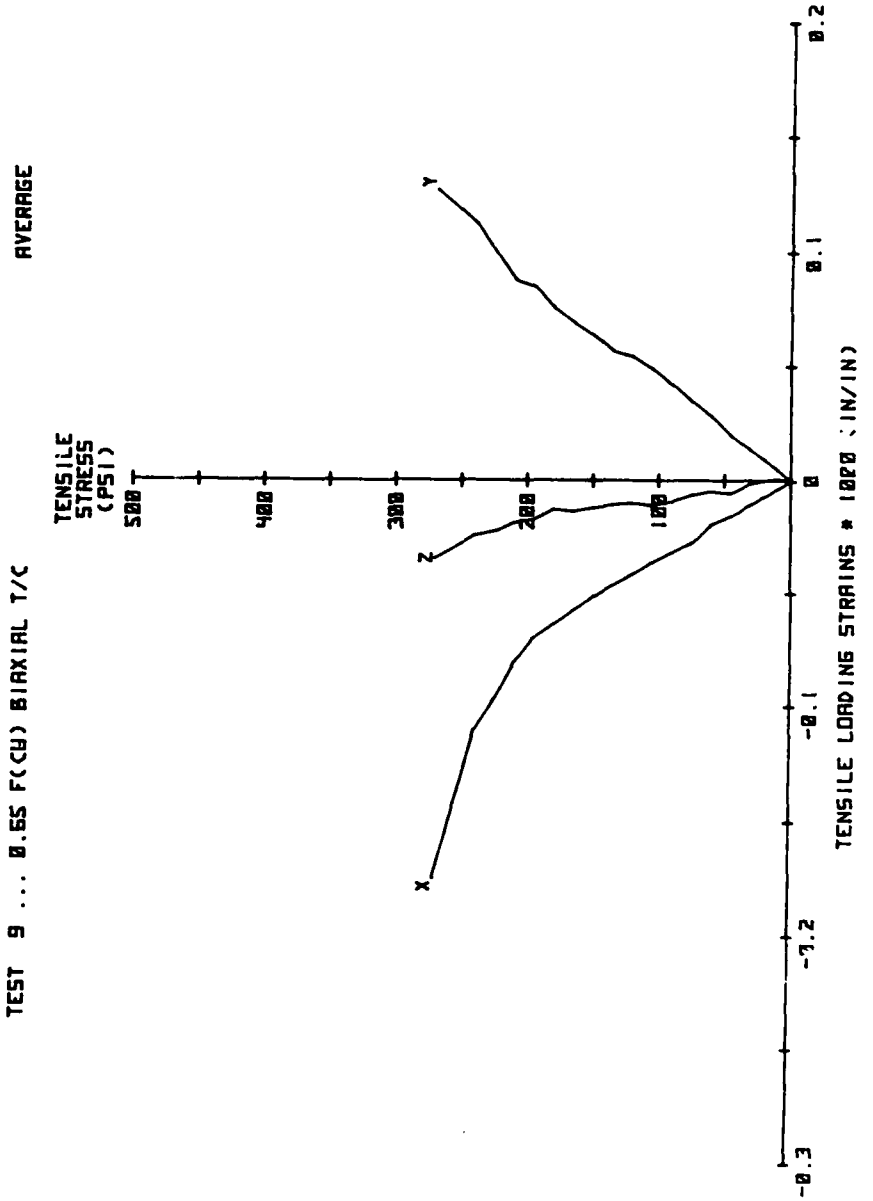

Fig. A.27 Test Results

Table A.28

TEST 9B ... 0.65 F(CU) SPEC 4,H4 8/4/82

STRESS - STRAIN DATA

	X-AXIS STRESS (PSI)	X-AXIS STRAIN (MILS/IN)	Y-AXIS STRESS (PSI)	Y-AXIS STRAIN (MILS/IN)	Z-AXIS STRESS (PSI)	Z-AXIS STRAIN (MILS/IN)
1	0	0.0000	0	0.0000	0	0.0000
2	0	-0.0112	200	0.0620	0	-0.0096
3	0	-0.0223	400	0.1239	0	-0.0193
4	0	-0.0335	600	0.1859	0	-0.0289
5	0	-0.0503	900	0.2788	0	-0.0434
6	0	-0.0576	1200	0.3738	0	-0.0579
7	0	-0.0854	1500	0.4659	0	-0.0724
8	0	-0.1025	1800	0.5569	0	-0.0845
9	0	-0.1229	2200	0.6811	0	-0.1050
10	0	-0.1410	2600	0.8048	0	-0.1317
11	0	-0.1664	3000	0.9267	0	-0.1504
12	0	-0.1960	3500	1.0789	0	-0.1623
13	0	-0.2243	4000	1.2459	0	-0.1889
14	0	-0.2437	4400	1.4128	0	-0.2106
15	0	-0.2616	4700	1.5293	0	-0.2246
16	0	-0.2748	4900	1.6207	0	-0.2348
17	0	-0.2813	5000	1.6660	0	-0.2487
18	-10	-0.2850	5000	1.6696	0	-0.2490
19	-20	-0.2886	5000	1.6732	0	-0.2493
20	-30	-0.2923	5000	1.6768	0	-0.2495
21	-45	-0.2978	5000	1.6817	0	-0.2558
22	-60	-0.3033	5000	1.6905	0	-0.2527
23	-75	-0.3124	5000	1.6964	0	-0.2515
24	-90	-0.3154	5000	1.7035	0	-0.2539
25	-105	-0.3182	5000	1.7101	0	-0.2560
26	-120	-0.3257	5000	1.7122	0	-0.2507
27	-135	-0.3304	5000	1.7102	0	-0.2506
28	-150	-0.3353	5000	1.7149	0	-0.2502
29	-165	-0.3425	5000	1.7194	0	-0.2480
30	-180	-0.3492	5000	1.7255	0	-0.2492
31	-195	-0.3513	5000	1.7265	0	-0.2506
32	-210	-0.3600	5000	1.7279	0	-0.2548
33	-225	-0.3703	5000	1.7371	0	-0.2535
34	-240	-0.3825	5000	1.7574	0	-0.2558
35	-255	-0.3975	5000	1.7598	0	-0.2551
36	-270	-0.4126	5000	1.7773	0	-0.2562
37	-285	-0.4259	5000	1.7795	0	-0.2587
38	-300	-0.4436	5000	1.7769	0	-0.2598

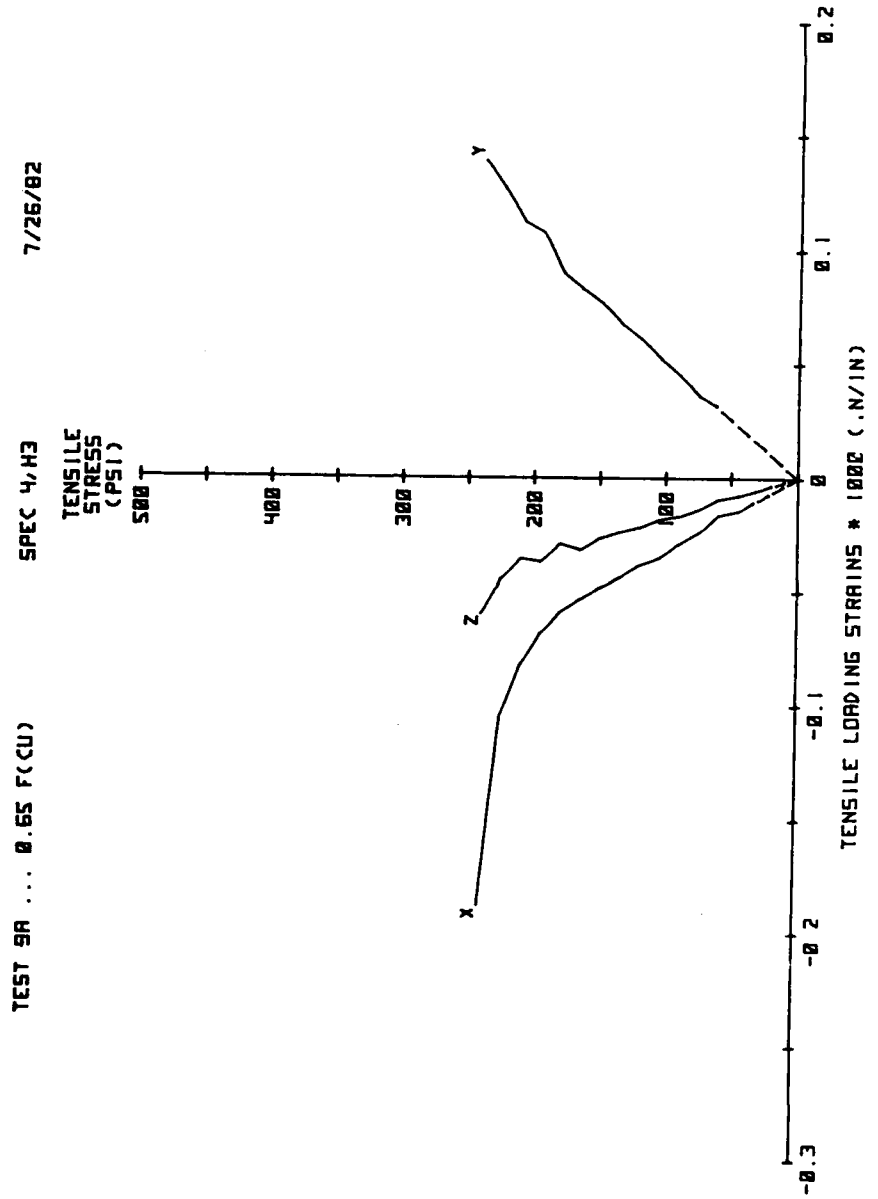

Fig. A.28 Test Results

Table A.29

TEST 7 ... 0.8 F(CU) BIAXIAL T/C AVERAGE

STRESS - STRAIN DATA

	X-AXIS STRESS (PSI)	X-AXIS STRAIN (MILS/IN)	Y-AXIS STRESS (PSI)	Y-AXIS STRAIN (MILS/IN)	Z-AXIS STRESS (PSI)	Z-AXIS STRAIN (MILS/IN)
1	0	0.0000	0	0.0000	0	0.0000
2	0	-0.0180	200	0.0651	0	-0.0180
3	0	-0.0231	400	0.1218	0	-0.0231
4	0	-0.0293	600	0.1677	0	-0.0293
5	0	-0.0423	900	0.2520	0	-0.0423
6	0	-0.0559	1200	0.3441	0	-0.0559
7	0	-0.0721	1600	0.4503	0	-0.0721
8	0	-0.0896	2000	0.5635	0	-0.0896
9	0	-0.1142	2500	0.7087	0	-0.1142
10	0	-0.1420	3000	0.8735	0	-0.1420
11	0	-0.1676	3500	1.0584	0	-0.1676
12	0	-0.2024	4000	1.2595	0	-0.2024
13	0	-0.2382	4500	1.4679	0	-0.2382
14	0	-0.2799	5000	1.6981	0	-0.2799
15	0	-0.3267	5500	1.9100	0	-0.3267
16	0	-0.3735	5800	2.1219	0	-0.3735
17	0	-0.4006	6000	2.2341	0	-0.4006
18	0	-0.4212	6100	2.2970	0	-0.4212
19	0	-0.4456	6200	2.3962	0	-0.4456
20	-10	-0.4595	6200	2.4084	0	-0.4483
21	-20	-0.4697	6200	2.4176	0	-0.4515
22	-30	-0.4805	6200	2.4272	0	-0.4549
23	-45	-0.4953	6200	2.4468	0	-0.4662
24	-60	-0.5112	6200	2.4594	0	-0.4700
25	-75	-0.5295	6200	2.4756	0	-0.4755
26	-90	-0.5505	6200	2.4891	0	-0.4813
27	-105	-0.5698	6200	2.5048	0	-0.4846
28	-120	-0.5956	6200	2.5227	0	-0.4904
29	-135	-0.6308	6200	2.5455	0	-0.4955
30	-150	-0.6745	6200	2.5707	0	-0.5026
31	-165	-0.7406	6200	2.6028	0	-0.5271
32	-180	-0.9652	6200	2.6718	0	-0.6001

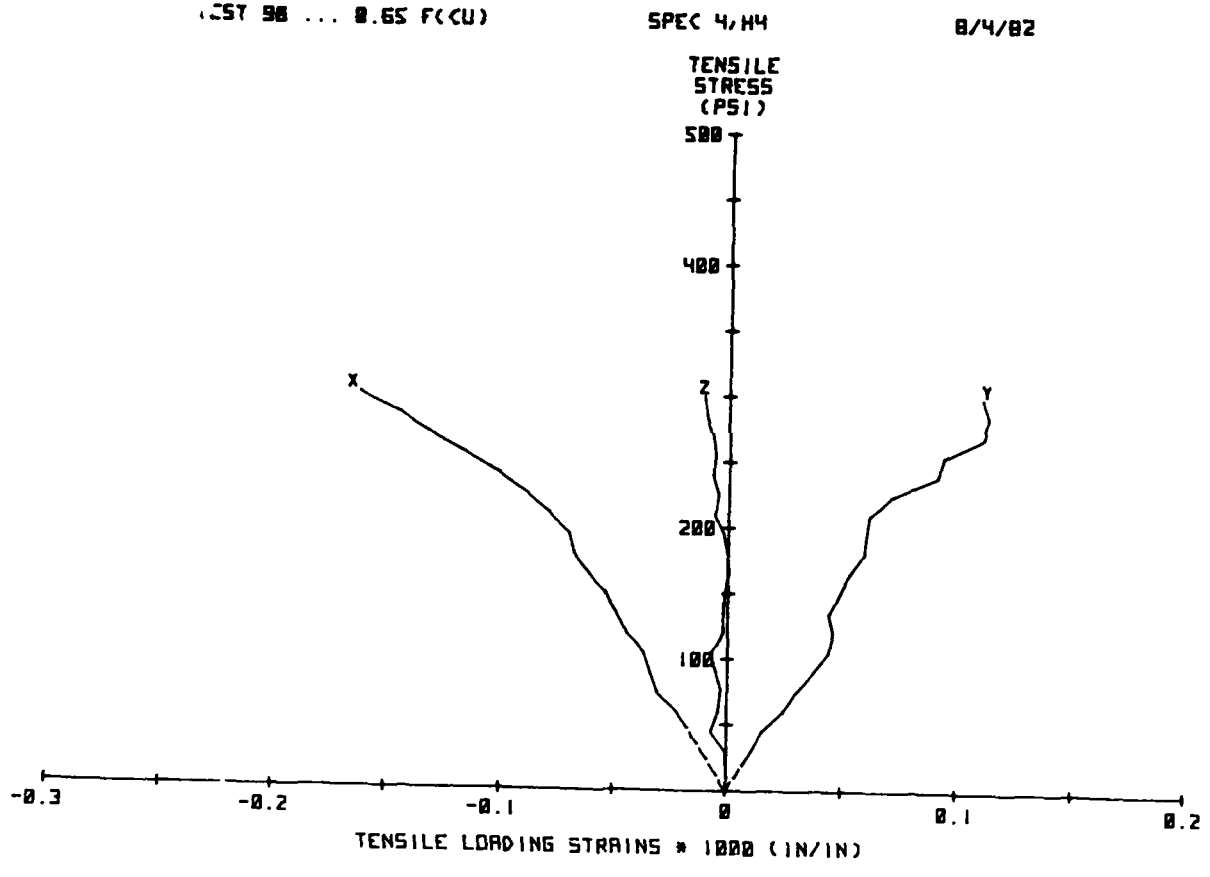

Fig. A.29 Test Results

Table A.30

TEST 7B ... 0.8 F(CU) SPEC 5,E6 7/28/82

STRESS - STRAIN DATA

	X-AXIS STRESS (PSI)	X-AXIS STRAIN (MILS/IN)	Y-AXIS STRESS (PSI)	Y-AXIS STRAIN (MILS/IN)	Z-AXIS STRESS (PSI)	Z-AXIS STRAIN (MILS/IN)
1	0	0.0000	0	0.0000	0	0.0000
2	0	-0.0181	200	0.0554	0	-0.0190
3	0	-0.0269	400	0.1085	0	-0.0182
4	0	-0.0297	600	0.1401	0	-0.0244
5	0	-0.0429	900	0.2142	0	-0.0382
6	0	-0.0525	1200	0.2852	0	-0.0517
7	0	-0.0737	1600	0.3936	0	-0.0634
8	0	-0.0896	2000	0.5019	0	-0.0813
9	0	-0.1152	2500	0.6426	0	-0.1031
10	0	-0.1403	3000	0.8109	0	-0.1280
11	0	-0.1686	3500	0.9930	0	-0.1509
12	0	-0.2037	4000	1.1830	0	-0.1814
13	0	-0.2403	4500	1.3853	0	-0.2061
14	0	-0.2876	5000	1.6148	0	-0.2386
15	0	-0.3409	5500	1.8386	0	-0.2848
16	0	-0.3826	5800	2.0046	0	-0.3059
17	0	-0.4138	6000	2.1292	0	-0.3292
18	0	-0.4356	6100	2.1900	0	-0.3379
19	0	-0.4722	6200	2.3197	0	-0.3563
20	-10	-0.4821	6200	2.3286	0	-0.3570
21	-20	-0.4910	6200	2.3356	0	-0.3572
22	-30	-0.5000	6200	2.3433	0	-0.3577
23	-45	-0.5111	6200	2.3647	0	-0.3644
24	-60	-0.5282	6200	2.3745	0	-0.3671
25	-75	-0.5423	6200	2.3892	0	-0.3707
26	-90	-0.5607	6200	2.3981	0	-0.3705
27	-105	-0.5800	6200	2.4114	0	-0.3754
28	-120	-0.6056	6200	2.4331	0	-0.3724
29	-135	-0.6438	6200	2.4597	0	-0.3747
30	-150	-0.6928	6200	2.4859	0	-0.3738
31	-165	-0.7846	6200	2.5222	0	-0.3821

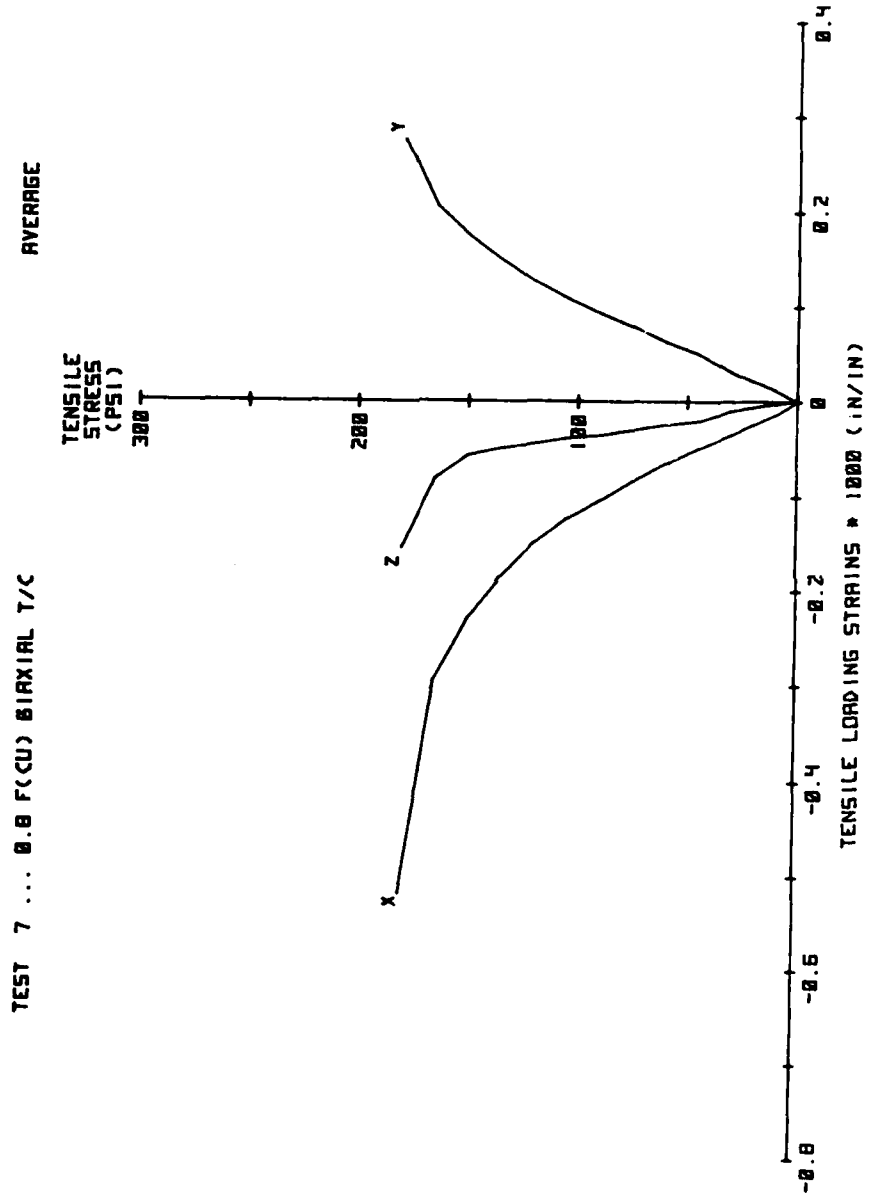

Fig. A.30 Test Results

Table A.31

TEST 7C ... 0.8 F(CU) SPEC 5,G4 8/6/82

STRESS - STRAIN DATA

	X-AXIS STRESS (PSI)	X-AXIS STRAIN (MILS/IN)	Y-AXIS STRESS (PSI)	Y-AXIS STRAIN (MILS/IN)	Z-AXIS STRESS (PSI)	Z-AXIS STRAIN (MILS/IN)
1	0	0.0000	0	0.0000	0	0.0000
2	0	-0.0137	200	0.0603	0	-0.0158
3	0	-0.0203	400	0.1206	0	-0.0216
4	0	-0.0328	600	0.1809	0	-0.0250
5	0	-0.0461	900	0.2755	0	-0.0366
6	0	-0.0586	1200	0.3887	0	-0.0556
7	0	-0.0745	1600	0.4925	0	-0.0715
8	0	-0.0939	2000	0.6107	0	-0.0880
9	0	-0.1264	2500	0.7604	0	-0.1067
10	0	-0.1582	3000	0.9218	0	-0.1360
11	0	-0.1903	3500	1.1095	0	-0.1555
12	0	-0.2291	4000	1.3216	0	-0.1899
13	0	-0.2729	4500	1.5363	0	-0.2279
14	0	-0.3210	5000	1.7670	0	-0.2668
15	0	-0.3828	5500	2.0278	0	-0.3192
16	0	-0.4404	5800	2.2248	0	-0.3596
17	0	-0.4649	6000	2.3246	0	-0.3891
18	0	-0.4949	6100	2.3896	0	-0.4110
19	0	-0.5181	6200	2.4584	0	-0.4305
20	-10	-0.5331	6200	2.4698	0	-0.4367
21	-20	-0.5446	6200	2.4812	0	-0.4430
22	-30	-0.5572	6200	2.4926	0	-0.4493
23	-45	-0.5756	6200	2.5104	0	-0.4651
24	-60	-0.5903	6200	2.5259	0	-0.4700
25	-75	-0.6128	6200	2.5435	0	-0.4774
26	-90	-0.6364	6200	2.5616	0	-0.4892
27	-105	-0.6557	6200	2.5797	0	-0.4909
28	-120	-0.6817	6200	2.5938	0	-0.5054
29	-135	-0.7140	6200	2.6129	0	-0.5133
30	-150	-0.7523	6200	2.6371	0	-0.5286
31	-165	-0.8012	6200	2.6632	0	-0.5487
32	-180	-0.8845	6200	2.7012	0	-0.5774
33	-195	-1.2420	6200	2.8030	0	-0.7152

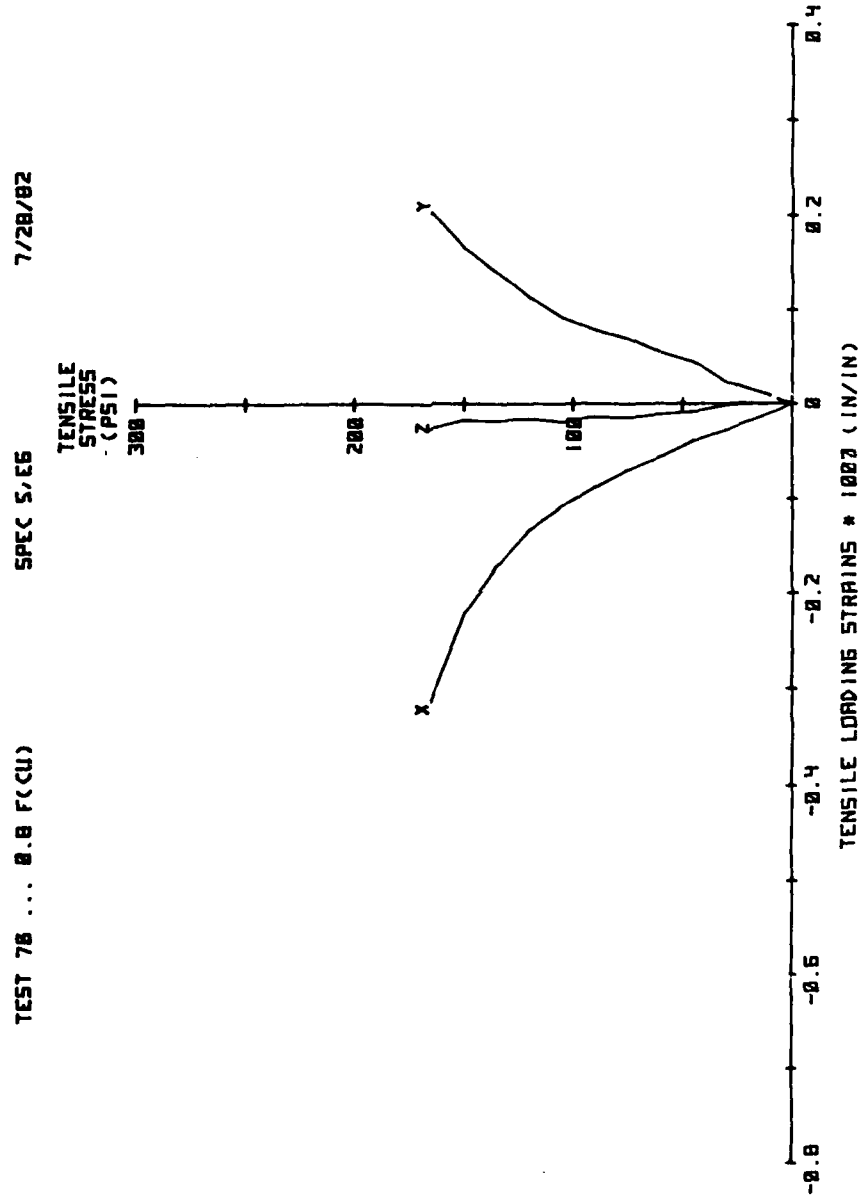

Fig. A.31 Test Results

Table A.32

TEST 7A ... 0.85 F(CU) SPEC 5,G2 7/17/82

STRESS - STRAIN DATA

	X-AXIS STRESS (PSI)	X-AXIS STRAIN (MILS/IN)	Y-AXIS STRESS (PSI)	Y-AXIS STRAIN (MILS/IN)	Z-AXIS STRESS (PSI)	Z-AXIS STRAIN (MILS/IN)
1	0	0.0000	0	0.0000	0	0.0000
2	0	-0.0097	200	0.0638	0	-0.0090
3	0	-0.0194	400	0.1163	0	-0.0179
4	0	-0.0317	600	0.1643	0	-0.0309
5	0	-0.0451	900	0.2518	0	-0.0404
6	0	-0.0591	1200	0.3312	0	-0.0564
7	0	-0.0740	1600	0.4423	0	-0.0715
8	0	-0.0943	2000	0.5684	0	-0.0888
9	0	-0.1178	2500	0.7338	0	-0.1083
10	0	-0.1451	3000	0.8949	0	-0.1341
11	0	-0.1738	3500	1.0579	0	-0.1599
12	0	-0.2057	4000	1.2480	0	-0.1909
13	0	-0.2368	4500	1.4809	0	-0.2258
14	0	-0.2734	5000	1.6718	0	-0.2598
15	0	-0.3262	5500	1.9379	0	-0.3121
16	0	-0.3916	6000	2.2166	0	-0.3622
17	0	-0.4405	6300	2.3912	0	-0.4134
18	0	-0.5103	6500	2.5696	0	-0.5042
19	0	-0.5963	6600	2.7512	0	-0.6211
20	-10	-0.6167	6600	2.7691	0	-0.6283
21	-20	-0.6370	6600	2.7871	0	-0.6355
22	-30	-0.6574	6600	2.8050	0	-0.6427
23	-40	-0.6778	6600	2.8230	0	-0.6537
24	-50	-0.6989	6600	2.8409	0	-0.6579
25	-60	-0.7186	6600	2.8598	0	-0.6641
26	-70	-0.7389	6600	2.8805	0	-0.6723
27	-80	-0.7592	6600	2.8993	0	-0.6757
28	-90	-0.7800	6600	2.9130	0	-0.6861
29	-100	-0.8033	6600	2.9365	0	-0.6945
30	-110	-0.8328	6600	2.9407	0	-0.7069
31	-120	-0.8646	6600	2.9531	0	-0.7232
32	-130	-0.9057	6600	2.9750	0	-0.7410
33	-140	-0.9671	6600	2.9950	0	-0.7676
34	-150	-1.1289	6600	3.0440	0	-0.8455

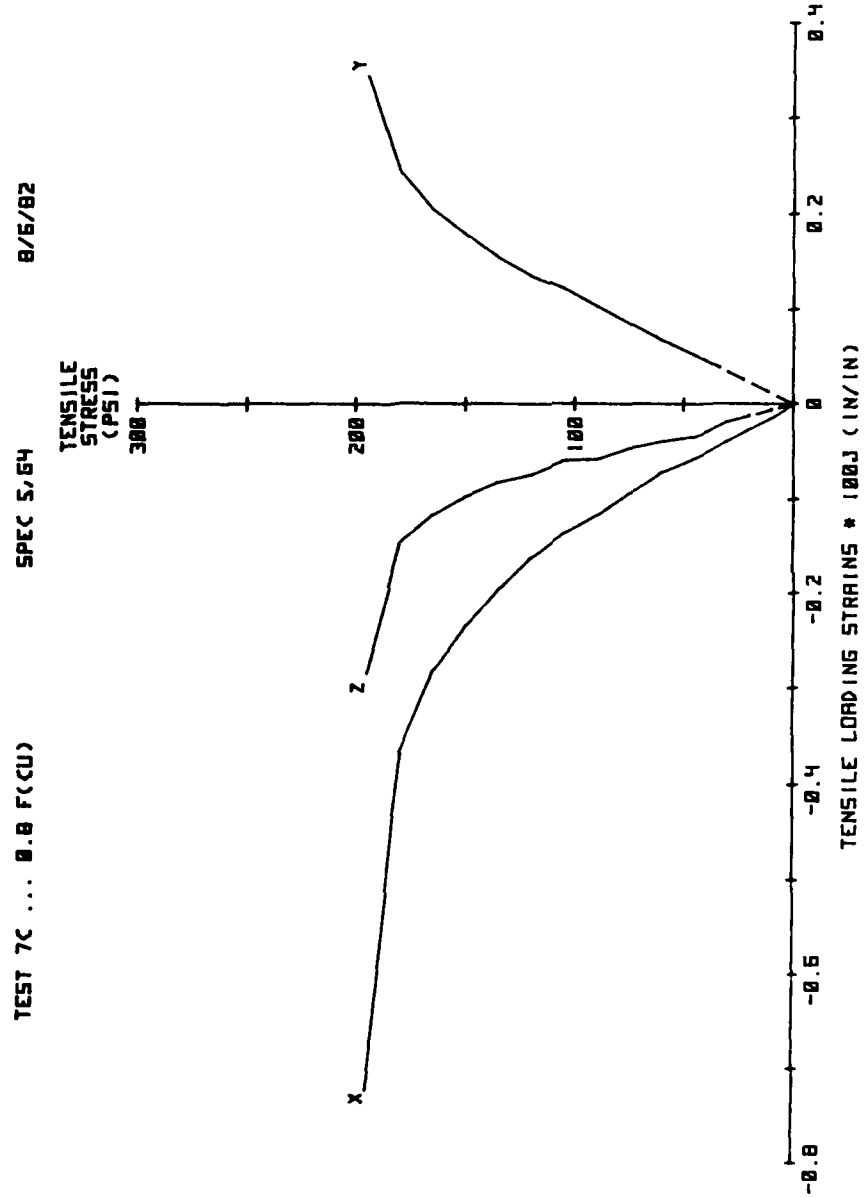

Fig. A.32 Test Results

Table A.33

TEST 2 ... UNIAXIAL COMPRESSION FIBERED CONCRETE AVERAGE

STRESS - STRAIN DATA

	X-AXIS STRESS (PSI)	X-AXIS STRAIN (MILS/IN)	Y-AXIS STRESS (PSI)	Y-AXIS STRAIN (MILS/IN)	Z-AXIS STRESS (PSI)	Z-AXIS STRAIN (MILS/IN)
1	0	0.0000	0	0.0000	0	0.0000
2	200	0.0702	0	-0.0076	0	-0.0076
3	400	0.1349	0	-0.0156	0	-0.0156
4	600	0.2036	0	-0.0236	0	-0.0236
5	800	0.2647	0	-0.0339	0	-0.0339
6	1000	0.3304	0	-0.0402	0	-0.0402
7	1200	0.3953	0	-0.0484	0	-0.0484
8	1400	0.4554	0	-0.0555	0	-0.0555
9	1600	0.5237	0	-0.0635	0	-0.0635
10	1800	0.5933	0	-0.0707	0	-0.0707
11	2000	0.6638	0	-0.0792	0	-0.0792
12	2200	0.7321	0	-0.0869	0	-0.0869
13	2400	0.7989	0	-0.0951	0	-0.0951
14	2600	0.8588	0	-0.1058	0	-0.1058
15	2800	0.9330	0	-0.1091	0	-0.1091
16	3000	1.0006	0	-0.1152	0	-0.1152
17	3200	1.0671	0	-0.1235	0	-0.1235
18	3400	1.1234	0	-0.1369	0	-0.1369
19	3600	1.1903	0	-0.1466	0	-0.1466
20	3800	1.2657	0	-0.1575	0	-0.1575
21	4000	1.3203	0	-0.1726	0	-0.1726
22	4200	1.3997	0	-0.1882	0	-0.1882
23	4400	1.4680	0	-0.2053	0	-0.2053
24	4600	1.5467	0	-0.2190	0	-0.2190
25	4800	1.6332	0	-0.2324	0	-0.2324
26	5000	1.7066	0	-0.2509	0	-0.2509
27	5200	1.7953	0	-0.2730	0	-0.2730
28	5400	1.8789	0	-0.2970	0	-0.2970
29	5600	2.0081	0	-0.3184	0	-0.3184
30	5800	2.0938	0	-0.3469	0	-0.3469
31	6000	2.2319	0	-0.3818	0	-0.3818
32	6200	2.3275	0	-0.4215	0	-0.4215
33	6400	2.4685	0	-0.4763	0	-0.4763
34	6600	2.5865	0	-0.5372	0	-0.5372
35	6800	2.7087	0	-0.6200	0	-0.6200
36	7000	2.8373	0	-0.7320	0	-0.7320
37	7200	3.0456	0	-0.8828	0	-0.8828
38	7400	3.3868	0	-1.0952	0	-1.0952
39	7600	3.7228	0	-1.3267	0	-1.3267

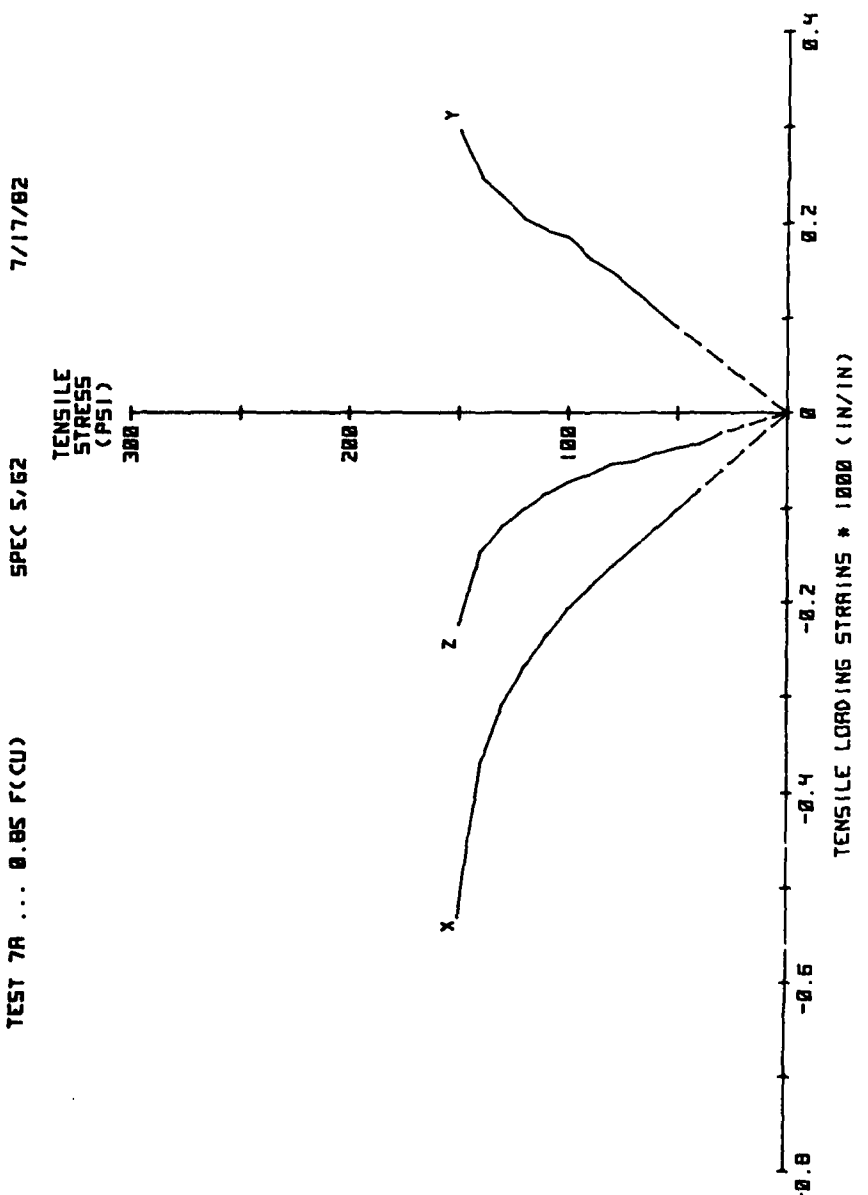

Fig. A.33 Test Results

Table A.34

TEST 2A ... UNIAX COMP SPEC 4.G6 3/19/82

STRESS - STRAIN DATA

	X-AXIS STRESS (PSI)	X-AXIS STRAIN (MILS/IN)	Y-AXIS STRESS (PSI)	Y-AXIS STRAIN (MILS/IN)	Z-AXIS STRESS (PSI)	Z-AXIS STRAIN (MILS/IN)
1	0	0.0000	0	0.0000	0	0.0000
2	200	0.0710	0	-0.0093	0	-0.0133
3	400	0.1420	0	-0.0101	0	-0.0129
4	600	0.2129	0	-0.0284	0	-0.0264
5	800	0.2839	0	-0.0374	0	-0.0357
6	1000	0.3549	0	-0.0418	0	-0.0372
7	1200	0.4259	0	-0.0493	0	-0.0489
8	1400	0.4968	0	-0.0638	0	-0.0531
9	1600	0.5678	0	-0.0690	0	-0.0571
10	1800	0.6388	0	-0.0761	0	-0.0715
11	2000	0.7098	0	-0.0799	0	-0.0783
12	2200	0.7807	0	-0.0906	0	-0.0888
13	2400	0.8517	0	-0.0983	0	-0.0947
14	2600	0.9227	0	-0.1066	0	-0.1027
15	2800	0.9937	0	-0.1034	0	-0.0975
16	3000	1.0646	0	-0.1034	0	-0.0976
17	3200	1.1356	0	-0.1073	0	-0.1044
18	3400	1.2066	0	-0.1163	0	-0.1229
19	3600	1.2776	0	-0.1340	0	-0.1356
20	3800	1.3452	0	-0.1482	0	-0.1459
21	4000	1.4246	0	-0.1604	0	-0.1699
22	4200	1.4943	0	-0.1764	0	-0.1862
23	4400	1.5535	0	-0.1949	0	-0.2054
24	4600	1.6270	0	-0.2084	0	-0.2261
25	4800	1.7177	0	-0.2249	0	-0.2399
26	5000	1.7681	0	-0.2473	0	-0.2609
27	5200	1.8788	0	-0.2695	0	-0.2858
28	5400	1.9763	0	-0.2938	0	-0.3131
29	5600	2.1403	0	-0.3130	0	-0.3353
30	5800	2.2575	0	-0.3413	0	-0.3635
31	6000	2.4355	0	-0.3779	0	-0.4043
32	6200	2.5523	0	-0.4115	0	-0.4441
33	6400	2.7020	0	-0.4583	0	-0.4913
34	6600	2.8294	0	-0.5091	0	-0.5458
35	6800	2.9270	0	-0.5707	0	-0.6220
36	7000	3.0016	0	-0.6706	0	-0.7995
37	7200	3.2666	0	-0.7890	0	-1.0021
38	7400	3.5924	0	-1.0802	0	-1.3119
39	7600	4.0144	0	-1.3831	0	-1.6628

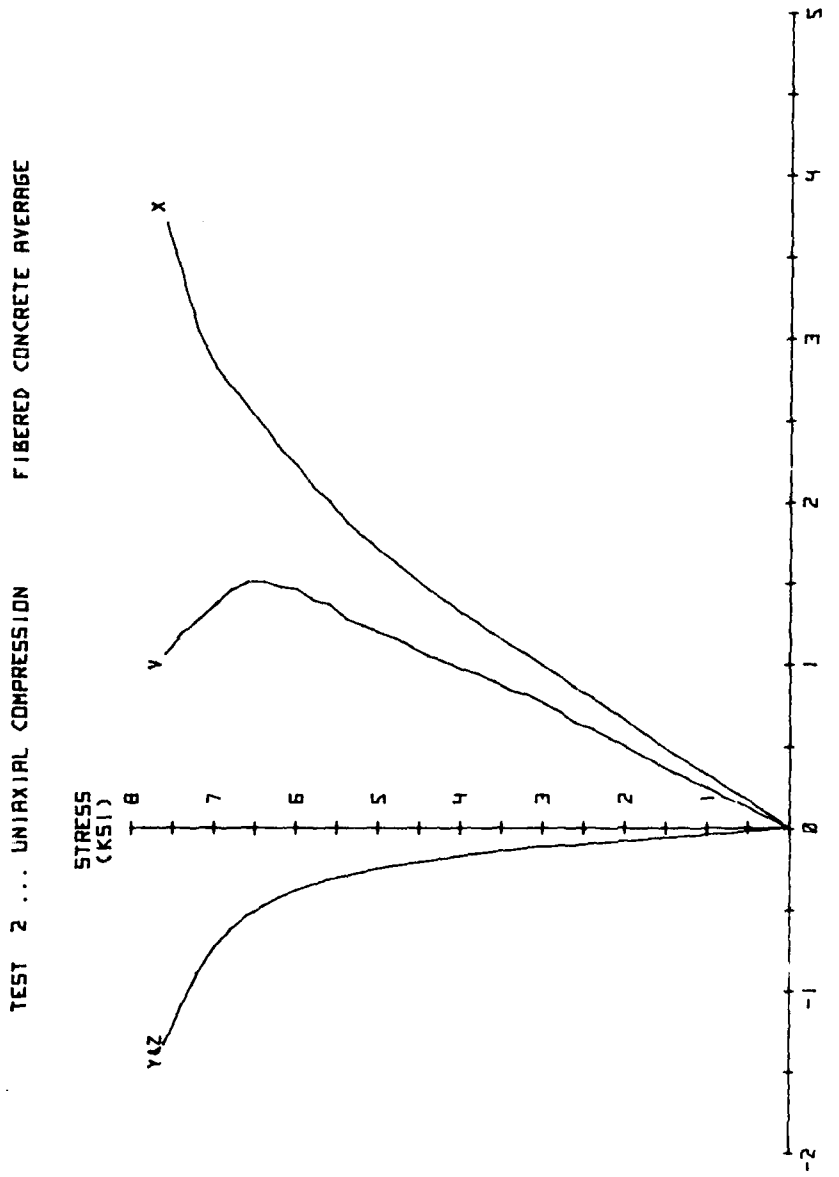

Fig. A.34 Test Results

Table A.35

TEST 2B ... UNIAX COMP SPEC 4,E6 3/20/82

STRESS - STRAIN DATA

	X-AXIS STRESS (PSI)	X-AXIS STRAIN (MILS/IN)	Y-AXIS STRESS (PSI)	Y-AXIS STRAIN (MILS/IN)	Z-AXIS STRESS (PSI)	Z-AXIS STRAIN (MILS/IN)
1	0	0.0000	0	0.0000	0	0.0000
2	200	0.0663	0	0.0194	0	-0.0094
3	400	0.1326	0	0.0050	0	-0.0212
4	600	0.1988	0	-0.0121	0	-0.0281
5	800	0.2578	0	-0.0241	0	-0.0347
6	1000	0.3192	0	-0.0397	0	-0.0445
7	1200	0.3879	0	-0.0431	0	-0.0530
8	1400	0.4525	0	-0.0542	0	-0.0541
9	1600	0.5116	0	-0.0612	0	-0.0567
10	1800	0.5892	0	-0.0638	0	-0.0666
11	2000	0.6736	0	-0.0753	0	-0.0788
12	2200	0.7379	0	-0.0760	0	-0.0842
13	2400	0.8200	0	-0.0813	0	-0.0899
14	2600	0.8702	0	-0.0894	0	-0.0969
15	2800	0.9527	0	-0.0939	0	-0.0999
16	3000	1.0236	0	-0.0938	0	-0.1136
17	3200	1.1033	0	-0.1081	0	-0.1189
18	3400	1.1158	0	-0.1198	0	-0.1399
19	3600	1.1784	0	-0.1257	0	-0.1497
20	3800	1.2608	0	-0.1328	0	-0.1591
21	4000	1.2897	0	-0.1431	0	-0.1716
22	4200	1.3783	0	-0.1524	0	-0.1893
23	4400	1.4477	0	-0.1698	0	-0.2041
24	4600	1.5357	0	-0.1772	0	-0.2222
25	4800	1.6137	0	-0.1893	0	-0.2305
26	5000	1.7160	0	-0.2032	0	-0.2445
27	5200	1.7788	0	-0.2181	0	-0.2667
28	5400	1.8833	0	-0.2368	0	-0.2957
29	5600	1.9734	0	-0.2540	0	-0.3114
30	5800	2.0814	0	-0.2801	0	-0.3386
31	6000	2.1696	0	-0.3047	0	-0.3592
32	6200	2.2849	0	-0.3327	0	-0.3925
33	6400	2.4349	0	-0.3808	0	-0.4404
34	6600	2.5452	0	-0.4130	0	-0.4833
35	6800	2.6839	0	-0.4713	0	-0.5379
36	7000	2.8949	0	-0.5426	0	-0.6123
37	7200	3.1061	0	-0.6225	0	-0.6907
38	7400	3.4627	0	-0.7493	0	-0.8127
39	7600	3.7127	0	-0.8965	0	-0.9376

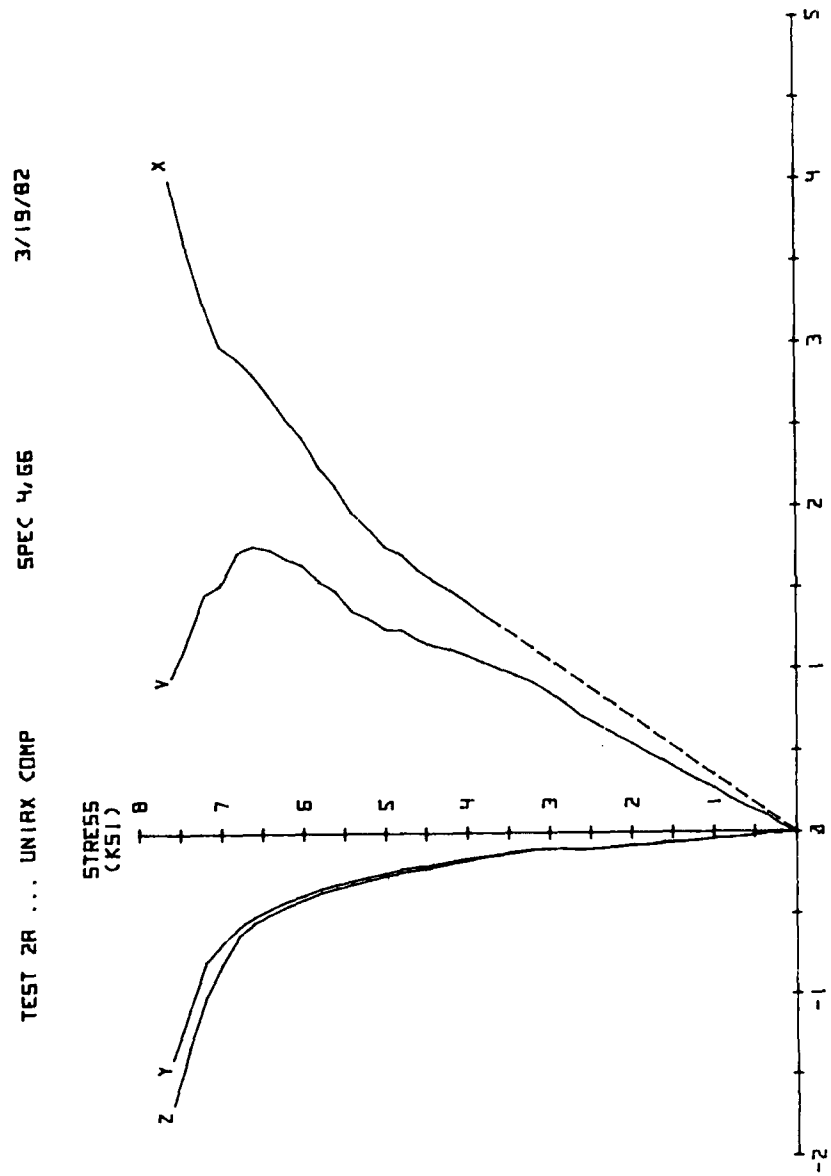

Fig. A.35 Test Results

Table A.36

TEST 2D ... UNIAX COMP SPEC 5,H4 3/23/82

STRESS - STRAIN DATA

	X-AXIS STRESS (PSI)	X-AXIS STRAIN (MILS/IN)	Y-AXIS STRESS (PSI)	Y-AXIS STRAIN (MILS/IN)	Z-AXIS STRESS (PSI)	Z-AXIS STRAIN (MILS/IN)
1	0	0.0000	0	0.0000	0	0.0000
2	200	0.0343	0	-0.0080	0	-0.0100
3	400	0.0687	0	-0.0161	0	-0.0201
4	600	0.1030	0	-0.0241	0	-0.0301
5	800	0.1296	0	-0.0285	0	-0.0470
6	1000	0.1776	0	-0.0374	0	-0.0546
7	1200	0.2173	0	-0.0455	0	-0.0628
8	1400	0.2414	0	-0.0563	0	-0.0711
9	1600	0.2802	0	-0.0693	0	-0.0794
10	1800	0.2973	0	-0.0740	0	-0.0819
11	2000	0.3386	0	-0.0811	0	-0.0985
12	2200	0.3630	0	-0.0887	0	-0.1078
13	2400	0.4139	0	-0.0965	0	-0.1236
14	2600	0.4602	0	-0.1136	0	-0.1353
15	2800	0.5363	0	-0.1159	0	-0.1372
16	3000	0.5487	0	-0.1204	0	-0.1461
17	3200	0.5705	0	-0.1259	0	-0.1587
18	3400	0.5925	0	-0.1330	0	-0.1724
19	3600	0.6311	0	-0.1412	0	-0.1798
20	3800	0.6490	0	-0.1523	0	-0.1953
21	4000	0.6862	0	-0.1671	0	-0.2178
22	4200	0.6789	0	-0.1863	0	-0.2382
23	4400	0.7274	0	-0.2029	0	-0.2567
24	4600	0.7898	0	-0.2234	0	-0.2739
25	4800	0.8728	0	-0.2422	0	-0.2836
26	5000	0.9322	0	-0.2749	0	-0.2962
27	5200	1.0397	0	-0.3059	0	-0.3172
28	5400	1.3223	0	-0.3358	0	-0.3436
29	5600	1.4333	0	-0.3702	0	-0.3638
30	5800	1.6293	0	-0.4166	0	-0.3915
31	6000	1.8002	0	-0.4794	0	-0.4292
32	6200	1.9868	0	-0.5506	0	-0.4735
33	6400	2.2624	0	-0.6488	0	-0.5434
34	6600	2.5058	0	-0.7701	0	-0.6364
35	6800	2.8169	0	-0.9385	0	-0.7672
36	7000	3.1233	0	-1.1493	0	-0.9296
37	7200	3.5364	0	-1.4590	0	-1.1908
38	7300	3.8268	0	-1.7952	0	-1.4442

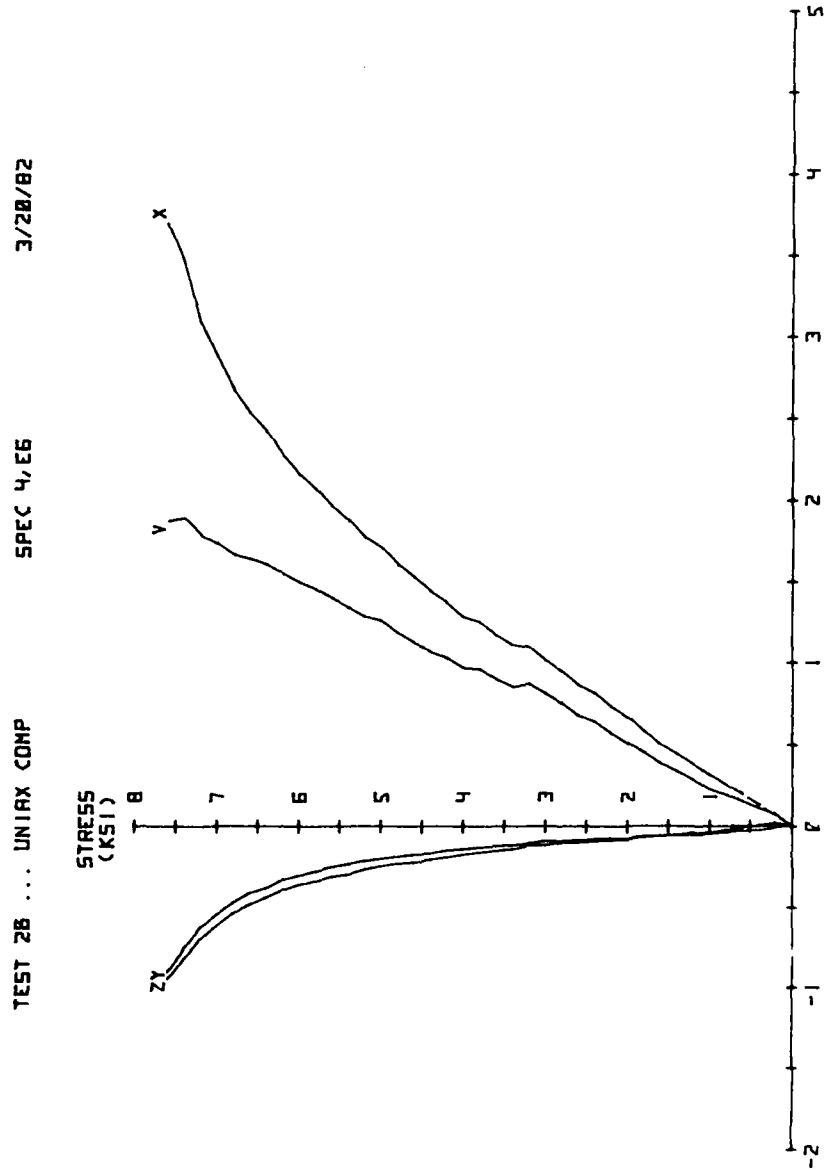

Fig. A.36 Test Results

Table A.37

TEST 2G ... UNIAX COMP SPEC 4,F5 7/8/82

STRESS - STRAIN DATA

	X-AXIS STRESS (PSI)	X-AXIS STRAIN (MILS/IN)	Y-AXIS STRESS (PSI)	Y-AXIS STRAIN (MILS/IN)	Z-AXIS STRESS (PSI)	Z-AXIS STRAIN (MILS/IN)
1	0	0.0000	0	0.0000	0	0.0000
2	200	0.0593	0	-0.0103	0	-0.0081
3	400	0.1160	0	-0.0225	0	-0.0317
4	600	0.1850	0	-0.0391	0	-0.0391
5	800	0.2383	0	-0.0462	0	-0.0465
6	1000	0.3029	0	-0.0509	0	-0.0448
7	1200	0.3580	0	-0.0597	0	-0.0540
8	1400	0.4028	0	-0.0654	0	-0.0553
9	1600	0.4775	0	-0.0825	0	-0.0621
10	1800	0.5378	0	-0.0917	0	-0.0694
11	2000	0.5939	0	-0.0971	0	-0.0741
12	2200	0.6637	0	-0.1064	0	-0.0820
13	2400	0.7109	0	-0.1155	0	-0.0904
14	2600	0.7695	0	-0.1334	0	-0.0977
15	2800	0.8386	0	-0.1458	0	-0.1087
16	3000	0.8996	0	-0.1575	0	-0.1185
17	3200	0.9482	0	-0.1645	0	-0.1290
18	3400	1.0336	0	-0.1756	0	-0.1442
19	3600	1.1009	0	-0.1877	0	-0.1480
20	3800	1.1770	0	-0.1977	0	-0.1580
21	4000	1.2325	0	-0.2073	0	-0.1728
22	4200	1.3124	0	-0.2246	0	-0.1811
23	4400	1.3887	0	-0.2411	0	-0.1964
24	4600	1.4632	0	-0.2473	0	-0.2029
25	4800	1.5541	0	-0.2637	0	-0.2139
26	5000	1.6217	0	-0.2833	0	-0.2263
27	5200	1.7143	0	-0.3062	0	-0.2440
28	5400	1.7631	0	-0.3234	0	-0.2632
29	5600	1.8965	0	-0.3447	0	-0.2840
30	5800	1.9285	0	-0.3660	0	-0.3067
31	6000	2.0764	0	-0.3949	0	-0.3339
32	6200	2.1311	0	-0.4258	0	-0.3704
33	6400	2.2546	0	-0.4678	0	-0.4092
34	6600	2.3708	0	-0.5112	0	-0.4578
35	6800	2.5012	0	-0.5699	0	-0.5119
36	7000	2.6013	0	-0.6142	0	-0.5673
37	7200	2.7501	0	-0.6908	0	-0.6472

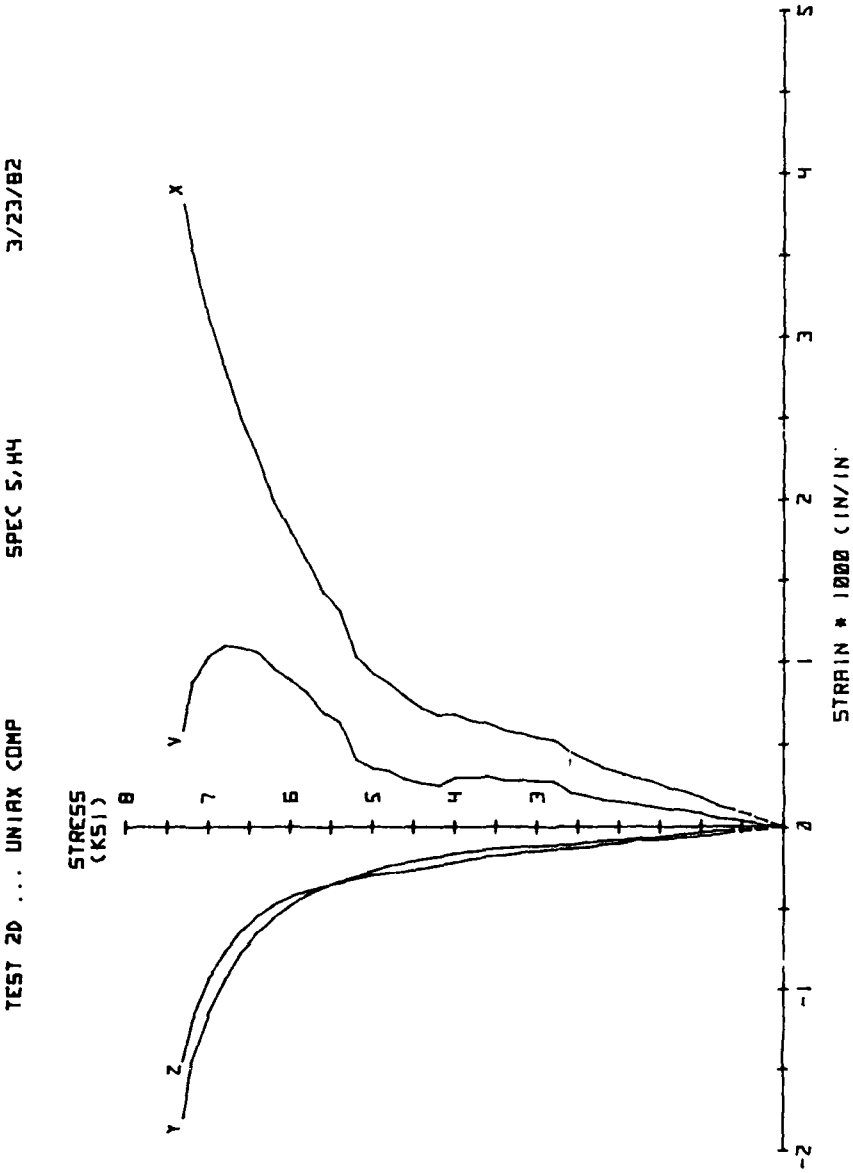

Fig. A.37 Test Results

Table A.38

TEST 2 ... UNIAXIAL COMPRESSION PLAIN CONCRETE AVERAGE

STRESS - STRAIN DATA

	X-AXIS STRESS (PSI)	X-AXIS STRAIN (MILS/IN)	Y-AXIS STRESS (PSI)	Y-AXIS STRAIN (MILS/IN)	Z-AXIS STRESS (PSI)	Z-AXIS STRAIN (MILS/IN)
1	0	0.0000	0	0.0000	0	0.0000
2	200	0.0695	0	-0.0090	0	-0.0090
3	400	0.1370	0	-0.0198	0	-0.0198
4	600	0.2045	0	-0.0327	0	-0.0327
5	800	0.2720	0	-0.0440	0	-0.0440
6	1000	0.3403	0	-0.0550	0	-0.0550
7	1200	0.4072	0	-0.0661	0	-0.0661
8	1400	0.4769	0	-0.0788	0	-0.0788
9	1600	0.5417	0	-0.0855	0	-0.0855
10	1800	0.6158	0	-0.0935	0	-0.0935
11	2000	0.6664	0	-0.1077	0	-0.1077
12	2200	0.7399	0	-0.1165	0	-0.1165
13	2400	0.8089	0	-0.1256	0	-0.1256
14	2600	0.8852	0	-0.1360	0	-0.1360
15	2800	0.9537	0	-0.1434	0	-0.1434
16	3000	1.0264	0	-0.1571	0	-0.1571
17	3200	1.1142	0	-0.1670	0	-0.1670
18	3400	1.1922	0	-0.1807	0	-0.1807
19	3600	1.2886	0	-0.1890	0	-0.1890
20	3800	1.3700	0	-0.2002	0	-0.2002
21	4000	1.4399	0	-0.2154	0	-0.2154
22	4200	1.5330	0	-0.2304	0	-0.2304
23	4400	1.6370	0	-0.2503	0	-0.2503
24	4600	1.7259	0	-0.2652	0	-0.2652
25	4800	1.8218	0	-0.2858	0	-0.2858
26	5000	1.9215	0	-0.3103	0	-0.3103
27	5200	2.0233	0	-0.3421	0	-0.3421
28	5400	2.1161	0	-0.3836	0	-0.3836
29	5600	2.2560	0	-0.4305	0	-0.4305
30	5800	2.3961	0	-0.5057	0	-0.5057
31	6000	2.5406	0	-0.5653	0	-0.5653
32	6200	2.7169	0	-0.6935	0	-0.6935
33	6400	2.9619	0	-0.8934	0	-0.8934

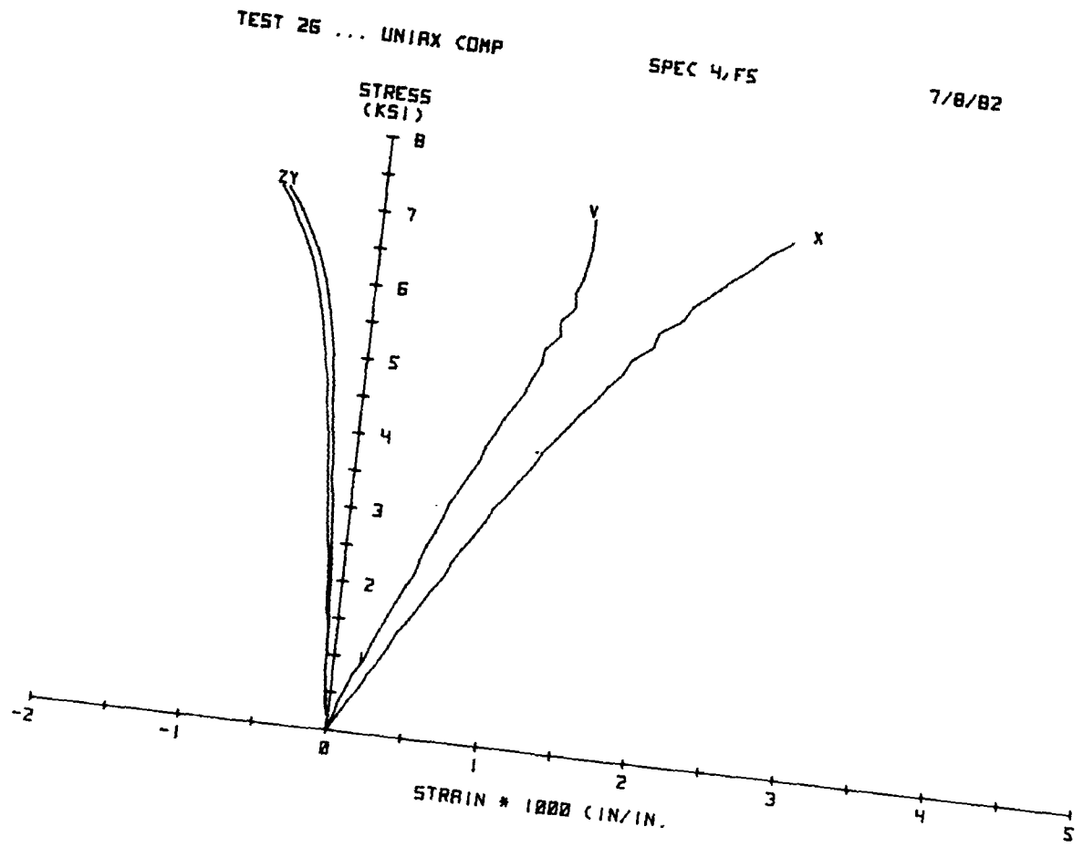

Fig. A.38 Test Results

Table A.39

TEST 2E ... UNIAX COMP SPEC 0,B4 6/12/82

STRESS - STRAIN DATA

	X-AXIS STRESS (PSI)	X-AXIS STRAIN (MILS/IN)	Y-AXIS STRESS (PSI)	Y-AXIS STRAIN (MILS/IN)	Z-AXIS STRESS (PSI)	Z-AXIS STRAIN (MILS/IN)
1	0	0.0000	0	0.0000	0	0.0000
2	200	0.0643	0	-0.0179	0	-0.0156
3	400	0.1287	0	-0.0357	0	-0.0313
4	600	0.1930	0	-0.0536	0	-0.0469
5	800	0.2573	0	-0.0714	0	-0.0626
6	1000	0.3217	0	-0.0893	0	-0.0782
7	1200	0.3860	0	-0.1071	0	-0.0939
8	1400	0.4720	0	-0.1250	0	-0.1095
9	1600	0.5154	0	-0.1428	0	-0.1252
10	1800	0.6027	0	-0.1607	0	-0.1408
11	2000	0.6081	0	-0.1768	0	-0.1850
12	2200	0.6769	0	-0.2016	0	-0.1837
13	2400	0.7433	0	-0.2150	0	-0.1906
14	2600	0.8526	0	-0.2321	0	-0.2053
15	2800	0.9330	0	-0.2400	0	-0.2151
16	3000	1.0232	0	-0.2623	0	-0.2330
17	3200	1.1579	0	-0.2917	0	-0.2529
18	3400	1.2509	0	-0.3103	0	-0.2649
19	3600	1.4124	0	-0.3243	0	-0.2818
20	3800	1.5140	0	-0.3416	0	-0.2860
21	4000	1.5983	0	-0.3504	0	-0.3234
22	4200	1.7466	0	-0.3665	0	-0.3282
23	4400	1.9094	0	-0.3943	0	-0.3585
24	4600	2.0203	0	-0.4045	0	-0.3831
25	4800	2.1716	0	-0.4251	0	-0.4147
26	5000	2.2932	0	-0.4471	0	-0.4400
27	5200	2.4660	0	-0.4700	0	-0.4801
28	5400	2.5930	0	-0.4902	0	-0.5261
29	5600	2.7175	0	-0.5144	0	-0.5798
30	5800	2.9283	0	-0.5499	0	-0.6107
31	6000	3.1269	0	-0.5816	0	-0.6664
32	6200	3.3384	0	-0.6369	0	-0.7593
33	6400	3.5399	0	-0.7104	0	-0.8822
34	6600	3.7828	0	-0.8002	0	-1.0274
35	6800	4.0292	0	-0.8981	0	-1.2408

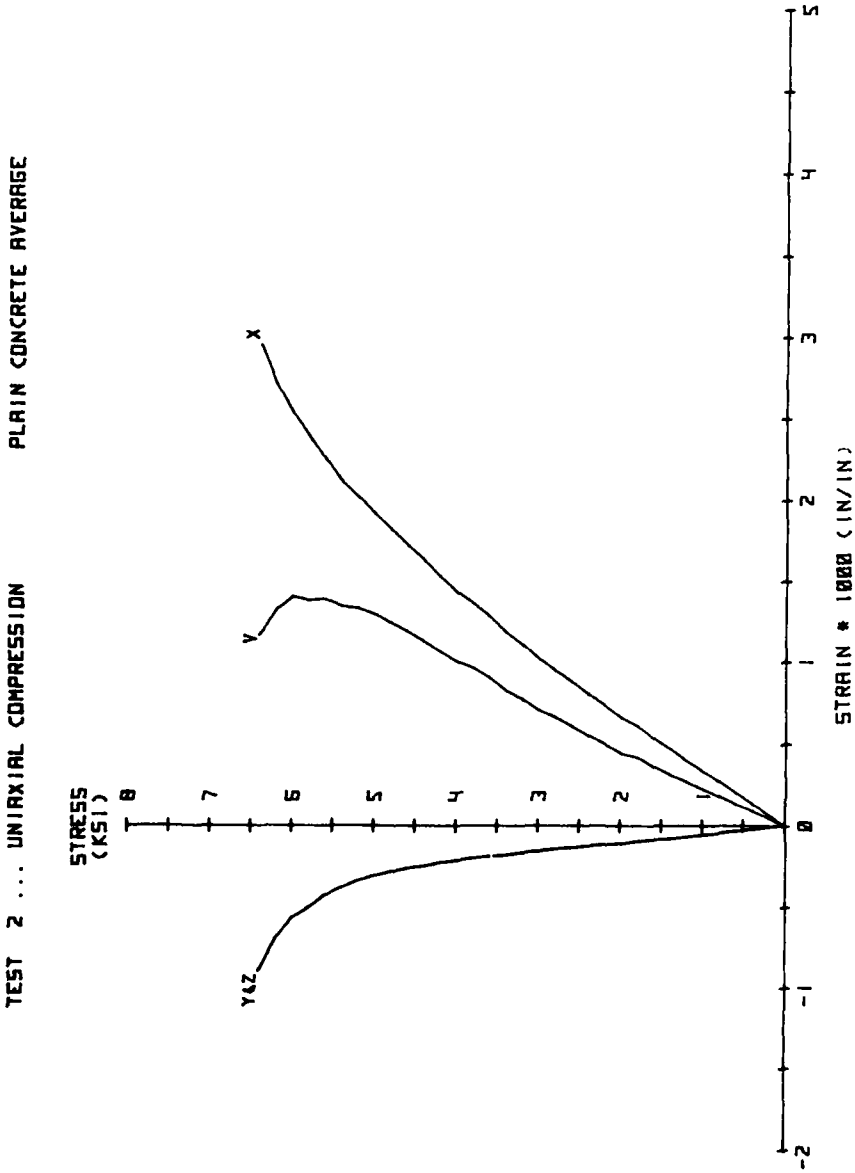

Fig. A.39 Test Results

Table A.40

TEST 2F ... UNIAX COMP SPEC 0,B5 7/9/82

STRESS - STRAIN DATA

	X-AXIS STRESS (PSI)	X-AXIS STRAIN (MILS/IN)	Y-AXIS STRESS (PSI)	Y-AXIS STRAIN (MILS/IN)	Z-AXIS STRESS (PSI)	Z-AXIS STRAIN (MILS/IN)
1	0	0.0000	0	0.0000	0	0.0000
2	200	0.0525	0	-0.0055	0	-0.0049
3	400	0.1049	0	-0.0098	0	-0.0113
4	600	0.1574	0	-0.0258	0	-0.0188
5	800	0.2098	0	-0.0279	0	-0.0261
6	1000	0.2653	0	-0.0314	0	-0.0314
7	1200	0.3151	0	-0.0363	0	-0.0378
8	1400	0.3547	0	-0.0411	0	-0.0345
9	1600	0.4171	0	-0.0429	0	-0.0313
10	1800	0.4729	0	-0.0401	0	-0.0411
11	2000	0.5315	0	-0.0465	0	-0.0441
12	2200	0.5843	0	-0.0544	0	-0.0441
13	2400	0.6330	0	-0.0583	0	-0.0566
14	2600	0.6896	0	-0.0704	0	-0.0612
15	2800	0.7312	0	-0.0763	0	-0.0585
16	3000	0.7756	0	-0.0865	0	-0.0741
17	3200	0.8330	0	-0.0880	0	-0.0727
18	3400	0.8982	0	-0.0977	0	-0.0914
19	3600	0.9748	0	-0.0902	0	-0.0872
20	3800	1.0344	0	-0.1058	0	-0.0942
21	4000	1.0946	0	-0.1140	0	-0.1074
22	4200	1.1511	0	-0.1293	0	-0.1134
23	4400	1.2322	0	-0.1437	0	-0.1359
24	4600	1.2993	0	-0.1530	0	-0.1445
25	4800	1.3487	0	-0.1665	0	-0.1627
26	5000	1.4506	0	-0.1950	0	-0.1747
27	5200	1.5030	0	-0.2149	0	-0.2036
28	5400	1.5336	0	-0.2428	0	-0.2383
29	5600	1.6930	0	-0.2760	0	-0.2743
30	5800	1.7694	0	-0.3172	0	-0.3244
31	6000	1.8537	0	-0.3659	0	-0.3745
32	6200	1.9443	0	-0.4390	0	-0.4567
33	6400	2.0382	0	-0.6057	0	-0.6746

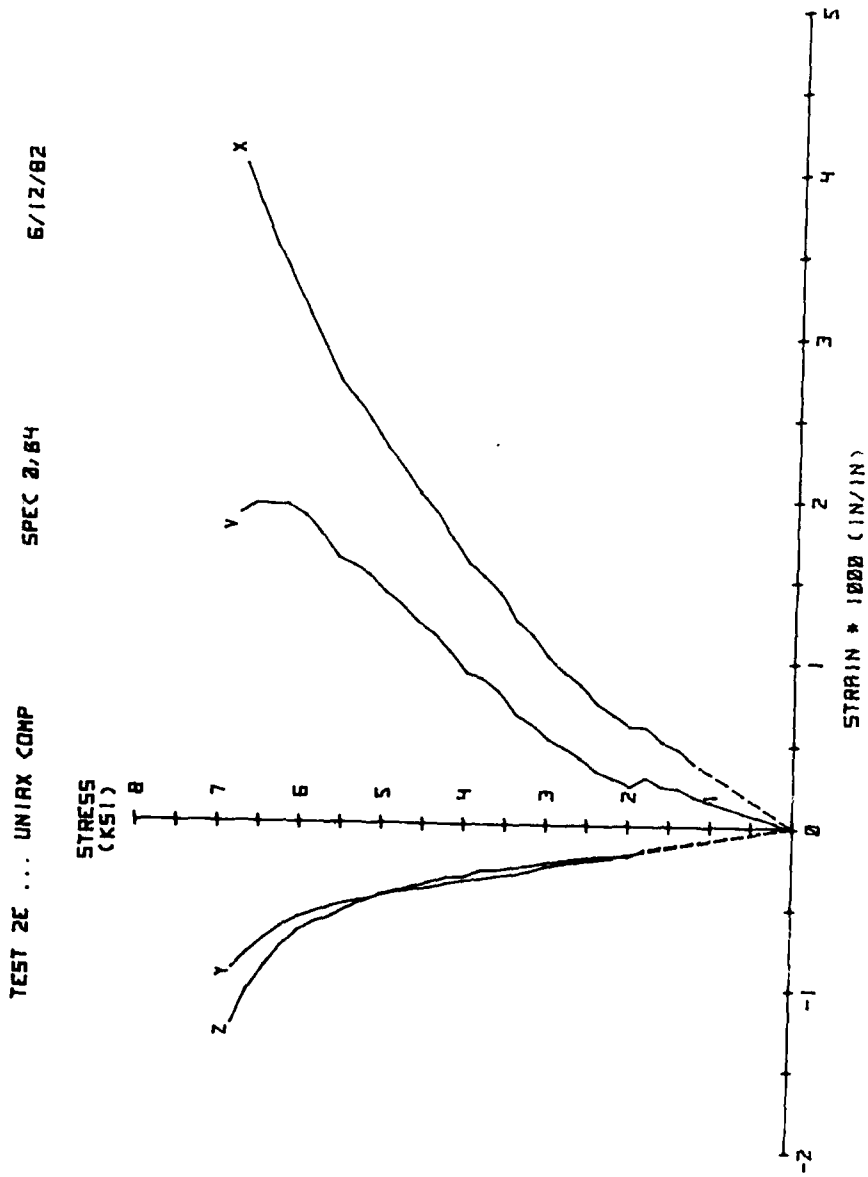

Fig. A.40 Test Results

Table A.41

TEST 2H ... UNIAX COMP SPEC 0,A5 8/9/82

STRESS - STRAIN DATA

	X-AXIS STRESS (PSI)	X-AXIS STRAIN (MILS/IN)	Y-AXIS STRESS (PSI)	Y-AXIS STRAIN (MILS/IN)	Z-AXIS STRESS (PSI)	Z-AXIS STRAIN (MILS/IN)
1	0	0.0000	0	0.0000	0	0.0000
2	300	0.1105	0	-0.0130	0	-0.0065
3	600	0.2209	0	-0.0281	0	-0.0256
4	900	0.3314	0	-0.0475	0	-0.0420
5	1200	0.4419	0	-0.0530	0	-0.0665
6	1500	0.5523	0	-0.0766	0	-0.0657
7	1800	0.6628	0	-0.0681	0	-0.0845
8	2100	0.7510	0	-0.0808	0	-0.0977
9	2400	0.8820	0	-0.0954	0	-0.1120
10	2700	0.9908	0	-0.1128	0	-0.1213
11	3000	1.1054	0	-0.1318	0	-0.1319
12	3300	1.2194	0	-0.1447	0	-0.1375
13	3600	1.3319	0	-0.1630	0	-0.1555
14	3900	1.4352	0	-0.1771	0	-0.1732
15	4200	1.5412	0	-0.2096	0	-0.1960
16	4500	1.6654	0	-0.2297	0	-0.2256
17	4800	1.7902	0	-0.2664	0	-0.2538
18	5100	1.9013	0	-0.3236	0	-0.2887
19	5400	2.0570	0	-0.4297	0	-0.3866
20	5600	2.1852	0	-0.5111	0	-0.4501
21	5800	2.3381	0	-0.7179	0	-0.6079

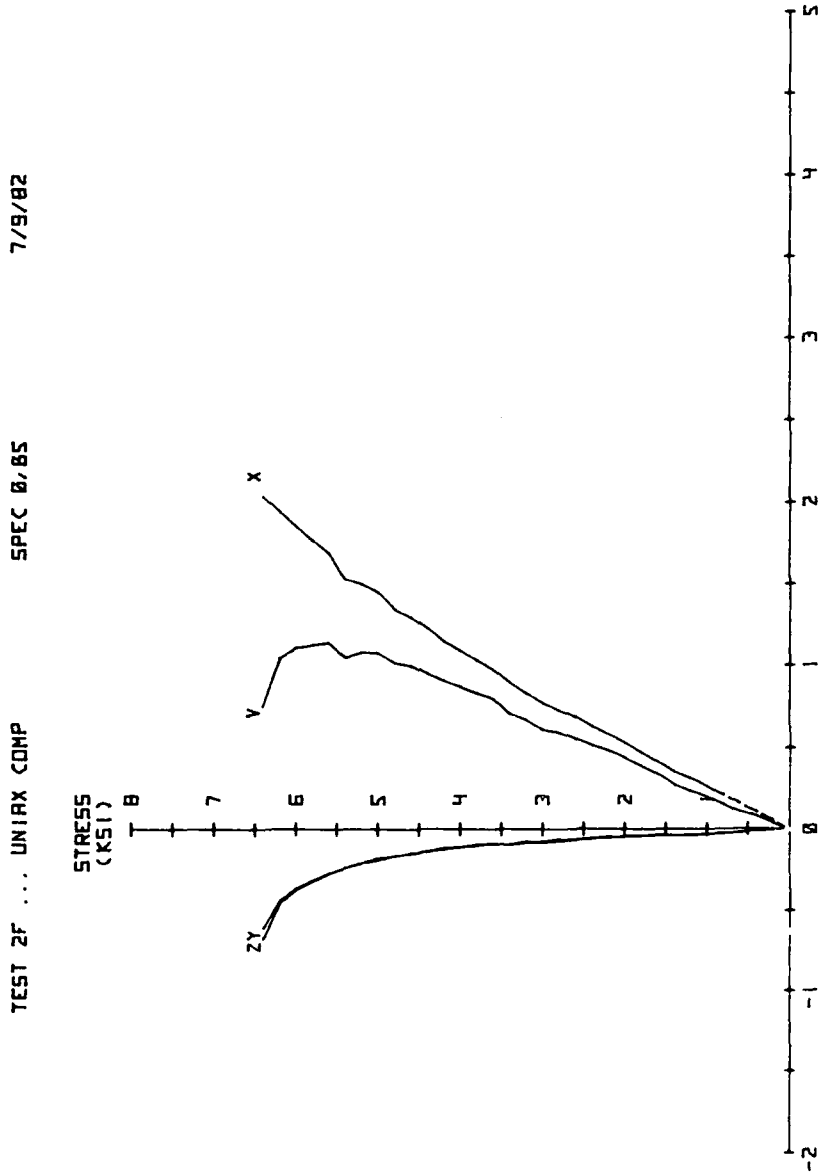

Fig. A.41 Test Results

Table A.42

TEST 2J ... UNIAX COMP SPEC 0,A6 8/10/82

STRESS - STRAIN DATA

	X-AXIS STRESS (PSI)	X-AXIS STRAIN (MILS/IN)	Y-AXIS STRESS (PSI)	Y-AXIS STRAIN (MILS/IN)	Z-AXIS STRESS (PSI)	Z-AXIS STRAIN (MILS/IN)
1	0	0.0000	0	0.0000	0	0.0000
2	200	0.0797	0	-0.0116	0	-0.0122
3	400	0.1593	0	-0.0231	0	-0.0245
4	600	0.2390	0	-0.0347	0	-0.0367
5	800	0.3186	0	-0.0462	0	-0.0490
6	1000	0.3983	0	-0.0578	0	-0.0612
7	1200	0.4779	0	-0.0693	0	-0.0735
8	1400	0.5576	0	-0.0939	0	-0.0999
9	1600	0.6372	0	-0.1007	0	-0.1036
10	1800	0.7169	0	-0.1041	0	-0.1172
11	2000	0.7966	0	-0.1224	0	-0.1254
12	2200	0.8960	0	-0.1286	0	-0.1397
13	2400	0.9697	0	-0.1388	0	-0.1467
14	2600	1.0363	0	-0.1488	0	-0.1537
15	2800	1.1137	0	-0.1596	0	-0.1625
16	3000	1.1937	0	-0.1701	0	-0.1754
17	3200	1.2768	0	-0.1750	0	-0.1884
18	3400	1.3551	0	-0.1889	0	-0.2068
19	3600	1.4273	0	-0.2020	0	-0.2164
20	3800	1.5232	0	-0.2121	0	-0.2304
21	4000	1.5884	0	-0.2246	0	-0.2435
22	4200	1.6856	0	-0.2483	0	-0.2606
23	4400	1.7747	0	-0.2629	0	-0.2768
24	4600	1.8692	0	-0.2790	0	-0.2892
25	4800	1.9692	0	-0.2995	0	-0.3065
26	5000	2.0703	0	-0.3255	0	-0.3271
27	5200	2.1635	0	-0.3515	0	-0.3453
28	5400	2.2732	0	-0.3836	0	-0.3801
29	5600	2.4207	0	-0.4307	0	-0.4158
30	5800	2.5410	0	-0.4787	0	-0.4471
31	6000	2.6915	0	-0.5528	0	-0.5085
32	6200	2.9183	0	-0.6923	0	-0.6195
33	6400	3.3579	0	-1.1307	0	-1.0146

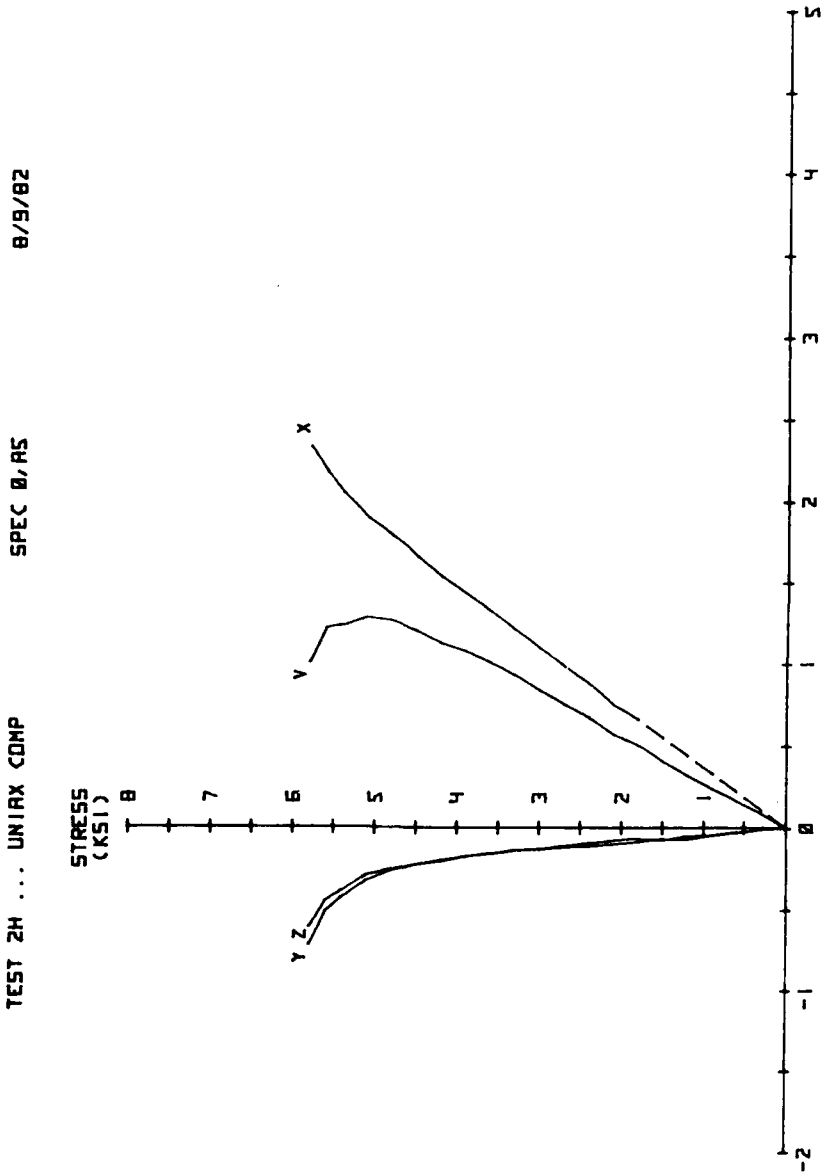

Fig. A.42 Test Results

Table A.43

TEST 11 ... BIAXIAL COMPRESSION (K = 1:10) AVERAGE

STRESS - STRAIN DATA

	X-AXIS STRESS (PSI)	X-AXIS STRAIN (MILS/IN)	Y-AXIS STRESS (PSI)	Y-AXIS STRAIN (MILS/IN)	Z-AXIS STRESS (PSI)	Z-AXIS STRAIN (MILS/IN)
1	0	0.0000	0	0.0000	0	0.0000
2	300	0.0888	30	-0.0108	0	-0.0254
3	600	0.2080	60	-0.0214	0	-0.0502
4	900	0.2771	90	-0.0320	0	-0.0761
5	1200	0.3546	120	-0.0426	0	-0.1036
6	1500	0.4390	150	-0.0719	0	-0.1258
7	1800	0.5168	180	-0.0747	0	-0.1509
8	2100	0.6174	210	-0.0766	0	-0.1746
9	2400	0.7171	240	-0.0915	0	-0.1979
10	2700	0.8109	270	-0.0974	0	-0.2192
11	3000	0.8827	300	-0.0949	0	-0.2514
12	3300	0.9957	330	-0.1009	0	-0.2770
13	3600	1.0984	360	-0.1279	0	-0.2989
14	3900	1.1936	390	-0.1363	0	-0.3169
15	4200	1.2974	420	-0.1558	0	-0.3402
16	4500	1.3938	450	-0.1613	0	-0.3681
17	4800	1.5018	480	-0.1775	0	-0.3991
18	5100	1.6284	510	-0.1943	0	-0.4287
19	5400	1.7504	540	-0.2096	0	-0.4606
20	5700	1.9182	570	-0.2286	0	-0.5073
21	6000	2.0719	600	-0.2519	0	-0.5574
22	6300	2.2053	630	-0.2780	0	-0.6181
23	6600	2.4188	660	-0.3023	0	-0.6858
24	6900	2.6297	690	-0.3371	0	-0.7838
25	7200	2.8681	720	-0.3830	0	-0.9054
26	7500	3.1238	750	-0.4353	0	-1.0652
27	7800	3.4687	780	-0.5175	0	-1.2916
28	8100	3.8656	810	-0.6076	0	-1.6174
29	8400	4.3678	840	-0.7400	0	-2.2736
30	8700	4.9687	870	-0.9194	0	-3.0767
31	9000	5.7533	900	-1.2068	0	-4.7161

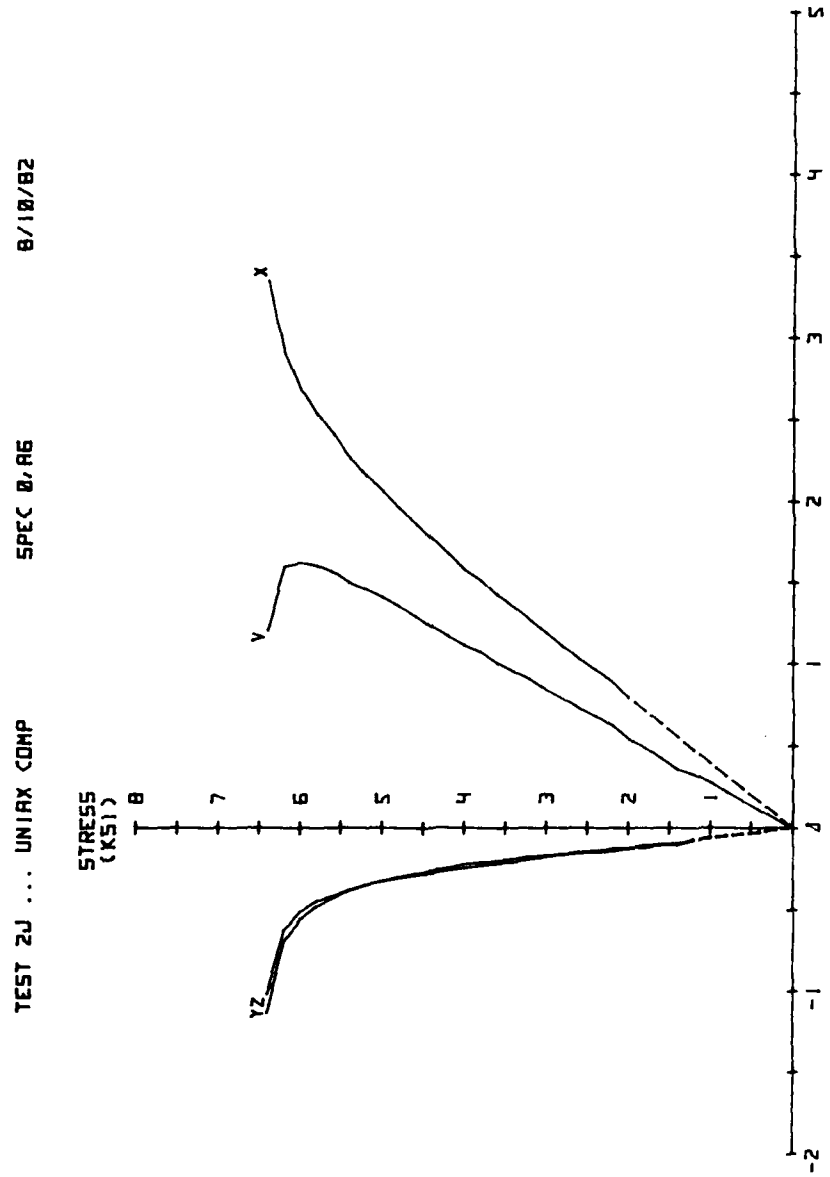

Fig. A.43 Test Results

Table A.44

TEST 11A... BIAX 1:10 SPEC 5-F1 7/28 82

STRESS - STRAIN DATA

	X-AXIS STRESS (PSI)	X-AXIS STRAIN (MILS/IN)	Y-AXIS STRESS (PSI)	Y-AXIS STRAIN (MILS/IN)	Z-AXIS STRESS (PSI)	Z-AXIS STRAIN (MILS/IN)
1	0	0.0000	0	0.0000	0	0.0000
2	300	0.0840	30	-0.0091	0	-0.0178
3	600	0.1652	60	-0.0182	0	-0.0357
4	900	0.2407	90	-0.0273	0	-0.0555
5	1200	0.3114	120	-0.0363	0	-0.0788
6	1500	0.3950	150	-0.0744	0	-0.0913
7	1800	0.4613	180	-0.0730	0	-0.1098
8	2100	0.5564	210	-0.0638	0	-0.1252
9	2400	0.6530	240	-0.0827	0	-0.1402
10	2700	0.7236	270	-0.0892	0	-0.1509
11	3000	0.7927	300	-0.0840	0	-0.1693
12	3300	0.8833	330	-0.0854	0	-0.1936
13	3600	0.9799	360	-0.1132	0	-0.2151
14	3900	1.0558	390	-0.1140	0	-0.2266
15	4200	1.1585	420	-0.1288	0	-0.2437
16	4500	1.2463	450	-0.1319	0	-0.2735
17	4800	1.3442	480	-0.1433	0	-0.2981
18	5100	1.4556	510	-0.1537	0	-0.3239
19	5400	1.5661	540	-0.1649	0	-0.3464
20	5700	1.6921	570	-0.1800	0	-0.3822
21	6000	1.8297	600	-0.2016	0	-0.4240
22	6300	1.9490	630	-0.2227	0	-0.4780
23	6600	2.1210	660	-0.2322	0	-0.5274
24	6900	2.2998	690	-0.2518	0	-0.6039
25	7200	2.5132	720	-0.2824	0	-0.7018
26	7500	2.7406	750	-0.3226	0	-0.8585
27	7800	3.0674	780	-0.3896	0	-1.1785
28	8100	3.5789	810	-0.5253	0	-2.0740
29	8400	4.1784	840	-0.6745	0	-2.9931
30	8700	5.0827	870	-0.9501	0	-4.4706

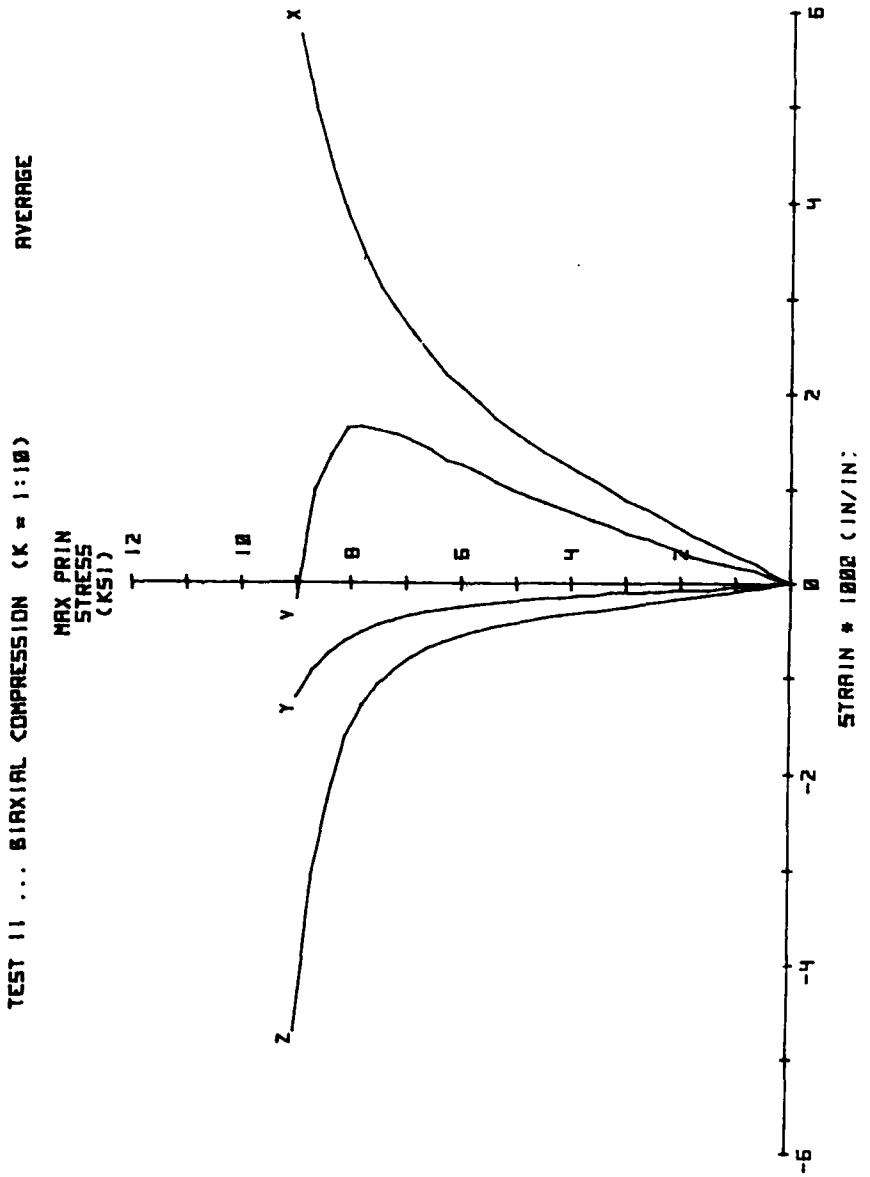

Fig. A.44 Test Results

Table A.45

TEST 11B... BIAX 1:10 SPEC 4,G5 8/7/82

STRESS - STRAIN DATA

	X-AXIS STRESS (PSI)	X-AXIS STRAIN (MILS/IN)	Y-AXIS STRESS (PSI)	Y-AXIS STRAIN (MILS/IN)	Z-AXIS STRESS (PSI)	Z-AXIS STRAIN (MILS/IN)
1	0	0.0000	0	0.0000	0	0.0000
2	300	0,0860	30	-0.0121	0	-0.0318
3	600	0.1629	60	-0.0243	0	-0.0636
4	900	0.2256	90	-0.0364	0	-0.0954
5	1200	0.3100	120	-0.0485	0	-0.1272
6	1500	0.3953	150	-0.0691	0	-0.1590
7	1800	0.4844	180	-0.0762	0	-0.1908
8	2100	0.5906	210	-0.0890	0	-0.2226
9	2400	0.6934	240	-0.1001	0	-0.2545
10	2700	0.8103	270	-0.1052	0	-0.2863
11	3000	0.8849	300	-0.1054	0	-0.3323
12	3300	1.0204	330	-0.1160	0	-0.3592
13	3600	1.1291	360	-0.1423	0	-0.3815
14	3900	1.2435	390	-0.1582	0	-0.4060
15	4200	1.3485	420	-0.1825	0	-0.4356
16	4500	1.4535	450	-0.1903	0	-0.4614
17	4800	1.5715	480	-0.2113	0	-0.4990
18	5100	1.7133	510	-0.2344	0	-0.5323
19	5400	1.8469	540	-0.2540	0	-0.5735
20	5700	2.0564	570	-0.2768	0	-0.6312
21	6000	2.2263	600	-0.3018	0	-0.6896
22	6300	2.3748	630	-0.3331	0	-0.7570
23	6600	2.6289	660	-0.3719	0	-0.8429
24	6900	2.8719	690	-0.4221	0	-0.9625
25	7200	3.1352	720	-0.4833	0	-1.1078
26	7500	3.4192	750	-0.5477	0	-1.2707
27	7800	3.7438	780	-0.6163	0	-1.4733
28	8100	4.1090	810	-0.7122	0	-1.7236
29	8400	4.5760	840	-0.8253	0	-2.0551
30	8700	5.0689	870	-0.9543	0	-2.4720
31	9000	5.6712	900	-1.1641	0	-3.1591
32	9300	6.3360	930	-1.4632	0	-4.9604

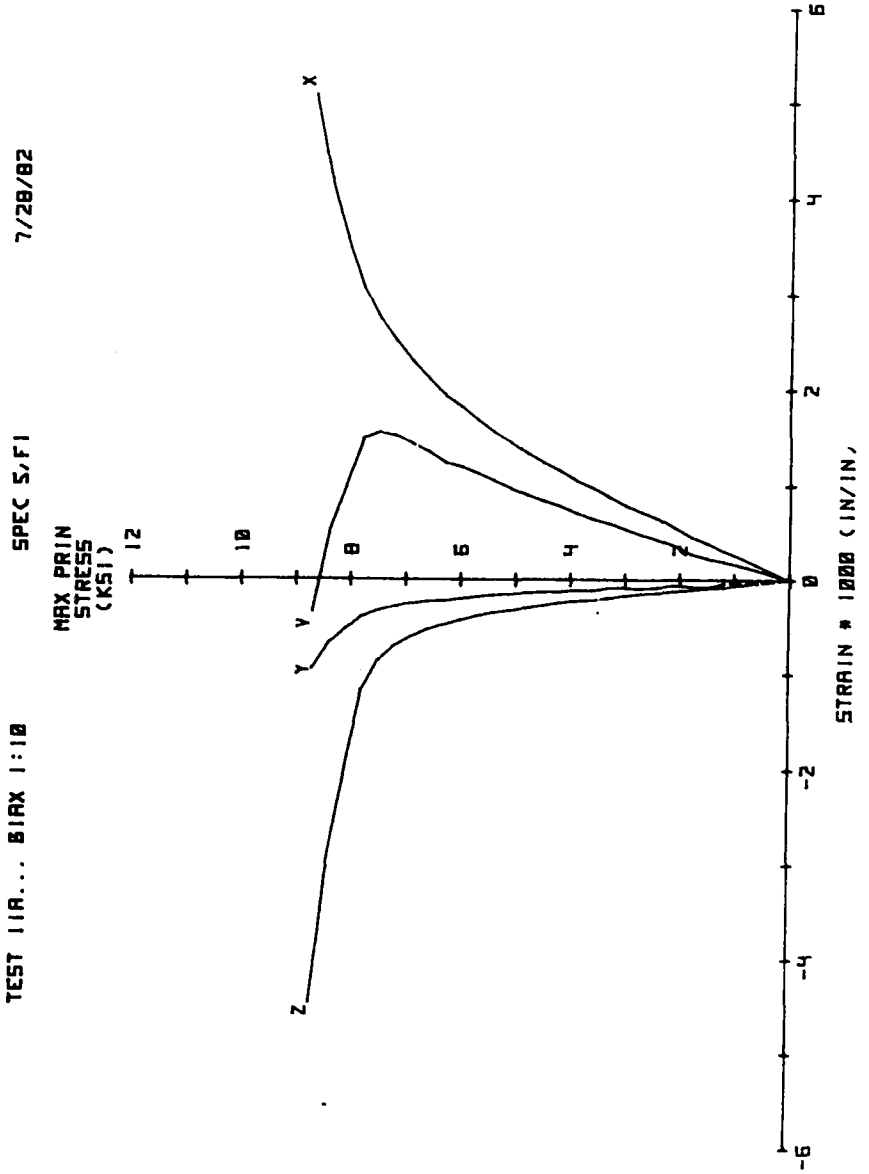

Fig. A.45 Test Results

Table A.46

TEST 3 ... BIAXIAL COMPRESSION (K = 1:3) AVERAGE

STRESS - STRAIN DATA

	X-AXIS STRESS (PSI)	X-AXIS STRAIN (MILS/IN)	Y-AXIS STRESS (PSI)	Y-AXIS STRAIN (MILS/IN)	Z-AXIS STRESS (PSI)	Z-AXIS STRAIN (MILS/IN)
1	0	0.0000	0	0.0000	0	0.0000
2	300	0.0802	100	0.0195	0	-0.0247
3	600	0.1595	200	0.0319	0	-0.0482
4	900	0.2388	300	0.0342	0	-0.0759
5	1200	0.3175	400	0.0396	0	-0.0992
6	1500	0.3935	500	0.0587	0	-0.1234
7	1800	0.4721	600	0.0850	0	-0.1378
8	2100	0.5541	700	0.0971	0	-0.1583
9	2400	0.6338	800	0.1128	0	-0.1817
10	2700	0.7255	900	0.1279	0	-0.2044
11	3000	0.7885	1000	0.1320	0	-0.2310
12	3300	0.8817	1100	0.1432	0	-0.2479
13	3600	0.9575	1200	0.1702	0	-0.2747
14	3900	1.0361	1300	0.1650	0	-0.3048
15	4200	1.0904	1400	0.1755	0	-0.3298
16	4500	1.1991	1500	0.2020	0	-0.3569
17	4800	1.3042	1600	0.2046	0	-0.3859
18	5100	1.4011	1700	0.2174	0	-0.4181
19	5400	1.5003	1800	0.2261	0	-0.4446
20	5700	1.5946	1900	0.2287	0	-0.4898
21	6000	1.7023	2000	0.2620	0	-0.5412
22	6300	1.7900	2100	0.2630	0	-0.5863
23	6600	1.9299	2200	0.3057	0	-0.6314
24	6900	2.0301	2300	0.3062	0	-0.7012
25	7200	2.1688	2400	0.3173	0	-0.7658
26	7500	2.3046	2500	0.3284	0	-0.8464
27	7800	2.4676	2600	0.3432	0	-0.9731
28	8100	2.6387	2700	0.3636	0	-1.0779
29	8400	2.7828	2800	0.3694	0	-1.2217
30	8700	2.9778	2900	0.3959	0	-1.3963
31	9000	3.1468	3000	0.4114	0	-1.6151
32	9300	3.3853	3100	0.4268	0	-1.9175
33	9600	3.6736	3200	0.4708	0	-2.2536
34	9900	3.9159	3300	0.4873	0	-2.5863
35	10200	4.1943	3400	0.5101	0	-2.9867
36	10500	4.5204	3500	0.5305	0	-3.4822
37	10650	4.8139	3550	0.5576	0	-4.0267

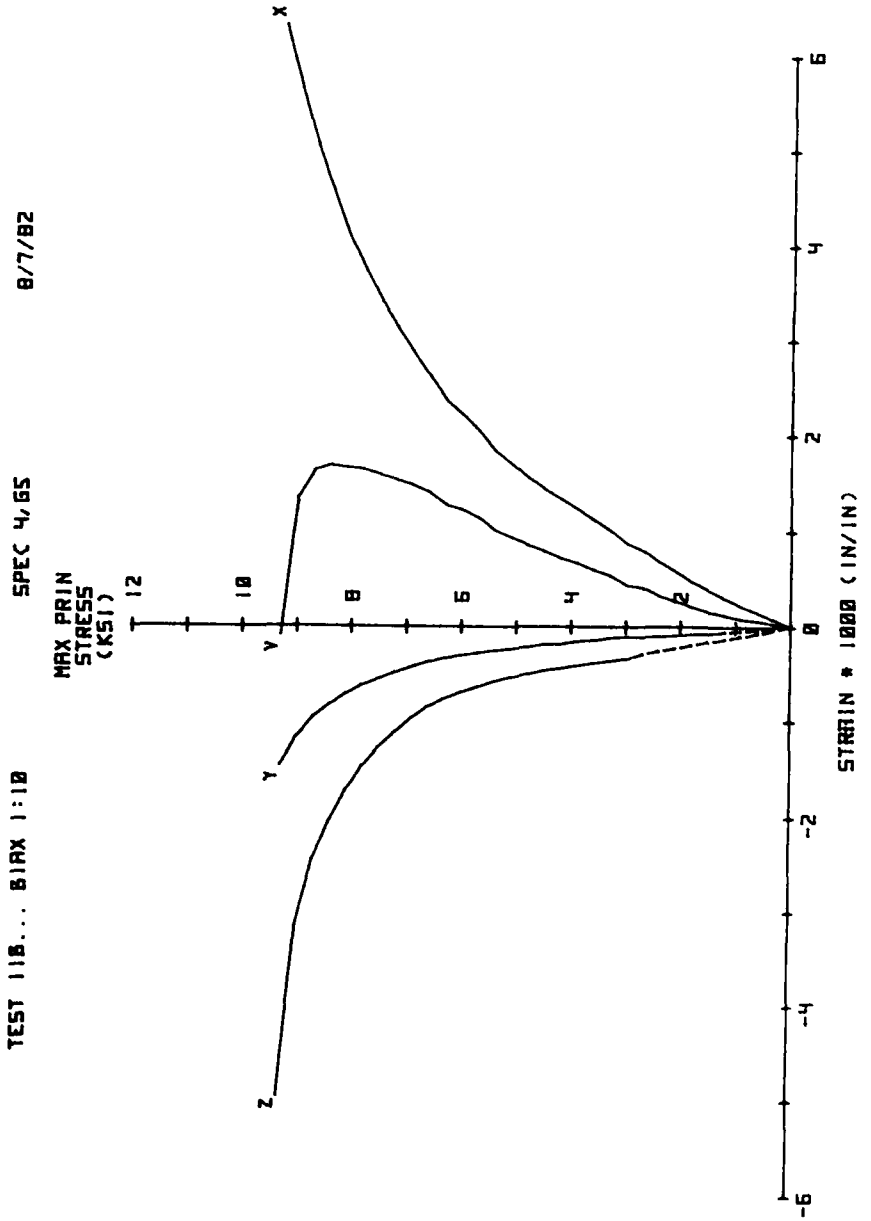

Fig. A.46 Test Results

Table A.47

TEST 3A ... BIAX 1:3 SPEC 5,H6 7/13/82

STRESS - STRAIN DATA

	X-AXIS STRESS (PSI)	X-AXIS STRAIN (MILS/IN)	Y-AXIS STRESS (PSI)	Y-AXIS STRAIN (MILS/IN)	Z-AXIS STRESS (PSI)	Z-AXIS STRAIN (MILS/IN)
1	0	0.0000	0	0.0000	0	0.0000
2	300	0.0763	100	0.0108	0	-0.0310
3	600	0.1526	200	0.0217	0	-0.0509
4	900	0.2289	300	0.0325	0	-0.0710
5	1200	0.3028	400	0.0131	0	-0.0858
6	1500	0.3739	500	0.0329	0	-0.1134
7	1800	0.4552	600	0.0631	0	-0.1280
8	2100	0.5282	700	0.0721	0	-0.1442
9	2400	0.6149	800	0.0845	0	-0.1684
10	2700	0.6963	900	0.1075	0	-0.1888
11	3000	0.7596	1000	0.1042	0	-0.2128
12	3300	0.8647	1100	0.1237	0	-0.2317
13	3600	0.9228	1200	0.1471	0	-0.2583
14	3900	0.9888	1300	0.1328	0	-0.2881
15	4200	1.0451	1400	0.1470	0	-0.3103
16	4500	1.1517	1500	0.1740	0	-0.3367
17	4800	1.2417	1600	0.1697	0	-0.3634
18	5100	1.3471	1700	0.1857	0	-0.3967
19	5400	1.4390	1800	0.1897	0	-0.4195
20	5700	1.5275	1900	0.1897	0	-0.4626
21	6000	1.6235	2000	0.2104	0	-0.5051
22	6300	1.7150	2100	0.2140	0	-0.5477
23	6600	1.8555	2200	0.2542	0	-0.5882
24	6900	1.9446	2300	0.2537	0	-0.6495
25	7200	2.0716	2400	0.2612	0	-0.6983
26	7500	2.1973	2500	0.2732	0	-0.7628
27	7800	2.3326	2600	0.2802	0	-0.8421
28	8100	2.4839	2700	0.2985	0	-0.9396
29	8400	2.6234	2800	0.3013	0	-1.0456
30	8700	2.8162	2900	0.3159	0	-1.1724
31	9000	2.9336	3000	0.3422	0	-1.3214
32	9300	3.1491	3100	0.3606	0	-1.5374
33	9600	3.3808	3200	0.3727	0	-1.7804
34	9750	3.5215	3250	0.3834	0	-1.9822
35	9900	3.6508	3300	0.4067	0	-2.1701
36	10050	3.7861	3350	0.4195	0	-2.3587
37	10200	3.9462	3400	0.4349	0	-2.5324
38	10350	4.0595	3450	0.4475	0	-2.7064
39	10500	4.2078	3500	0.4657	0	-2.8868
40	10650	4.3208	3550	0.4774	0	-3.0728
41	10800	4.4718	3600	0.4941	0	-3.2637
42	10950	4.6120	3650	0.5102	0	-3.4632
43	11100	4.7670	3700	0.5272	0	-3.6758
44	11250	4.9225	3750	0.5431	0	-3.8862
45	11400	5.1367	3800	0.5596	0	-4.1436
46	11550	5.4960	3850	0.6039	0	-4.7178

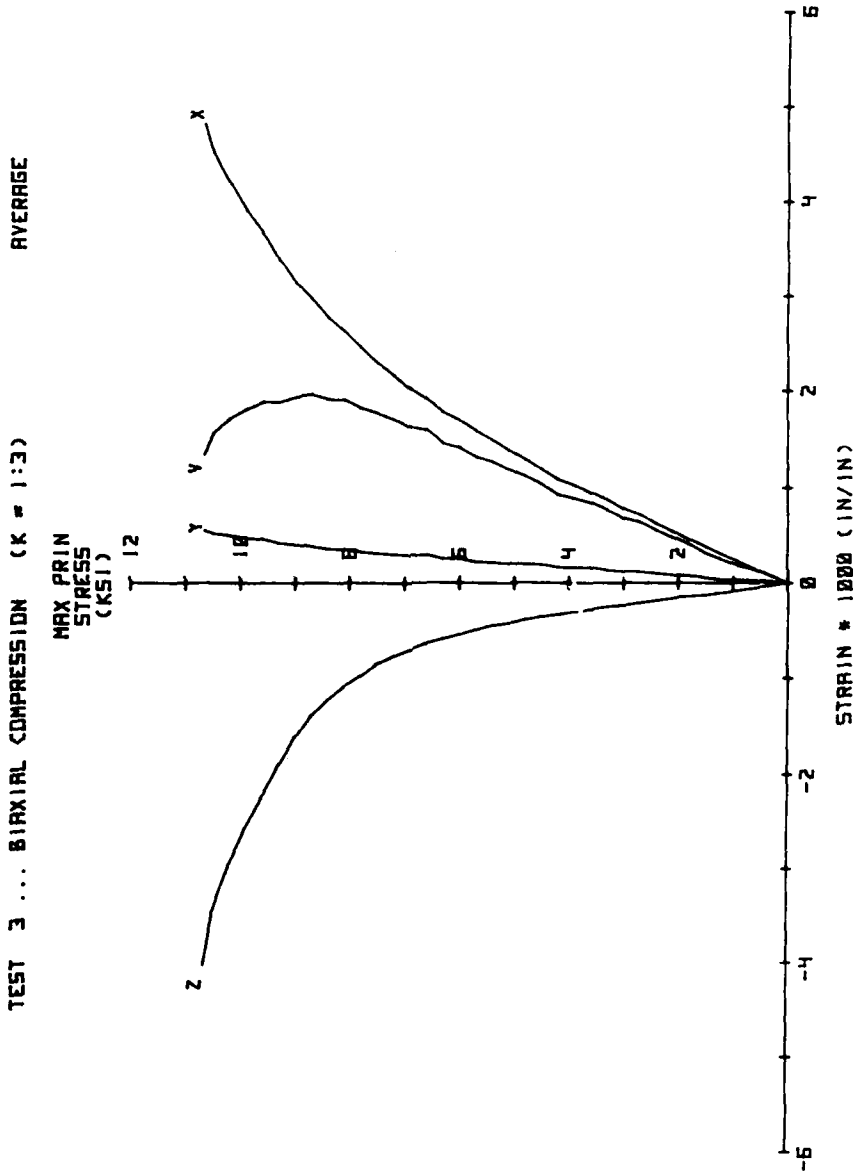

Fig. A.47 Test Results

Table A.48

TEST 3B ... BIAX 1:3 SPEC 4,E2 7/22/82

STRESS - STRAIN DATA

	X-AXIS STRESS (PSI)	X-AXIS STRAIN (MILS/IN)	Y-AXIS STRESS (PSI)	Y-AXIS STRAIN (MILS/IN)	Z-AXIS STRESS (PSI)	Z-AXIS STRAIN (MILS/IN)
1	0	0.0000	0	0.0000	0	0.0000
2	300	0.0823	100	0.0140	0	-0.0250
3	600	0.1645	200	0.0184	0	-0.0597
4	900	0.2513	300	0.0217	0	-0.0836
5	1200	0.3303	400	0.0520	0	-0.1101
6	1500	0.4111	500	0.0704	0	-0.1310
7	1800	0.4870	600	0.0927	0	-0.1452
8	2100	0.5781	700	0.1079	0	-0.1700
9	2400	0.6508	800	0.1269	0	-0.1925
10	2700	0.7527	900	0.1342	0	-0.2174
11	3000	0.8155	1000	0.1457	0	-0.2467
12	3300	0.8967	1100	0.1485	0	-0.2616
13	3600	0.9902	1200	0.1792	0	-0.2887
14	3900	1.0814	1300	0.1830	0	-0.3189
15	4200	1.1338	1400	0.1900	0	-0.3467
16	4500	1.2446	1500	0.2159	0	-0.3746
17	4800	1.3649	1600	0.2254	0	-0.4059
18	5100	1.4531	1700	0.2349	0	-0.4370
19	5400	1.5597	1800	0.2484	0	-0.4672
20	5700	1.6597	1900	0.2536	0	-0.5145
21	6000	1.7792	2000	0.2994	0	-0.5747
22	6300	1.8631	2100	0.2979	0	-0.6225
23	6600	2.0024	2200	0.3430	0	-0.6720
24	6900	2.1137	2300	0.3447	0	-0.7504
25	7200	2.2640	2400	0.3592	0	-0.8308
26	7500	2.4100	2500	0.3695	0	-0.9275
27	7800	2.6008	2600	0.3920	0	-1.1016
28	8100	2.7915	2700	0.4145	0	-1.2137
29	8400	2.9403	2800	0.4234	0	-1.3954
30	8700	3.1375	2900	0.4618	0	-1.6178
31	9000	3.3581	3000	0.4664	0	-1.9063
32	9300	3.6196	3100	0.4788	0	-2.2951
33	9600	3.9021	3200	0.4872	0	-2.8183
34	9750	4.1299	3250	0.4971	0	-3.3332

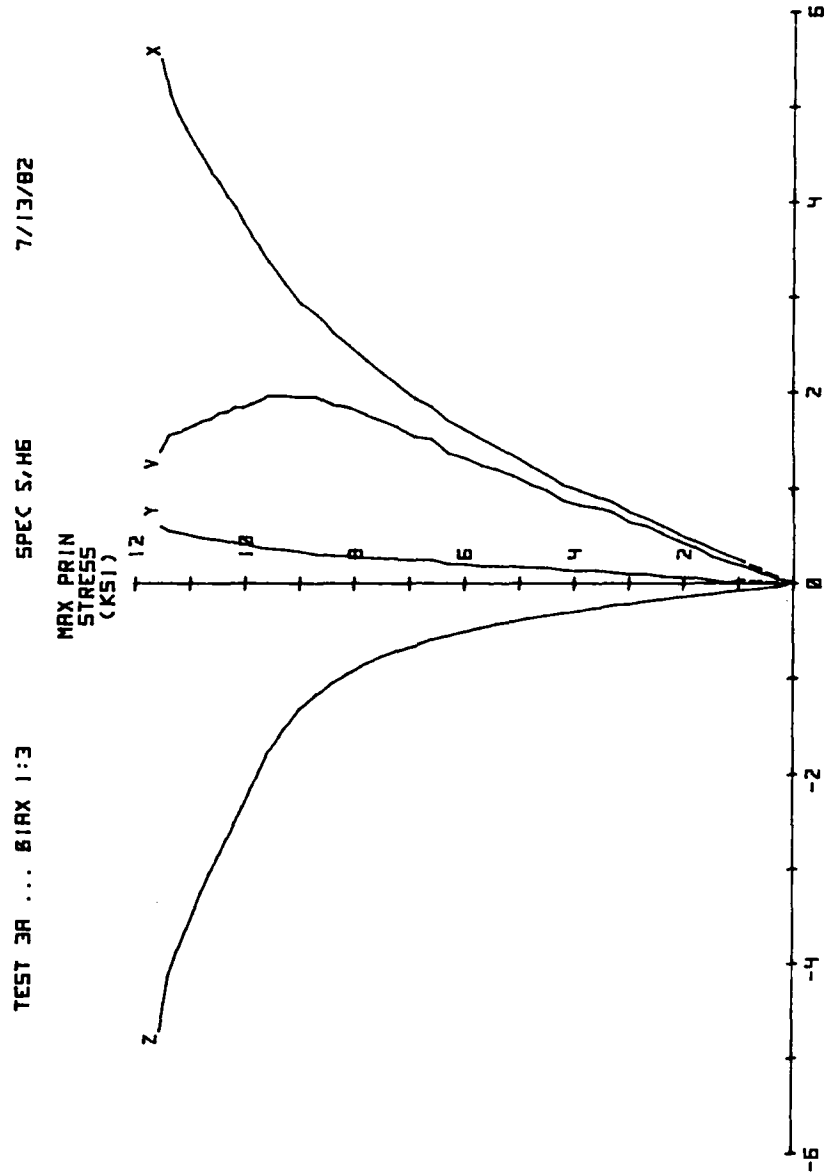

Fig. A.48 Test Results

Table A.49

TEST 4 ... BIAXIAL COMPRESSION (K = 2:3) AVERAGE

STRESS - STRAIN DATA

	X-AXIS STRESS (PSI)	X-AXIS STRAIN (MILS/IN)	Y-AXIS STRESS (PSI)	Y-AXIS STRAIN (MILS/IN)	Z-AXIS STRESS (PSI)	Z-AXIS STRAIN (MILS/IN)
1	0	0.0000	0	0.0000	0	0.0000
2	300	0.0712	200	0.0463	0	-0.0262
3	600	0.1647	400	0.0946	0	-0.0474
4	900	0.2351	600	0.1450	0	-0.0672
5	1200	0.3033	800	0.1779	0	-0.0861
6	1500	0.3801	1000	0.2365	0	-0.1125
7	1800	0.4576	1200	0.2764	0	-0.1283
8	2100	0.5318	1400	0.3217	0	-0.1521
9	2400	0.6449	1600	0.3704	0	-0.1750
10	2700	0.6746	1800	0.4118	0	-0.1951
11	3000	0.7694	2000	0.4599	0	-0.2248
12	3300	0.8527	2200	0.5001	0	-0.2448
13	3600	0.9236	2400	0.5550	0	-0.2732
14	3900	1.0135	2600	0.6164	0	-0.3069
15	4200	1.1056	2800	0.6466	0	-0.3317
16	4500	1.2098	3000	0.6932	0	-0.3676
17	4800	1.2983	3200	0.7515	0	-0.4052
18	5100	1.3930	3400	0.8103	0	-0.4374
19	5400	1.4787	3600	0.8607	0	-0.4759
20	5700	1.5769	3800	0.9297	0	-0.5203
21	6000	1.6626	4000	0.9770	0	-0.5742
22	6300	1.7898	4200	1.0312	0	-0.6283
23	6600	1.8953	4400	1.0884	0	-0.6880
24	6900	2.0260	4600	1.1607	0	-0.7632
25	7200	2.1565	4800	1.2017	0	-0.8488
26	7500	2.2791	5000	1.2613	0	-0.9453
27	7800	2.4355	5200	1.3433	0	-1.0531
28	8100	2.5814	5400	1.4086	0	-1.1846
29	8400	2.7339	5600	1.4669	0	-1.3303
30	8700	2.9021	5800	1.5634	0	-1.5117
31	9000	3.0703	6000	1.6442	0	-1.6984
32	9300	3.3299	6200	1.7196	0	-1.9288
33	9600	3.5719	6400	1.8205	0	-2.1906
34	9900	3.8064	6600	1.9052	0	-2.5038

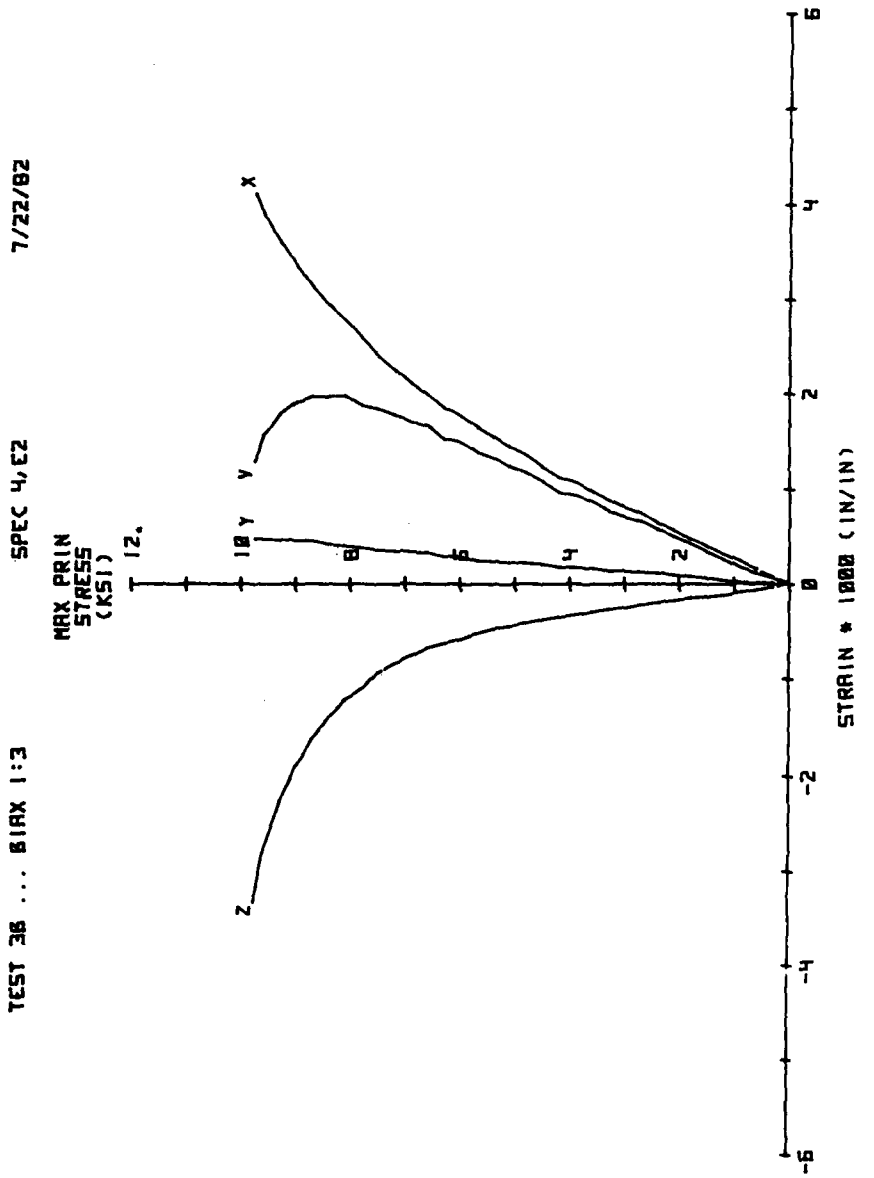

Fig. A.49 Test Results

Table A.50

TEST 4A ... BIAX 2:3 SPEC 4;G1 7/10/82

STRESS - STRAIN DATA

	X-AXIS STRESS (PSI)	X-AXIS STRAIN (MILS/IN)	Y-AXIS STRESS (PSI)	Y-AXIS STRAIN (MILS/IN)	Z-AXIS STRESS (PSI)	Z-AXIS STRAIN (MILS/IN)
1	0	0.0000	0	0.0000	0	0.0000
2	300	0.0737	200	0.0463	0	-0.0222
3	600	0.1657	400	0.0907	0	-0.0476
4	900	0.2295	600	0.1394	0	-0.0668
5	1200	0.2882	800	0.1834	0	-0.0861
6	1500	0.3623	1000	0.2379	0	-0.1117
7	1800	0.4413	1200	0.2806	0	-0.1313
8	2100	0.5020	1400	0.3233	0	-0.1503
9	2400	0.6139	1600	0.3722	0	-0.1804
10	2700	0.6425	1800	0.4125	0	-0.2026
11	3000	0.7277	2000	0.4619	0	-0.2345
12	3300	0.8018	2200	0.5003	0	-0.2559
13	3600	0.8620	2400	0.5532	0	-0.2888
14	3900	0.9583	2600	0.6146	0	-0.3231
15	4200	1.0346	2800	0.6414	0	-0.3487
16	4500	1.1371	3000	0.6821	0	-0.3865
17	4800	1.2139	3200	0.7405	0	-0.4234
18	5100	1.3099	3400	0.7931	0	-0.4605
19	5400	1.3693	3600	0.8366	0	-0.5004
20	5700	1.4651	3800	0.9085	0	-0.544[illegible]
21	6000	1.5594	4000	0.9587	0	-0.601[illegible]
22	6300	1.6905	4200	0.9975	0	-0.6491
23	6600	1.7834	4400	1.0570	0	-0.7062
24	6900	1.9121	4600	1.1280	0	-0.7817
25	7200	2.0299	4800	1.1633	0	-0.8650
26	7500	2.1527	5000	1.2125	0	-0.9520
27	7800	2.3152	5200	1.3034	0	-1.0581
28	8100	2.4757	5400	1.3638	0	-1.1783
29	8400	2.6280	5600	1.4046	0	-1.3100
30	8700	2.7540	5800	1.4939	0	-1.4695
31	9000	2.9706	6000	1.5647	0	-1.6225
32	9300	3.2021	6200	1.6519	0	-1.8420
33	9600	3.4419	6400	1.7268	0	-2.0633
34	9900	3.6939	6600	1.8063	0	-2.3038
35	10200	3.9739	6800	1.9172	0	-2.6068
36	10500	4.2493	7000	1.9939	0	-2.9395
37	10800	4.6382	7200	2.0773	0	-3.5332

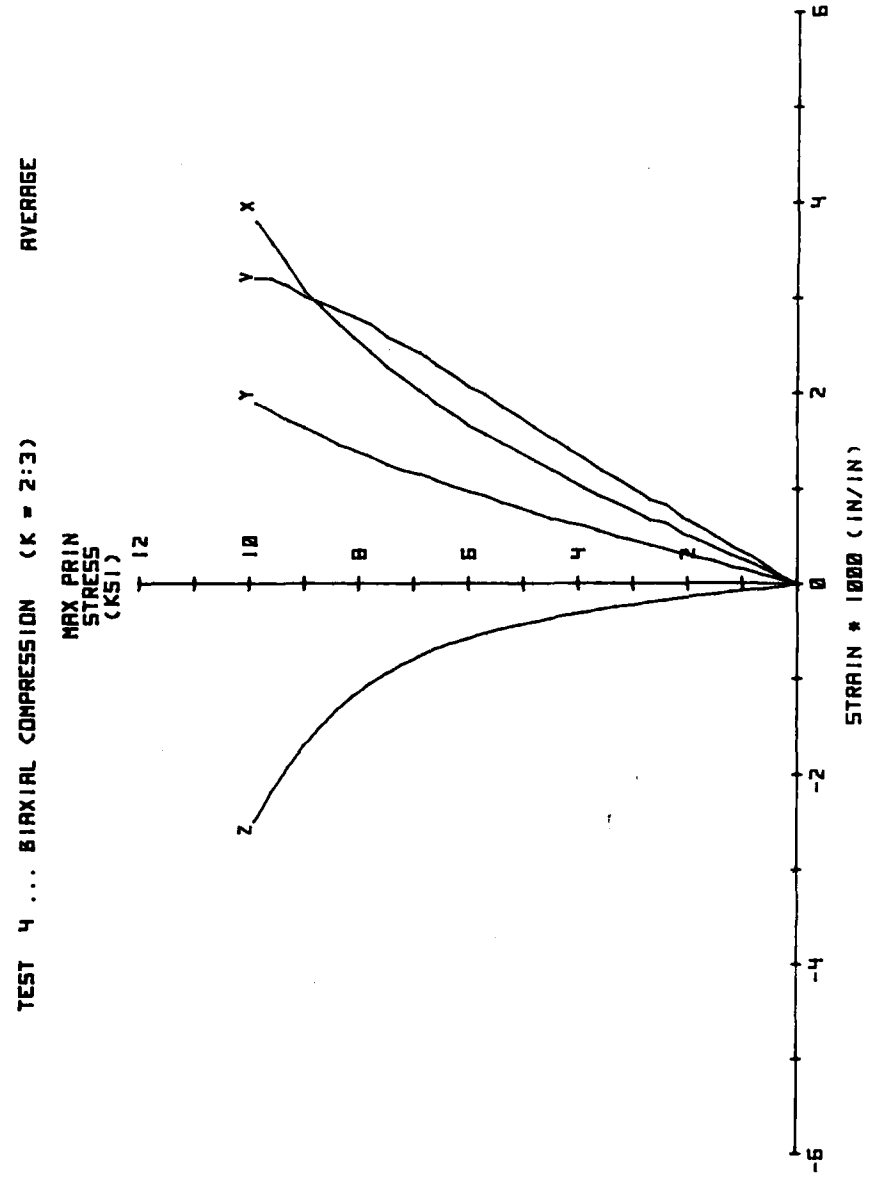

Fig. A.50 Test Results

Table A.51

TEST 4B ... BIAX 2:3 SPEC 5.H3 7/27 82

STRESS - STRAIN DATA

	X-AXIS STRESS (PSI)	X-AXIS STRAIN (MILS/IN)	Y-AXIS STRESS (PSI)	Y-AXIS STRAIN (MILS/IN)	Z-AXIS STRESS (PSI)	Z-AXIS STRAIN (MILS/IN)
1	0	0.0000	0	0.0000	0	0.0000
2	300	0.0804	200	0.0486	0	-0.0265
3	600	0.1755	400	0.1007	0	-0.0434
4	900	0.2524	600	0.1528	0	-0.0640
5	1200	0.3302	800	0.1746	0	-0.0825
6	1500	0.4096	1000	0.2372	0	-0.1096
7	1800	0.4857	1200	0.2743	0	-0.1216
8	2100	0.5733	1400	0.3223	0	-0.1502
9	2400	0.6876	1600	0.3707	0	-0.1660
10	2700	0.7183	1800	0.4132	0	-0.1839
11	3000	0.8227	2000	0.4602	0	-0.2114
12	3300	0.9154	2200	0.5021	0	-0.2301
13	3600	0.9969	2400	0.5590	0	-0.2539
14	3900	1.0805	2600	0.6205	0	-0.2871
15	4200	1.1884	2800	0.6540	0	-0.3111
16	4500	1.2943	3000	0.7066	0	-0.3451
17	4800	1.3945	3200	0.7646	0	-0.3834
18	5100	1.4877	3400	0.8297	0	-0.4106
19	5400	1.5998	3600	0.8870	0	-0.4477
20	5700	1.7004	3800	0.9532	0	-0.4923
21	6000	1.7775	4000	0.9975	0	-0.5434
22	6300	1.9008	4200	1.0671	0	-0.6039
23	6600	2.0190	4400	1.1220	0	-0.6660
24	6900	2.1516	4600	1.1957	0	-0.7409
25	7200	2.2949	4800	1.2423	0	-0.8289
26	7500	2.4173	5000	1.3123	0	-0.9350
27	7800	2.5676	5200	1.3854	0	-1.0444
28	8100	2.6989	5400	1.4556	0	-1.1871
29	8400	2.8515	5600	1.5314	0	-1.3469
30	8700	2.9777	5800	1.6351	0	-1.5502
31	9000	3.1817	6000	1.7260	0	-1.7707
32	9300	3.3752	6200	1.8187	0	-2.0645

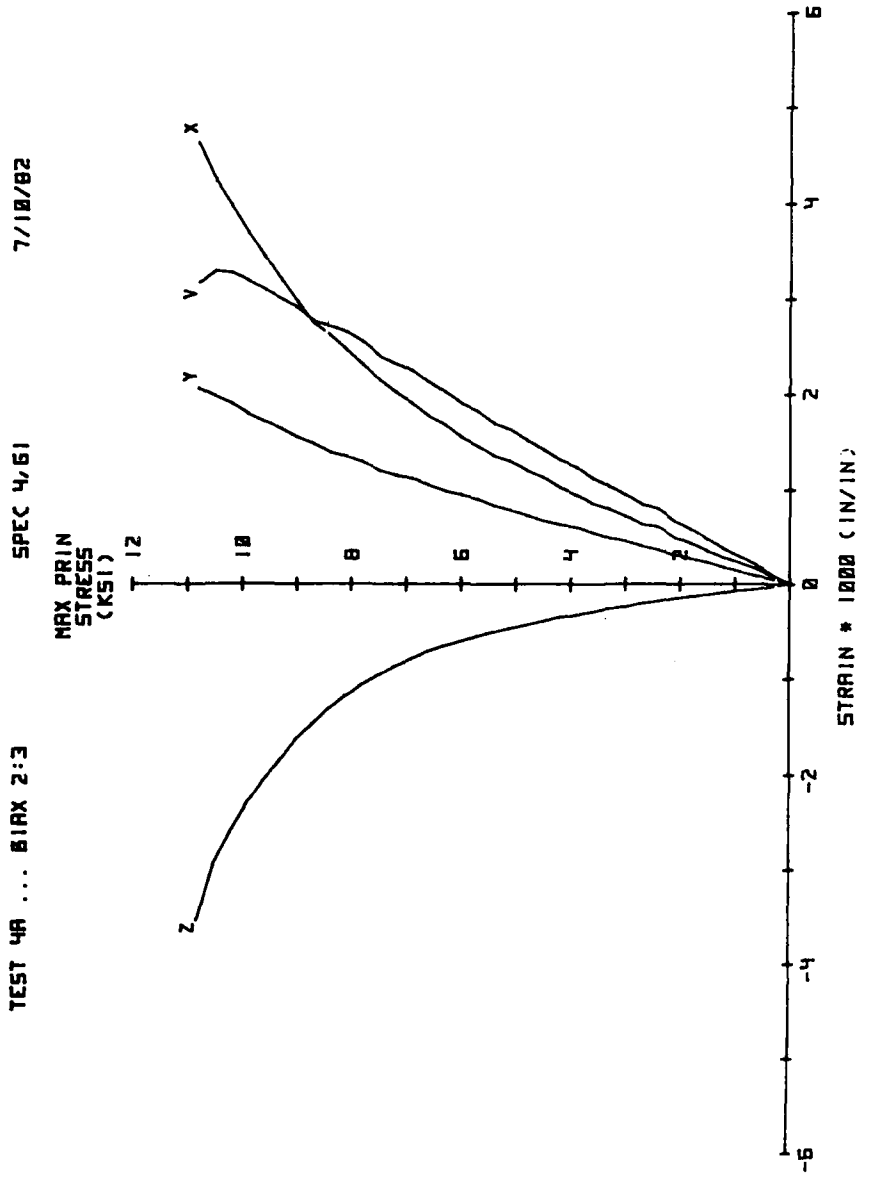

Fig. A.51 Test Results

Table A.52

TEST 5 ... BIAXIAL COMPRESSION (K = 3:3) AVERAGE

STRESS - STRAIN DATA

	X-AXIS STRESS (PSI)	X-AXIS STRAIN (MILS/IN)	Y-AXIS STRESS (PSI)	Y-AXIS STRAIN (MILS/IN)	Z-AXIS STRESS (PSI)	Z-AXIS STRAIN (MILS/IN)
1	0	0.0000	0	0.0000	0	0.0000
2	300	0.0809	300	0.0809	0	-0.0303
3	600	0.1584	600	0.1584	0	-0.0643
4	900	0.2225	900	0.2225	0	-0.0983
5	1200	0.3004	1200	0.3004	0	-0.1323
6	1500	0.3579	1500	0.3579	0	-0.1762
7	1800	0.4370	1800	0.4370	0	-0.2095
8	2100	0.5157	2100	0.5157	0	-0.2346
9	2400	0.5850	2400	0.5850	0	-0.2704
10	2700	0.6636	2700	0.6636	0	-0.3035
11	3000	0.7494	3000	0.7494	0	-0.3287
12	3300	0.8251	3300	0.8251	0	-0.3583
13	3600	0.8934	3600	0.8934	0	-0.3963
14	3900	0.9653	3900	0.9653	0	-0.4387
15	4200	1.0417	4200	1.0417	0	-0.4741
16	4500	1.1503	4500	1.1503	0	-0.5289
17	4800	1.2349	4800	1.2349	0	-0.5753
18	5100	1.3051	5100	1.3051	0	-0.6400
19	5400	1.3933	5400	1.3933	0	-0.7063
20	5700	1.4973	5700	1.4973	0	-0.7702
21	6000	1.6023	6000	1.6023	0	-0.8625
22	6300	1.7213	6300	1.7213	0	-0.9493
23	6600	1.8269	6600	1.8269	0	-1.0980
24	6900	1.9651	6900	1.9651	0	-1.3450
25	7200	2.1027	7200	2.1027	0	-1.7361
26	7500	2.2789	7500	2.2789	0	-2.2422
27	7800	2.4516	7800	2.4516	0	-2.7975
28	8100	2.6504	8100	2.6504	0	-3.4092
29	8400	2.8742	8400	2.8742	0	-4.0424
30	8700	3.1309	8700	3.1309	0	-4.7833
31	8900	3.3079	8900	3.3079	0	-5.3265

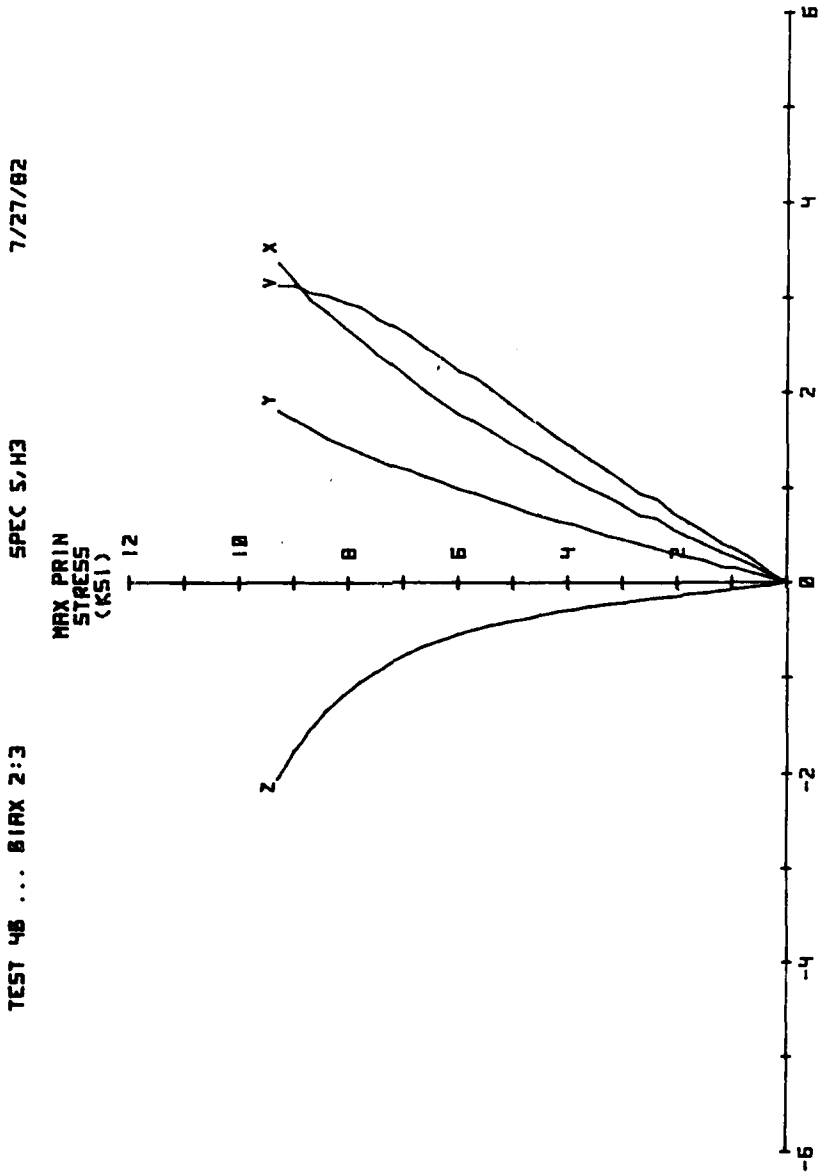

Fig. A.52 Test Results

Table A.53

TEST 5A ... BIAX 3:3 SPEC 5,F3 7/13/82

STRESS - STRAIN DATA

	X-AXIS STRESS (PSI)	X-AXIS STRAIN (MILS/IN)	Y-AXIS STRESS (PSI)	Y-AXIS STRAIN (MILS/IN)	Z-AXIS STRESS (PSI)	Z-AXIS STRAIN (MILS/IN)
1	0	0.0000	0	0.0000	0	0.0000
2	300	0.0837	300	0.0890	0	-0.0302
3	600	0.1685	600	0.1678	0	-0.0604
4	900	0.2331	900	0.2320	0	-0.0906
5	1200	0.3083	1200	0.3162	0	-0.1208
6	1500	0.3538	1500	0.3889	0	-0.1707
7	1800	0.4274	1800	0.4716	0	-0.1865
8	2100	0.5052	2100	0.5587	0	-0.2088
9	2400	0.5773	2400	0.6404	0	-0.2420
10	2700	0.6626	2700	0.7176	0	-0.2759
11	3000	0.7521	3000	0.8088	0	-0.2957
12	3300	0.8277	3300	0.8883	0	-0.3235
13	3600	0.9068	3600	0.9575	0	-0.3615
14	3900	0.9686	3900	1.0300	0	-0.3958
15	4200	1.0598	4200	1.1202	0	-0.4276
16	4500	1.1825	4500	1.2204	0	-0.4731
17	4800	1.2684	4800	1.3054	0	-0.5019
18	5100	1.3493	5100	1.3773	0	-0.5569
19	5400	1.4330	5400	1.4591	0	-0.6041
20	5700	1.5266	5700	1.5457	0	-0.6666
21	6000	1.6236	6000	1.6675	0	-0.7433
22	6300	1.7277	6300	1.7677	0	-0.8172
23	6600	1.8287	6600	1.8993	0	-0.9164
24	6900	1.9548	6900	2.0368	0	-0.9927
25	7200	2.0572	7200	2.1717	0	-1.1554
26	7500	2.2106	7500	2.3315	0	-1.4190
27	7800	2.3686	7800	2.5066	0	-1.7153
28	8100	2.5177	8100	2.6933	0	-1.9899
29	8400	2.6751	8400	2.9109	0	-2.3182
30	8700	2.8524	8700	3.1561	0	-2.6988
31	9000	3.0734	9000	3.4413	0	-3.1586
32	9300	3.2828	9300	3.7369	0	-3.7030
33	9600	3.4761	9600	4.0499	0	-4.4170

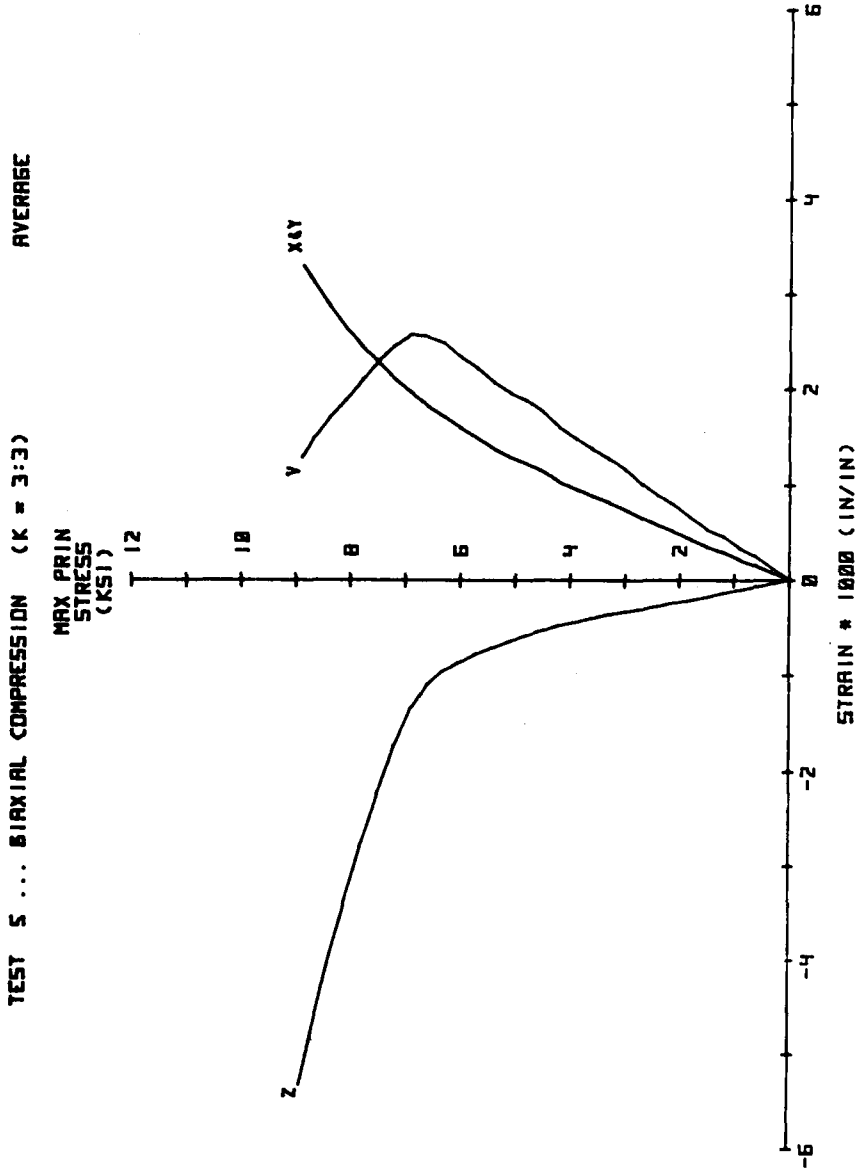

Fig. A.53 Test Results

Table A.54

TEST 5B ... BIAX 3:3 SPEC 4,G4 7/21/82

STRESS - STRAIN DATA

	X-AXIS STRESS (PSI)	X-AXIS STRAIN (MILS/IN)	Y-AXIS STRESS (PSI)	Y-AXIS STRAIN (MILS/IN)	Z-AXIS STRESS (PSI)	Z-AXIS STRAIN (MILS/IN)
1	0	0.0000	0	0.0000	0	0.0000
2	300	0.0943	300	0.0674	0	-0.0378
3	600	0.1606	600	0.1471	0	-0.0756
4	900	0.2203	900	0.2150	0	-0.1134
5	1200	0.2935	1200	0.2943	0	-0.1512
6	1500	0.3534	1500	0.3462	0	-0.1891
7	1800	0.4359	1800	0.4237	0	-0.2399
8	2100	0.5053	2100	0.5043	0	-0.2679
9	2400	0.5638	2400	0.5692	0	-0.3062
10	2700	0.6401	2700	0.6445	0	-0.3384
11	3000	0.7193	3000	0.7282	0	-0.3692
12	3300	0.7946	3300	0.8005	0	-0.4004
13	3600	0.8657	3600	0.8541	0	-0.4387
14	3900	0.9423	3900	0.9310	0	-0.4891
15	4200	1.0063	4200	0.9919	0	-0.5281
16	4500	1.1181	4500	1.0909	0	-0.5923
17	4800	1.2068	4800	1.1697	0	-0.6562
18	5100	1.2692	5100	1.2354	0	-0.7306
19	5400	1.3721	5400	1.3198	0	-0.8159
20	5700	1.4717	5700	1.4326	0	-0.9133
21	6000	1.5680	6000	1.5214	0	-1.0481
22	6300	1.6871	6300	1.6417	0	-1.2786
23	6600	1.8081	6600	1.7379	0	-1.7644
24	6900	2.0029	6900	1.9125	0	-2.5019
25	7200	2.1809	7200	2.0500	0	-3.2842
26	7400	2.3043	7400	2.1638	0	-3.8520
27	7600	2.4424	7600	2.2966	0	-4.4023
28	7800	2.5610	7800	2.4316	0	-4.9337
29	8000	2.7066	8000	2.6062	0	-5.4987
30	8200	2.9132	8200	2.8030	0	-6.2435

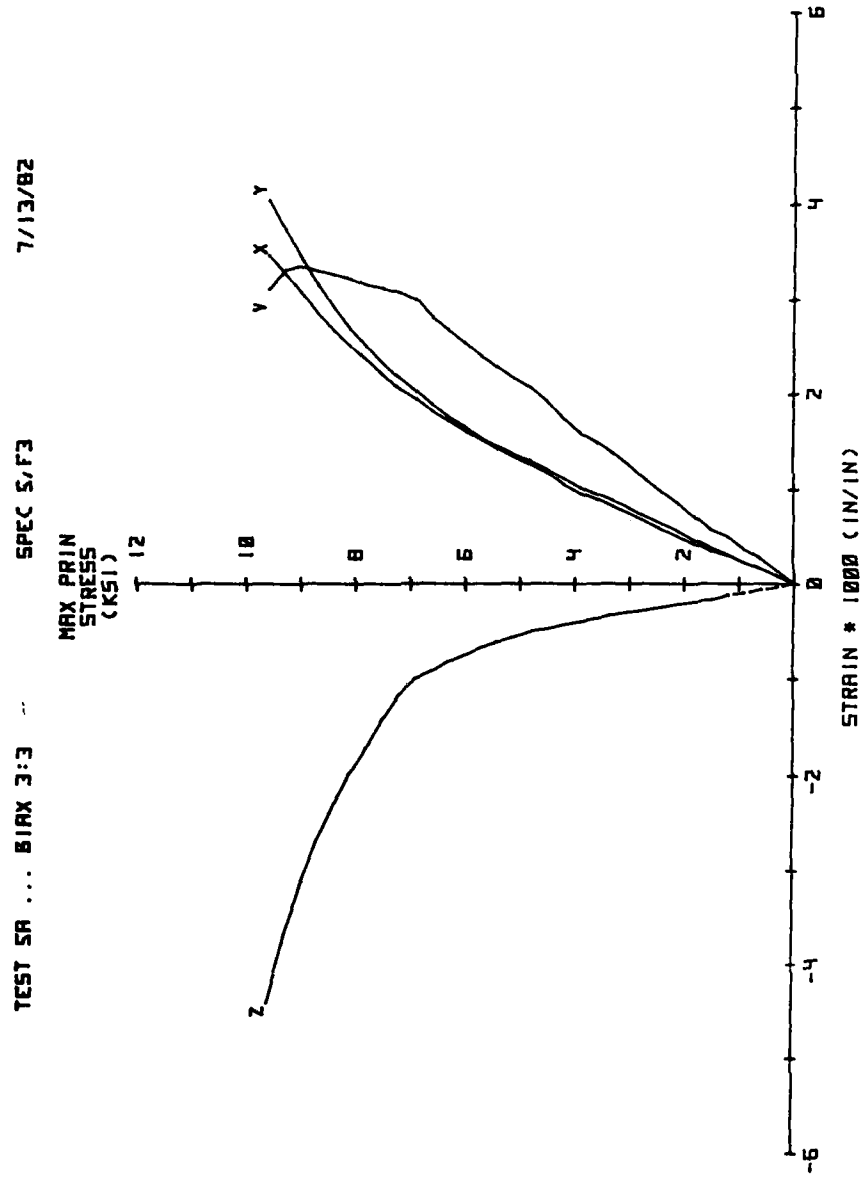

Fig. A.54 Test Results

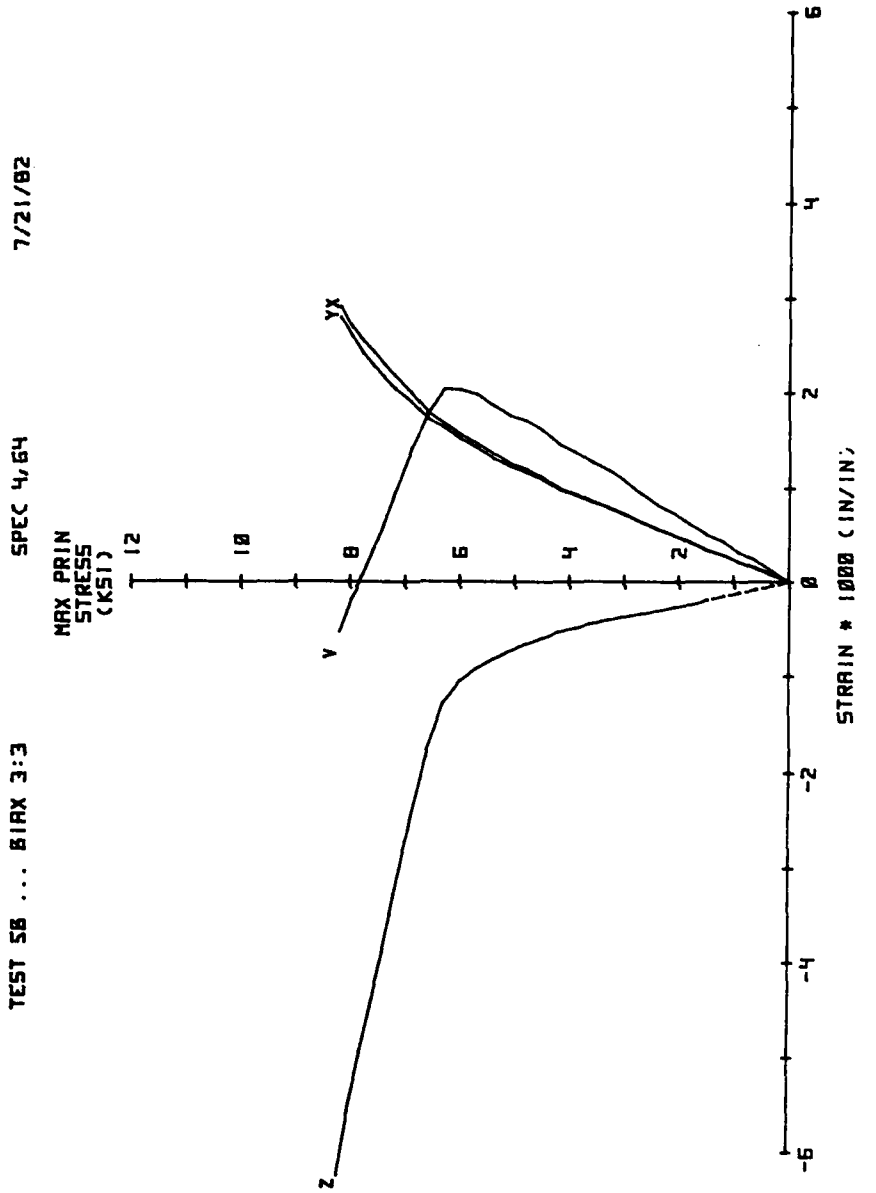

Fig. A.55 Test Results

END

FILMED

1-84

DTIC